



**HAL**  
open science

# Resonant spin dynamics and 3D-1D dimensional crossovers in ultracold Fermi gases

Thomas Reimann

► **To cite this version:**

Thomas Reimann. Resonant spin dynamics and 3D-1D dimensional crossovers in ultracold Fermi gases. Quantum Physics [quant-ph]. Université Paris sciences et lettres, 2018. English. NNT : 2018PSLEE029 . tel-02121773

**HAL Id: tel-02121773**

**<https://theses.hal.science/tel-02121773>**

Submitted on 6 May 2019

**HAL** is a multi-disciplinary open access archive for the deposit and dissemination of scientific research documents, whether they are published or not. The documents may come from teaching and research institutions in France or abroad, or from public or private research centers.

L'archive ouverte pluridisciplinaire **HAL**, est destinée au dépôt et à la diffusion de documents scientifiques de niveau recherche, publiés ou non, émanant des établissements d'enseignement et de recherche français ou étrangers, des laboratoires publics ou privés.

# THÈSE DE DOCTORAT

de l'Université de recherche Paris Sciences et Lettres  
PSL Research University

Préparée à l'École Normale Supérieure

Resonant spin dynamics and 3D-1D dimensional crossovers  
in ultracold Fermi gases

**École doctorale n°564**

PHYSIQUE EN ÎLE-DE-FRANCE

**Spécialité** PHYSIQUE QUANTIQUE

Soutenue par **Thomas Reimann**  
le 13 Décembre 2018

Dirigée par **Christophe Salomon**

## COMPOSITION DU JURY :

M Arnaud Landragin  
CNRS, Président du jury

M Servaas Kokkelmans  
TU Eindhoven, Rapporteur

M Joseph Thywissen  
University of Toronto, Rapporteur

M Ludovic Pricoupenko  
UPMC, Examineur

Mme Juliette Simonet  
Universität Hamburg, Examinatrice

M Christophe Salomon  
CNRS, Directeur de thèse

M Frédéric Chevy  
ENS, Co-Directeur de thèse





Département de physique  
École Normale Supérieure

Laboratoire Kastler Brossel



**THÈSE de DOCTORAT de l'ÉCOLE NORMALE SUPÉRIEURE**  
Spécialité : Physique Quantique

présentée par  
**Thomas Reimann**  
pour obtenir le grade de Docteur de l'École Normale Supérieure

---

**Resonant spin dynamics and 3D-1D dimensional crossovers  
in ultracold Fermi gases**

---

**Soutenu le 13 décembre 2018**  
devant le jury composé de :

<b>Arnaud Landragin</b> .....	Président du jury
<b>Servaas Kokkelmans</b> .....	Rapporteur
<b>Joseph Thywissen</b> .....	Rapporteur
<b>Ludovic Pricoupenko</b> .....	Examineur
<b>Juliette Simonet</b> .....	Examinatrice
<b>Christophe Salomon</b> .....	Directeur de thèse
<b>Frédéric Chevy</b> .....	Co-Directeur de thèse



## Abstract

The exploration of strongly correlated quantum many-body systems represents one of the most challenging fields of research of contemporary physics. Over the past thirty years, dilute vapors of neutral atoms suspended in vacuum and controlled with laser light have become a versatile and powerful platform for the study of such systems. At the very heart lies the ability to arbitrarily tune the interaction strength by means of magnetically induced Feshbach resonances as well as the possibility to create a wide range of potential landscapes via precisely tailored optical fields.

This thesis reports on the recent results of the FerMix experiment, which is dedicated to the study of fermionic quantum many-body-systems at ultralow temperatures using the Alkali atoms  $^{40}\text{K}$  and  $^6\text{Li}$ . The main results presented in this text are twofold. First, we report on the experimental characterization of a novel (s,d)-wave Feshbach resonance in  $^{40}\text{K}$ , the results of which are compared to the corresponding theoretical predictions. In particular, the spectrum of the inelastic loss rate is determined for different temperatures and trap depths, which enables us to identify the losses as two-body processes. Moreover, the dominant entrance channel is confirmed to be s-wave in nature. Using rate equation models we analyze the observed heating of the atomic ensemble and find the behavior to be consistent with the predicted  $L = 2$  bound state present in the exit channel. Finally, we investigate experimentally the dynamics of the spin populations driven by resonantly enhanced inelastic collisions in d-wave, observing good agreement with our numerical models. Second, we summarize our progress towards the study of dimensional crossovers between the Tomonaga-Luttinger liquid in 1D and the Landau-Fermi liquid in 3D using Fermi gases of  $^{40}\text{K}$  confined in a large spacing optical lattice. This includes both the fundamental design considerations as well as the implementation of the required experimental hardware.



## Résumé

L'exploration de systèmes quantiques à  $N$  corps fortement corrélés représente l'un des domaines de recherche les plus stimulants de la physique contemporaine. Au cours des trente dernières années, les vapeurs diluées d'atomes neutres en suspension dans le vide et contrôlées par un laser sont devenues une plate-forme polyvalente et formidable pour l'étude de tels systèmes. L'intérêt principal réside dans la capacité d'ajuster arbitrairement la force de l'interaction atomique au moyen de résonances de Feshbach induites magnétiquement, ainsi que la possibilité de créer une large gamme de potentiels via des champs optiques précisément adaptés.

Cette thèse présente les résultats récents de l'expérience FerMix, consacrée à l'étude des systèmes quantiques à plusieurs corps fermioniques à des températures ultra-basses utilisant les atomes alcalins  $^{40}\text{K}$  et  $^6\text{Li}$ . Les principaux résultats présentés dans ce texte sont doubles. Premièrement, nous rapportons la caractérisation expérimentale d'une nouvelle résonance de Feshbach (s,d)-wave du  $^{40}\text{K}$ , dont les résultats sont comparés aux prédictions théoriques correspondantes. En particulier, le spectre du taux de perte inélastique est déterminé pour différentes températures et profondeurs de piège, ce qui nous permet d'identifier les pertes en tant que processus à deux corps. De plus, il est confirmé que le canal d'entrée dominant est de type s-wave. À l'aide de modèles d'équation de taux, nous analysons le réchauffement observé de l'ensemble atomique et trouvons que le comportement est cohérent avec l'état lié prévu  $L = 2$  présent dans le canal de sortie. Enfin, nous étudions expérimentalement la dynamique des populations de spin induite par les collisions inélastiques renforcées par résonance dans l'onde d, en observant un bon accord avec nos modèles numériques. En second lieu, nous résumons nos progrès dans l'étude des croisements dimensionnels entre le liquide de Tomonaga-Luttinger en 1D et le liquide de Landau-Fermi en 3D en utilisant les gaz de Fermi de  $^{40}\text{K}$  confinés dans un réseau optique à grand pas. Cela inclut à la fois les considérations de conception fondamentales et l'installation du matériel expérimental requis.



# Contents

<b>1. Introduction</b>	<b>13</b>
<b>2. General overview of the experimental apparatus</b>	<b>21</b>
2.1. Overview of the vacuum system . . . . .	23
2.2. Atomic properties of Potassium and Lithium . . . . .	24
2.3. New resonant laser systems . . . . .	26
2.4. Upgrades to computer control of the experiment . . . . .	29
2.5. Lithium oven section and Zeeman slower . . . . .	30
2.6. 2D magneto-optical trap and new Potassium reservoir . . . . .	31
2.7. Dual-species 3D magneto-optical trap . . . . .	34
2.8. $\Lambda$ -enhanced gray optical molasses on the Alkali D1 line . . . . .	36
2.9. Magnetic trapping and transport . . . . .	39
2.10. Evaporation of Potassium in the quadrupole trap . . . . .	42
2.11. Preparation of a degenerate Fermi gas of Potassium-40 . . . . .	45
2.11.1. New optical and magnetic setup around the science cell . . . . .	45
2.11.2. Optical dipole traps and evaporation in the positive states . . . . .	53
2.11.3. Landau-Zener adiabatic passage to the negative states . . . . .	58
2.11.4. New crossed optical dipole trap and evaporation to degeneracy . . . . .	60
 <b>Resonant spin dynamics and Feshbach spectroscopy of Potassium-40</b>	
<b>3. Spin selective detection at low magnetic fields and high temperatures</b>	<b>65</b>
3.1. Stern-Gerlach imaging . . . . .	66
3.2. Optical repumping during time-of-flight . . . . .	69
3.3. Spin selective detection via microwave spectroscopy . . . . .	71
3.3.1. Magnetic dipole transitions in Potassium-40 . . . . .	71
3.3.2. Landau-Zener adiabatic passage . . . . .	74
3.3.3. Microwave spectrum and detection of spin populations . . . . .	75
<b>4. Spin dynamics in the vicinity of a (s,d)-wave Feshbach resonance</b>	<b>79</b>
4.1. Feshbach resonances in ultracold gases . . . . .	80
4.2. Initial experimental findings . . . . .	84

4.3.	Characterization of the resonance via inelastic loss spectroscopy . . . . .	86
4.3.1.	Derivation of the loss rate equations for the shallow trap limit . . . . .	86
4.3.2.	Extraction of the loss rate coefficients from life time measurements . . . . .	91
4.3.3.	Loss rate spectrum and resonance structure . . . . .	94
4.4.	Resonant spin dynamics in (s,d)-wave collisions . . . . .	98
4.4.1.	Calculation of the collision channels' branching ratio . . . . .	98
4.4.2.	Rate equations in the limit of deep trapping potentials . . . . .	100
4.4.3.	Spectrum of the initial heating rates . . . . .	102
4.4.4.	Spin dynamics and verification of the branching ratio . . . . .	103
4.5.	Summary and additional resonances . . . . .	105

## **Towards 3D-1D dimensional crossovers in strongly interacting Fermi gases**

<b>5.</b>	<b>From Fermi- to Luttinger liquids</b>	<b>109</b>
5.1.	Landau Fermi-liquid theory . . . . .	111
5.2.	Tomonaga-Luttinger theory . . . . .	114
5.3.	Momentum-resolved RF spectroscopy . . . . .	117
5.4.	Mapping of the momentum distribution . . . . .	118
5.5.	Dimensional crossovers between normal states in 3D and 1D . . . . .	120
<b>6.</b>	<b>Experimental realization of dimensional crossovers with Potassium-40</b>	<b>123</b>
6.1.	Fundamental design considerations and physical requirements . . . . .	124
6.1.1.	Creation of optical lattices with large spacings . . . . .	124
6.1.2.	Tuning the dimensionality of the atomic dynamics . . . . .	127
6.2.	Preparation and detection of a single row of tubes . . . . .	131
6.2.1.	High power laser system . . . . .	131
6.2.2.	Generation of the tube lattice . . . . .	132
6.2.3.	Calibration of the lattice spacing via matter wave diffraction . . . . .	134
6.2.4.	Site-resolved imaging system . . . . .	135
6.2.5.	Spin selective imaging at high magnetic fields . . . . .	137
6.2.6.	Isolation of a single row of tubes . . . . .	141
6.2.7.	Harmonic confinement for momentum refocusing . . . . .	143
6.2.8.	Optical compensation of gravity . . . . .	150
<b>7.</b>	<b>Summary and outlook</b>	<b>155</b>
<b>8.</b>	<b>Acknowledgements</b>	<b>161</b>

## Appendix

<b>A. Quasi-thermalization of collisionless Fermions</b>	<b>165</b>
<b>B. Additional experimental setups and data</b>	<b>187</b>
B.1. Tailoring arbitrary optical potentials using a digital micromirror device . . .	187
B.2. Magnetic field stability for RF spectroscopy . . . . .	194
B.3. A high power optical dipole trap for Lithium . . . . .	197
B.4. Electronics schematics . . . . .	203
B.4.1. Atomic source security system . . . . .	203
B.4.2. Driver for solenoid valves . . . . .	204
B.4.3. AOM driver supply and breakout box . . . . .	204
B.5. Additional figures and tables . . . . .	205
<b>C. Supplementary theoretical references and experimental methods</b>	<b>207</b>
C.1. Absorption imaging and thermometry of fermionic Potassium . . . . .	207
C.2. Determination of trapping frequencies . . . . .	211
C.3. Calibration of imaging magnification . . . . .	214
C.4. Alkali atoms in static magnetic fields . . . . .	215
C.5. Survey of the known Feshbach resonances of $^{40}\text{K}$ . . . . .	219
<b>Bibliography</b>	<b>242</b>



# Chapter 1

## Introduction

*“The breaking of a wave cannot explain the whole sea.”*

---

(Vladimir Nabokov, *The Real Life of Sebastian Knight*)

The standard model of elementary particles contains the basic building blocks of nature known to date [1]. Among many properties, each of its constituents is characterized fundamentally by its spin, which can be thought of as an internal form of angular momentum [2]. Its magnitude can be either half-integer or integer, dividing the set of elementary particles into two distinct groups, Fermions and Bosons. Matter is made up exclusively of the former while interactions are mediated by bosonic force carriers. Larger composite objects such as neutral atoms consist of many Fermions, whose individual spins add up to form the total angular momentum. Then, depending on whether the result is half-integer or integer, the object is going to stay a Fermion or behave like a Boson, respectively. This fact alone has important consequences for the way matter interacts at the microscopic level [3]. When two identical bosons described by quantum mechanical wavefunctions are brought together, they interfere constructively. Conversely, indistinguishable fermions will interfere destructively. The latter is closely connected to the exclusion principle introduced by W. Pauli in 1925, which states that identical fermions with the same spin cannot occupy the same quantum state simultaneously [4]. For larger assemblies of fermions this principle thus imposes a very strong constraint on how they can occupy the available states, which defines the quantum statistics of the many-body system. By extension, this seemingly basic rule has far-reaching consequences for the physical reality as we know it. For example, apart from dictating how multiple electrons with spin-1/2 are bound to a nucleus, the Pauli principle is directly responsible for the stability of large systems such as solids, that would otherwise collapse due to electrostatic forces [5, 6].

When considering a non-interacting many-body system made up of identical particles at temperature  $T$ , the properties of its ground state attained at very low temperatures change drastically depending on whether Bose- or Fermi-statistics have to be obeyed [7]. This situation is illustrated in fig. 1.1. Bosons will undergo a phase transition when dropping below a certain critical temperature, after which they simultaneously populate

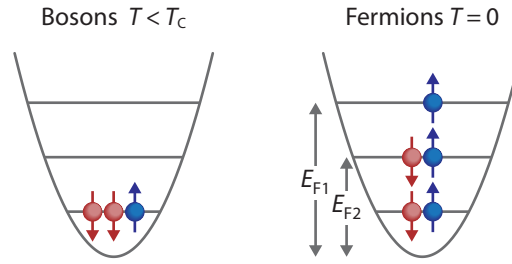


**Figure 1.1.: Quantum statistics of ideal Bosons and Fermions.** Here the simple case of a harmonic potential containing many bound states is depicted, which is populated by identical particles. Bosons (left) undergo a phase transition below a certain critical temperature  $T_C$ , after which all constituents occupy the absolute ground states. Fermions (right) form a Fermi-sea with the states being populated by two particles at a time. Note that here a spin-1/2 system with two possible spin-configurations is considered. If the spin was larger, the maximum occupancy of a given state would increase accordingly.

the lowest energy level (Bose-Einstein condensation). This behavior is driven purely by quantum statistics and stands in stark contrast to Fermions, which must populate the available states from the bottom up, even at zero temperature. The energy of the highest occupied level is referred to as the Fermi energy  $E_F$ , which naturally depends on the total number of particles and available orientations of the spin. The resulting many-body state is referred to as a Fermi-sea, whose edge at  $E_F$  is sharp at  $T = 0$  and begins to blur as the temperature increases. Contrary to bosons, this behavior corresponds to a smooth cross-over between the deeply quantum-degenerate regime and the classical behavior obtained at large temperatures and low densities  $n$ . The departure from quantum mechanical behavior is caused by the decrease of the particles' wavelengths  $\lambda = h/(2\pi mk_B T)^{1/2}$ , which are now much smaller than the average spacing  $n^{-1/3}$  between them. As a result, the gas behaves classically and its statistics are given by Boltzmann distributions, irregardless of whether the constituents are Bosons or Fermions.

Apart from mere quantum statistics, the macroscopic properties of a many-body system are also affected by the nature and strength of the interactions between its constituents. Surprisingly, the assumption of weak or even negligible coupling already allows for the description of many materials, even when the underlying interactions are strong. A prominent example in this regard is the conductivity of metals as well as the associated distinction between insulators and (semi-)conductors, which can be understood in terms of the band-structure of free, non-interacting electrons moving in periodic potentials [8]. Conventional BCS superconductivity represents another effect that can be explained via weak attractive interactions mediated by phonons, albeit non-perturbative, which lead to pairing of electrons in momentum space forming so-called cooper pairs [9]. Moreover, despite the presence of (strong) Coulomb interactions in solids, electronic phenomena

can be mapped within certain limits onto systems of weakly interacting fermionic quasiparticles. This notion is the very foundation of Landau's Fermi-liquid theory [10, 11], which, for example, successfully describes at low temperatures the normal state of most metals and of liquid Helium-3 [12].

Notwithstanding these past breakthroughs, strongly correlated quantum many-body systems still represent one of the most challenging fields of research of contemporary physics, oftentimes defying both theoretical and numerical analysis. An emblematic example in this context is the strongly debated mechanism giving rise to high- $T_C$  superconductivity, which was discovered in quasi-2D cuprates in 1986 [13]. Even in situations where the microscopic Hamiltonian is known, the sheer complexity arising from strong correlations and large particle numbers increases the dimension of the Hilbert space of a given problem exponentially such that modern computational capacities are quickly rendered insufficient [14]. In addition, quantum Monte Carlo techniques applied to fermionic systems suffer from the so-called sign problem since the required antisymmetry of the wavefunction requires the numerical integration of rapidly oscillating functions [15, 16].

Historically, the alternative to theoretical analysis is the use of a device that mimics the behavior of the system of interest [17]. This way, the position of stars and planets could already be predicted during the Classical Antiquity by making use of mechanical astrolabes [18], well before gravitational forces were understood in a quantitative fashion. This notion was reformulated in 1982 by R. Feynman [19] in that the problem of 'solving' strongly correlated quantum systems may be addressed by resorting to artificially engineered quantum systems, which are designed to emulate the same behavior. The technical realization of such analog simulators on the quantum mechanical level requires extremely high degrees of control, accessibility and absence of dissipation. It must be possible to implement the Hamiltonian under consideration, prepare the correct quantum state and read it out via precision measurements. These prerequisites cannot be met within the experimental scope of traditional condensed matter physics, especially in the context of local probing and the control over interactions.

### **Quantum simulation with cold atoms**

Owing to the progress of laser cooling- and trapping techniques for neutral atoms suspended in vacuum [20], dilute quantum degenerate gases have evolved into a promising platform for the study and simulation of quantum many body systems. The first proposals for laser cooling were put forward in the 1970s by A. Ashkin [21] as well as T. Hänsch and A. Schawlow [22]. After only 10 years, cooling [23] and trapping [24–26] of neutral atoms was realized experimentally, to be quickly followed by the preparation of the first Bose-Einstein condensates in 1995 [27, 28] with the help of evaporative cooling techniques. This scientific milestone demonstrated for the first time that cold atoms are indeed suitable

to create many-body states exhibiting properties like superfluidity [29] or spatial coherence [30, 31]. The first degenerate Fermi gas soon followed in 1999 [32].

Since these early breakthroughs, the field of cold atom research has undergone incredible growth [14, 17, 33, 34], both in terms of technological capabilities as well as regarding the plethora of systems which have already been studied in the search for novel states of matter. Several key aspects represent the foundation of this ever-increasing toolbox used for quantum simulation. A great variety of conservative potentials can be tailored by means of appropriate laser beam shaping since the dipole gradient force inherits its spatial properties directly from the underlying optical intensity field [35]. Cold neutral atoms can thus be trapped practically without dissipation, either in the form of bulk systems or in periodic potentials created by optical lattices to implement, for example, Bose- or Fermi-Hubbard models [36]. Moreover, this also allows for the creation of disordered potentials [37] as well as to adjust the dimensionality of the dynamics at hand. Detection of atoms can be achieved, for example, by means absorption or fluorescence imaging with the latter reaching even the single atom level [38], providing direct access to the microscopic correlations. Conversely, (near-)resonant electromagnetic radiation can be used for the control of quantum state populations via optical pumping or Landau-Zener transitions as well as for probing the effects of inter-atomic interactions [39]. Furthermore, artificial Gauge fields can be realized in a large variety of systems by using laser assisted transitions [40], which allows to mimic the physics of charged particles.

Finally, the interaction strength between ultracold atoms can be tuned almost arbitrarily via magnetically induced Feshbach resonances [41]. This makes it possible to reach the strongly correlated regime in otherwise weakly interacting quantum many-body systems or to turn off interactions entirely to prepare ideal, non-interacting systems. Typically, such resonances are used to tune the  $s$ -wave scattering length of contact interactions at low collision energies. In this context, the experimental characterization of a previously unreported ( $s, d$ )-wave Feshbach resonance in  $^{40}\text{K}$  represents one of the main results of this thesis.

Apart from resonant scattering, the nature of the interactions as well as the quantum statistics depends on the choice of atomic species. Alkalis typically collide via short-ranged van-der-Waals forces at low temperatures [33]. However, (strong) long-range interactions can be obtained when working with highly magnetic atoms, such as Erbium [42] and Dysprosium [43], or with polar molecules [44] or Rydberg atoms [45].

### **Fermi gases with tunable interactions**

Ultracold Fermi gases are about one million times less dense than air and roughly 100 million times colder than interstellar space. Fermi energies usually lie in the  $E_F/k_B \sim 1 \mu\text{K}$  range, which is to be contrasted with the corresponding values obtained for electrons in

Metals where  $E_F$  typically assumes values between  $k_B \times 10^4$  K and  $10^5$  K. In both cases, however, interactions are typically short-ranged. In metals, this is due to Coulomb-screening while in cold atom systems it stems from the effective range of the Van-der-Waals forces. At low temperature the properties of elastic scattering between atoms can be described by using a single parameter, the  $s$ -wave scattering length  $a$ . This is due to the fact that the de Broglie wavelength of scattered waves is much larger than the range of the interaction potential, so that the microscopic details of the interaction do not matter. The resulting two-body physics arising from such contact-type collisions is then sufficient to account for the entire Fermionic many-body system [34]. At zero collision energy,  $a$  can be made to diverge by means of Feshbach resonances so that the scattering cross section reaches its unitary upper bound as set by quantum mechanics. A detrimental side effect of using Feshbach resonances is that they tend to enhance inelastic losses such as three-body recombination as well. While this does represent a stringent limitation for Bosons, Fermions are at least partially protected against such inelastic three-body losses by the Pauli exclusion principle.

The possibility to tune the strength of interactions has enabled the study of superfluidity and pair condensation in the smooth crossover [46, 47] from a Bose-Einstein condensed phase of tightly bound dimers to a Bardeen-Cooper-Schrieffer type superfluid consisting of large Cooper pairs. The exploration of the corresponding phase diagram has been the subject of numerous experiments, both for spin-balanced [34] and imbalanced Fermi gases [48]. The former is shown in fig. 1.2, which depicts as well the normal regions of the gas at higher temperatures. Imbalanced Fermi gases will be discussed in great detail in chapter 5, including their normal states which exist beyond the regimes of superfluidity, such as the Landau Fermi-liquid (FL) in three dimensions and the Tomonaga-Luttinger-liquid (TLL) in one dimension.

As there are only contact interactions present in the system's Hamiltonian, in the spin-balanced case all thermodynamic quantities depend only on the three length scales:<sup>1</sup> The inter-particle spacing  $n^{-1/3}$ , the de Broglie wavelength  $\lambda$  and the  $s$ -wave scattering length  $a$ . The corresponding energy scales are the Fermi energy  $E_F$ , the 'thermal' energy  $k_B T$  and  $\hbar^2/ma^2$ , the latter describing the energy of a molecular bound state when  $a > 0$ . The equations of state depend only on these energy and length scales and are universal in the sense that they neither reflect the microscopic properties of the interaction nor the species of the atoms constituting the gas [52]. On top of a Feshbach resonance where the interactions become unitary, the Fermi gas furthermore enters a universal regime of scale-invariance. The sole remaining energy scales in the system are the Fermi Energy  $E_F$  and the temperature. With the absence of any length scale, the thermodynamics of such a gas are universal and may be related, for instance, to the physics occurring in the crust of

<sup>1</sup>Imbalanced spin populations introduce two additional length scales.

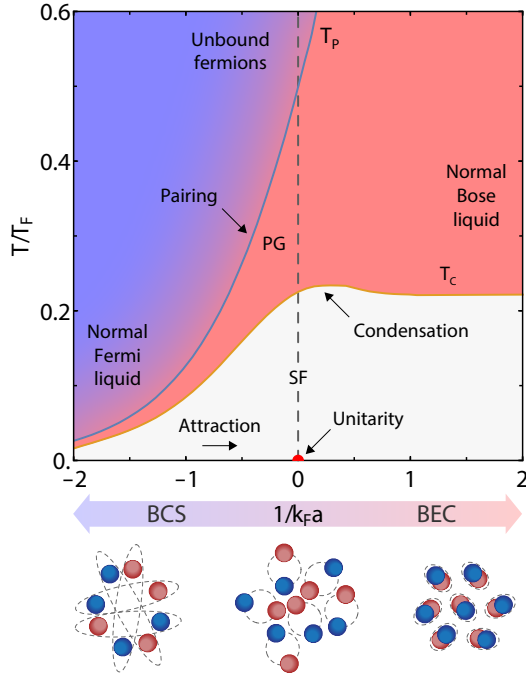


**Figure 1.2.: Phase diagram of the BEC-BCS crossover in a balanced Fermi gas.** The figure shows the evolution of the ground state with increasing attractive interactions and temperature. The latter has two relevant scales: At  $T_P$  pairs begin to form in momentum space and the critical temperature  $T_C$  indicates the onset of phase-coherence between them [49]. When  $1/k_{Fa} < 0$  and  $T < T_C$  the fermions are in a superfluid state consisting of large spatially overlapping Cooper pairs. Here,  $T_C$  and  $T_P$  are essentially the same. Contrarily, when  $1/k_{Fa} > 0$ ,  $T_C$  and  $T_P$  differ and the particles are tightly bound in real space, forming a molecular non-interacting Bose-Einstein condensate. In the unitary limit  $1/k_{Fa} = 0$  the ground state consists of strongly correlated pairs of size  $\sim 1/k_F$ . Figure based on [50, 51].

neutron stars. At zero temperature, the Fermi energy  $E_F$  is the only remaining intensive energy scale. As a result, the total energy  $E$  of the gas is given by its non-interacting counterpart  $E_0$  through a universal constant as per:

$$E = \xi E_0,$$

Similarly, one has for the chemical potential that  $\mu = \xi E_F$ . The dimensionless constant  $\xi = 0.37$  is referred to as the Bertsch parameter, which has received a great deal of theoretical interest in the past [53]. It only became accessible experimentally in recent years, through the advent of ultracold Fermi gases with resonant interactions.

### Role of dimensionality

Apart from the strength of the interatomic interactions, the dimensionality of a quantum gas can be tuned as well by compressing strongly one or two spatial degrees of freedom of an optical trap [36]. Along these directions, the corresponding dynamics can be frozen out if the thermal energy of the gas is insufficient to occupy excited states of center-of-mass motion. The possibility to prepare Fermi gases with reduced dimensionality and tunable interactions paves the way for a wide range of scientific inquiry and overcomes fundamental limitations of traditional condensed matter physics.

One-dimensional systems enhance the role of interactions and excitations always affect the entire many-body system. The physics is defined by the velocities of collective spin and

charge (mass) excitations as well as by the parameters governing the decay of correlations, which are linked to the underlying interactions. In solid state physics, Tomonaga-Luttinger-like behavior has been observed in organic conductors [54], nanotubes [55] and in the context of edge states [56], including spin-charge separation which was observed in quantum wires [57]. However, the screening of the long-ranged Coulomb interactions in electronic systems makes it challenging to obtain quantitative comparisons with the TLL model. Furthermore, control of interactions has not yet been accomplished. These problems can be overcome within the capabilities of cold atom systems, in the context of which the Fermi Tomonaga-Luttinger liquid remains largely unexplored [58]. One main objective of this thesis is the preparation of a strongly interacting Fermi gas in its normal, non-superfluid state, whose dimensionality can be tuned from 3D to 1D in order to study the crossover between the Fermi-liquid and the Tomonaga-Luttinger liquid, respectively.

### Outline of this thesis

In this text we present the recent accomplishments and progress of the FerMix experiment. The main results are threefold. We characterized a previously unreported  $(s, d)$ -wave Feshbach resonance in  $^{40}\text{K}$ , both in terms of the accompanying inelastic losses as well as regarding the resonant spin dynamics. The findings are compared to numerical simulations and theoretical predictions. Moreover, we describe the experimental progress towards the study of dimensional crossovers in strongly interacting Fermi gases using  $^{40}\text{K}$  confined in a large spacing 2D optical lattice. Finally, we studied the unusual thermalization dynamics of collisionless fermions in non-separable linear potentials and mapped the observed dynamics onto non-interacting harmonically trapped Weyl particles.

The text is structured in the following way:

- Chapter 2 describes the experimental apparatus and the general procedure to prepare a degenerate Fermi gas of  $^{40}\text{K}$ . Particular emphasis is put on the various additions to the setup as well as the many technical upgrades implemented over the course of this thesis.
- Chapter 4 presents the latest results of an ongoing study of resonant scattering properties of  $^{40}\text{K}$  at low magnetic fields. In this context, we present a detailed study of a previously unreported  $(s, d)$ -wave Feshbach resonance between the two highest lying positive spin states. We characterize both the nature of the losses as well as the resonant spin dynamics and compare the experimental findings to theoretical predictions.
- Chapter 6 summarizes the experimental progress towards the realization of dimensional crossovers in strongly interacting Fermi gases of  $^{40}\text{K}$ . This includes both

the initial design considerations in view of the underlying physics as well as the technical details of the constructed experimental hardware.

- Chapter 7 gives a summary of the main achievements of this thesis and provides perspectives for the near future.
- Appendix A contains the experimental and the more recent theoretical results of our study of the thermalization dynamics of collisionless fermions in non-separable potentials.
- Appendices B and C provide additional technical details of experimental setups and theoretical references, respectively, which have been omitted from the main text for the sake of brevity.

## Chapter 2

### General overview of the experimental apparatus

---

2.1. Overview of the vacuum system . . . . .	23
2.2. Atomic properties of Potassium and Lithium . . . . .	24
2.3. New resonant laser systems . . . . .	26
2.4. Upgrades to computer control of the experiment . . . . .	29
2.5. Lithium oven section and Zeeman slower . . . . .	30
2.6. 2D magneto-optical trap and new Potassium reservoir . . . . .	31
2.7. Dual-species 3D magneto-optical trap . . . . .	34
2.8. $\Lambda$ -enhanced gray optical molasses on the Alkali D1 line . . . . .	36
2.9. Magnetic trapping and transport . . . . .	39
2.10. Evaporation of Potassium in the quadrupole trap . . . . .	42
2.11. Preparation of a degenerate Fermi gas of Potassium-40 . . . . .	45
2.11.1. New optical and magnetic setup around the science cell . . . . .	45
2.11.2. Optical dipole traps and evaporation in the positive states . . . . .	53
2.11.3. Landau-Zener adiabatic passage to the negative states . . . . .	58
2.11.4. New crossed optical dipole trap and evaporation to degeneracy . . . . .	60

---

This chapter provides a detailed summary of the current status of the experiment as well as of its technical capabilities. Particular emphasis is put on the various major changes and upgrades implemented over the course of this thesis.

FerMix is a dual-species experiment designed to produce quantum gases of the two fermionic Alkali metals  $^{40}\text{K}$  and  $^6\text{Li}$ . A typical sequence takes roughly 60 s. A double species magneto optical trap (3D MOT) is loaded for up to 30 s, capturing atoms from two atomic beams which intersect at the center of the main chamber. The jets of atoms are generated by a two-dimensional magneto-optical trap with longitudinal molasses plus push beam (2D+ MOT) and by a Zeeman slower in case of Potassium-40 and Lithium-6, respectively. After MOT loading, the optical intensities are reduced and the magnetic gradient is raised in order to increase the atomic densities of the trapped atomic samples. Afterwards, the magnetic fields are switched off and the atoms are subjected to gray optical molasses on the Alkali D1 lines, which increases significantly the phase space

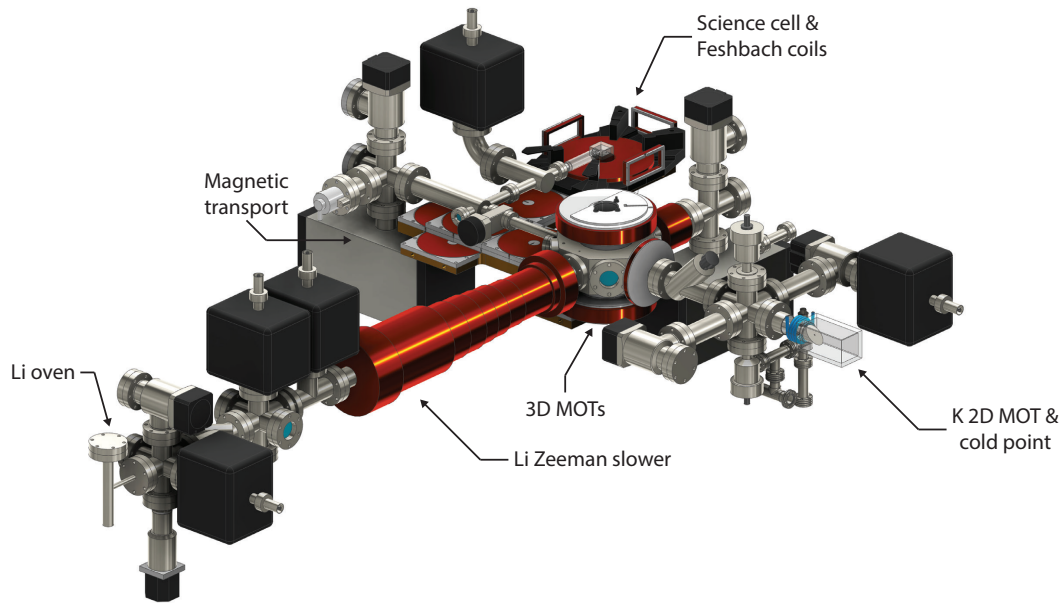


**Figure 2.1.: 3D CAD drawing of the main vacuum system.** The vacuum assembly consists of two source regions for  ${}^6\text{Li}$  and  ${}^{40}\text{K}$ , a central chamber hosting the 3D MOT and the L-shaped magnetic transport tube leading to the science cell. The upper transport plate and the coils of the Potassium 2D MOT are not shown for clarity.

density of the clouds. This stage of laser cooling is essential to ensure sufficiently high levels of efficiency for the ensuing magnetic transport, during which the atoms are first recaptured by a magnetic quadrupole potential, which is then adiabatically displaced by an array of partially overlapping Helmholtz coils. Prior to loading, optical pumping is performed in order to transfer all of the atoms to magnetically trappable states as they occupy random Zeeman levels after the molasses phase. The transport then moves the atoms to the science cell, where they are transferred into an optical dipole trap following microwave-evaporation to reverse some of the heating effects occurring during magnetic transport. Once loaded, the optical trap's intensity is lowered in order to evaporatively cool the trapped atoms, eventually reaching the quantum degenerate regime. During this phase of cooling, the atoms are also transferred into the desired Zeeman states and the spatial density is increased by adding a crossed dipole trap, without which quantum degeneracy would be much more challenging to reach due to marginal collision rates. The atoms are then either kept in the optical dipole trap or they are transferred into an optical tube lattice. Finally, we employ standard absorption imaging to record the column density profile of the atoms using highly sensitive CCD cameras.

## 2.1. Overview of the vacuum system

All of the operations described above do require an extremely clean and well isolated environment. While direct contact with the walls is avoided by means of optical and magnetic trapping fields, any residual gases present in the vacuum chamber are naturally in thermal equilibrium with its walls and therefore carry kinetic energy on the order of the ambient room temperature. Typical trap depths for neutral atoms cover a large range of comparatively small energies, spanning from some tens of mK for magnetic traps all the way to only a few  $\mu\text{K}$  after optical evaporation. Therefore, any collision with the remaining background gases entails immediate loss of atoms from their traps. The rate at which these collisions occur represents a fundamental technical limitation of the experiment as they ultimately fix the longest possible lifetime of the atomic ensembles in optical traps. As a consequence, pressures of well below  $10^{-11}$  mbar are a requirement in order to obtain reasonable lifetimes of up to several minutes in optically trapped (non-interacting) gases. While this might seem overly long at the first glance it should be pointed out that, for instance, evaporative cooling alone might already take tens of seconds when the collision rate happens to be low and there is no means of enhancement available.<sup>1</sup> Combining this with all of the steps of the sequence mentioned earlier already implies time scales of about one minute.

While background gases are harmful during the advanced stages of the experimental sequence, well controlled gaseous phases of  $^{40}\text{K}$  and  $^6\text{Li}$  with pressures of  $10^{-7}$  mbar to  $10^{-8}$  mbar are needed in order to produce the dilute atomic jets, which are then caught by the 3D MOTs. As these vapors cannot be switched on or off quickly,<sup>2</sup> they need to be kept ready at all times while being in a well regulated thermal equilibrium with the surrounding walls of the vacuum assembly. The dynamic range of pressures that need to be present in the vacuum chamber is thus rather large considering that the science cell needs to be kept at  $\sim 10^{-11}$  mbar. This makes it necessary to connect the various functional parts of the experiment by differential pumping tubes, so that unequal pressure levels can be maintained by ion pumps on adjacent sides.

A CAD drawing depicting the vacuum assembly of FerMix is given in Figure 2.1. It is comprised of four main sections: Two source regions of elevated vapor pressure in which the atomic beams of  $^6\text{Li}$  and  $^{40}\text{K}$  are generated by means of Zeeman pre-slowing and transversal cooling, respectively; the central octagon chamber where said jets of atoms intersect to load a dual species magneto-optical trap and where initial laser cooling is performed; the L-shaped transport tube along which the atoms are guided via a magnetic conveyor belt and finally the science cell with increased optical access and specialized

<sup>1</sup>For example, Feshbach resonances, which can enhance the elastic collision rate, are tuned using magnetic bias fields and thus cannot be used in a deep magnetic trap.

<sup>2</sup>In the case of  $^{40}\text{K}$  one could use dispensers.

coil assemblies to create strong magnetic fields to make use of Feshbach resonances. The pressure in the vacuum chamber is maintained by several ion pumps of different pumping strength as well as by non-evaporable getter materials (St707) which, once heated up, begins to absorb gases that are otherwise hard to remove with ion pumps (e.g.  $H_2$ ). In addition, the transport section was coated at CERN with a special Ti-Zr-V alloy that acts as an additional getter pump. The rectangular glass cell is made of uncoated<sup>3</sup> vycor (Hellma GmbH) and has external dimensions of 23 mm  $\times$  23 mm  $\times$  10 mm with a wall thickness of 4 mm. The closest ion pump in the vicinity of the science cell is shielded by a box made of mu-metal in order to reduce the amount of potentially disruptive stray magnetic fields.

## 2.2. Atomic properties of Potassium and Lithium

An overview of the lower level structures of  $^{40}K$  and  $^6Li$  is given in figure 2.2. Lithium-6 has the ground state  $2S_{1/2}$  with zero orbital angular momentum as well as the two excited states  $2P_{1/2}$  and  $2P_{3/2}$ , which are separated by the fine structure splitting of only 10 GHz. The corresponding optical transitions have a wavelength of 671 nm and a natural linewidth of  $\Gamma/2\pi = 5.87$  MHz. The nuclear spin  $I$  is equal to one, giving rise to hyperfine levels  $F = 1/2, 3/2$  for a total electronic angular momentum of  $J = 1/2$ , and  $F = 1/2, 3/2, 5/2$  in the case of  $J = 3/2$ . The corresponding hyperfine energy splitting in the ground state is relatively small with  $a_{\text{hfs}}/h = 228.205$  MHz, implying that the coupling of the nuclear spin  $I$  to the electronic angular momentum  $J$  is rather weak. As a result,  $I$  starts to decouple from  $J$  at comparatively low magnetic fields of  $\sim 100$  G (Paschen-Back regime). Another side effect of this weak coupling are the small energy splittings of the excited states, which amount to only 26.1 MHz for  $2P_{1/2}$  and less than 2 MHz for  $2P_{3/2}$ , the latter being smaller than the natural linewidth of the transition. As will be elaborated upon further in sec. 2.8, it is these small splittings in the excited state that render efficient sub-Doppler cooling for  $^6Li$  challenging to implement. Laser cooling and imaging are performed on the  $F = 3/2 \rightarrow 2^2P_{3/2}$  transition with an additional repumper  $F = 1/2 \rightarrow 2^2P_{3/2}$  to remove parasitic population from the lower hyperfine ground state.

The situation is notably different for  $^{40}K$ . It carries a nuclear spin of  $I = 4$  and possesses an inverted hyperfine structure in the  $4S_{1/2}$ ,  $4P_{1/2}$  and  $4P_{3/2}$  manifolds as it points in the opposite direction with respect to the nuclear magnetic moment. The splitting of the ground states  $F = 7/2$  and  $F = 9/2$  of 1.28 GHz is much larger than for  $^6Li$ , as is

<sup>3</sup>The number of distinct optical wavelengths which need to traverse the science cell is quite large, especially for an experiment working with mixtures of different atoms. In our case, there are 532 nm, 671 nm, 767 nm, 770 nm, 808 nm, 1064 nm and 1070 nm. Having a coating optimized for such a large variety of wavelengths is very elaborate and also introduces potentially harmful constraints, as it might reduce the transmission of other frequencies that one might want to use in the future. Therefore, the glass cell was left uncoated so that all wavelengths share the standard reflectivity of 4%.

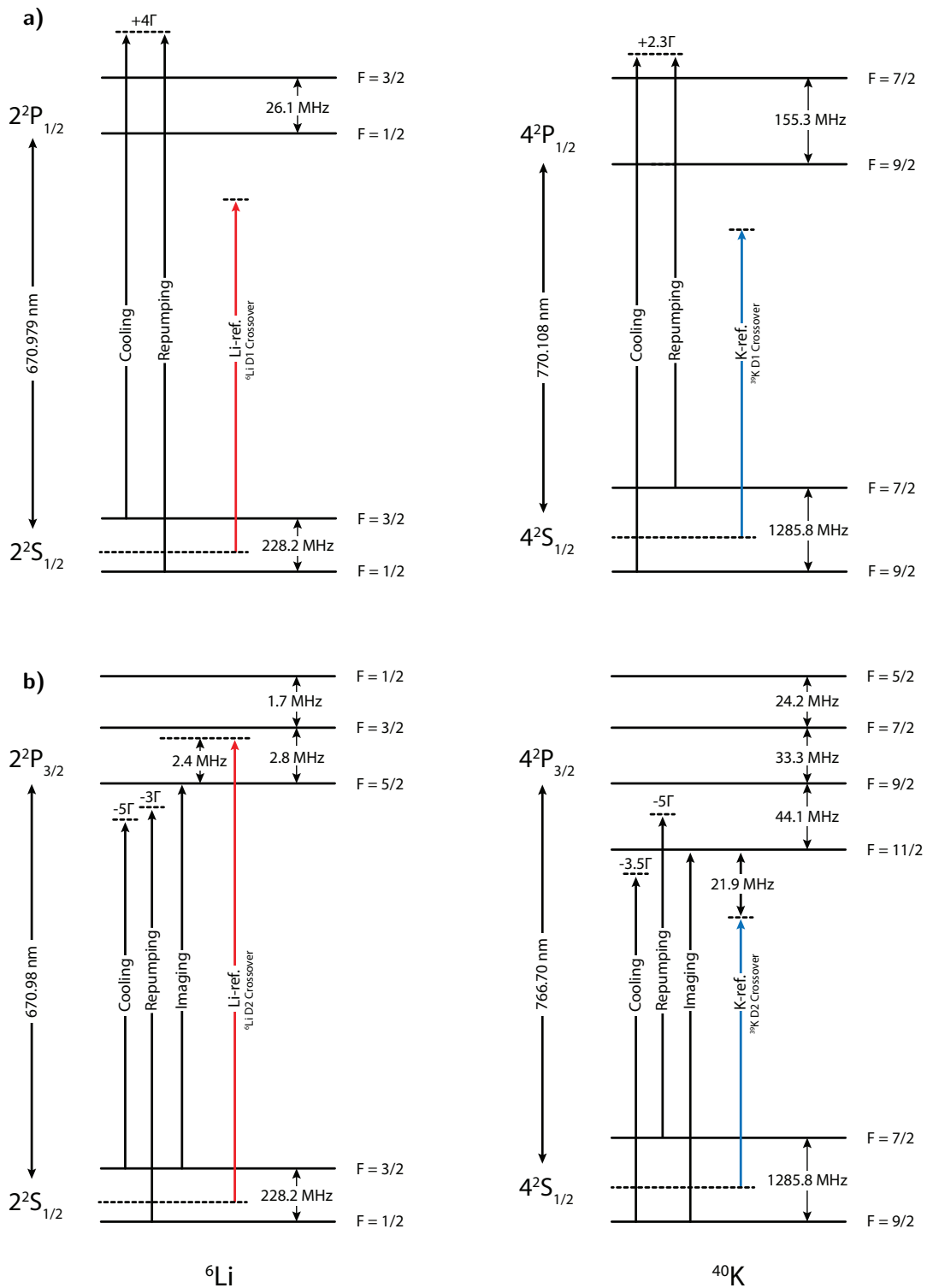


**Figure 2.2.: Overview of the lower hyperfine level structure of  ${}^6\text{Li}$  and  ${}^{40}\text{K}$ .** a) Hyperfine levels at zero magnetic field along the D1 line connecting the Alkali ground-  $nS_{1/2}$  and second excited states  $nP_{1/2}$ . b) Level structure for the D2 line between the ground states to the second excited states  $nP_{3/2}$ .

the case for the hyperfine splittings in the excited states. Laser cooling and imaging are performed on the  $F = 9/2 \rightarrow F' = 11/2$  transitions while the repumper is tuned to  $F = 7/2 \rightarrow F' = 9/2$ .

Because of its large angular total momentum there are many magnetically trappable Zeeman levels in the ground state, most notably the positive ones of the  $F = 9/2$  manifold. Moreover, a mixture of  $m_F = +9/2$  and  $m_F = +7/2$  is also stable with respect to spin changing collisions because the conservation of the projection of angular momentum cannot hold without ending up with identical spin states after the collision. This is of great importance for the ability to evaporatively cool  $^{40}\text{K}$  in a magnetic trap. A spin-polarized sample, which of course is free of any destructive spin exchange processes, cannot rethermalize via elastic s-wave collisions due to Pauli blocking or via higher partial wave ones as they are usually suppressed at low temperatures. Consequently, either a (stable) spin mixture or an additional buffer gas acting as coolant are required to evaporatively cool down  $^{40}\text{K}$ , with the former being much less cumbersome from a technical point of view. Unfortunately,  $^6\text{Li}$  does not have a stable spin mixture in the ground states, rendering evaporative cooling more challenging. The ground state of  $^{40}\text{K}$  also enters the Paschen-Back regime much slower than its excited state (or than  $^6\text{Li}$ ), which is a concern at typical fields of around 200 G when optical imaging and -pumping is concerned as the good quantum numbers of the excited state will be different from the ones of the ground state. Another positive aspect of  $^{40}\text{K}$ 's level structure is that hyperfine changing collisions driving  $F = 9/2 \rightarrow \bar{F} = 7/2$  are already energetically suppressed as the gas is cooled below the relatively high temperature of 10 mK [59]. Moreover, with wavelengths of 770 nm and 776.7 nm for the D1 and D2 lines, respectively, one directly benefits from the advanced state of development of many commercial optical technologies available for Rubidium at 780 nm.

### 2.3. New resonant laser systems

In order to perform laser cooling, optical pumping and imaging of the atoms using the transitions mentioned above, coherent beams of light of appropriate frequencies and optical intensities need to be generated in a controllable and tunable way. The D2 and D1 laser systems for Potassium and Lithium, while quite different in terms of wavelength, are constructed in a similar fashion and schematic overviews can be found in figs. 2.3 and 2.4 as well as in [60] and [61]. A master diode laser is stabilized via modulation transfer spectroscopy on a Doppler-free absorption signal of the D2 or D1 crossover line<sup>4</sup>, and amplified by a homebuilt tapered amplifier system (see [62] for technical details) before

<sup>4</sup>In the case of Lithium the D1 laser is offset-locked to the D2 master as the fine structure splitting amounts to only 10 GHz. In contrast, the splitting for  $^{40}\text{K}$  assumes a value of roughly 3 nm, which necessitates to use a separate spectroscopy setup for locking on the D1 line.

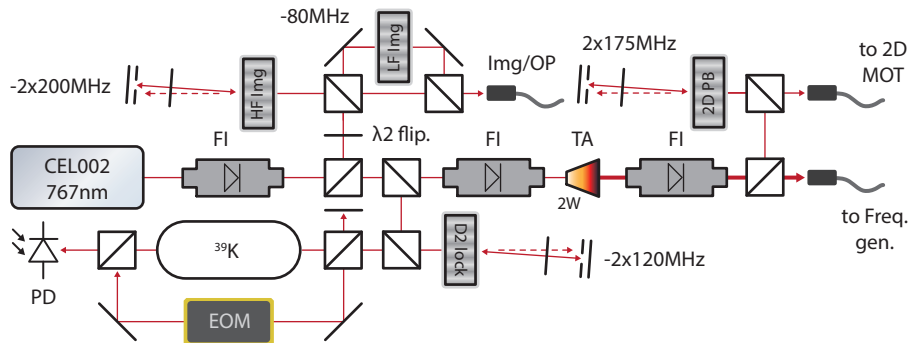


**Figure 2.3.: New D2 Master Laser Setup for  $^{40}\text{K}$ .** Functional parts: Master laser, Doppler-free absorption spectroscopy, First stage of frequency generation for absorption imaging/optical pumping in the science cell (3.1 and 6.2.5), optical amplification, 2D MOT push beam (2.6), cleaning fiber to frequency generation setup shown in fig. 2.4.

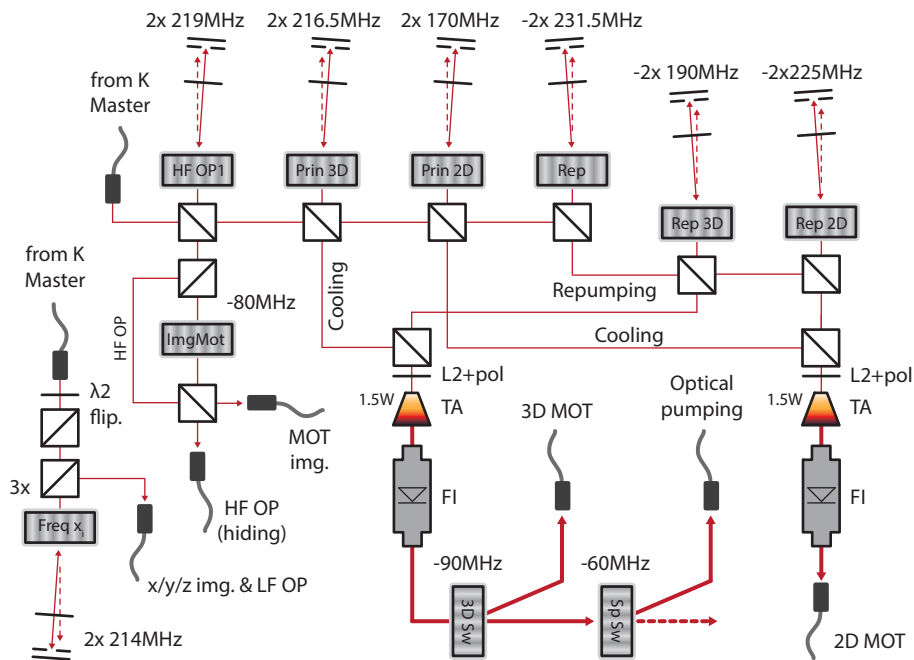


**Figure 2.4.: Expanded and upgraded setup for D2 frequency generation and additional optical amplification stages for  $^{40}\text{K}$ .** Functional units from left to right: New imaging and optical pumping for the science cell at low- and high magnetic field (3.1 and 6.2.5); New high field optical repumping into the upper hyperfine states (6.2.6) and MOT imaging; Frequency generation and optical amplification for the 2D MOT (2.6) and 3D MOT (2.7) as well as for optical pumping in the MOT chamber (2.8).

being mode-cleaned by an optical fiber. In the case of Potassium, one would prefer to lock the laser directly to the isotope  $^{40}\text{K}$ , however this is unfeasible due to the extremely low natural abundance of this isotope of only 0.012 %, which makes the mere detection of the absorption line technically challenging<sup>5</sup>. Therefore, the laser is referenced with a fixed offset created by an acousto-optical modulator (AOM) to the crossover line of Potassium-39 instead, which is in close proximity to the frequency needed to address  $^{40}\text{K}$ . In the case of  $^6\text{Li}$ , the (enriched) sample is contained in a special spectroscopy cell that has to be heated to roughly 300 °C in order to generate sufficiently high levels of vapor pressure. After mode cleaning, the appropriate frequencies are generated by a chain of tunable acousto-optical modulators and partially superimposed to form the seed light for an additional stage of tapered amplifiers (see fig. 2.4). Here, the appropriate optical powers for the 3D MOT, spin polarization and 2D MOT (Zeeman slower) are generated, before the light is being sent to the main table via single mode fibers. Several single pass AOMs serve as fast switches whenever speeds of a few  $\mu\text{s}$  are required while additional mechanical shutters, both homebuilt and commercial, are used to completely block the optical paths on much slower timescales of 6 ms and 100 ms, respectively.

Over the course of this thesis, several major parts of the Potassium laser table were rebuilt and extended in order to improve the overall stability of the experiment and to add new functionality. The original master laser setup based on a homebuilt diode laser in Littrow configuration (see [62] for details) was re-designed and its main laser source replaced by a commercial diode laser (MogLabs CEL002) to increase overall stability. The setup also provides the light for the new independent push beam of the 2D MOT (see sec. 2.6) and for the new stages of low- and high magnetic field optical pumping and imaging in the science cell (see sec. 3.1). The latter is facilitated by an additional network of AOMs allowing to address multiple spin states of  $^{40}\text{K}$  (see fig. 2.4) with the imaging/pumping light. Furthermore, the RF sources of the AOMs which were primarily made up of voltage controlled oscillators (VCO), have been largely replaced by direct digital synthesizer modules (WindFreak MixNV/SynthNV & DS Instruments SG4400L). This was done to reduce the sensitivity of the RF system to fluctuations of the lab's air conditioning unit and to allow to tune light frequencies digitally instead of by using analog channels (see sec. 2.4 for details). Initially, in order to reduce the amount of harmful stray light during during sequences, the TA chips were unseeded for extended periods of time. This mode of operation reduces the lifetime of the amplifier chips due to heat dissipation as well as abrupt out-of-equilibrium operation and was rectified by optimizing the timing of the sequence in conjunction with the installation of additional fast mechanical shutters.

---

<sup>5</sup>...and at a cost of several thousand EUR per milligram, also somewhat expensive.

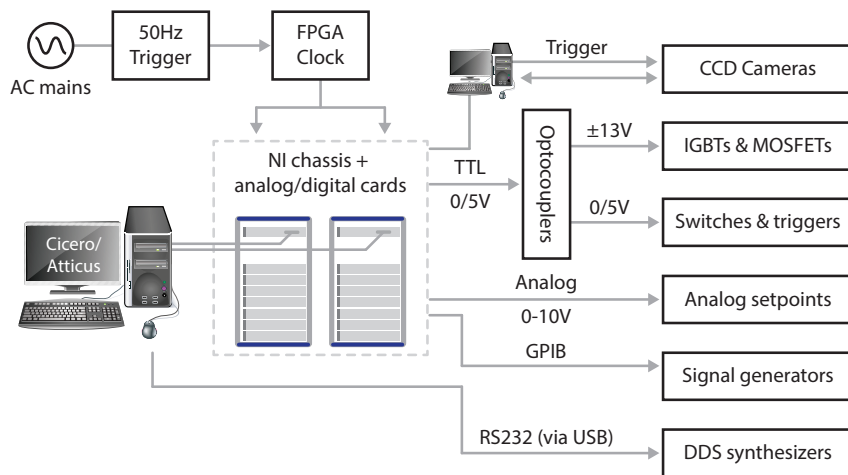


**Figure 2.5.: Organigram of the current experiment's control hardware.** The two NI chassis are addressed by a special PCIe card with two PXI slots and required both a dedicated input for the external clock. The cameras, while being triggered by the main NI system, are handled by a separate computer that communicates with them by means of specialized software.

## 2.4. Upgrades to computer control of the experiment

FerMix is controlled and operated by Cicero Word Generator in combination with Atticus Server, which is a software bundle developed at MIT specifically for cold atom experiments. It greatly facilitates the programming of experimental sequences by virtue of its clear interface and server/client architecture at the expense of flexibility as no additional features can be added without changing the underlying source code. Sequences, once started, are transferred from the buffer to a PXI system by National Instruments made up of two chassis. They contain all of the digital (TTL), analog (0 – 10 V) as well as GPIB cards providing the numerous output channels<sup>6</sup> necessary to control all of the various pieces of equipment making up the experiment, such as shutters, AM inputs, TTL channels and triggers for RF sources, to give but a few examples. A schematic overview of the hardware outlined so far is given in fig. 2.5.

As the buffers do have a limited size, the maximum duration of a sequence is bound by the time resolution of each of its steps. In order to be able to choose the resolution of each step independently to conserve buffer space, an external FPGA device (Opal Kelly XEM 3001) is used as an external master clock. This way, the maximum duration of a sequence is increased as the time resolution per step can easily vary between 1  $\mu$ s and 1 s.

While the PXI system operates at low voltages and currents, it needs to be connected to devices carrying comparatively high currents of up to several hundred amperes (e.g. IGBTs for magnetic coils). In order to protect the PXI system from voltage spikes, level shifting,

<sup>6</sup>Digital cards: NI PXI-6533 & 6536, Analog cards: NI PXI 6713 (12bit resolution)

ground loops and system voltage drops due to excessive current drain, a buffer stage in the form of amplified digital and analog opto-couplers mediates the communication with the final devices. They allow for maximum switching speeds of  $0.5 \mu\text{s}$  and  $20 \mu\text{s}$ , respectively. In addition, the most sensitive analog channels are hooked up using doubly shielded coaxial cables to reduce the risk of stray pickups, which might translate into fluctuations of the experiment's performance and hence of its reproducibility. This concerns, for example, the analog set point of the current supply generating the Feshbach field, which must have a current stability of at least  $10^{-4}$  to ensure consistent scattering lengths.

The control infrastructure of the experiment has undergone multiple upgrades over the course of this thesis. This was motivated, in part, by the need for 50 Hz-triggering in order to be able to perform RF spectroscopy on strongly interacting Fermi gases (see 5). In order to be able to straightforwardly implement mains synchronization in the sequence, the previous customized version of Cicero had to be replaced with the newest one. An Arduino-based mains trigger [63] is used to provide feedback to the clock. Moreover, the experiment's signal generators were switched from LAN to GPIB and the new DDS sources were integrated into Cicero by means of emulated RS232 interfaces to allow for more flexible programming. Moreover, the imaging software to communicate with the previous cameras was redone to include as well the newly added highly sensitive CCD camera needed for the study of the dimensional crossover in the tube lattice (see ch. 6).

## 2.5. Lithium oven section and Zeeman slower

As this part of the experiments' atomic sources was already covered in great detail in previous thesis [62, 64], only a brief summary will be given here for completeness.

The  ${}^6\text{Li}$  is contained in a tee-shaped oven section, which is connected to the Zeeman slower via a collimation tube with a diameter of 6 mm as well as a differential pumping stage (see fig. 2.1). The sample is highly enriched as the natural abundance of  ${}^6\text{Li}$  is only 5%, which would limit the atomic flux created by the slower. In order to produce a gaseous phase inside of the oven container, the sample is heated to temperature of about  $470^\circ\text{C}$ , which is stabilized using an Omega temperature controller. When the experiment is not running, the temperature is reduced to  $270^\circ\text{C}$  in order to avoid clogging of the collimation tube.

As the hot atomic beam of  ${}^6\text{Li}$  traverses the Zeeman slower's vacuum tube, it is opposed by a counter-propagating red-detuned laser beam of circular polarization. Through many absorption and spontaneous reemission processes, the atoms are slowed down since the only net transfer of momentum, which does not vanish on average over multiple cycles, is exactly opposite to their direction of motion. In order to ensure that the atoms stay in resonance with the laser beam (of fixed frequency) despite the Doppler-shift, which decreases as the atoms slow down, the tube is surrounded by a tapered coil assembly that

creates an inhomogeneous magnetic field. The latter translates into an inhomogeneous Zeeman shift of the atomic energy levels covering the atoms' travel distance from the oven to the main chamber, where the  ${}^6\text{Li}$  atoms will be captured by a magneto-optical trap (see fig. 2.1). In order to maintain the resonance condition along the entire length of the slower, the B-field is specifically designed to match the Zeeman shift to the thermal velocity distribution of the oven and to account for the slowing rate as the atoms travel to the MOT chamber, given the fixed frequency of the slowing light as a constraint.

Once in the MOT chamber, the resonant light of the Zeeman slower is no longer needed and might even disturb the atoms, which have already been captured by the 3D MOT. To circumvent this problem, the Zeeman slower used in this experiment is of the so-called 'spin-flip' type, whereby the magnetic field is made to cross the zero just before reaching the MOT chamber. This can cause the atoms to undergo a non-adiabatic spin flip during an absorption cycle, which renders them off-resonant to the slowing light. However, a repumping component needs to be added to the light to ensure that the atoms can still get captured by the subsequent 3D MOT. Another advantage of this particular implementation is the reduced need of electrical current in order to generate a low B-field in the vicinity of the 3D MOT, which reduces in turn the heat load that must be dissipated and removed from the coils via water cooling [63]. Since the coils create some residual magnetic fields at the position of the 3D MOT, another compensation coil is installed on the opposite side of the central chamber.

Concerning dual species operation, the presence of the atomic jet of  ${}^6\text{Li}$  does decrease the loading of  ${}^{40}\text{K}$  in the 3D MOT, but does not reduce the loaded atom number in the saturated regime.

## 2.6. 2D magneto-optical trap and new Potassium reservoir

${}^{40}\text{K}$  has a very low natural abundance of only 0.012 % [65], so that the use of a Zeeman slower would require extremely high vapor pressure in order to establish a sufficient flux of atoms to load a sufficiently large 3D MOT. In such a situation, the partial pressure of the other isotopes would be even higher, causing the ion pumps to clog up over the course of several months before they eventually lose their pumping capacity. The use of an enriched sample in combination with a Zeeman slower is possible in principle, but extremely costly as the slower is rather lossy in its use of the available atoms, making it necessary to frequently replenish the source.

We therefore use a 2D MOT to benefit from its comparatively high flux of up to  $10^9 \text{ s}^{-1}$  as well as from its efficiency in terms of the sample depletion rate. As it has to be loaded from a background vapor phase of Potassium, we have to use an enriched sample as the collisions with the other isotopes would prevent the formation of a  ${}^{40}\text{K}$  MOT if its partial pressure was only 0.012 %. Even with an 4 % enriched sample, the parasitic collisions start

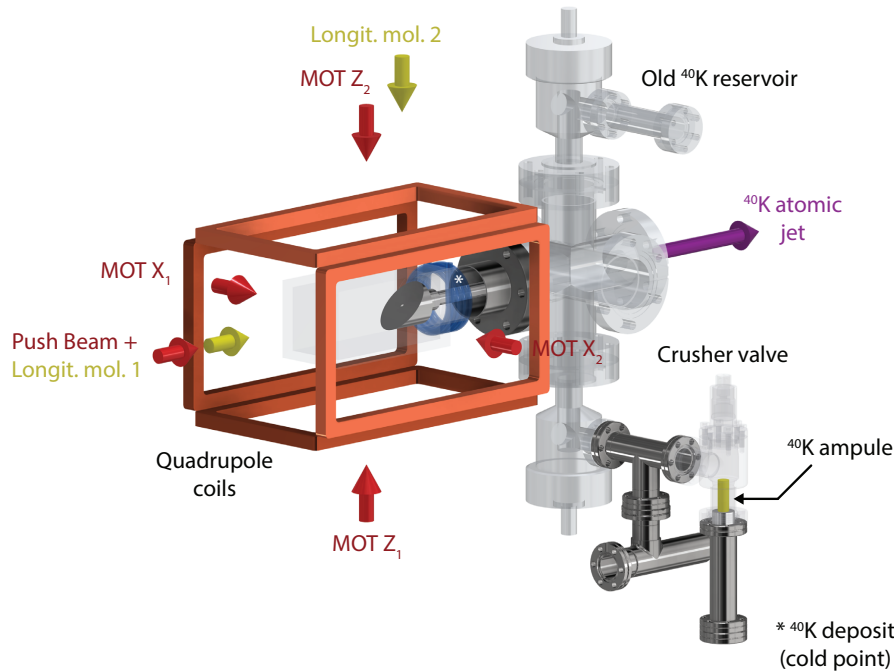


**Figure 2.6.:** CAD drawing of the 2D MOT section of the vacuum system. The new Potassium source region is attached to the main vacuum system on right lower right. The differential pumping stages to the 3D MOT chamber are not visible.

to degrade the MOT once the partial pressures of potassium 39 and -41 increase above 60%.<sup>7</sup>

The 2D MOT is made up of two pairs of transversal, retro-reflected cooling beams as well as a longitudinal molasses (see fig. 2.6 and [62, 64]). In addition, a small push beam is accelerating the atoms towards the 3D MOT chamber, which leads to a substantial increase of the atomic flux [66]. The push beam was split off directly from the 2D MOT light near the vacuum chamber and could not be tuned independently in terms of frequency composition or intensity. Moreover, this arrangement entailed an extremely long optical path, which, in combination with the small beam diameter of only 2.4 mm, rendered the push beam unstable with respect to beam pointing fluctuations. This can result in unpredictable fluctuations of the atomic flux on a shot-to-shot timescale, thereby compromising the reproducibility of the loaded atom numbers. In order to overcome this problem, a new optical setup to deliver a (frequency-tunable) push beam via singlemode fiber was constructed in the form of an ancillary setup added to the new D2 master laser system (see fig. 2.3).

<sup>7</sup>This figure corresponds to the amount of resonant light scattered by the vaporous phase, i.e.  $I_{\text{out}}/I_{\text{in}}$ . It can be used to calculate the absolute partial pressures since the isotope abundances and dimensions of the 2D MOT glass cell are known (see [62] for details).

### Controlled generation of a vaporous phase of $^{40}\text{K}$

The atomic sample is stored in two places: The main reservoir, which contains the bulk of the solid material, and the cold point in the vicinity of the 2D MOT glass cell. The latter is replenished regularly by migrating Potassium from its oven compartment and serves as an intermediate source, with which the vaporous phase of  $^{40}\text{K}$  is created. The cold point is made up of a small hose cycling around a circular 'throat' of the glass cell. It carries a temperature regulated flow of anti-freeze coolant, which can be cooled down all the way to  $0^\circ\text{C}$  and heated up to a maximum temperature of  $45^\circ\text{C}$ . Given that the surrounding vacuum assembly as well as the glass cell of the 2D MOT are kept at elevated temperatures greater than  $60^\circ\text{C}$  at all times, the cold point acts as a highly efficient pump, especially at its low temperature setting. When increasing the temperature, small amounts of Potassium begin to evaporate and to fill out the 2D MOT glass cell, creating a vaporous phase. To further enhance its pressure, several UV-LEDs are installed around the glass cell. The light with a wavelength of 395 nm induces atomic desorption [67] from the surfaces on the inside of the vacuum chamber as well as from the cold point, which can temporarily increase the vapor pressure by up to 50 % and hence the flux of the 2D MOT. Their total output power is approximately 1.4 W, which can disturb the loading of the 3D MOT if they are left active for too long. Therefore, they are only switched on for 1-2 s at the very beginning of the loading phase, where the majority of the atoms is captured. Additional technical details regarding the UV LED system and its characterization can be found in [63]. Given that the pressure needs to be elevated by design, the 2D MOT section is connected to the rest of the vacuum assembly via a differential pumping stage.

### New Potassium reservoir and sample migration

The original sample container which was used to break the first ampule of enriched  $^{40}\text{K}$  remains connected at the top of the 2D MOT section of the vacuum chamber (see fig. 2.6), but cannot be used any longer due to a leak in the opening- and closing mechanism of the valve. As was mentioned earlier, this reservoir had been depleted already at some point in the past, so that the only remaining Potassium was the deposit on the cold point. During the course of this thesis, the remaining  $^{40}\text{K}$  eventually ceased to be able to sustain an acceptable level of vapor pressure in the 2D MOT glass cell. In order to replenish the Potassium, a new reservoir had to be designed and installed as the top valve and its sample container cannot be operated without compromising the integrity of the vacuum of the 2D MOT chamber. The new oven section is depicted in figs. 2.6 as well as B.19. It is connected to the bottom valve of the 2D MOT chamber and can be evacuated before establishing direct contact between the two chambers. The reservoir is made up of two valves, one of which serves as connection to a turbo pump while the other one is used to

crush under vacuum the glass ampule containing the Potassium. Given that the enriched sample consists of only a few milligrams, it needs to be contained in an airtight glass vessel to prevent it from oxidizing completely.<sup>8</sup>

In order to migrate Potassium onto the cold point, the source region is slowly heated to 85 °C while the connecting vacuum system is kept at its usual 100 °C. Due to the increased temperature, part of the solid Potassium will start to evaporate and migrate through the vacuum assembly. Due to the elevated temperatures of the surrounding inner surfaces of the vacuum chamber, the gas is prevented from undergoing sublimation along the way. As the ion pump is closed off as well, only the cold points remains as a possible area for <sup>40</sup>K to deposit. Its temperature during migration is dropped to 0 °C to increase its pumping capacity further.

In case of power cuts the lack of cooling provided by the highly stable chiller (Coherent ThermoTek T257P-30 210 W) will cause the comparatively small cold point deposit to dissipate quickly as the surrounding vacuum parts represent a large thermal load that will heat it up quickly before cooling down after several hours. To prevent such losses of the atomic source, a high capacity interruption-free power supply (Riello Sentinel Dual 10000VA) was installed that can sustain the chiller with power for up to 16 h, which is much longer than the cool-down time of the vacuum assembly. Moreover, a homebuilt security system was conceived to monitor the interlock pin of the chiller and the temperature of the cold point as well as of the new <sup>40</sup>K reservoir. In case of overheating or chiller failure it can cut the power to the vacuum system's heating tape to reduce the potential damage to the Potassium samples. Technical details can be found in appendix B.4.1.

## 2.7. Dual-species 3D magneto-optical trap

The two atomic jets of <sup>40</sup>K and <sup>6</sup>Li converge in the central chamber of the vacuum system (see fig. 2.1), where they are captured by a dual species magneto-optical trap (MOT). This type of trap is a typical first cooling stage in most contemporary cold atom experiments [68] as it allows to capture up to a billion atoms and to cool them down to temperatures approaching the Doppler limit of  $T_D = \hbar\Gamma/2k_B = 144 \mu\text{K}$ . The trap itself is made up of three pairs of red-detuned counter-propagating laser beams of circular polarization and a magnetic quadrupole field, as is shown in fig. and 2.7. The former forms a so-called optical molasses which cools the atoms while the latter provides a trapping potential that prevents them from leaving the active volume [69].

<sup>8</sup>In the case of <sup>6</sup>Li, oxidation of the material before loading and evacuation of the oven is no concern as it only occurs on the surface of the sample. Since enriched lithium is very cheap in comparison to Potassium, the sample can easily weigh many grams, so that the oxidation of the surface is negligible compared to the total volume. Once the oven is brought to its operational temperature, the lithium melts and the pure core of the once solid sample is exposed.

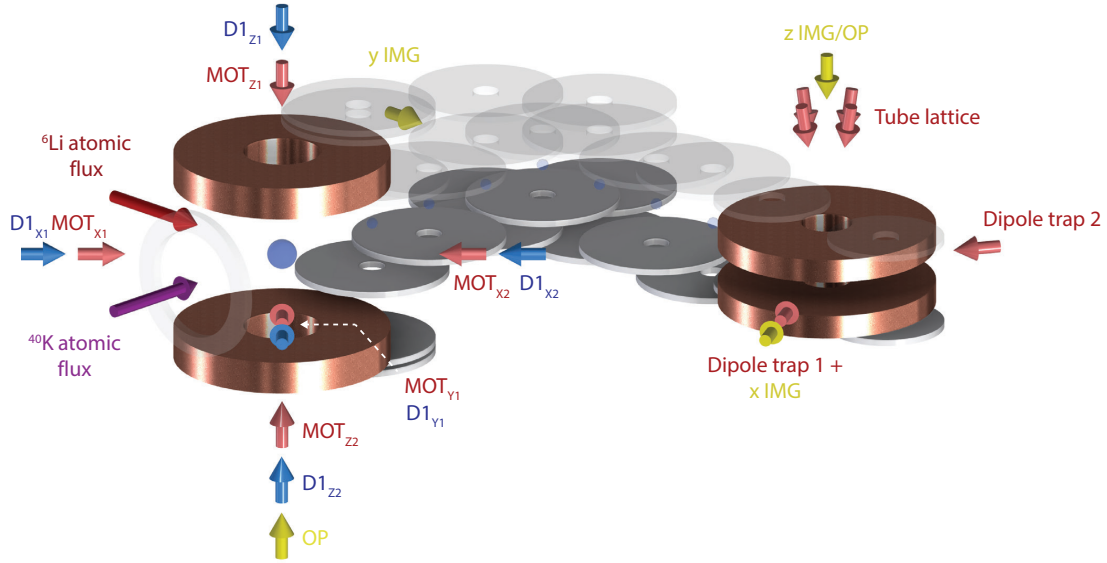


**Figure 2.7.:** Overview of the magnetic coil assemblies and laser beams used in the experiment. The transport coils are rendered in white to distinguish them from the main quadrupole/bias coils used in the MOT chamber and in the science cell on the left- and right-hand side, respectively.

In our setup, the polarization optics are optimized for  $^{40}\text{K}$  and the horizontal axes are retro-reflected while the vertical MOT axis is made up of two counter-propagating laser beams. At ideal conditions, the MOT can simultaneously capture up to  $2 \times 10^9$  atoms of  $^6\text{Li}$  and  $3.2 \times 10^9$  atoms of  $^{40}\text{K}$ . A full characterization as well as additional technical details can be found in [62, 64]. Due to detrimental effects arising from dual species operation, the steady state temperatures are limited to roughly  $800 \mu\text{K}$  and  $300 \mu\text{K}$  for  $^6\text{Li}$  and  $^{40}\text{K}$ , respectively [63]. Consequently, additional stages of cooling are required before the atoms can be transported efficiently to the science cell. To that end, a dual-species gray optical molasses was implemented at FerMix in order to lower the temperature well below the Doppler limit. This cooling stage is a special type of Sisyphus cooling and will be described in greater detail in the following section.

In order to improve the transfer to the molasses, the MOT is compressed over the course of 5 ms after loading is complete, i.e. after the MOT fluorescence reaches a plateau implying a steady state. During this step, the magnetic gradient is increased from  $9 \text{ G cm}^{-1}$  to  $40 \text{ G cm}^{-1}$ , which entails approximately a five-fold increase of the atomic densities [61, 63].

## 2.8. $\Lambda$ -enhanced gray optical molasses on the Alkali D1 line

As was detailed in the previous section, the typical phase space densities (PSD) achievable in magneto-optical traps of  $^{40}\text{K}$  and  $^6\text{Li}$  are much too low in order to enable efficient (magnetic) transport or the loading of a typical optical dipole trap<sup>9</sup>. Several common cooling techniques can be implemented at this stage, however they all suffer from certain drawbacks that render them impractical for our specific situation. For example, radio-frequency evaporation in a dual species magnetic trap would certainly increase the PSD of both elements, but the loss in terms of atom numbers would be too high given that this is just a pre-cooling stage. A more realistic alternative is the implementation of an additional MOT stage using the higher-lying ultra-violet transitions of  $^6\text{Li}$  [70] and  $^{40}\text{K}$ . While the narrow linewidth of these transitions gives rise to much lower Doppler temperatures, the technical realization comes at great cost, especially for two species, and brings with it all of the disadvantages of UV lasers.<sup>10</sup> Finally, one can employ conventional bright Sisyphus cooling [69]. Here, a polarization gradient gives rise to a spatially varying Zeeman shift, which in turn creates a periodic potential for the atoms. Particles moving in such a potential landscape will lose kinetic energy as they 'climb the hills' and regain it when returning to the 'valleys'. By adding optical pumping on a closed transition, one can create a situation where, on average, the atoms are most likely to be excited just after having lost some of their kinetic energy. After the subsequent decay back to the ground state, the cycle repeats and the gas continues to cool down [69]. Theoretically, the lowest temperatures one can achieve via this mechanism are given by the photon recoil limit  $T_{\text{rec}} = p_{\gamma}^2/2mk_{\text{B}}$ , which is 3.5  $\mu\text{K}$  and 0.4  $\mu\text{K}$  for  $^6\text{Li}$  and  $^{40}\text{K}$ , respectively. Unfortunately, the D2 line's excited state hyperfine structure of the two species at hand is not well resolved with respect to the natural linewidth  $\Gamma \sim 6 \text{ MHz}$ , which precludes the existence of a closed transition and therefore negates any cooling effect of the Sisyphus mechanism, unless a repumping laser is added. However, even when turning to such a bichromatic molasses on the unresolved D2 line, the obtained results remain insufficient for our situation in terms of overall efficiency.

A possible solution can be found by turning to the D1 line, which possesses a much larger hyperfine splitting in the excited state, but still lacks a cycling transition at low magnetic fields. In conventional molasses the repumping transition is used to return stray atoms to the main cooling line while, in our case, it forms a so-called  $\Lambda$ -system. It can be shown theoretically that when the cooling transition is chosen as either  $F \rightarrow \bar{F} = F$  or  $F \rightarrow \bar{F} = F - 1$ , multiple dark states will emerge as eigenstates of the underlying

<sup>9</sup>Note that the situation is different when employing broadband fiber CW lasers with powers of up to 300 W, see B.3.

<sup>10</sup>To give but a few examples: heightened skin cancer risk; rapid degradation of fibers enforcing a free-air implementation; home-built laser systems are very time-consuming while commercial ones tend to be very expensive.

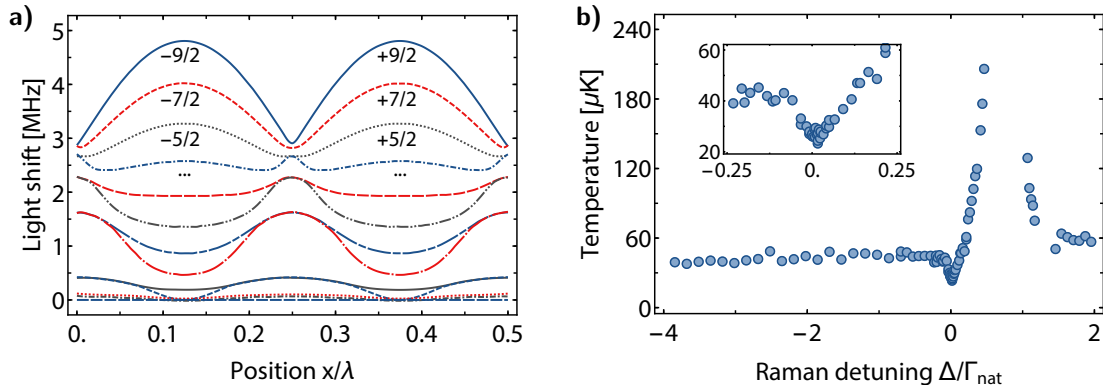


**Figure 2.8.:** Gray optical molasses on the D1 line of  $^{40}\text{K}$ . a) Eigenenergies as a function of position (as in [71]). b) Equilibrium temperature as a function of Raman detuning (data adapted from [72]).

Hamiltonian [69]. These states of vanishing eigenenergy are linear superpositions of the ground state's Zeeman levels and do not couple to the light field. However, the other eigenstates are not dark and possess a spatial modulation in their energies that is reminiscent of conventional bright molasses. Now, if the laser is detuned onto the blue side of the D1 line, the bright states are shifted to higher-lying, positive energies, as shown in fig. 2.8 for  $^{40}\text{K}$ . The implied cooling mechanism is referred to as gray molasses and can be seen as a combination of polarization gradient cooling and velocity selective population trapping [69]. Atoms of elevated kinetic energy in the dark states are transferred to the bright states by motional coupling, most likely at the position of the potential minima due to the reduced amount of transition energy. The atoms then proceed to shed additional kinetic energy while climbing up the potential hills, to be then pumped back into a dark state after reaching the apex. The cooling arises from the same type of Sisyphus effect as in conventional molasses.

### Experimental realization

$\Lambda$ -enhanced gray molasses on the Alkali D1 line was realized for the first time at the Fer-Mix experiment with  $^6\text{Li}$  and  $^{40}\text{K}$ . It has, since then, found widespread use in numerous research groups [73–81] (in some cases even using the D2 line) owing to its formidable overall efficiency in terms of cooling power and capture efficiency as well as its straightforward implementation. The experimental and technical details have already been elaborated upon in great detail in previous PhD theses [60, 66] and in [71, 72]. Therefore, only a brief summary of the most important operational parameters shall be given here for the sake of completeness, and in order to highlight the significance of the role of this cooling step in the context of the experiment as a whole.

The performance of gray molasses cooling depends on several experimental parameters. The involved transitions and their respective detunings are depicted in fig. 2.2. The optimum of the relative optical intensities of the cooling and ‘repumping’ light was found to be 20:1 and 8:1 for  ${}^6\text{Li}$  and  ${}^{40}\text{K}$ , respectively. The total intensity  $I$  and the detuning from the excited state  $\delta$  are related to the capture velocity  $v_c$  and equilibrium temperature  $T_f$  as per  $v_c \sim I/\delta^2$  and  $T_f = I/k_B\delta$ , respectively. In order to capture as many atoms as possible from the comparatively hot compressed MOT, the intensity of the molasses is kept at its maximum at first and then ramped down to a much lower value to reach a low steady state temperature. The overall duration of the intensity ramp can be chosen as low as 5 ms without sacrificing any cooling efficiency. Moreover, as the energy splittings between the involved Zeeman states are supposed to be created through the AC stark shift alone, any stray magnetic fields have to be canceled by using appropriate compensation coils.

The common detuning  $\delta$  and the relative Raman detuning  $\Delta$  relate to the coherence among the bare ground states and the emergence of dark states. The molasses produces the lowest possible temperature exactly when one fulfills the Raman condition  $\Delta = 0$ . One finds that for  $\delta = 4\Gamma$  in the case of  ${}^6\text{Li}$  and  $\delta = 2.3\Gamma$  for  ${}^{40}\text{K}$  the captured atom numbers are maximized while the steady state temperatures are near their minimal values (see fig. 2.8b). Under these conditions, samples of  $4 \times 10^8$   ${}^6\text{Li}$  atoms at temperatures as low as 60  $\mu\text{K}$  can be prepared. In the case of  ${}^{40}\text{K}$ , one can reach 20  $\mu\text{K}$  with  $1.4 \times 10^9$  atoms. At this time it is unclear why these temperatures do not yet approach the recoil limit.

Since the fine structure splitting between the D2 and D1 lines is large and high optical powers are required, separate laser systems were constructed to deliver the light fields needed for gray molasses. They are depicted in figs. [60] and [66]. In the case of  ${}^{40}\text{K}$ , the D1 master laser is locked to the crossover line of  ${}^{39}\text{K}$  using frequency modulation transfer spectroscopy and the ‘cooling’ frequency is then created by means of an electro-optical modulator, which is set exactly to the ground state hyperfine splitting of 1285.8 MHz. For  ${}^6\text{Li}$ , the laser is stabilized to the main D2 master laser via an offset lock of roughly 10 GHz. Here as well the second frequency, in this case the ‘repumper’, is created in the form of a sideband modulated onto the light by an EOM driven at 228 MHz. After amplification the light is delivered via polarization maintaining single mode fibers to the main optical table and superimposed with the 3D MOT light under a small angle before being enlarged and split on the way to the MOT vacuum chamber. Additional details regarding the laser setups can be found in [60, 66].

### Optical pumping

Following the gray molasses phase, the atoms have to be loaded into a magnetic quadrupole trap in order to transport them by means of a dynamic magnetic potential to the science cell. As will be detailed in the section 2.9, both  ${}^6\text{Li}$  and  ${}^{40}\text{K}$  only possess a few Zeeman

states, which are magnetically trappable and stable with respect to inelastic (exothermic) spin-changing collisions. During the gray molasses phase, the atoms occupy dressed states made up of the two hyperfine ground states of  ${}^6\text{Li}$  and  ${}^{40}\text{K}$ , respectively. Once the light fields are switched off, the particles are projected onto numerous Zeeman states, most of which cannot be trapped magnetically. Therefore, the atoms are optically pumped into their stretched Zeeman states  $|F = 3/2, m_F = +3/2\rangle$  ( ${}^6\text{Li}$ ) and  $|F = 9/2, m_F = +9/2\rangle$  ( ${}^{40}\text{K}$ ) via  $\sigma^+$ -polarized light in the presence of a weak magnetic bias field. A detailed study of this process can be found in [63].

In the case of  ${}^{40}\text{K}$ , we alter the frequency composition of the 3D MOT light and reroute it to pass through the atomic cloud along the quantization axis. The former 'cooling' component is tuned to address the two excited state hyperfine manifolds  $\bar{F} = 11/2$  and  $\bar{F} = 9/2$  at minimal intensity in order to reduce heating effects while the  $F = 7/2$  manifold is depleted by the repumping light. The total duration of the pump pulse is  $70\ \mu\text{s}$ .  ${}^6\text{Li}$  is repumped via the transitions  $F = 3/2 \rightarrow \bar{F} = 3/2$  and  $F = 1/2 \rightarrow \bar{F} = 3/2$  with the latter being provided by the laser setup of the gray molasses.

## 2.9. Magnetic trapping and transport

After spin polarization of the atoms as described above, they can be loaded into a magnetic quadrupole trap. It is typically created by using two coils in anti Helmholtz configuration, which create near their symmetry center a magnetic flux density of the form  $\mathbf{B}(\mathbf{r}) \simeq b'(x, y, -2z)$ , where  $b'$  is a geometrical constant describing the steepness of the gradient, given typically in units of G/cm. Atoms with magnetic moment  $\mu$  couple to the magnetic field via the magnetic dipole interaction and experience an energy shift given by  $\Delta E = -\mu\mathbf{B}$ . The magnetic moment depends on the internal state of the atom (i.e. the valence electron) and, in general, needs to be calculated numerically for a given state and field  $\mathbf{B}$ . A detailed discussion of the behavior of neutral Alkali atoms in magnetic fields can be found in appendix C.4. In the limit of small field magnitude, the total angular momentum basis  $\{F, m_F\}$  represents a set of good quantum numbers and under the assumption that the magnetic moment follows the local direction of the magnetic field adiabatically, one can express the eigenenergy as function of the atom's center-of-mass positions as per

$$\Delta E = -\mu_B g_F m_F B(\mathbf{r}) \quad \text{with} \quad B(\mathbf{r}) = |\mathbf{B}(\mathbf{r})| = b\sqrt{x^2 + y^2 + 4z^2}. \quad (2.1)$$

Here,  $\mu_B$  is the Bohr Magnetron and  $g_F$  represents the Landé factor of the hyperfine Zeeman state  $|F, m_F\rangle$ .

Given that static magnetic fields cannot have a local maximum according to Maxwell's equations, atoms necessarily need to be trapped around the minima of the B-field. However, this is only possible if the eigenenergy of a given internal state increases as the mag-

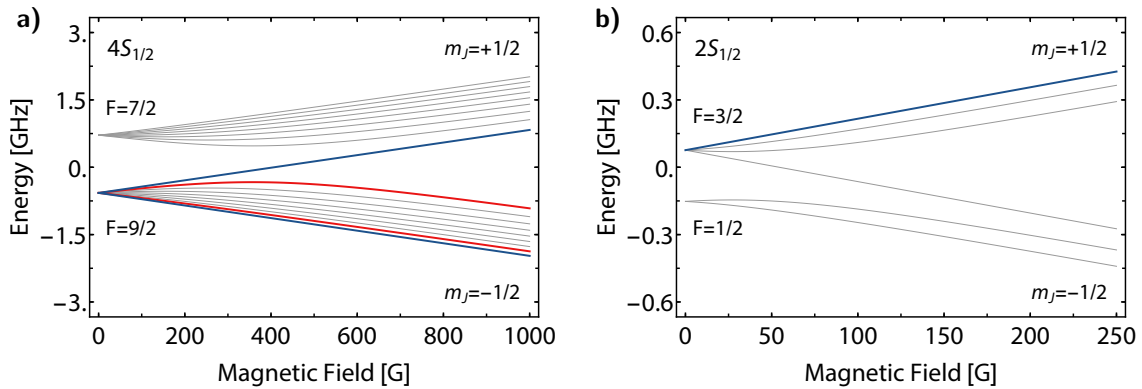


**Figure 2.9.: Energy shifts of the hyperfine ground state manifolds of  ${}^6\text{Li}$  and  ${}^{40}\text{K}$ .** a,b) Energy levels of the electronic ground states  $4S_{1/2}$  and  $2S_{1/2}$  of  ${}^{40}\text{K}$  and  ${}^6\text{Li}$ , respectively, for weak and strong magnetic fields. The lines indicated in red (blue) correspond to the (stretched) states commonly used in the experiment.

netic field grows stronger in magnitude, which is the case when its magnetic moment has a positive slope. All Zeeman levels with this property are usually called ‘low-field-seeking states’, whereas their anti-trapped counterparts are referred to as ‘high-field-seeking states’.

As was mentioned earlier, the notion of the atom’s spin following the local direction of the magnetic field adiabatically as it moves about the trap is the key requirement for stable magnetic trapping. However, as is evident from eq. 2.1, the B-field does change its sign abruptly when crossing through the symmetry center. At this point, the magnetic moment of any atom will not be able to follow the field’s direction slowly in terms the Larmor frequency. As a result, spin flips to anti-trapped states might occur. The magnetic zero is also the region where the coldest atoms accumulate, so as the phase space density of the gas increases, so will the Majorana spin flips due to the increased atomic density in the vicinity of the magnetic zero. In essence, they can be thought of as a form of anti-evaporation since these losses affect mostly the low energy part of the gases thermal distribution. These processes become relevant as soon as atomic ensembles are sufficiently cold, which is going to be the case at the end of magnetic evaporation.

### Hyperfine structure of ${}^6\text{Li}$ and ${}^{40}\text{K}$

The Zeeman energy shift as a function of B-field of the ground states of  ${}^{40}\text{K}$  and  ${}^6\text{Li}$  are given in fig 2.9. Lithium has four low-field seekers in its absolute ground state  $2^2S_{1/2}$ . Up to its turning point at 30 G, the state  $|F = 1/2, m_F = -1/2\rangle$  is trappable but only at a rather low trap depth of 0.3 mK.  $|F = 3/2, m_F = -1/2\rangle$  becomes low-field seeking only at fields stronger than 30 G.  $|F = 3/2, m_F = +1/2\rangle$  is trappable, but not stable against

the exothermic spin-changing collision  $|F = 3/2, m_F = +1/2\rangle + |F = 3/2, m_F = +1/2\rangle \rightarrow |F = 3/2, m_F = +3/2\rangle + |F = 1/2, m_F = -1/2\rangle + E_{\text{rel}}$ . The released energy of  $E_{\text{rel}} = 11$  mK is essentially equal to the hyperfine splitting of 228 MHz and more than enough to expel atoms from the trap. Only the stretched state  $|F = 3/2, m_F = +3/2\rangle$  is at the same time collisionally stable and low-field seeking [82].

Potassium has an inverted hyperfine structure and several magnetically trappable Zeeman levels in its ground state  $4^2S_{1/2}$ . The two most energetic states in the lower hyperfine manifold  $F = 9/2$ ,  $|F = 9/2, m_F\rangle = +9/2$  and  $|F = 9/2, m_F\rangle = +7/2$ , are typically used in Potassium experiments as they have favorable collisional properties and are stable with respect to spin-changing collisions. However, in the presence of  $|F = 9/2, m_F = +5/2\rangle$ , the mixture becomes unstable as inelastic collisions of the form  $|F = 9/2, m_F = +7/2\rangle + |F = 9/2, m_F = +5/2\rangle \rightarrow |F = 9/2, m_F = +9/2\rangle + |F = 9/2, m_F = 3/2\rangle + E_{\text{rel}}$  can now occur [83].

### Magnetic transport to the science cell

In order to increase optical access to the atoms and to be able to control them using more specialized coil assemblies, the sample is moved from the MOT chamber to the science glass cell. Transport over longer distances is realized by moving a deep trapping potential at an optimal speed with respect to the typical timescales of the trap orbits. The cloud's center-of-mass can then adiabatically adapt to the new trap center and excess heating is minimized. One common technique is to displace the waist of an optical dipole trap by changing the optical path of the laser beam using a highly precise mechanical stage [84]. Another option is to use a magnetic trap whose entire coil assembly is moved [85]. By extension, a magnetic 'conveyor belt' can be created when employing a large number of static successive pairs of coils, which smoothly propagate the center of the quadrupole field by means of optimized current ramps. While the setup and optimization of an optical transport tends to be less time consuming, it is also more susceptible to misalignment and requires a much higher degree of (daily) maintenance. A magnetic transport, once implemented, is quite robust and requires only good starting conditions in terms of temperature and atom number, which is also the case for optical transport techniques. Moreover, it also facilitates transport along bent or angled paths. This robustness and flexibility is obviously compromised to some extent when the entire coil pair is moved as high degrees of mechanical stability and reproducibility are required. Therefore, FerMix uses a magnetic transport consisting of 12 pairs of static Helmholtz coils, as was depicted in figs. 2.1 and 2.7). At a given time, three coils are active in order to ensure smooth movement of the magnetic zero as well as a constant aspect ratio of the quadrupole field. The latter measure minimizes the heating during transport. The optimized currents, a measurement of which is depicted in fig. 2.10, are rather high and do tend to heat up

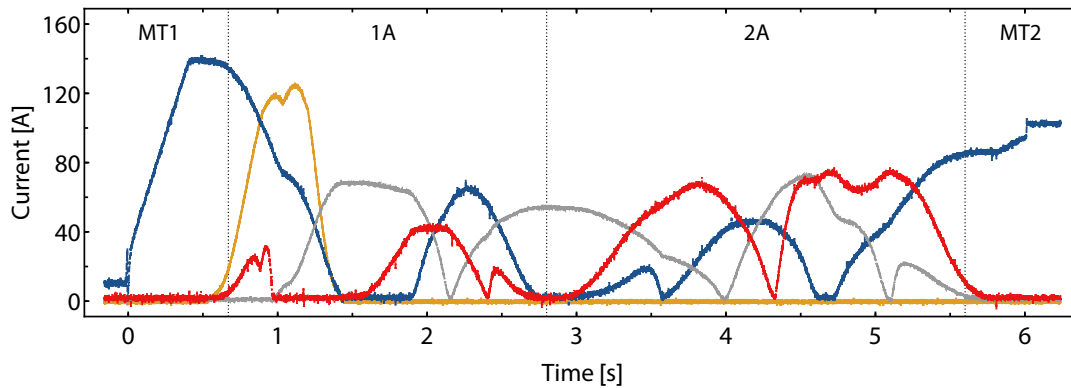


**Figure 2.10.: Magnetic transport currents.** Different colors correspond to the various power supplies involved in the transport. The curves were recorded directly at the output of the current supplies. The orange curve (push-coil) is not drawn to scale. MT1/2: Magnetic traps 1 (MOT chamber) and 2 (science cell), 1A/2A: Transport stage till and after 90° elbow, respectively.

the coils over time. Therefore, the bottom and top layer of the transport assembly are connected to a large water-cooled plate made of brass serving as heat sink. Given that these cooling plates have to extend all the way to the science cell, they can be hosts to long-lived eddy currents (in our case up to 12 ms) when switching strong magnetic fields in proximity of the science cell. The entire transport sequence takes 5.3 s and moves the atomic clouds over a distance of 65 cm. Due to the unavoidable imperfections of the magnetic transport, the atomic samples heat up as they approach the science cell and lose a certain fraction of their initial atom number. For  $^{40}\text{K}$ , the transport has an overall one-way efficiency of 77 % and heats up the ensemble by roughly 200  $\mu\text{K}$  with respect to the temperature in the magnetic trap of the MOT chamber. This increase is due to the compression of the magnetic field and parametric heating occurring during transport. Once arrived in the science cell, these heating effects are reversed by means of evaporative cooling and adiabatic cooling.

## 2.10. Evaporation of Potassium in the quadrupole trap

Following magnetic transport the atoms are kept in a deep magnetic quadrupole trap with a gradient of  $250\text{ G cm}^{-1}$ . Typical atom numbers at this stage are between  $4 \times 10^8$  and  $8 \times 10^8$  at a temperature of  $\sim 360\text{ }\mu\text{K}$ . The implied phase-space density is insufficient to facilitate good mode-matching between the magnetic trap after adiabatic opening and a tight optical dipole trap. Therefore, in order to prepare favorable initial conditions for an efficient transfer, microwave (MW) evaporation is performed in the steep magnetic trap to cool the sample well below  $100\text{ }\mu\text{K}$ .

The working principle of evaporative cooling consists of the selective removal of the most

energetic particles and the ensuing rethermalization of the remaining ensemble via elastic collisions. This energy-selective removal of the high energy tail of the Maxwell-Boltzmann distribution will cause the system to settle at a lower temperature at the expense of atom number. This way, given the proper conditions in terms of collision rates and trap properties, the phase space density (PSD) of the ensemble can be increased by several orders of magnitude, eventually reaching even the quantum degenerate regime. The onset of the latter is signified by an increase of the central PSD  $f_0 = n_0 \lambda_{\text{dB}}^3$  above unity, where  $\lambda_{\text{dB}} = \hbar \sqrt{2\pi\beta/m}$  denotes the thermal de Broglie wavelength and  $n_0 = N/V_e$  the peak spatial density. The trap volume  $V_e$  is given by  $V_e = \int d^3r \exp[-\beta U(\mathbf{r})]$  with  $U(\mathbf{r})$  representing the trapping potential and  $T = 1/k_B\beta$  the temperature of the equilibrated sample. The basic quantity

$$\alpha = -\frac{d \log(f_0)}{d \log(N)} \quad (2.2)$$

quantifies the efficiency of the cooling process and is very useful for experimental optimization of evaporation ramps. In essence,  $\alpha$  quantifies how many atoms have to be removed to gain one order of magnitude in phase space density. The full theoretical description of the evaporative cooling dynamics can be challenging since it represents an out-of-equilibrium problem with time-dependent parameters. Deep potentials inherently tend to enhance the efficiency of evaporation, however there are several other factors contributing to the dynamics at hand. Spilling- and inelastic losses as well as parasitic heating, for example via Majorana spin flips, counteract the cooling effect on their own timescales. If the trap is too high, only very few elastic collisions will be able to cause atoms to actually leave the trap carrying away excess energy, which in turn causes the evaporation to be slow. In this case, the dynamics of the harmful processes mentioned before would dominate and negate any cooling effect. When the trap depth is decreased using a properly tuned ramp, the elastic collision rate can be made to increase and diverge as the evaporation continues (runaway regime), which is a consequence of the nonlinear scalings governing the dynamics [86]. A condition to reach this regime is that the average number of elastic collisions must exceed by far the rate of inelastic loss from the trap.

### Microwave evaporation

Instead of lowering the trapping potential itself to remove hot atoms, one can instead flip their internal states to high-field seekers. This causes the affected atoms to perceive the magnetic gradient field as anti-trapping and results in their immediate ejection from the trap. In order to selectively remove only the hottest atoms from a magnetic trap, one can make use of the spatially varying Zeeman shift that gives rise to the trapping potential. As only the most energetic atoms make up the wings of the trapped sample, one can shine in RF/MW radiation driving transitions to untrappable states, which is resonant only

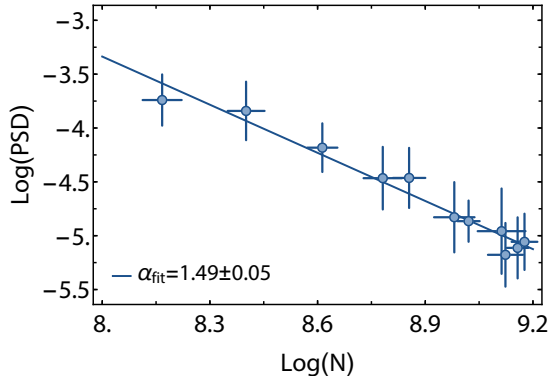


**Figure 2.11.: Microwave evaporation of Potassium-40.** LogLog-plot of the phase space density versus atom number. The sample arriving after transport consists of a mixture of the positive states  $m_F = +9/2, +7/2, +5/2$  and is evaporated for 5 s in the example depicted here. In comparison to optical evaporation, the efficiency is low with  $\alpha \sim 1.5$ . Numerical data adapted from [60].

with a certain energy shell of the trap (i.e. only atoms within a certain spatial region are resonant).

In practice, for  $^{40}\text{K}$  we drive hyperfine changing magnetic dipole transitions from  $F = 9/2$  to  $\bar{F} = 7/2$  using the MW antenna located directly next to the science cell (see sec. 3.3 for details). Over the course of 4 s the frequency is ramped in two consecutive linear ramps from 1.15 GHz to 1.26 GHz, which is equivalent to saying that the 'RF/MW knife' starts on the wings of the trap and then moves towards its center as the frequency decreases. The situation is illustrated in fig. 2.11. The corresponding process for  $^6\text{Li}$  is described elsewhere [61, 87].

Provided that the ramp is slow enough, the atoms have enough time to rethermalize and the sample grows colder as the knife becomes more resonant with the atoms occupying the low energy regions of the trap. The final value of the frequency ramp  $\nu_{\text{cut}}$  defines an upper bound of the temperature  $T_{\text{cut}}$  of the evaporated sample. Using the Breit-Rabi formula one can determine the corresponding resonant magnetic field  $B_{\text{cut}}$  and, by extension, the spatial region or, equivalently, the energy shell at which the knife stops. The cut temperature is then given by  $T_{\text{cut}} = \mu B_{\text{cut}}/k_B$  with the magnetic field being extracted from the resonance condition,

$$h\nu_{\text{cut}} = E(F = 7/2, m_F = 7/2; B_{\text{cut}}) - E(F = 9/2, m_F = 9/2; B_{\text{cut}}),$$

where  $E$  denote the eigenenergies of the hyperfine Zeeman states, which can be calculated using the Breit-Rabi formula. At the center of the magnetic trap the B-field vanishes and the energy difference becomes exactly equal to the ground state hyperfine splitting of 1285.8 MHz, corresponding to  $T_{\text{cut}} = 0$  mK.

The start and cut frequencies mentioned above correspond to temperatures of 3.7 mK and 0.7 mK, respectively. When starting with a rather large sample of  $\sim 1.5 \times 10^9$  atoms at  $T = 320 \mu\text{K}$  after transport, one obtains a cloud containing  $\sim 1 \times 10^8$  atoms at  $95 \mu\text{K}$  after evaporation. This is equivalent to an increase of the phase-space density from  $7 \times 10^{-6}$  to

$2 \times 10^{-4}$  and an efficiency of  $\alpha = -1.49 \pm 0.05$  (see fig. 2.11) [61]. However, in order to obtain consistent transfer efficiencies during the ensuing loading of the optical dipole trap, we typically evaporate further until reaching 60  $\mu\text{K}$ . At this point one is typically left with  $^{40}\text{K}$  samples of  $4 \times 10^7$  to  $8 \times 10^7$  atoms.

The gradient of the magnetic trap is chosen to facilitate reasonable collision rates while keeping the lifetime at low temperatures high enough. Overly steep gradients would increase the collision rate and by extension the final PSD at the end of evaporation, but they also imply a smaller cloud size. The latter will lead to an enhancement of Majorana losses since a larger portion of cold atoms is located near the magnetic zero. This compromise can be made obsolete by shining in a repulsive laser beam with a very small waist, which blocks the center of the trap ('Plugged quadrupole trap'). With this technique, one can increase the final atom number after evaporation by up to 20 % while maintaining the same temperature [61, 63]. However, as the plug needs to have a very small waist of 20  $\mu\text{m}$ , it is also more susceptible to pointing fluctuations. In the case of  $^{40}\text{K}$ , it was found that the benefits of the plug were outweighed by the instabilities which caused the need for frequent realignment.

## 2.11. Preparation of a degenerate Fermi gas of Potassium-40

### 2.11.1. New optical and magnetic setup around the science cell

In this section, the essential experimental techniques required to prepare, control and image an ultracold Fermi gas of  $^{40}\text{K}$  be described. Alongside this summary, the many technical changes that have taken place in the vicinity of the science cell over the course of this thesis will be highlighted as well. Most notably, all of the optical systems have been rebuilt and improved upon in order to free up the high NA optical access to the atoms. This facilitated the implementation of the tube lattice as well as of several new imaging systems, which will also be used to project custom optical potentials onto the atoms.

**Optical dipole traps.** A schematic overview of all optical- and RF/MW systems around the science cell is given in fig. 2.12. The main optical dipole trap ('ODT1') has a wavelength of 1064 nm and is provided by an Innolight Mephisto MOPA 16 W, the light of which is mode-cleaned and propagated to the science cell by means of a high power photonic crystal fiber. In order to be able to produce a small enough waist<sup>11</sup> while still using moderate focal lengths above 100 mm to keep aberrations minimal, the fiber output is enlarged to a beam size of 2 mm using a large aperture collimator with an effective focal length of 30 mm. The collimated beam of up to 7 W is then polarization-cleaned before

<sup>11</sup>As the ODT is loaded from a magnetic trap there is an ideal choice for the waist given the available optical intensities in order to transfer the atoms efficiently. This compromise between trap volumes will be described in greater detail later on.

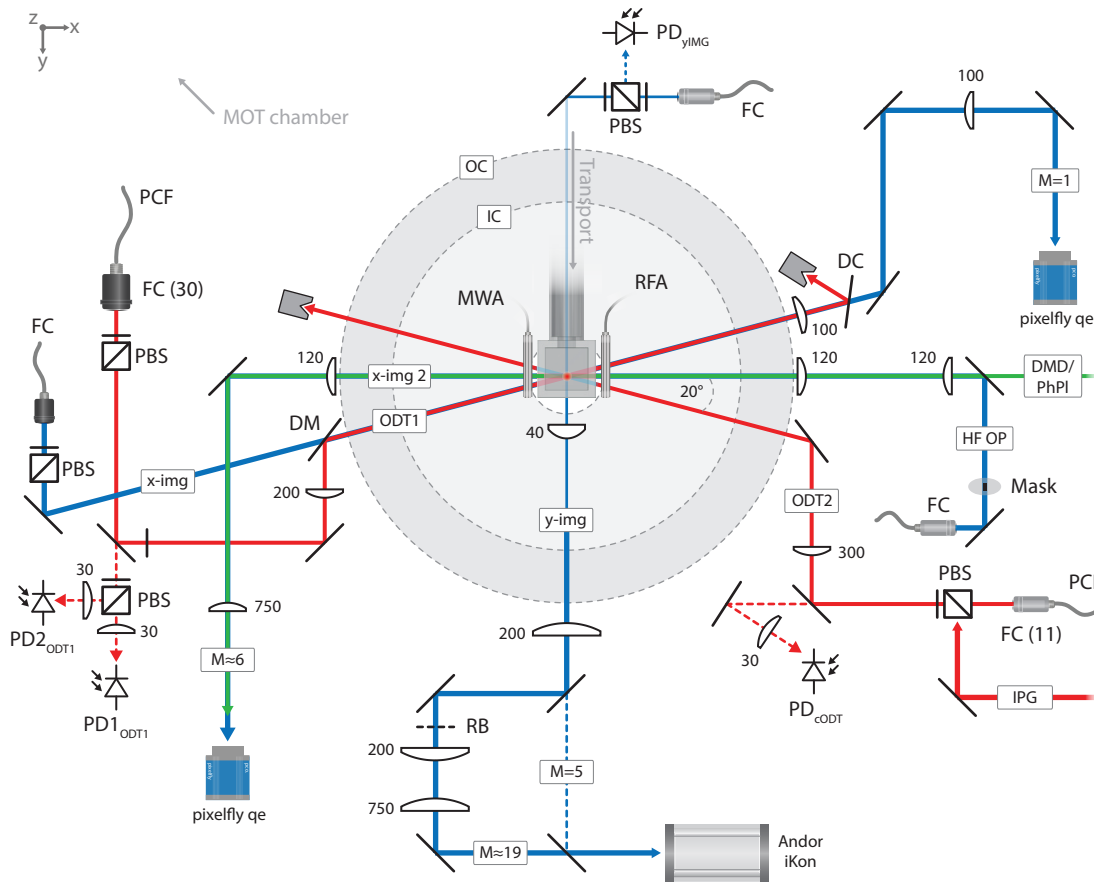


**Figure 2.12.:** New optical setup around the science cell as seen from the top. PBS: polarizing beam splitter cube and half-waveplate, FC: fiber collimators, ODT1/2 outcouplers: Schäfter-Kirchoff 60FC-SMA-0-M30-37 and 60FC-0-A11-03, PD: photodiode, PM: Picomotor, DM: dichroic mirror.

being focused down to a spot size of  $39\ \mu\text{m}$ , corresponding to a maximum trap depth of roughly  $290\ \mu\text{K}$  for  $^{40}\text{K}$ . The beam is sent into the science cell under an oblique angle of  $20^\circ$  with respect to the  $x$ -axis, with the final pointing being controlled by a piezo-actuated mirror. This particular choice of beam geometry was implemented to free up the central access to the science cell along the  $x$ -axis, which is needed to shine in custom optical potentials (6.2.8,6.2.7) and pumping beams (6.2.6). The crossed optical dipole trap ('ODT2') is shone in from the other side in a symmetrical manner. It intersects with the ODT1 under an angle of roughly  $140^\circ$  and has a maximum trap depth of  $16\ \mu\text{K}$  at a waist of  $110\ \mu\text{m}$ . Both beams originate from the same laser setup, which is described in greater detail in sec. 2.11.2. The power of both dipole traps is stabilized by providing feedback to their respective AOMs using high bandwidth PID regulators that monitor the intensity via pickup photodiodes placed behind back-polished mirrors.

This implementation of the dipole traps has two limitations. First, the available optical

power is rather limited and requires small beam waists to achieve sufficiently deep trap depths. While this set of parameters does work well for the loading of  $^{40}\text{K}$  after magnetic MW evaporation, it is borderline for  $^6\text{Li}$  due to its elevated temperature after sympathetic cooling with the former. Second, the interdependency of the maximum powers of the ODT1 and ODT2 makes it impossible to strongly recompress a crossed dipole trap in a balanced manner. This can become an issue as soon as high atomic densities are required, for example for the study of three-body losses in Fermi gases (see ch. 7). To circumvent these limitations, a second high power laser setup was installed near the science cell, which can deliver up to 150 W at the position of the atoms. Its main laser source is a broadband Ytterbium fiber laser (IPG Photonics YLR-300-LP-WC) running at 1070 nm, which can be sent to the atoms free-space or via fiber if powers of less than 30 W are required. The setup is described in greater detail in appendix B.3. It should be pointed out that such high CW optical powers come at the price of large laser linewidths of several nm. When crossing with another beam, there is a risk of exciting molecular photo-association lines which could compromise the usefulness of the crossed dipole trap. It was found that the combination of the narrowline Innolight MOPA at 1064 nm (linewidth  $< 100$  kHz) with the IPG YLR-300 at 1070 nm did not give rise to detectable enhanced molecular losses in  $^{40}\text{K}$ .

**Magnetic fields.** A vertical cross section of the coil assemblies is shown in fig. 2.13. There are two principal pairs of circular coils, which are used to create strong bias and gradient fields at the position of the atoms. The inner coils can create a bias field of  $8.00 \text{ G A}^{-1}$  with a curvature of  $+0.31 \text{ G cm}^{-2} \text{ A}^{-1}$  or a gradient field of  $2.50 \text{ G cm}^{-1} \text{ A}^{-1}$  when the currents are circulating in opposite directions. The latter is used to provide the deep quadrupole trap containing the hot atoms delivered by the magnetic transport. The large currents required are produced by a high power DC supply (Delta Eletronica SM45-140) with a maximum current of 150 A, which is equivalent to a trap steepness of  $375 \text{ G cm}^{-1}$ . This coil configuration is also used to create strong magnetic field gradients for the purpose of Stern-Gerlach imaging (see sec. 3.1). By switching certain IGBTs this coil assembly can also be used in bias configuration powered by a weaker but highly stable current supply (High Finesse UCS 30/15), which can deliver up to 30 A corresponding to maximum bias fields of 240 G. The specified current stability is some  $10^{-5}$ , which essentially sets the fluctuations of the interaction strength  $1/k_{\text{F}}a$  when tuning the magnetic field on top of the Feshbach resonance of the states  $m_{\text{F}} = -9/2, -7/2$  at 202.1 G. This issue will be discussed further in sec. 2.11.4. It should be pointed out that the positive curvature implies that there is a weak repulsive harmonic potential for negative Zeeman states at the symmetry center of the coils. If desired, this effect can be compensated by using the outer coils in combination with the inner ones to create the bias field [63]. They

have a negative curvature of  $-0.026 \text{ G cm}^{-2}$  and create a bias field of  $2.05 \text{ G A}^{-1}$  as well as a weak gradient field of  $0.24 \text{ G cm}^{-1} \text{ A}^{-1}$  if the currents are anti-parallel.

Stray DC magnetic fields that occur naturally in the vicinity of the science cell have to be compensated at certain stages of the experiment. This is the case, for example, during dipole trap loading where the magnetic trap center might move while its current is being ramped down slowly due to the presence of sufficiently strong DC fields. Three large square coils were used for that purpose in the past, however they turned out to occupy space that was needed for the new imaging systems as well as for the new tube lattice breadboard. Therefore, new smaller coil assemblies were devised that could be placed much closer to the science cell. Along  $x$ , a pair of rectangular coils with 23 windings each was designed and constructed to fit precisely into the openings of the non-metallic mount of the inner and outer coils, but without sacrificing any optical access (see fig. 2.1). Along  $z$ , two circular coils with 65 windings each were fixed directly on top and on the bottom of the transport cooling plate avoiding any metal-to-metal contact. The mounting frames of both the  $x$  and  $z$  coil assemblies were cut open in order to prevent eddy currents from being able to run alongside the magnet wire. Along  $y$ , a single rectangular coil with 60 windings has to be used as the transport tube prevents the straightforward installation of a second coil.

**Radio-frequency system.** Two different antennas are installed in close proximity to the science cell (see figs. 2.12 and 2.13), covering two distinct frequency ranges. They are used to excite magnetic dipole transitions in various experimental conditions, such as during MW/RF evaporation in a magnetic trap or during MW spectroscopy, to give but two examples. The antenna 'MWA' consists of a single loop and was impedance-matched to send out microwave pulses with frequencies on the order of the hyperfine splitting of  $^{40}\text{K}$  of 1.285 GHz. The second antenna 'RWA' has multiple windings and covers part of the lower radio-frequency range of up to  $\sim 50$  MHz, which is typically used to manipulate spin populations of a given hyperfine manifold of Potassium at magnetic fields of up to 240 G.

Electronic dipole transitions can only couple states of different parities (i.e.  $\Delta L = \pm 1$ ), which means that one cannot couple two neighboring Zeeman levels of a given hyperfine manifold  $F$  or states belonging to the two ground state manifolds  $F$  and  $F + 1$  as seen above in the case of MW evaporation. Apart from more elaborate two-photo transitions, the most convenient way to couple such pairs or states is to use magnetic dipole transitions, which obey different selection rules (see sec. 3.3). While lasers need to be used to address electronic transitions in the optical domain, radio-frequency or microwave radiation sources are required to drive transitions between neighboring Zeeman- and hyperfine states.

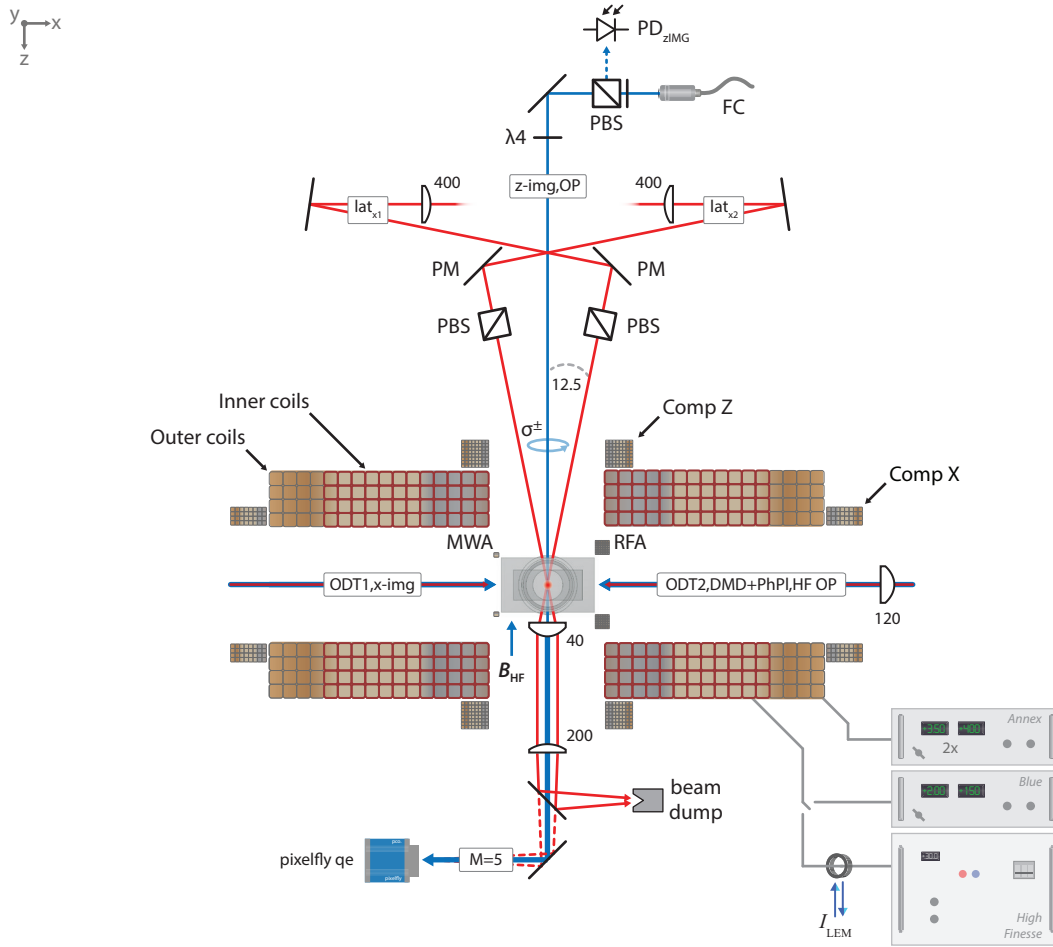


**Figure 2.13.: Magnetic coil assembly and new optical setups along the vertical direction.** Inner coils: Feshbach bias field ( $8 \text{ G A}^{-1}$ ;  $0.31 \text{ G cm}^{-2}$ ) via HighFinesse UCS 30/15 and Stern Gerlach gradient field ( $2.5 \text{ G cm}^{-1}$ ) via Delta Electronica SM45-140, Outer coils: auxiliary bias- ( $-2.05 \text{ G A}^{-1}$ ;  $-0.026 \text{ G cm}^{-2}$ ) and gradient field ( $0.24 \text{ G cm}^{-1}$ ) via two Delta Electronica connected in parallel. Comp Z/X: magnetic compensation/offset fields, MW/RF: antennas for radio-frequency or microwave pulses. PM: remotely controlled mirror mounts (Newport picomotor).

In our case, three different frequency ranges need to be generated. As detailed above transitions between the hyperfine ground states of  $^{40}\text{K}$  require MW pulses on the order of the hyperfine splitting of 1.28 GHz. For Lithium-6 the corresponding splitting is lower, so that the RF knife has to be ramped from 228 MHz to 400 MHz instead. When coupling between Zeeman states is required, the frequencies typically vary between 5 MHz (e.g. for the Landau-Zener adiabatic passage at 17.6 G, see sec. 2.11.3) and 50 MHz (e.g. incoherent spin state equilibration at 230 G) for  $^{40}\text{K}$  depending on the value of the magnetic field.

Experimentally, we use two different antennas, one of which is impedance matched for the MW regime while the other one is optimized for the low MHz frequency range.

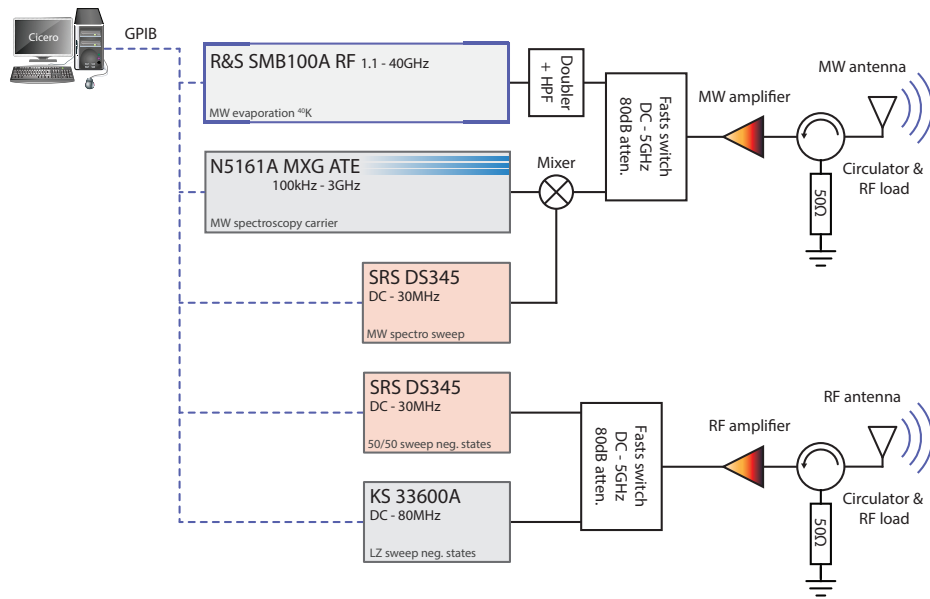


**Figure 2.14.: Simplified overview of the modified MW/RF system for  $^{40}\text{K}$ .** All signal generators are programmed via GPIB at the beginning of the sequence and triggered later on by TTL pulses during the appropriate time steps. Fast high attenuation switches facilitate the use of multiple sources per antenna and circulators are installed after the amplifiers to redirect harmful back-reflections to ground. Circulator, MW amplifier: ZHL-30W-252+, Fast switch: ZASW-2-50DR+, Signal generators: Stanford Research Systems DS345, Agilent Technologies MXG ATE N5161A, Rohde & Schwarz SMB100A, Keysight Technologies 33600A (digital arbitrary waveform generator).

The corresponding AC signals are generated by several RF/MW sources, which are controlled via GBIP as well as high attenuation switches before being sent through high power amplifiers to the antennas. Additional circulators protect the generators from back reflections. A schematic overview of the entire RF/MW system is given in fig. 2.14.

**2D optical lattice.** The tube lattice to study dimensional crossovers is generated by four far off-resonant Gaussian beams with a wavelength of 1064 nm, which intersect at a full angle of approximately  $28^\circ$  at the position of the atoms (see fig. 2.13). Each axis carries a total power of about 8 W and has a waist of 250  $\mu\text{m}$ , corresponding to a single beam trap depth of 9  $\mu\text{K}$ . The main laser is a 50 W AzurLight MOPA system, which is delivered via two high power optical fibers ( $x$  and  $y$ -lattice) to the optical setup installed above the science cell on a custom breadboard. There, the beams are split and sent downwards towards the atoms in pairs of two, generating a 2D optical lattice of tube-shaped microtraps oriented along  $z$  (i.e. parallel to gravity). Being one of the main topics of this thesis, the tube lattice is described in great detail in chapter 6.

**Custom optical potentials and high field re-pumping.** Given that the 2D lattice possesses only very little vertical confinement along  $z$ , gravity has to be compensated as it would otherwise drag the atoms downward and remove them from the tubes. As will be detailed later, the typical means of gravity compensation such as magnetic gradients or curvature are not applicable in our situation. Therefore, a blue detuned gradient light field with a wavelength of 532 nm is generated by a digital micromirror device (DMD), which is going to be installed near the science cell and imaged onto the atoms. The reflectivity pattern of the DMD is tailored to exactly match and negate gravity while remaining as insensitive as possible with respect to pointing drifts. The setup is described in sec. 6.2.8 and appendix B.1. An additional repulsive TEM<sub>00</sub>-like mode is to be shone in via the same direction in order to provide harmonic confinement along the vertical direction. This harmonic potential will be used to extract the momentum distribution via momentum refocusing, as will be detailed in sec. 5.4 and 6.2.7.

Furthermore, a spatially modulated optical pumping beam will be superimposed with the two repulsive light fields, the purpose of which is to hide all but one layer of the tube lattice. This is achieved by optically pumping the atoms into the upper hyperfine ground state, rendering them invisible during imaging at high magnetic fields of 230 G. The necessary intensity pattern is created by illuminating first a small rectangular mask with resonant light at 767 nm, which is then imaged onto the atoms at sufficiently high resolution. This ensures that the row in the focal plane of the high resolution imaging system along  $y$  does not receive any parasitic pumping photons. Further details regarding this setup are provided in sec. 6.2.6.

**Imaging systems.** In order to reconstruct the optical density, three images are needed: A destructive absorption shot during which the atoms scatter photons while expanding ballistically; An exposure of only the imaging light that provides the reference to isolate the atomic density distribution and a third image that records both the noise of the camera as well as the ambient noise due to stray light. The duration of the imaging pulse is set to 25  $\mu\text{s}$  with an intensity of  $I/I_s \approx 0.1$ .<sup>12</sup> A brief summary of the working principles of absorption imaging is given in appendix C.1.

There are three new and distinct imaging systems with different magnifications and functions around the science cell. With the exception of  $y$ -imaging, they are all equipped with standard scientific CCD cameras operated in double shutter mode (Pixelfly QE 270XD, quantum efficiency 25 % at 767 nm), the sensitivity of which is sufficient as long as the signal-to-noise ratio ('SNR') does not get too low. The latter condition depends both on the atom number and magnification at hand, and is usually fulfilled until the

<sup>12</sup>The past pulse duration of 80  $\mu\text{s}$  as well as the overall intensity were found to be too high, causing Doppler-broadening as well as excessive optical pumping during the imaging. The latter had detrimental effects on the detectivity of certain spin states, especially at low or transient magnetic fields.

very end of optical evaporation with typically  $\sim 10^5$  atoms and magnifications of  $\sim 2 - 5$ . However, in the case of the lattice the atom number per tube will drop well below  $10^4$ . In combination with the fact that a high degree of magnification is required to resolve and image the lattice structure across multiple pixels with typical sizes of up to  $\sim 10 \mu\text{m}$ , a highly sensitive camera is used as part of the  $y$ -imaging axis (Andor iKon, see ch. 6.2.5 for details).

*Along ODT1 ('x-imaging').* This imaging system with magnification of  $M = 1$  serves primarily to optimize the loading of the main dipole trap and its evaporation ramp as well as to measure the trapping frequencies. Since one integrates the atomic density along the entire length of the single beam dipole trap, the signal-to-noise ratio is quite favorable for loss measurements (see chapter 4). Moreover, it can be used to inspect the atomic ensembles as they arrive in the science cell or to optimize the MW evaporation. As the optical axis of this imaging system is perpendicular to the vertical quantization axis of the atomic sample, the polarization cannot be tuned to be purely  $\sigma^+$  or  $\sigma^-$ . Rather, in our situation where the incident light field oscillates horizontally the polarization corresponds to an equal superposition of  $\sigma^+$  and  $\sigma^-$ . As a result, optical pumping into a stretched state or imaging on a cycling transition along  $x$  are only possible at high magnetic fields.

*Along gravity ('z-imaging').* While being used also for inspecting the crossed optical dipole trap, this imaging axis serves, more importantly, to observe Kapitza-Dirac scattering along both directions of the tube lattice (see sec. 6.2.3) as well as for optical pumping at low and high magnetic fields (see sec. 3.1). It has a magnification of  $M = 4$  and is oriented along the main quantization axis. Because of this, it is the only imaging system with which optical pumping and imaging on a cycling transition are possible at low magnetic fields. The polarization can be tuned by rotating a quarter-waveplate in order to be able to work with positive and negative Zeeman states.

*Along transport ('y-imaging').* In order to resolve the tube-like density modulation of the new optical lattice with a lattice constant of roughly  $2.5 \mu\text{m}$ , this imaging axis has a resolution of  $1.6 \mu\text{m}$ . It has a total magnification of  $M \approx 19$  and is therefore equipped with a highly sensitive CMOS camera to be able to detect the implied weak atomic signals. Just like in the case of  $x$ -imaging, the polarization is linear and perpendicular to the quantization axis, which necessitates the use of high magnetic fields in order to image on a quasi-closed transition. More details about this imaging setup are given in sec. 6.2.4.

### 2.11.2. Optical dipole traps and evaporation in the positive states

Following MW evaporation in the quadrupole trap (sec. 2.10), the atoms are loaded into a single beam optical dipole trap. The use of optical potentials in the absence of strong magnetic gradient fields makes it possible to use Feshbach resonances and gets rid of Majorana spin flips, which would otherwise tend to be enhanced at low temperatures and high phase space densities. Since the coupling of neutral atoms to off-resonant light fields is a crucial prerequisite for the experimental techniques described in chapter 6, some of the most crucial features will be summarized in the following.

#### Alkali atoms in far off-resonant optical potentials

An off-resonant AC electric field induces an oscillating electric dipole moment in neutral atoms. The strength of this coupling is determined by the complex polarizability tensor of the atom (valence electron), which depends on their internal level structure as well as on the light polarization and its frequency. In the case where the fine-structure is resolved but all state- and polarization-dependencies can be neglected<sup>13</sup>, the dipole potential for any Alkali hyperfine ground state  $|F, m_F\rangle$  is fixed by the scalar polarizability originating from the virtual coupling to the D-line doublet  $2^2S_{1/2} \rightarrow 2^2P_{1/2}, 2^2P_{3/2}$  [68],

$$U(\mathbf{r}) = \frac{\pi c^2 \Gamma_{\text{nat}}}{2\omega_{\text{D1}}^3} \left( \frac{1}{\Delta_{\text{D1}}} + \frac{2}{\Delta_{\text{D2}}} \right) I_{\text{L}}(\mathbf{r}) \quad (2.3)$$

Here,  $\Gamma_{\text{nat}}$  is the natural line-width of the D1-line and  $\omega_{\text{D1}}$  denotes its angular transition frequency.  $\Delta_{\text{D1}/2}$  is the angular detuning of the driving light field from the particular resonance. The summands appearing in the above expression reflect the contributions from the D1- and D2-line, weighed with respect to the former. The counter-rotating terms have been dropped within the rotating wave approximation. The corresponding off-resonant scattering rate is given by:

$$\Gamma(\mathbf{r}) = \frac{\pi c^2 \Gamma_{\text{nat}}^2}{2\hbar\omega_{\text{D1}}^3} \left( \frac{1}{\Delta_{\text{D1}}^2} + \frac{2}{\Delta_{\text{D2}}^2} \right) I_{\text{L}}(\mathbf{r}). \quad (2.4)$$

The equations (2.4) and (2.3) exhibit two properties which are crucial for optical trapping of neutral atoms: First, the sign of the detuning defines the position of the potential minima. If the light field frequency is red detuned with respect to the atomic resonances, the potential is negative and, consequently, atoms are attracted to the points of maximum intensity. This is the physical operation principle of focused beam traps ('dipole traps') in which atoms are pulled toward the beam's waist. In the case where the light is tuned above

<sup>13</sup>This is equivalent to either choosing linear polarization or a semi-large detuning with respect to the fine-structure splitting.

the D-lines (blue detuning) the potential has a positive sign. As a result atoms are pushed away from regions of high optical power. Such anti-confinement can be used for example to plug magnetic traps or to compensate gravity optically (see sec. 6.2.8) as well as to create tight harmonic confinement (see 6.2.7). The second important property regards the scaling with intensity and detuning. While the dipole potential grows monotonically with  $I_L/\Delta_L$ , the off-resonant scattering rate scales as  $I_L/\Delta_L^2$ .<sup>14</sup> This is a major design parameter for optical traps since a combination of large detuning and high optical intensity enables one to keep the scattering rates as low as possible for a given potential depth.

In practice, one typically creates dipole traps by using red-detuned Gaussian TEM<sub>00</sub> beams, which are focused down to an appropriate spot size  $\omega_0$ . The intensity field  $I_L$  can be described by the basic expression

$$I_L(\mathbf{r}) = \frac{2P_{\text{tot}}}{\pi\omega(z)^2} \exp\left(-\frac{2r^2}{\omega(z)^2}\right), \quad (2.5)$$

which is only valid after the focusing lens.  $P_{\text{tot}}$  denotes the total optical power contained within the mode,  $\omega(z) = \omega_0\sqrt{1 + (z/z_R)^2}$  gives the evolution of the waist  $\omega_0$  along the axis of propagation  $z$  and  $z_R = \pi\omega_0^2/\lambda$  represents the Rayleigh length of the beam. The optical system used to generate the two dipole traps of the experiment has already been detailed in 2.11.1. In the vicinity of the waist where  $z \ll z_R$  and  $r^2 = x^2 + y^2 \ll \omega_0^2$  hold, the potential can be approximated to be harmonic as per

$$U(\mathbf{r}) \simeq U_0 + \frac{1}{2}m\left(\omega_x^2x^2 + \omega_y^2y^2 + \omega_z^2z^2\right), \quad (2.6)$$

where  $U_0 = U(\mathbf{r} = \mathbf{0})$  is the trap depth. The transverse and axial trapping frequencies are given by  $\omega_{x,y} = \omega_{\perp} = \sqrt{4U_0/m\omega_0^2}$  and  $\omega_z = \omega_{\parallel} = \sqrt{2U_0/mz_R^2}$ , respectively. At full powers of 6 W and 3 W at the position of the atoms, the two dipole traps have maximum trap depths of  $U_0 = 290 \mu\text{K}$  and  $16 \mu\text{K}$ , respectively. The corresponding transverse and axial trapping frequencies of the main dipole trap are given by  $\omega_{\perp} = 2\pi \times 2 \text{ kHz}$  and  $\omega_{\parallel} = 2\pi \times 12 \text{ Hz}$ . Correspondingly, the transverse trapping frequencies of the crossed dipole trap amounts to  $2\pi \times 155 \text{ Hz}$ . The experimental techniques to calibrate these frequencies are described in greater detail in appendix C.2.

### New high power laser system

High optical intensities are required to obtain reasonable trap depths of  $> 0.1 \text{ mK}$  when working at very large detunings of hundreds of nm from resonance. Moreover, while the optical power at the position of the atoms can be stabilized using a fast servo loop, the laser source itself should display as little intensity noise as possible as certain frequency

<sup>14</sup> $\Delta_L$  is meant to represent some average detuning.

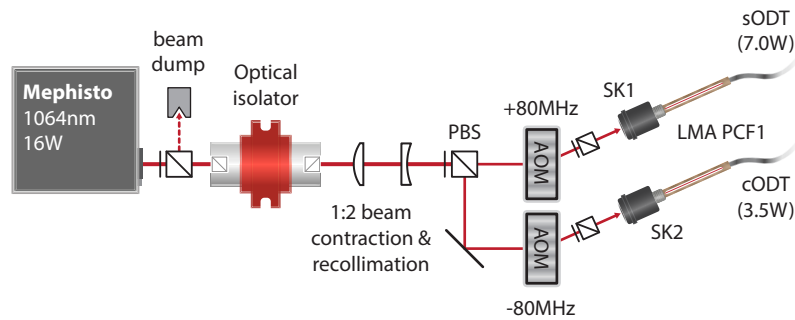


**Figure 2.15.: Simplified schematic overview of the laser system.** LMA-PCF1/2: Large mode area photonic crystal fiber (NKT Photonics LMA-PM-10), SK1/2: Fiber collimator  $F = 11$  mm (Schäfter-Kirchoff 60FC-SMA-T-4-A11-03), AOMs: Gooch & Housego 3110-197.

components exceeding the PID bandwidth can cause parametric heating of the atoms [88]. While the linewidth of a far-off-resonance trap usually does not matter in terms of trap depth or parasitic photon scattering rate, it does come into play when generating a crossed trap using two beams originating from the same laser. If the laser is very broad with e.g. a linewidth of  $\sim 1$  nm, one risks to excite molecular photo-association lines when crossing the beams on the atoms, which can only be prevented by polarizing with extremely high extinction ratios [89].

To avoid these problems, we use a Mephisto Innolight MOPA laser as main laser source, which offers relatively high powers of up to  $25\text{ W}^{15}$  at a specified linewidth of  $100\text{ kHz}$  and low relative intensity noise (RIN) of less than  $-130\text{ dB Hz}^{-1}$  according to specs. A schematic overview of the optical system is depicted in fig. 2.15. After some initial mode shaping, the laser output is split and passed through high power AOMs that also act as a fast switches and the means to stabilize and ramp the optical intensity through via their RF power. The beams corresponding to the sODT and cODT, respectively, are then coupled into single mode photonic crystal fibers. The fibers are outfitted with copper heat sinks on either side to relieve some of the thermal stress arising from the absorption of uncoupled parts of the incident optical power. Angled SMA connectors are used on both sides to reduce potential back reflections that could harm the amplification stages of the laser and the fiber is protected by a stainless steel sleeve preventing damage due to mechanical stress. The setup is contained within a cast aluminum enclosure to reduce the amount of fluctuations in the air, which would otherwise compromise the stability of the fiber coupling despite the active stabilization.

The beam path after of the dipole trap after the fiber was already described in sec. 2.11.1. After polarization cleaning, a fast biased photodiodes is placed behind the ensuing mirror to pick up the weak transmitted portion of the light. Its voltage output is fed into commer-

<sup>15</sup>Unfortunately, the power has since then degraded to  $16\text{ W}$ , an effect that was also observed in a spare laser of the same age that remained essentially unused.

cial PID regulators (Stanford Research Systems SIM960) with a bandwidth of 100 kHz. The desired setpoint is given by an analog channel of the NI control system (see sec. 2.4) and the active intensity control is achieved by providing feedback to the analog modulation input of the AOM's RF driver. The complete servo loop is depicted in fig. 2.16a. Given that the light intensity has to be varied over only four decades, one linear photo diode is in principle sufficient in terms of dynamic range. However, due to resolution restrictions of the analog card providing the setpoint of the PID, intensity sweeps become noticeably discrete at optical powers below  $\sim 100$  mW. This is detrimental to the efficiency of the final evaporation ramp in the crossed optical dipole trap, which is the crucial step to reach the deeply quantum degenerate regime. To circumvent this problem, the intensity regulation is handed over to a second servo loop well before reaching the resolution limit, i.e. when the first photodiode reaches voltages around 1 V. This additional stabilization circuit has its own photodiode and analog channel providing the setpoint (see fig. 2.12), which are optimized to cover only the regime of low optical intensities. The alternation between the two PID controllers is handled by an analog IC switch. As is described in appendix B.3, much larger ranges of optical powers can also be controlled via a single PID by making use of a logarithmic amplifier placed after the photodiode. However, this approach comes at the expense of increased electronic noise and was therefore avoided in the case of the main dipole traps.

### Dipole trap loading

As the atoms arrive in the science cell to undergo MW evaporation, they are much too hot to notice the presence of the optical potential. As they cool down, the dipole trap begins to act like a dimple inside of the magnetic trap, which must not coincide with the magnetic zero as it would otherwise strongly enhance Majorana losses. The atoms are subject to the total potential given by  $U_{\text{tot}} = U_{\text{mag}}(\mathbf{r}) + U_{\text{odt}}(\mathbf{r}) + U_{\text{grav}}(z)$ , where  $U_{\text{grav}} = mgz$  is the gravitational sag,  $U_{\text{mag}}$  denotes the quadrupole potential as defined in 2.1 and  $U_{\text{odt}}$  represents the optical potential created by a Gaussian beam. In order to transfer the cold atomic sample from the magnetic trap to the dipole trap, we slowly ramp down over the course of 0.8 s the magnetic gradient from  $250 \text{ G cm}^{-1}$  to  $5.1 \text{ G cm}^{-1}$ , the latter value being just below the levitation threshold with respect to gravity. This way, the atoms drift gradually towards the dipole trap as the magnetic confinement weakens, the former being located at an experimentally optimized distance of about  $d_z = 80 \mu\text{m} \simeq 2\omega_0$  below the magnetic center. During this ramp, additional magnetic bias fields are used to compensate permanent DC fields which are present in the vicinity of the science cell. If left in place, these stray fields would cause the magnetic quadrupole trap to move as soon as its gradient reaches sufficiently low values. After recapture by the ODT and a short settling time of 50 ms, we typically obtain  $^{40}\text{K}$  samples with  $9 \times 10^6$  to  $2 \times 10^7$  atoms at

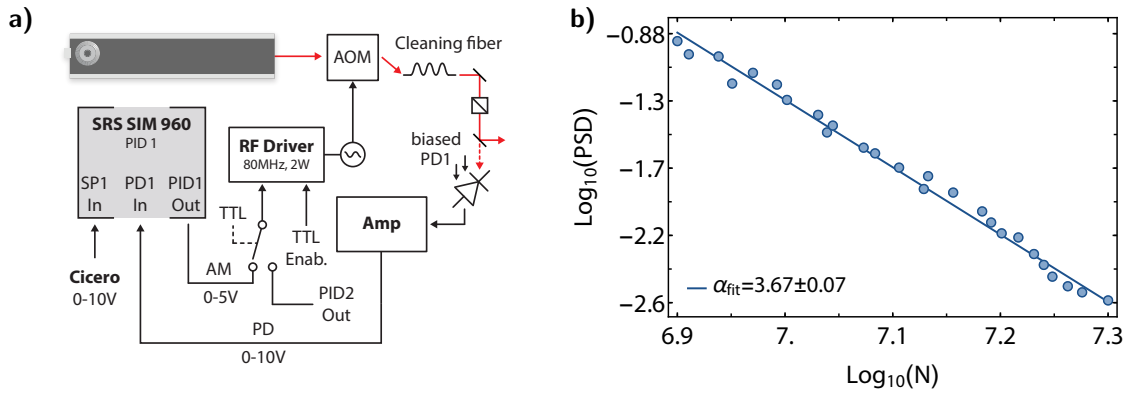


**Figure 2.16.: Evaporation in the optical dipole trap.** a) Schematic illustration of the dual-PID servo loop. b) LogLog plot of the phase space density versus atom number at certain stages during the evaporation ramp. Numerical data adapted from [61].

temperatures of 30  $\mu\text{K}$ . The overall transfer efficiency is typically around 25 %.

The optimization of this transfer relies on a good ‘mode matching’ between the two trap volumes. This is a function of the PSD of the quadrupole trap, which is set by initial conditions after magnetic transport as well as by the final cut of the MW evaporation, and the trap volume of the dipole trap. The latter is essentially given by the waist and the optical intensity, both of which are chosen to optimize loading efficiency. More details regarding this optimization can be found in [61]. The final trap geometry is a hybrid configuration between the remaining magnetic restoring forces and the optical potential. Along the ODT’s transverse direction the magnetic gradient field serves mainly to compensate gravity, while along its axial direction it provides additional confinement with an angular trapping frequency of  $\omega_{m,ax} \simeq \sqrt{\mu b / 4 m d_z}$ . This confinement complements the weak longitudinal trapping power of a single Gaussian beam trap and thus increases the collision rate along this direction, which is of importance for the ensuing optical evaporation.

### Optical evaporation in the positive states

At the time of loading, the atoms occupy the three positive spin states  $m_F = +9/2$ ,  $+7/2$  and  $+5/2$ , which have singlet and triplet scattering lengths of  $104a_0$  and  $170a_0$ , respectively [90]. In order to further increase the atoms’ PSD we accelerate the evaporation of the trapped atoms by ramping down exponentially the optical power of the dipole trap from its loading set point of 6 W to 93 mW over the course of 4 s. Additional axial confinement is provided by the weak magnetic gradient field as mentioned above, the strength of which is increased from  $5.1 \text{ G cm}^{-1}$  to  $6.15 \text{ G cm}^{-1}$  over the course of the evaporation ramp as it was found to slightly increase the final PSD. The ambient magnetic

bias field is set to 3 G, which is sufficient to conserve the polarization of the gas and avoids harmful Feshbach resonances of  $^{40}\text{K}$  between  $B = 7\text{ G}$  and  $12\text{ G}$  as well as increasing inelastic losses occurring as of  $15\text{ G}$  (see chapter 4). During the evaporation step the initially loaded atom numbers of between  $9 \times 10^6$  and  $2 \times 10^7$  drop to low  $10^6$  with the temperature decreasing from  $30\ \mu\text{K}$  to  $1\ \mu\text{K}$ . Among other factors, the final temperature largely depends on the chosen final trap depth of the ODT. In good conditions, one can reach temperatures as low as  $300\ \text{nK}$ . The efficiency of the evaporation process can be extracted from the log-plot of the PSD against the atom number and assumes a rather high value with  $\alpha = -3.67 \pm 0.07$ . As the temperature of the atoms is already well below  $100\ \mu\text{K}$  at the time of loading, the remaining elastic p-wave collisions quickly cease to play a role as the gas cools down further [59]. The remaining s-wave interactions between  $|m_F = 9/2\rangle$  and  $|m_F = 7/2\rangle$  can maintain efficient evaporative cooling until about  $T \sim 0.7\ \mu\text{K}$ , which is when the gas stops cooling efficiently as a result of marginal collision rates. At this point, one is left with about  $\sim 10^6$  atoms at  $T/T_F \sim 2.5$ . The Fermi-temperature in a harmonic trap is given by  $T_F = E_F/k_B = (6N_\sigma)^{1/3}\hbar\bar{\omega}$  with  $\bar{\omega} = (\omega_\perp^2\omega_\parallel)^{1/3}$ . Using Stern-Gerlach imaging (see sec. 3.1), the cloud's spin composition at this stage is found to be 55 %  $|m_F = 9/2\rangle$ , 33 %  $|m_F = 7/2\rangle$  and 12 %  $|m_F = 5/2\rangle$ .

In order to bring the sample to quantum degeneracy, we first increase the density before evaporating further by ramping up the crossed optical dipole trap ODT2 once the gas reaches a temperature of roughly  $4\ \mu\text{K}$  (see sec. 2.11.4). Moreover, the atoms are transferred into the lowest energy Zeeman states to increase the collisional stability of the mixture<sup>16</sup> and in order to be able to take advantage of the Feshbach resonance at  $202\text{ G}$ .

### 2.11.3. Landau-Zener adiabatic passage to the negative states

After removing the magnetic gradient as well as the compensation bias fields, we rapidly increase the strength of the homogeneous z-bias field defining the quantization axis from  $3\text{ G}$  to  $60.5\text{ G}$ , allowing for sufficient time for the power supply to stabilize after the ramp. The atoms are then subjected to a radio-frequency sweep over the course of  $20\text{ ms}$ , which is emitted by an antenna in the vicinity of the science cell driven by the RF system already described in sec. 2.11.1.<sup>17</sup> By ramping the frequency slowly in a linear fashion from  $22\text{ MHz}$  to  $16\text{ MHz}$  the populations of  $|m_F = +9/2\rangle$  and  $|m_F = +7/2\rangle$  are transferred to their negative counter parts  $|m_F = -9/2\rangle$  and  $|m_F = -7/2\rangle$ , as is shown in fig. 2.17a. Further details regarding this so-called Landau-Zener adiabatic passage and the involved

<sup>16</sup>Spin-changing collisions are endothermic between the lowest two negative Zeeman states. At low temperatures one is thus energetically protected against such inelastic processes due to the sheer absence of kinetic energy.

<sup>17</sup>The antenna's symmetry axis is perpendicular with respect to the quantization axis. The emitted radiation therefore consists mostly of a superposition of  $\sigma^+$  and  $\sigma^-$  polarization as well as of some  $\pi$  polarization as the antenna is not perfectly planar.

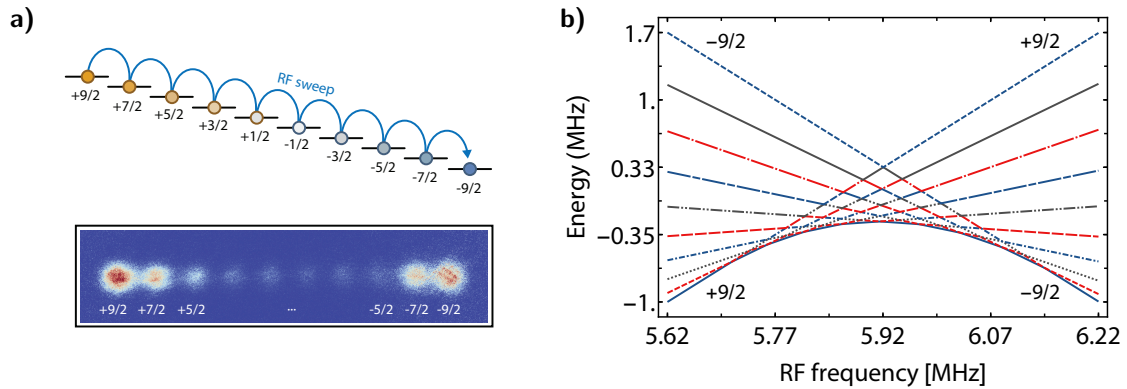


**Figure 2.17.: Landau-Zener adiabatic passage to the negative states.** a) Top: schematic illustration of the successive independent radio-frequency sweeps moving the atomic population down the ladder of Zeeman levels. Bottom: overlay of three absorption images of spatially separated spin populations using SG imaging (see 3.1). Data adapted from [60]. b) Eigenenergies of the RF-dressed states in  $F = 9/2$ . For this calculation, the magnetic bias field was set to  $B = 19$  G with a realistic Rabi frequency of  $\Omega_0 = 2\pi \times 1$  kHz. For these parameters, there are avoided crossings (not visible here) for  $m_F = 9/2, 7/2$ , but not for  $m_F = 5/2$ , which is why its population is not transferred to the negative counterpart in a).

transitions are given in secs. 3.3.1 and 3.3.2. Due to the presence of several avoided crossings in the dressed eigenenergies, the transfer for these two pairs of states can be greater than 90 %. However, the situation is different for  $m_F = +5/2$  which does have crossings that prevent an efficient transfer. The eigenenergies for a magnetic field of 19 G are plotted in fig. 2.17b.

Incoherent mixtures of two neighboring Zeeman states can be prepared in a similar fashion. While performing a Landau-Zener sweep, the phase angle changes continuously so that the dressed eigenstates sample through all kinds of superpositions. In order to produce a balanced mixture of two states, we interrupt the sweep at the exact time when the populations happen to be equal. The timing naturally depends on the initial conditions and must be optimized experimentally. However, after this incomplete ramp the spin state of a given atom will be in a *coherent* superposition of the two Zeeman states. Decoherence can be introduced by subjecting these atoms to a magnetic gradient field, which will cause the unitary time evolution of the two contributing states to occur at different frequencies because of their unequal magnetic moments. In addition, the spatial trajectories in the gradient field will dephase as well. Experimentally, we perform the 50:50 mixing of  $\pm 9/2$  and  $\pm 7/2$  at the same bias field of 60.5 G, where the energy splittings between the various Zeeman levels are sufficiently distinct to prevent accidental population of  $m_F = \pm 5/2$ . The duration of the sweep amounts to 1 ms and the ensuing dephasing time of 1 s is chosen to be noticeably longer than the slowest timescale of the single particle orbits.

#### 2.11.4. New crossed optical dipole trap and evaporation to degeneracy

The crossed optical dipole trap is superimposed symmetrically with the main dipole trap under an angle of about  $140^\circ$ , as was previously shown in fig. 2.12. It has a comparatively large waist of  $110 \mu\text{m}$  with optical powers of up to  $3 \text{ W}$  at the position of the atoms, which corresponds to a maximum trap depth of  $16 \mu\text{K}$ . In order to avoid cross-interference the polarization of the cODT is chosen to be orthogonal with respect to the first one. In addition, the frequency is shifted by  $160 \text{ MHz}$  so that any remaining beat node in the crossing region will oscillate much faster than the atomic timescales and thus average out. The new trapping frequencies of the incoherently superimposed traps  $U_{\text{cODT}}(\mathbf{r}) = U_{\text{ODT1}}(\mathbf{r}) + U_{\text{ODT2}}(\mathbf{r})$  in terms of the orthonormal system  $\{x, y, z\}$  are then given by

$$\begin{aligned}\omega_x^2 &= \left(\omega_{\perp,1}^2 + \omega_{\perp,2}^2\right) \sin^2 \alpha + \left(\omega_{\parallel,1}^2 + \omega_{\parallel,2}^2\right) \cos^2 \alpha, \\ \omega_y^2 &= \left(\omega_{\perp,1}^2 + \omega_{\perp,2}^2\right) \cos^2 \alpha + \left(\omega_{\parallel,1}^2 + \omega_{\parallel,2}^2\right) \sin^2 \alpha, \\ \omega_z^2 &= \omega_{z,1}^2 + \omega_{z,2}^2,\end{aligned}$$

where  $\alpha = (\pi - 140^\circ)/2 = 20^\circ$  is the angle between ODT1/ODT2 and the x-axis. These frequencies must be known very precisely in order to correctly calculate atomic densities, both in the classical and the quantum degenerate limit (see below). They can be characterized experimentally by exciting breathing modes or center-of-mass oscillations, the timescale of which is set by the underlying trapping frequencies. Another method is to modulate the potential depth to drive parametric excitations between the vibrational states of the trap. All of these methods are covered in detail in appendix C.2.

After preparing a balanced mixture of the negative spin states  $|-9/2\rangle$  and  $|-7/2\rangle$ <sup>18</sup> at  $60.5 \text{ G}$ , the magnetic bias field is ramped within  $100 \text{ ms}$  to  $239 \text{ G}$ . This field corresponds to a background s-wave scattering length of  $+137a_0$  (see fig.2.18a) on the attractive side of the Feshbach resonance located at  $202.1 \text{ G}$ . At this point, the sample is contained in a partially loaded crossed dipole trap and consists of  $1 \times 10^6$  atoms per spin state at a temperature of roughly  $4 \mu\text{K}$ .

In order to cool down further, the magnetic field is ramped to  $205.9 \text{ G}$ , increasing the scattering length to  $-183a_0$ . The sample is then evaporated for  $10 \text{ s}$  by ramping down exponentially the intensity of both dipole traps. After this step, only the harmonic center of the crossed ODT remains densely populated as the wings have evaporated. The sample now contains typically  $2 \times 10^5$  atoms per spin state at a temperature of around  $300 \text{ nK}$ , corresponding to a degeneracy parameter of  $T/T_{\text{F,harm}} \simeq 0.35$ . The experimental optimization of the magnetic field for this evaporation ramp is shown in fig.2.18b.

<sup>18</sup>Note that these are not good quantum numbers at high magnetic fields. They are used here as labels only with the actual states adiabatically connecting to  $|-9/2\rangle$  and  $|-7/2\rangle$  as  $B \rightarrow 0$ .

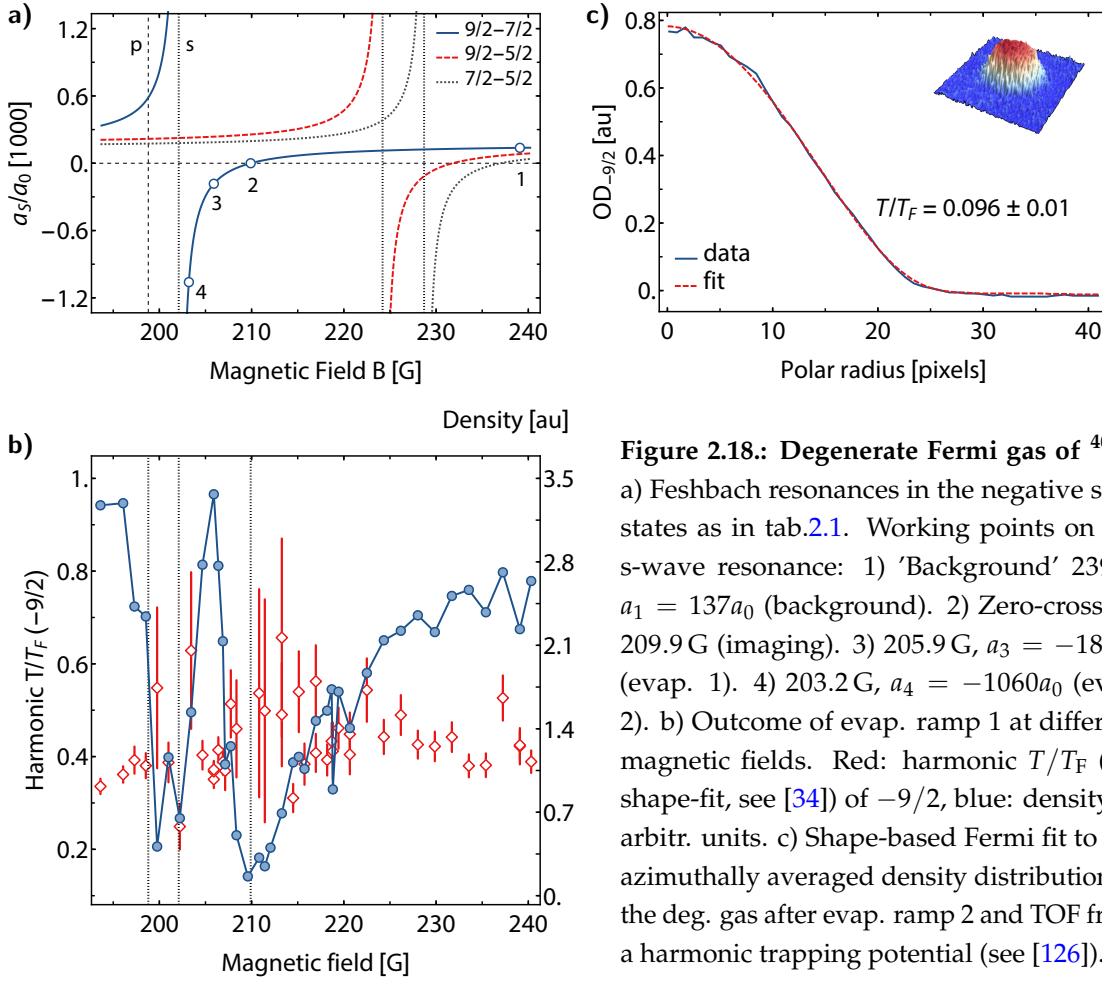


**Figure 2.18.: Degenerate Fermi gas of  $^{40}\text{K}$ .**

a) Feshbach resonances in the negative spin states as in tab.2.1. Working points on the s-wave resonance: 1) 'Background' 239 G,  $a_1 = 137a_0$  (background). 2) Zero-crossing 209.9 G (imaging). 3) 205.9 G,  $a_3 = -183a_0$  (evap. 1). 4) 203.2 G,  $a_4 = -1060a_0$  (evap. 2). b) Outcome of evap. ramp 1 at different magnetic fields. Red: harmonic  $T/T_F$  (2D shape-fit, see [34]) of  $-9/2$ , blue: density in arbitr. units. c) Shape-based Fermi fit to the azimuthally averaged density distribution of the deg. gas after evap. ramp 2 and TOF from a harmonic trapping potential (see [126]).

To reach the deeply quantum degenerate regime, the scattering length is increased to  $-1060a_0$  by ramping the magnetic field to 203.2 G. After another stage of forced evaporation for 1 s, we obtain samples of about  $2 \times 10^4$  atoms per spin state at a temperature of  $T/T_{F,\text{harm}} = 0.103(14)$  (2D Fermi fit). The corresponding absorption picture and the 1D Fermi fit to the azimuthally averaged density distribution are shown in fig. 2.18c.

In the quantum degenerate limit, the integrated column density can no longer be described by a Gaussian distribution since the classical Boltzmann statistics of the thermal limit are replaced by Fermi-Dirac statistics. As a result, a polylogarithmic function has to be used for thermometry of a (non-interacting) degenerate Fermi gas. The degeneracy parameters  $T/T_{F,\text{harm}}$  indicated earlier are obtained by using a 2D Fermi fit containing the shape parameter  $q$  [34],

$$\frac{T}{T_F} = [-6 \text{Li}_3(-e^q)]^{-1/3}. \quad (2.7)$$

This relation is valid for harmonic trapping potentials and depends *only* on the logarithm of the fugacity,  $q = \mu\beta$ , which in turn determines the shape of the cloud. Note that this

**Table 2.1.:** Common s- and p-wave Feshbach resonances in the negative ground states of  $^{40}\text{K}$ .

$m_{F,1}, m_{F,2}$	$M_T$	Partial wave	$B_0$ [G]	$\Delta B_L$ [G]	Ref.
$-9/2, -7/2$	-8	s	202.10(7)	7.5(1), 7.80(6)	[92, 126]
$-9/2, -5/2$	-7	s	224.21(5)	9.7(6), 7.6(1)	[91, 92]
$-7/2, -5/2$	-6	s	174	7	[91]
$-7/2, -5/2$	-6	s	228.8(4)	2.4(3)	[91]
$-7/2, -7/2$	-7	p	198.8		[93]

approach does not require the explicit knowledge of the underlying trapping frequencies and can thus be used to conveniently extract  $T/T_{F,\text{harm}}$  from a single shot. More detailed descriptions of the analysis of density profiles of degenerate Fermi gases are given in appendix C.1 as well as in [34, 63, 126].

Strongly interacting Fermi gases of  $^{40}\text{K}$  are realized by tuning the scattering length on top of the s-wave Feshbach resonance and controlling the spin imbalance by means of RF transfers. Unfortunately, a p-wave resonance between the states  $|9/2, -7/2\rangle$  and  $|9/2, -7/2\rangle$  is located at 199 G, just below the center of the s-wave resonance. Consequently, one cannot safely approach the latter from the repulsive side due to the potential onset of inelastic losses, which also depend on temperature. For RF spectroscopy (see sec. 5.3) we use  $|9/2, -5/2\rangle$  as weakly interacting target state. Therefore, the additional resonances at 224.21 G and 228.7 G (see tab.2.1) have to be avoided to prevent this state from coupling strongly to the two lower lying Zeeman levels. A detailed survey of the known Feshbach resonances between all of the spin states of  $^{40}\text{K}$  can be found in appendix C.5.

The s-wave resonance has the positive property of being comparatively narrow while still being entrance-channel-dominated. When working with the strongly interacting gases, the interactions between  $|9/2, -9/2\rangle$  and  $|9/2, -7/2\rangle$  need to be switched off rapidly when they are released from the trap for free time-of-flight. This is necessary due to the fact that interactions may render the expansion non-ballistic, thereby altering the observed momentum distribution which then no longer reflects the one originally present in the trap. This problem can be circumvented by quickly ramping the magnetic field to the zero-crossing of the scattering length at 209.9 G. The speed at which this ramp can be performed depends on the power supply's capacity as well as on the response of the coil in terms of  $\text{G A}^{-1}$ . If ramps in excess of 100 G were required, as would be the case for  $^6\text{Li}$ , the procedure could take several ms during which the atoms would continue to scatter. In the case of  $^{40}\text{K}$ , owing to the small width of the resonance one needs to change the magnetic field by only 7.8 G to reach the zero-crossing. With the response of the inner coils of  $8.05 \text{ G A}^{-1}$  (see sec. 2.11.1), this corresponds to a change in current of only 970 mA (3.86 %) when working at unitarity. Such a ramp can be executed well below 1 ms.

**Resonant spin dynamics and Feshbach spectroscopy  
of Potassium-40**



## Chapter 3

### Spin selective detection at low magnetic fields and high temperatures

---

3.1. Stern-Gerlach imaging . . . . .	66
3.2. Optical repumping during time-of-flight . . . . .	69
3.3. Spin selective detection via microwave spectroscopy . . . . .	71
3.3.1. Magnetic dipole transitions in Potassium-40 . . . . .	71
3.3.2. Landau-Zener adiabatic passage . . . . .	74
3.3.3. Microwave spectrum and detection of spin populations . . . . .	75

---

In the preceding sec. 2.11.3 we have described how the ground state spin populations of an atomic ensemble can be precisely controlled by means of radio-frequency transfers. This makes it possible to prepare balanced or imbalanced Fermi gases (see sec. 5) and provides access to different Feshbach resonances, which occur between different Zeeman states. In order to reliably calibrate these preparation methods, the respective populations can be probed in conjunction with absorption imaging. Apart from diagnostics, this furthermore represents a crucial prerequisite in order to investigate spin-changing physics, as will be the case for the study of a new Feshbach resonance presented in chapter 4.

Spin selective detection for  $^{40}\text{K}$  is typically implemented at high magnetic fields greater than 200 G, near the canonical s-wave Feshbach resonance at 202 G for the lowest-lying negative spin states. At these fields the energy splittings between the Zeeman levels become much larger than the natural linewidth, so that optical imaging can become resonant with one state at a time (see sec. 6.2.5). However, for the analysis of collisional phenomena at magnetic fields of up to 20 G, the necessity to increase the field by a factor of ten for the mere purpose of spin selective detection is not recommended since it cannot be done faster than a few hundred ms. During this time, the atoms might be subjected to additional spin dependent physics occurring as the ramping process forcibly scans over many values of the magnetic bias field<sup>1</sup>. Such unpredictable effects could alter the initial spin state composition that was to be probed and obscure the actual experimental

---

<sup>1</sup>For example due to additional scattering resonances along the way.

signatures. To circumvent this problem, we probe the spin composition using Stern-Gerlach pulses in conjunction with optical pumping prior to absorption imaging. This method works well only at low temperatures around 1  $\mu\text{K}$ . At higher sample temperatures of above 5  $\mu\text{K}$ , Stern-Gerlach separation loses its 'resolving power' due to experimental and technical constraints. In this case we infer the spin populations from calibrated microwave spectra, as will be detailed in sec. 3.3.

### 3.1. Stern-Gerlach imaging

By subjecting the atoms to a steep magnetic field gradient at the moment they are released from the optical trap, one can impart onto them a spin-dependent acceleration by virtue of the magnetic dipole interaction. The achievable velocities depend on the magnetic moments  $\mu_k$  of the involved states, which in turn vary with the transient value of the magnetic field  $B(\mathbf{r}_0, t)$  with  $\mathbf{r}_0$  denoting the CoM position of the cloud. As the atoms begin to move they sample different regions of the (transient) magnetic field, which in turn changes the magnitude of their magnetic moments and hence the amount of speed they pick up. Since the cloud diameter is usually small with respect to the typical gradients created by large coils, one can neglect the differential acceleration across the sample and treat only the center-of-mass movement. The latter assumption is only valid if the magnetic field pulse is short with respect to the initial rate of expansion of the cloud. More energetic samples of atoms will expand faster, eventually causing the Stern-Gerlach spectrum to become unresolved because the maximum level of technically achievable acceleration is reached (especially since the pulse duration must be decreased as well). In order to determine in a quantitative fashion for which temperature range the Stern-Gerlach method is expected to work for  $^{40}\text{K}$ , one has to consider the species-specific kinematics at hand. The total acceleration due to the magnetic gradient field as well as the gravitational force is given by,

$$\mathbf{a}_k(\mathbf{r}, t) = -g - \frac{1}{m} \nabla \mu_k(\mathbf{r}, t) B(\mathbf{r}, t) \quad , \quad \mu_k(\mathbf{r}, t) = \left. \frac{\partial E_k}{\partial B} \right|_{B=B(\mathbf{r}, t)} \quad (3.1)$$

The magnetic moment is obtained as derivative of the eigenenergy  $E_k(B)$  of the Zeeman state  $|m_F = k\rangle$  with respect to the magnetic field (see appendix C.4 for details). The distance covered by each spin state is formally obtained by integration, yielding the indirect expression,

$$z_k(\tau) = -\frac{g}{2} \tau^2 - \frac{1}{m} \int_0^\tau dt' \int_0^{t'} dt'' \left[ \frac{\partial}{\partial z} \mu_k(\mathbf{r}, t) B_z(\mathbf{r}, t) \right]_{\mathbf{r}=\mathbf{r}_k(t''), t=t''} \quad (3.2)$$

still containing the single-particle trajectories on the right-hand-side. The time  $\tau$  denotes the duration of the entire ramp until the absorption image is taken, i.e.  $\tau = \tau_{\text{pulse}} + \tau_{\text{flight}}$ . The differential equation underlying eqn. (3.2) can be solved numerically for each spin state provided that the magnetic field is known as function of space and time. The varying levels of acceleration, given a sufficiently long time of free ballistic flight  $\tau_{\text{flight}}$  after the magnetic field pulse, are going to cause the different spin states to separate spatially with final spacings of  $\Delta z_{kl}(\tau) = z_k - z_l$ . The lowest temperature under consideration for the analysis of the Feshbach resonance is  $T \sim 3 \mu\text{K}$ , so that the ballistic increase of the cloud size  $\sigma$  given by eqn. (C.8) can be detected reliably up to only 10 ms after release from the dipole trap. At that point the cloud becomes too dilute due to its increased size so that the SNR crosses the detection threshold of the imaging system. Consequently, the total duration of the Stern-Gerlach separation must already be kept much shorter than the detection threshold and, in addition, one must ensure that  $\Delta z_{kl}(\tau) > \sigma(\tau)$  holds after the free flight to be able to resolve the spin states. In order to quantify the degree of spatial separation between the states, one has to normalize the corresponding spacings with respect to the cloud diameters  $2\sigma$ . Therefore, we are interested in the quantity:

$$\Delta \tilde{z}_{kl}(\tau) = \frac{\Delta z_{kl}(\tau)}{2\sigma(\tau; \omega, T)} \quad \text{where} \quad \sigma(t; \omega, T) = \sqrt{\sigma_0^2(\omega, T) + \frac{k_B T}{m} t^2}. \quad (3.3)$$

with  $\sigma_0(\omega, T) = (k_B T / m \omega^2)^{1/2}$  denoting the in-situ cloud size in the trap at the moment of release. A numerical simulation tailored to our experimental situation and coil parameters is given in fig. 3.1. Because of the high temperatures at hand, the atoms will expand quickly after their release from the dipole trap. In order to clearly separate the spin components, strong magnetic gradients are thus required for a short period of time of  $\sim 1 - 2$  ms which, by extension, imply large magnetic fields. A secondary consequence arising from the latter is that the atoms are no longer in the linear weak field regime during the acceleration phase. As a result, the magnetic moments of the non-stretched states vary significantly as the magnetic field builds up and decays, as is shown in fig. 3.1a. Due to the nature of  $^{40}\text{K}$ , the moments of the non-stretched positive states decrease and increase during the pulse, with some of them approaching zero. While this limits the amount of acceleration felt by the atoms and gives rise to non-trivial velocity trajectories, the magnetic field can only be reduced within certain limits to compensate this effect because the stretched state already sets a minimum gradient necessary to separate it from the other ones. Given this compromise, the resulting travel distance and velocities of the three highest lying positive spin states are depicted in fig. 3.1b and the normalized spacings for three temperatures (and corresponding trapping frequencies) as per (3.3) are given in 3.1c. The asymmetric splittings arise from the nonlinear coupling to the magnetic field and reproduce well the experimentally observed SG spectrum shown in fig. 3.2c. Comparing

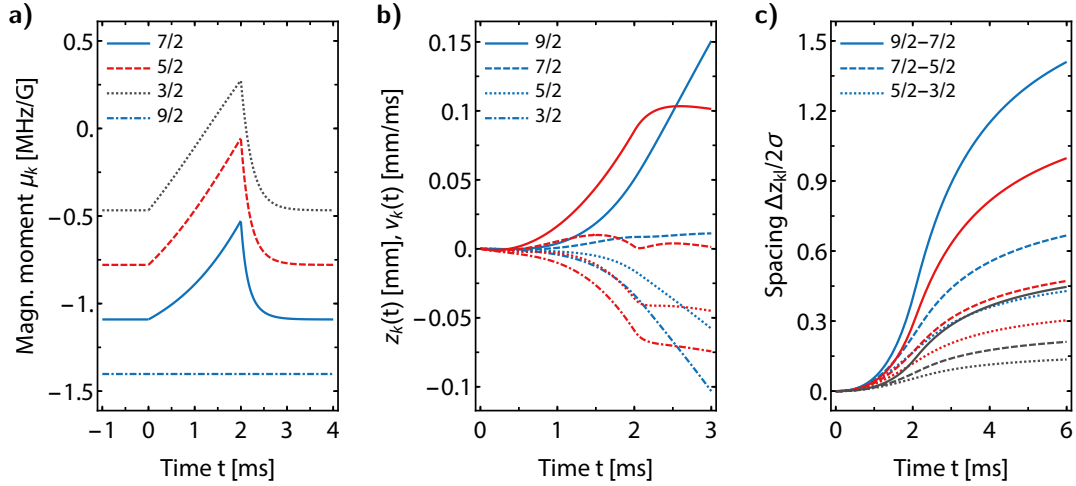


**Figure 3.1.: Simulation of the temperature dependent resolving power of the Stern-Gerlach method for the positive Zeeman states.** The magnetic field along the quantization axis is modeled as  $B_z(z, t) = (b_0 + b_1 z)I(t)$  with realistic parameters  $b_0 = 4 \text{ G A}^{-1}$  and  $b_1 = 1.25 \text{ G A}^{-1} \text{ cm}^{-1}$ . The current ramp  $I(t)$  is defined piecewise to resemble the actual experimental situation with a linear rise to 60 A over the pulse duration of 2 ms, corresponding peak magnetic fields of around 240 G, after which an exponential decay with a half time of 0.5 ms ensues. a) Magnetic moment of the four spin states  $m_F = +9/2, \dots, +3/2$  as function of time as per  $\mu_k = \mu_k[B(\mathbf{r}_k(t), t)]$ . b) Travel distance  $z_k(t)$  (blue) and velocity  $v_k(t)$  (red) of spin state  $k$ . c) Spacing between the three pairs of adjacent spin states in units of the cloud diameter at time  $t$  for different experimental conditions. Blue:  $T_1 = 3.2 \mu\text{K}$ ,  $\omega_1 = 2\pi \times 475 \text{ Hz}$ ; Red:  $T_2 = 6.2 \mu\text{K}$ ,  $\omega_2 = 2\pi \times 672 \text{ Hz}$ ; Black:  $T_3 = 32 \mu\text{K}$ ,  $\omega_3 = 2\pi \times 1.5 \text{ kHz}$ .

the numerical results plotted for the three temperatures of 3  $\mu\text{K}$ , 6  $\mu\text{K}$  and 30  $\mu\text{K}$  implies that the Stern-Gerlach method will cease to work (in our specific case) for temperatures above 10  $\mu\text{K}$ . As will be detailed later, some parts of the analysis of the Feshbach resonance require spin selective detection at temperatures of up to 30  $\mu\text{K}$ , motivating the methods presented in sec. 3.3. While limited in temperature range, the Stern-Gerlach method nevertheless has the advantage of probing all relevant spin populations at the same time. This can be helpful in order to circumvent the impact of fluctuations of the total atom number from shot to shot since the experiment is quite stable with respect to the relative spin populations due to the magnetic transport acting as a highly reliable filter.

On the experimental side, in order to create the strong magnetic fields necessary without long delays<sup>2</sup>, we precharge the capacitors of a strong power supply connected to one of the inner quadrupole coils (see sec. 2.11.1 for details), and close the corresponding IGBT just after switching off the optical trap<sup>3</sup>. This way, peak currents of around 100 A can be

<sup>2</sup>Typical current supplies will take at least a few milliseconds to establish high currents of up to 50 A.

<sup>3</sup>Alternatively, using two coils in anti-Helmholtz configuration would double the gradient, they also create a magnetic zero that was found to be able to interfere with the atoms. This was caused by the high currents

reached within 2 ms, corresponding to transient magnetic gradient fields of up to 400 G with  $125 \text{ G cm}^{-1}$  at the position of the atoms. After the pulse, the IGBT is opened and the accelerated atoms fly against gravity, achieving detectable levels of separation after 3 ms for  $T \sim 3 \text{ } \mu\text{K}$  as given by our imaging system's magnification of  $M = 1$ . The maximum flight time tied to the temperature of the atoms is found to be roughly 10 ms in practice. The best compromise regarding the specifics of the field ramp to resolve all of the relevant spin states was found to correspond to a peak current of 60 A with a pulse duration of 2 ms.

Due to the high currents involved, strong persistent Foucault currents are induced in the surrounding metallic parts that decay only after 12 ms, which may be longer than the typical timescales of the preceding SG procedure depending on the temperature of the sample being probed. As a consequence, there may be stray magnetic fields present during absorption imaging which can alter the imaging resonance frequencies by up to 20 MHz and, more importantly, the (relative) detectivities of the various spin states, most notably the ones of  $5/2$  and  $3/2$ . In order to accurately detect the relative spin populations their detectivity has to be equalized, which can be done by means of optical pumping into the stretched Zeeman state  $m_F = \pm 9/2$  prior to imaging.

### 3.2. Optical repumping during time-of-flight

To obtain a calibrated Stern-Gerlach spectrum yielding reliable atom numbers, all clouds corresponding to different spin states must be imaged on closed transitions to avoid population transfer to other states. As is detailed in appendix C.1 this problem can be reduced, but not circumvented entirely, by reducing the atoms' exposure time to the lowest possible value before SNR issues come into play. In order to ensure that imaging of the different spin components occurs on cycling transitions, one has to first optically pump them into the stretched states  $m_F = \pm 9/2$  by shining in  $\sigma^\pm$  polarized light along the quantization axis. The pumping scheme for the positive states is shown in fig. 3.2a. This transfer must be performed after the SG separation has occurred and in the absence of trapping forces in order to preclude parasitic heating and light-assisted collisions.

The optimization of the experimental parameters of the repumping step prior to imaging needs to be done in conjunction with Stern-Gerlach separation to clearly determine the ideal parameters. Since the  $z$ -axis is collinear with the direction of motion during SG probing, it cannot be used to image the atoms afterwards. The  $x$ -axis, however, cannot provide pure  $\sigma^\pm$  polarization as it is orthogonal to the quantization axis. The resulting imaging dynamics after pumping into the stretched state are depicted in fig. 3.2b. While some parasitic population transfer is then still to be expected during imaging, it will

---

involved, which, in combination with the long flight times, made it difficult to displace the zero by means of additional offset fields.

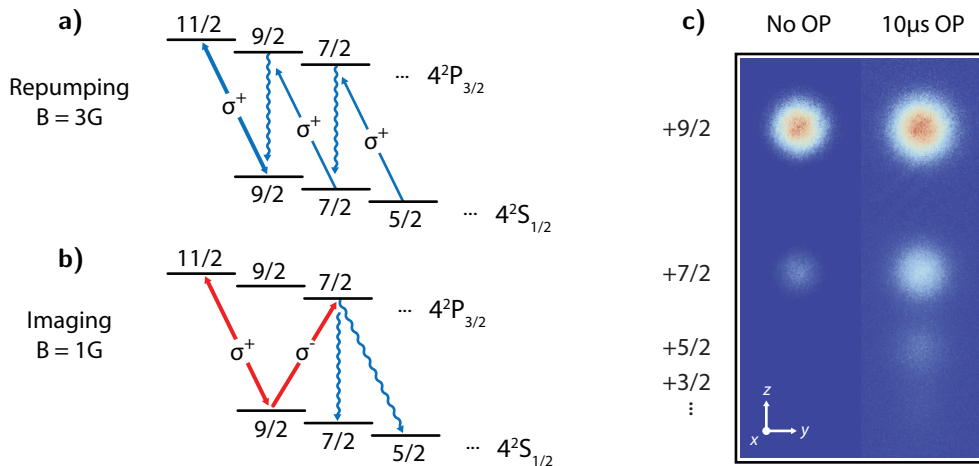


**Figure 3.2.: Optical pumping and imaging transitions at low magnetic fields.** Left: Repumping transitions into the stretched state for the positive Zeeman states prior to absorption imaging, usually performed at  $B = 3$  G due to technical compatibility with MW spectroscopy (see sec. 3.3). Right: Imaging along the  $x$ -axis with horizontal polarization with respect to the quantization axis. The ambient magnetic field is usually set to  $B = 1$  G to avoid depolarization. Note that the magnetic fields given here do refer to the situation in which no Foucault currents are present near the science cell.

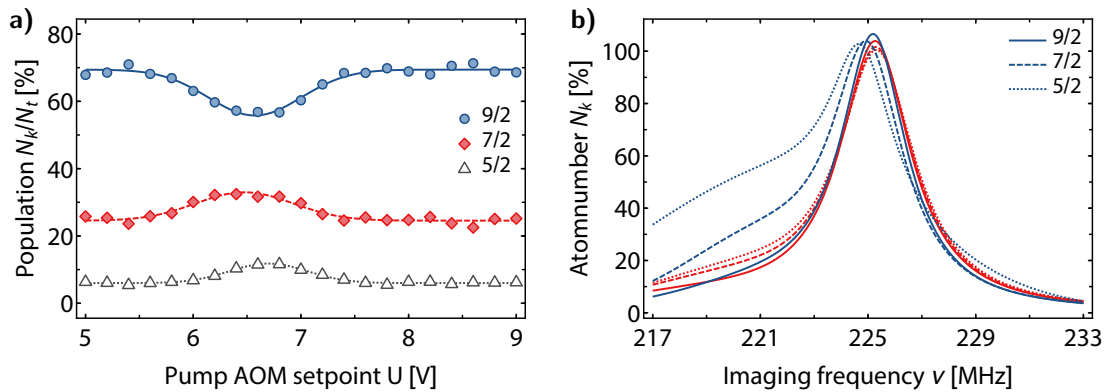


**Figure 3.3.: Experimental signatures of the optical repumping as seen after Stern-Gerlach separation.** a) Scan of the repumping frequency at a fixed imaging frequency in the ensuing absorption imaging. b) Imaging frequency curves of the three spin states with (orange) and without (blue) repumping. Data points were omitted for clarity. The solid lines are fits to the data using pseudo-Voigt profiles of the form  $fL(\nu) + (1 - f)G(\nu)$  to account for the asymmetric lineshape caused by Doppler-broadening due to elevated imaging light intensities [94].  $L$  and  $G$  refer to Lorentzian and Gaussian profiles, respectively, with  $0 \leq f \leq 1$  denoting the relative weight. Both scans shown in a) and b) were taken shortly after the SG pulse plus flight time, implying the presence of transient magnetic fields. They are the reason for the slight offset of the resonance position of 5/2 in a).

nevertheless be the same for all spin states after optical pumping so that relative populations will still be detected correctly. Despite this unavoidable shortcoming one is still in a position to directly observe the effect of tuning the light frequency, polarization (angle of  $\lambda/4$  waveplate) as well as the pulse duration by monitoring the relative increase of spin state detectivity. The corresponding experimental optimization for the positive states is shown in fig. 3.3a. The resonance positions of the pump frequency is slightly shifted between the spin states because some transient magnetic fields due to Eddy currents still remain. Otherwise, the pump frequencies would all be equal to the imaging resonance frequency at zero field. The visible effect of the repumping on the appearance of the SG spectrum is also shown in fig. 3.2c. Another means to observe the effect of OP is during the imaging step. Due to the remaining magnetic fields, the resonant values of the imaging frequencies of the various spin states will not be equal, as was the case for the optical pumping resonance. When fixing the pump at its resonant value and then scanning the imaging frequency, one obtains the various resonance curves shown in fig. 3.3b. Without optical pumping prior to imaging, one can clearly see the disparity between the states, which vanishes as soon as it is present.

The new hardware in terms of optical systems and acousto-optical modulators that needed to be added to the  $^{40}\text{K}$  laser system in order to generate the light for optical pumping was already described in sec. 2.3 and 2.11.1.

### 3.3. Spin selective detection via microwave spectroscopy

Due to the limited range of temperatures at which the Stern-Gerlach technique can provide well-resolved population spectra, another means of spin selective probing needs to be devised. As was already mentioned at the beginning of this section, the method needs to work irregardless of the sample temperature and at low magnetic fields in the vicinity of the Feshbach resonance under consideration. While optical transitions become spin selective only at high magnetic fields due to the large natural linewidth of the D2 line of  $^{40}\text{K}$ , magnetic dipole transitions in the ground state have linewidths of only a few kHz, which is far less than the typical Zeeman energy splitting between the states. As will be described in the following, using them in a reliable fashion for spin selective detection will still require calibration measurements using Stern-Gerlach separation and optical repumping.

#### 3.3.1. Magnetic dipole transitions in Potassium-40

Magnetic dipole transitions (M1) are governed by the Hamiltonian  $H_B = -\hat{\mu}\hat{B} = \mu_B(\hat{L} + 2\hat{S})\hat{B}$  [95]. The associated typical transition amplitudes are on the order of the Bohr Magnetron  $\mu_B$ , implying that their transition strengths are approximately five orders of

magnitude times smaller than the ones of E1 transitions since  $(d/\mu_B)^2 = (2/\alpha)^2 \simeq 10^5$  with  $\alpha$  denoting the fine-structure constant. However, in combination with the fact that the transitions frequencies are very small, it follows that the spontaneous decay rate  $A \sim \omega^3 |\mu|^2$  via M1 channels is small in comparison to E1 transitions [96]. This makes magnetic dipole transitions an extremely important tool for state preparation, even more so as they complement the selection rules of electric dipole transitions by allowing to couple electronic states of the same parity, as is the case, for instance, for all of the Zeeman levels of the ground state hyperfine manifolds for which  $L = 0$ . Accordingly, M1 transitions are forbidden between opposite-parity states. The selection rules regarding the total angular momentum remain the same  $\Delta J = 0, \pm 1$  with  $J = 0 \rightarrow J' = 0$  forbidden. However, coupling between states with different principle quantum number  $n$  is not allowed, which can be understood by recalling that  $H_B$  contains only angular-momentum operators that do not affect the radial part of the wavefunction. Consequently, any matrix element with two states of unequal  $n$  will be zero since they are orthogonal with respect to one another. The aforementioned role of parity can be understood by considering the effect of parity reversal on electric and magnetic dipoles. An electric dipole moment originates from two spatially separated charges of opposite sign. A parity transformation flips its sign because the position of the charges is effectively reversed by the inversion of the coordinate axis, which is why the electric dipole moment is a proper (polar) vector. The magnetic dipole moment originates from the angular momentum  $\mathbf{L} = \mathbf{r} \times \mathbf{p}$  of a charged particle, which is a pseudovector as it is invariant under parity reversal. Consequently, the parity selection rules for M1 transitions must be opposite to the ones for electric dipole transitions.

The first set of important M1 transitions in  $^{40}\text{K}$  are the 23 cm-lines<sup>4</sup> connecting the two ground hyperfine manifolds  $F = 9/2$  and  $F = 7/2$ , some of which are shown in fig. 3.4a. These transitions can be used to probe and hence calibrate the magnetic bias field with high sensitivity. An example of such a measurement is shown in fig. 3.5.

More importantly, by removing population from the lower Zeeman states and transferring it to the upper ground state, atoms can be made to be transparent to the imaging light due to the large detuning of  $\sim a_{\text{hfs}}/h = 1285.8$  MHz. Since the linewidth of these M1 transitions is less than  $\sim 100$  kHz (including also the uncertainty of our magnetic fields) is much smaller than the typical Zeeman splittings at weak magnetic fields of greater than  $\sim 1$  MHz, the perceived drop in atom number will originate from the loss of population belonging to exactly one single spin state. Provided the transition probability is known, one can infer the initial number of atoms in the spin state under consideration. As will be

---

<sup>4</sup>This transition is quite similar to the well known 21 cm-line between the hyperfine ground states of hydrogen, which is frequently used in radio astronomy where it was discovered by Ewen and Purcell in 1951 [97]. It facilitated the mapping of neutral hydrogen in our galaxy which revealed for the first time the spiral structure of the Milky Way [98]. Moreover, the analogous transition in Cs is currently used as the international frequency standard defining the length of a second [99].

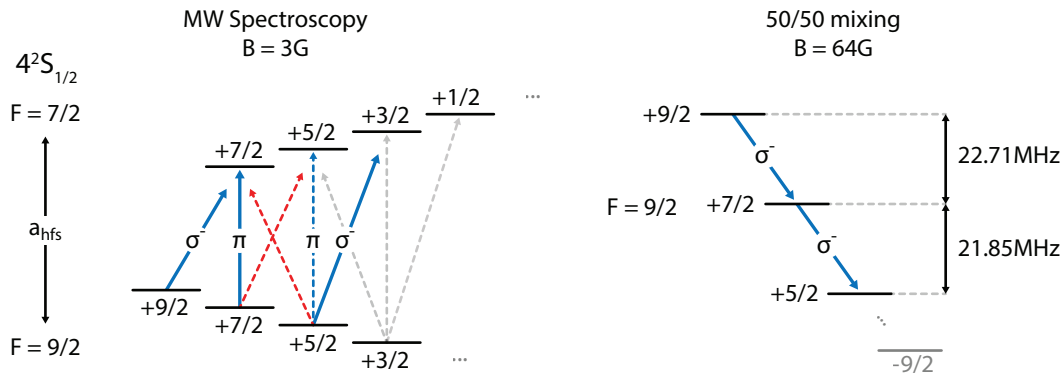


**Figure 3.4.: Microwave and radio frequency transitions for the positive Zeeman states of  $^{40}\text{K}$ .** Left: Possible hyperfine transitions of the four spin states  $m_F = +9/2, \dots, +3/2$  with  $F = 9/2$  to the upper ground state manifold  $F = 7/2$ . The corresponding hyperfine splitting amounts to  $a_{\text{hfs}}/h = 1.2858$  GHz. Right: Radio-frequency transitions connecting the spin states  $m_F = +9/2, +7/2, +5/2$  of the lower hyperfine manifold to one another.

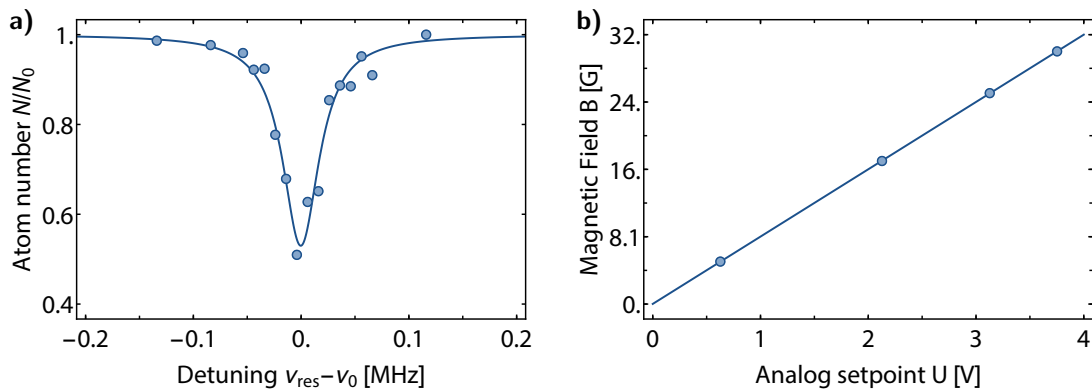


**Figure 3.5.: Magnetic field spectroscopy and -calibration.** a) Resonance curve of a narrow microwave sweep obtained by driving hyperfine transitions  $F = 9/2 \rightarrow F = 7/2$ . b) Calibration of the magnetic field as a function of the current supply's analog setpoint. The values of the B-field are obtained through the positions of several resonance peaks as seen in a).

detailed later on, this opens up a way to probe the spin composition of the atomic cloud confined in an optical trap without the stringent restrictions regarding sample temperature that were encountered in the case of Stern-Gerlach probing.

The second important kind of magnetic dipole transitions occurs between neighboring Zeeman states of a given hyperfine manifold, which are also referred to as Hertzian resonances [100].<sup>5</sup> These transitions represent the basis for the passage from the positive to the negative Zeeman states described in sec. 2.11.3 and will be used later in order to

<sup>5</sup>Equivalent transitions between nuclear levels are used for nuclear magnetic resonance (NMR) and magnetic resonance imaging (MRI) [95].

tailor the initial population of the atoms in the positive spin states.

### 3.3.2. Landau-Zener adiabatic passage

As was hinted on earlier, magnetic dipole transitions can be used to transfer atoms into different spin states as long as the principle quantum number does not change and the parity is conserved. However, one problem arises due to the fact that the detuning varies over time with the intrinsic fluctuations of the magnetic field, which are much larger than the linewidth of the transition. When radiating atoms with AC magnetic fields of fixed frequency<sup>6</sup>, the transition probability will thus vary with time depending on the noise spectrum of the bias magnetic field. In order to avoid such issues, one can instead drive so-called adiabatic passages between the atomic spin states, which are possible due to the presence of avoided crossings between the dressed eigenstates of atom and photon. Following [101], in a two level system these eigenstates are given by the superpositions  $|+\rangle = \sin\theta|1\rangle + \cos\theta|2\rangle$  and  $|-\rangle = \cos\theta|1\rangle + \sin\theta|2\rangle$  with  $\theta = -\Omega/\Delta$  denoting the Stückelberg angle,  $\Omega \sim \sqrt{P}$  the Rabi-frequency<sup>7</sup> and  $\Delta$  representing the detuning from resonance. When chirping the photon frequency, the eigenstates change accordingly and, if done slowly enough, the system will adiabatically follow this evolution. For  $\Delta \ll -\Omega$  one has  $|-\rangle \simeq |1\rangle$  since the phase angle  $\theta$  is zero. As the frequency is swept slowly towards higher values, the atom will remain in the state  $|-\rangle$  as per the adiabatic theorem, eventually reaching the limit  $\Delta \gg \Omega$  where  $\theta = \pi/4$  and hence  $|-\rangle \simeq |2\rangle$ . In essence, the mixing of the two states allows one to transfer the population in  $|1\rangle$  with unit probability to the state  $|2\rangle$  because the avoided crossing exchanges the role of the uncoupled eigenstates. However, in practice the frequency ramp cannot be made arbitrarily slow due to the presence of other limiting timescales in the experiment (e.g. fluctuations of the magnetic field at 50 Hz) and the detuning, naturally, cannot be swept from  $-\infty$  to  $+\infty$ .

If the chirp is very fast, the atom will merely tunnel through the avoided crossing so that the population remains unchanged. The question of what happens for intermediate, non-adiabatic chirps was addressed independently by Landau, Zener, Stückelberg and Majorana in 1932 [102–105]. Since there will be some probability to tunnel through the gap, the atom will most likely end up in a superposition state of  $|1\rangle$  and  $|2\rangle$  after the chirp. The underlying generalized atom-field Hamiltonian can be reduced to Weber's equations, which can be solved by parabolic-cylinder functions. In the end, one finds that the probability to (adiabatically) end up in the intended state  $|2\rangle$  is given by the expression

$$P = 1 - \exp\left(-\frac{\pi\Omega^2}{2|\partial_t\Delta|}\right). \quad (3.4)$$

<sup>6</sup>The linewidth of commercial RF and MW sources is very small and therefore no concern.

<sup>7</sup>For most typical RF- and MW antennas, this frequency will be on the order of 1 kHz.

The Landau-Zener tunneling probability to the upper branch is consequently  $1 - P$ . In the limit of slow sweeps with respect to the Rabi-frequency  $\Omega^2 \gg |\partial_t \Delta|$  the transition probability to the second state approaches unity. In the opposite limit of weak coupling and fast sweeps the population will tend to remain in the initial state. Note that here one can safely neglect the influence of spontaneous decay since we are considering only magnetic dipole transitions with very long lifetimes. This assumption would not necessarily hold for sweeps over an optical E1 transition, to give but one example. The expression (3.4) can also be used as fit function to extract the Rabi-frequency from data points taken with different sweep durations  $|\partial_t \Delta|$  (see [61] for additional details).

The advantage of these transitions lies in the fact that one can make the range of the chirp larger than the time-varying detuning caused by magnetic field fluctuations while staying at the same time well below the Zeeman energy splittings and maintaining reasonable transition probabilities. An additional complication arises in case one is dealing with more than two levels (see e.g. [106]) which, for example, concerns also the adiabatic passage to the negative Zeeman states described in sec. 2.11.3. Here one needs to explicitly calculate the dressed eigenenergies of all involved states numerically in order to ensure that crossings are indeed avoided, as was done for the aforementioned case in fig. 2.17.

### 3.3.3. Microwave spectrum and detection of spin populations

Turning to the application to Potassium-40, by driving hyperfine transitions to the upper ground state manifold using Landau-Zener sweeps one can, in a spin selective manner, render a fraction of the atoms transparent to the imaging light during absorption imaging due to the large detuning of  $\sim 1.28$  GHz. In doing so, we can then infer the initial population of a given spin state from the apparent loss, provided the transfer probability (3.4) is well known and robust with respect to the intrinsic noise of the magnetic field. The latter requirement can be fulfilled by choosing a ramp whose chirp bandwidth is sufficiently large to cover the range of possible detunings due to magnetic field fluctuations and by setting its duration to be shorter than their typical timescales.

The calibration of the transfer efficiencies is done by recording the spectrum of the M1 transitions using Stern-Gerlach separation and optical pumping to reliably detect the changes in the spin populations. Once calibrated, the SG method will no longer be needed and the MW probing technique can then be applied on its own to much hotter clouds. For the positive Zeeman states  $m_F = 9/2, 7/2$  and  $5/2$  involved in the analysis of the

Feshbach resonance, the following hyperfine transitions are possible:

$$|9/2, +9/2\rangle \rightarrow |7/2, +7/2\rangle, \quad (\sigma^-) \quad (3.5)$$

$$|9/2, +7/2\rangle \rightarrow |7/2, +7/2\rangle, \quad (\pi) \quad (3.6)$$

$$|9/2, +7/2\rangle \rightarrow |7/2, +5/2\rangle, \quad (\sigma^+) \quad (3.7)$$

$$|9/2, +5/2\rangle \rightarrow |7/2, +7/2\rangle, \quad (\sigma^-) \quad (3.8)$$

$$|9/2, +5/2\rangle \rightarrow |7/2, +5/2\rangle, \quad (\pi) \quad (3.9)$$

$$|9/2, +5/2\rangle \rightarrow |7/2, +3/2\rangle, \quad (\sigma^+) \quad (3.10)$$

which were already shown schematically in fig. 3.4a. Their exact transition frequencies can be determined using the Breit-Rabi formula (see C.4 for details). Unfortunately, the two lines (3.7) and (3.8) coincide at low magnetic fields of a few G, which means that they cannot be used for probing the spin population of either Zeeman state due to potential cross-coupling. In the case of optical photons contained in well directed laser beams, one could easily prevent or at least reduce this effect by polarizing the light at high extinction ratios using, for example, birefringent Glan-Thompson polarizers. However, when working with microwaves or radio-frequency radiation which have very long wavelengths, this is not possible without tremendous technical effort in terms of hardware and space. While this represents a drawback in the context of the two mixed transitions above, it does renders MW spectroscopy also quite flexible since any mechanical deformations of the emitter will ensure that all types of polarization are present (with different proportions) at the position of the atoms.

The microwave itself is created using the setup described in sec. 2.10 and 2.11.1. The carrier frequency  $\nu_0 \sim 1.257$  GHz is provided by an analog signal generator, which is mixed down with the linearly chirped ramp  $\nu_2(t) = \nu_{2,0} + \nu(t)$  generated by a second RF source where  $\nu_{2,0} = 28.5$  MHz. The resulting AC signal consisting of the carrier as well as the two chirped sidebands  $\nu(t) = \nu_0 \pm \nu_2(t)$  is amplified and passed through a MW circulator before being emitted by the antenna situated next to the science cell. Note that only one sideband will be resonant due to the detuning  $\nu_{2,0}$  and the small linewidths. A typical sweep duration is between 1 ms - 10 ms and the ambient bias field is set to a value of 3 G. This choice of magnetic field is motivated by the fact that the corresponding Zeeman splittings are still large enough to allow for sweep bandwidths larger than the magnetic field fluctuations.

The full spectrum of the hyperfine transitions of the three highest lying positive spin states of  $^{40}\text{K}$  is shown in fig. 3.6. Here, the carrier frequency  $\nu_0$  was varied while using the same chirp modulation  $\nu_2(t)$  throughout the measurement. After subjecting the atoms to the microwave sweep, the spin states were separated using a Stern-Gerlach pulse and optical pumping was applied prior to absorption imaging. This was done to ensure

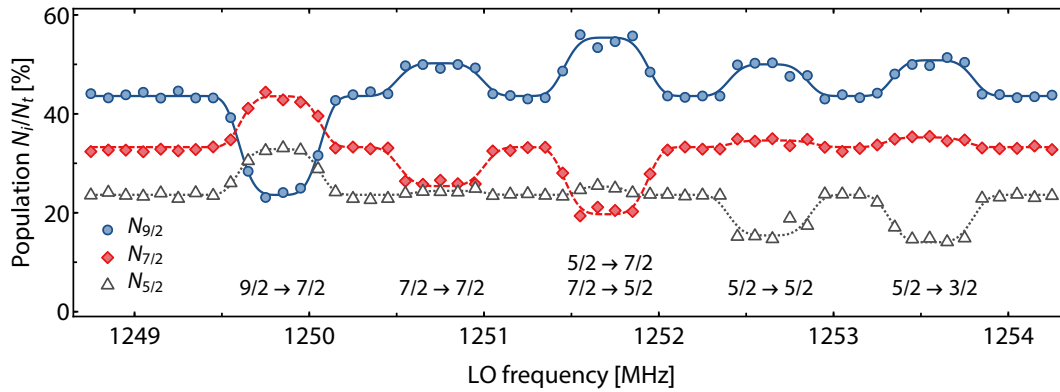


**Figure 3.6.: Microwave spectrum of the positive Zeeman spin states.** After the MW sweep the cloud was subjected to a 2 ms long Stern-Gerlach pulse accelerating the different spin states and separating them during the ensuing free flight over 4 ms. Prior to absorption imaging, the three distinct clouds were optically pumped into  $m_F = +9/2$  to guarantee equal optical detectivity. Note that, for every frequency, the three corresponding spin populations are always normalized to the total atom number. As a consequence, the relative norm. populations of two states can thus increase when the actual population of the third states decreases. Parameters:  $m_F = +9/2, +7/2, +5/2$ ,  $B = 3\text{ G}$ ,  $\nu = \nu_{10} + 28.5\text{ MHz}$ ,  $\Delta\nu = 0.5\text{ MHz}$ ,  $\tau = 10\text{ ms}$ . Solid lines are super-Gaussian fits serving as guide to the eye.

equal detectivity for all spin states, so that one can extract accurate relative populations. Moreover, a sample containing increased amounts of  $m_F = +5/2$  was used in order to increase the corresponding SNR. This way, the observed transition probabilities can be calibrated and used later on to infer the atom number in a given spin state by means of MW spectroscopy in situations when Stern-Gerlach probing is no longer possible. Note that since the atom numbers plotted here are referenced to the total atom number, a decrease of the population of one spin state will cause the ones of the unaffected states to increase by virtue of normalization. The sweep bandwidth of  $\Delta\nu = 500\text{ kHz}$  was chosen as large as possible with respect to the Zeeman splitting between the states at 3 G which amounts to roughly  $E_z/h = 940\text{ kHz}$ .

Depending on the initial population of the spin states and the Landau-Zener efficiencies, the MW transfers can give rise to substantial population of the upper hyperfine states. It should be pointed out that such mixtures of spin states in the lower and upper ground states are not necessarily stable with respect to inelastic collisions<sup>8</sup>. For this reason, the spectrum discussed above was obtained by performing SG separation and subsequent optical pumping for absorption imaging as fast as possible after the 10 ms microwave pulse. This choice of timing was motivated by the observation of strong inelastic losses

<sup>8</sup>Even among the lower Zeeman states only very few combinations do not undergo spin-changing collisions!

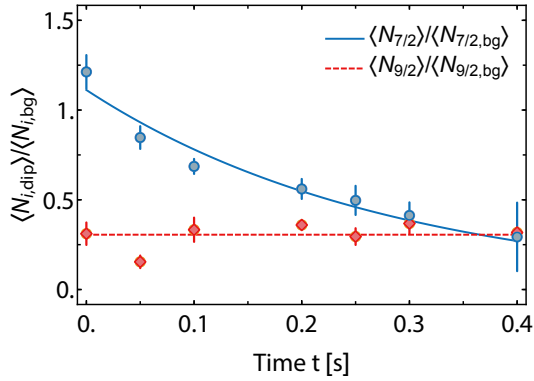


**Figure 3.7.: Inelastic hyperfine collisions.** A MW sweep has a broad step-like loss feature due to the non-zero bandwidth of the chirp. In order to obtain the data shown here, the atom numbers of the bottom (i.e. res. transfer to  $F = 7/2$ ) and of the top (off-res.) of the step were averaged and divided by one another. The evolution of this ratio is shown for  $+9/2$  and  $+7/2$  as function of hold time after population of the upper hyperfine state.

in some of the created mixtures occurring at timescales longer than 50 ms. In fig. 3.7 the evolution of the populations in  $|9/2, 9/2\rangle$  and  $|9/2, 7/2\rangle$  in the presence of  $|7/2, 5/2\rangle$  are shown as function of time. The population of the upper states was created via a 10 ms Landau-Zener sweep on the  $\sigma^-$ -transition (3.7). The initial spin composition of the cloud prior to applying the MW pulse consisted of roughly 55 %  $m_F = 9/2$  and 33 %  $m_F = 7/2$ . Tracking the evolution of the lower spin state atom numbers after population of the upper hyperfine manifold clearly shows the onset of exothermic hyperfine collisions between  $|9/2, 9/2\rangle$  and  $|7/2, 5/2\rangle$  as of 50 ms. Given that the released energy of such a collision is on the order of the ground state hyperfine splitting, it entails the immediate loss of both atoms from the trap. Since the choice of MW transition determines which type of collision will take place, the corresponding (two-body) losses effectively take on a spin-dependent character. It is these losses that represent the main limitation of the MW spectroscopy-based approach to spin population probing because they cannot be suppressed other than by Pauli-Blocking. Consequently, one has to ensure that the optical detection via absorption imaging after MW probing occurs much faster than the various timescales of the different combinations of hyperfine collisions.

## Chapter 4

### Spin dynamics in the vicinity of a (s,d)-wave Feshbach resonance

---

4.1. Feshbach resonances in ultracold gases . . . . .	80
4.2. Initial experimental findings . . . . .	84
4.3. Characterization of the resonance via inelastic loss spectroscopy . . . . .	86
4.3.1. Derivation of the loss rate equations for the shallow trap limit . . . . .	86
4.3.2. Extraction of the loss rate coefficients from life time measurements . . . . .	91
4.3.3. Loss rate spectrum and resonance structure . . . . .	94
4.4. Resonant spin dynamics in (s,d)-wave collisions . . . . .	98
4.4.1. Calculation of the collision channels' branching ratio . . . . .	98
4.4.2. Rate equations in the limit of deep trapping potentials . . . . .	100
4.4.3. Spectrum of the initial heating rates . . . . .	102
4.4.4. Spin dynamics and verification of the branching ratio . . . . .	103
4.5. Summary and additional resonances . . . . .	105

---

The successful realization of quantum simulators using ultracold Fermi or Bose gases relies crucially on the ability to alter in a controlled manner the strength of inter-atomic interactions. In such two-body collisions, a Feshbach resonance occurs when a bound state is tuned via external fields to coincide with the threshold of the entrance channel. This can strongly modify both elastic and inelastic scattering properties, even when the two channels are only weakly coupled [41]. The position of the bound state is usually controlled using magnetic fields, which renders Feshbach resonances an indispensable tool as they allow, for instance, to tune the s-wave scattering length of low energy collisions from  $-\infty$  to  $+\infty$ . Moreover, they can be used to couple colliding atoms into molecules (see e.g. [107–109]). To give but a few examples, this means of control has enabled the study of the BEC-BCS crossover in Fermi gases (see ch. 1) [46] and the observation of Efimov molecules created in resonant Bose gases [110].

Feshbach resonances have been and continue to be studied extensively in numerous homonuclear atomic species [111–114] and heteronuclear mixtures [107, 115–123]. Recently, enhancement of elastic collisions in p- and d-waves has also been achieved without overly strong inelastic losses [117, 124, 125].

In this chapter, we report on the characterization of two previously unreported Feshbach resonances in  $^{40}\text{K}$  in terms of inelastic loss rate constants and resonant spin dynamics. Several resonances of  $^{40}\text{K}$  were already described in 2.11.4 and a comprehensive survey is given in appendix C.5. In the following, a brief summary of the salient properties of Feshbach resonances will be given, providing the foundation for the experimental methods presented afterwards.

#### 4.1. Feshbach resonances in ultracold gases

The occurrence of Feshbach resonances in neutral atoms can be understood from a simple picture containing only two collision channels [41]. A given channel is labeled by the internal quantum numbers  $\{\psi, \phi\}$  of the colliding atoms and has the total energy  $E_{\text{tot}} = E(\psi) + E(\phi) + E_{\text{kin}}$ , where  $E_{\text{kin}}$  denotes the relative kinetic energy. If atoms are prepared in this channel, then any other channel with  $E < E_{\text{tot}}$  is referred to as closed while  $E > E_{\text{tot}}$  is called open. Fig. 4.1 shows schematically the molecular potentials of a closed channel and the background, which connects asymptotically to two free atoms. For low collision energies, the latter corresponds to the energetically open channel. A Feshbach resonance occurs when a (virtual) bound state of the closed channel approaches the threshold of the open channel and mixing is facilitated by the hyperfine- or magnetic dipole interaction. Given that the spin configurations of the two collision channels are different, their energy difference can be tuned with external magnetic fields. At low collisional energy, the modification of the s-wave scattering length due to the presence of the additional bound state can be described by the simple dispersive expression [91],

$$a(B) = a_{\text{bg}} \left( 1 - \frac{\Delta}{B - B_0} \right), \quad (4.1)$$

where  $a_{\text{bg}}$  denotes the scattering length originating from the background molecular potential of the entrance channel.  $\Delta$  represents the width of the resonance, which fixes the zero crossing of the scattering length at  $B_{\text{zc}} = B_0 + \Delta$ . The binding energy of the weakly bound molecular state approaches the threshold on the side of the resonance where the scattering length is large and positive. At large detunings the binding energy scales linearly with the magnetic field with the slope given by the differential magnetic moments of the open and closed channels. Close to resonance the dressed molecular state has an energy given by  $E_{\text{b}} = \hbar^2/2\mu a^2$  [126], where  $\mu$  denotes the reduced mass of the pair. In this regime the properties of the bound state take on a universal character, which can be described by a single molecular potential of scattering length  $a$ . The two-body wavefunction corresponds to a halo state with size  $a$  and the molecule is referred to as a halo dimer.

It is worthwhile to point out two other types of scattering resonances for completeness, which are also indicated in fig. 4.1. Shape resonances occur when the collision energy

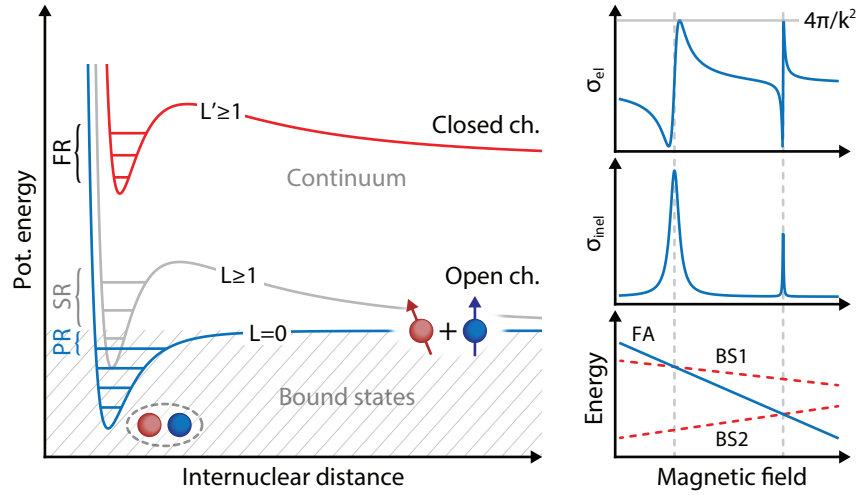


**Figure 4.1.: Schematic illustration of Feshbach resonances in cold collisions.** Left: Typical Alkali molecular potentials of an s-wave (blue) and HPW wave (gray) entrance channel as well as a HPW closed channels. True bound states lie below the dissociation threshold while virtual bound states are embedded in the continuum. The energy difference between the closed channel and the open channel can be tuned via magnetic fields. Right: Magnetic field scaling of the elastic cross section (top), inelastic cross section (middle) and the energies of the closed (BS1/2) and entrance channels (FA).

of the atoms becomes comparable to the binding energy of a quasi-bound state located behind a centrifugal barrier in the entrance channel with  $l \geq 1$ . A potential resonance, on the other hand, corresponds to a situation where there is a bound/virtual state just above or below the collision threshold of the (background) s-wave incoming channel. In the case of  $^{40}\text{K}$  and  $^6\text{Li}$ , such states are directly responsible for the large s-wave scattering lengths [82, 83], which exceed by far the range of the interaction potential.

### Scattering in the ultracold regime

The interaction of two Alkali atoms at a given magnetic field  $B$  are described by the following Hamiltonian,

$$\hat{H} = \frac{\hat{p}^2}{2\mu} + \sum_{i=1}^2 \underbrace{(\hat{H}_i^{\text{hf}} + \hat{H}_i^z)}_{\text{HFS + Zeem.}} + \underbrace{\hat{H}_c + \hat{H}_{\text{dd}}}_{\text{Int.}}$$

Here,  $\mu$  denotes the effective mass and  $\hat{p}$  the relative momentum operator. The (single particle) energy shifts of the atoms' internal spin states due hyperfine splitting and the Zeeman coupling to the magnetic field are contained in the second term under the sum. Further details regarding the behavior of Alkali atoms in magnetic fields are provided in appendix C.4 and are thus omitted here.

The term  $\hat{H}_c$  contains all of the Coulomb interactions between the two atoms, which only depend on the modulus of the relative distance  $r$ . This interaction conserves both the projection of the total spin  $\hat{F} = \hat{s}_1 + \hat{s}_2 + \hat{i}_1 + \hat{i}_2$  as well as the total orbital angular momentum  $\hat{L} = \hat{l}_1 + \hat{l}_2$ , i.e.  $\Delta m_F = \Delta l = \Delta m_l = 0$ . Furthermore, the total nuclear and electronic spin are conserved separately, such that one can write the central interaction as the sum of a singlet and triplet term and their respective projection operators as per  $\hat{H}_c(r) = U_S(r)\hat{P}_S + U_T(r)\hat{P}_T$ . In the asymptotic limit of large  $r$  the two potentials are the same and contain the familiar van der Waals interaction as well as an exchange term pertaining to the symmetry of the wavefunction.

The second term  $\hat{H}_{dd}$  corresponds to the magnetic dipole interaction between the electronic spins as well as second-order spin-orbit coupling. The former is given by the expression [127]:

$$\hat{H}_{ss} = -\frac{\alpha^2}{r^3} [3(\hat{r}\hat{s}_1)(\hat{r}\hat{s}_2) - \hat{s}_1\hat{s}_2],$$

where  $\alpha$  denotes the fine structure constant and  $\hat{r}$  the unit vector along the relative separation of the atoms. This anisotropic interaction is typically weak, however it can couple quasi-bound states with  $l = 2$  to incoming atoms colliding in s-wave.  $\hat{H}_{ss}$  mixes states with different angular momentum, obeying the selection rule  $\Delta l = 0, 2$  with  $l = 0 \rightarrow l' = 0$  being forbidden. The projections of the total spin and orbital angular momentum are no longer conserved separately, but their sum is  $\Delta M = 0$ .

The scattering problem can be solved by recasting the time-independent Schrödinger equation in terms of the properly symmetrized channel states for indistinguishable atoms,

$$|\psi, \phi; l, m_l\rangle = \frac{1}{\sqrt{2(1 + \delta_{\psi\phi})}} (|\psi\rangle_1 |\phi\rangle_2 \pm |\psi\rangle_2 |\phi\rangle_1) |l, m_l\rangle.$$

Here,  $|\psi\rangle$  and  $|\phi\rangle$  represent the hyperfine states of the single atoms 1 and 2, respectively.  $|l, m_l\rangle$  are the eigenstates of the two-body orbital motion, which correspond to the usual spherical harmonics in position representation. One finds a coupled set of differential equations for the radial wavefunctions, where the coupling matrix element between two channels is given by [128]:

$$U_{\psi\phi, \psi'\phi'}^{lm_l, l'm'_l}(r) = \langle \psi, \phi; l, m_l | \hat{H}_c + \hat{H}_{dd} | \psi', \phi'; l', m'_l \rangle.$$

Solutions of the coupled-channel problem is usually obtained numerically and, in principle, require the knowledge of the full interaction potential. Formally, the outcome of the collision is given by the Lippmann-Schwinger equation which expresses the solution in terms of the unitary  $T$  and  $S$ -matrices. The partial cross section for a collision process starting in the open channel  $\alpha = \{\psi, \phi\}$  and ending in  $\beta = \{\psi', \phi'\}$  can be expressed as matrix element of the scattering matrix  $S_{\alpha, \beta}$ . Following [41], elastic scattering occurs

when atoms remain in the same channel,  $\sigma_\alpha^{\text{el}}(E_{\text{kin}}) = g_\alpha \pi |1 - S_{\alpha,\alpha}(E_{\text{kin}})|^2 / k^2$ , while inelastic scattering corresponds to a loss from the incoming channel,  $\sigma_\alpha^{\text{inel}}(E_{\text{kin}}) = g_\alpha \pi (1 - |S_{\alpha,\alpha}(E_{\text{kin}})|^2) / k^2$ . The rate coefficients for these collisions are given by  $K_\alpha^{\text{el}} = \hbar k \sigma_\alpha^{\text{el}} / \mu$  and  $K_\alpha^{\text{inel}} = \hbar k \sigma_\alpha^{\text{inel}} / \mu$ . The prefactor  $g_\alpha$  depends on the underlying statistics of the collision process. Furthermore, there exist upper bounds for the elastic and inelastic cross sections by reason that the S-matrix is unitary. They are given by  $\sigma_\alpha^{\text{el}} = 4\pi g_\alpha / k^2$  and  $\sigma_\alpha^{\text{inel}} = \pi g_\alpha / k^2$ , respectively.

### Resonant collisions

The complex scattering phase shift  $\eta_\alpha(E)$  characterizes the asymptotic solutions of the radial Schrödinger equation and incorporates the effect of the entire (short-range) potential on the collision event [41]. For low energy s-wave scattering  $k \rightarrow 0$ , it can be written as  $\eta_\alpha \rightarrow -k\hat{a}_\alpha$  where  $\hat{a}_\alpha = a_\alpha - ib_\alpha$  denotes the complex scattering length of channel  $\alpha$ . The threshold behavior of the partial cross sections then read  $\sigma_\alpha^{\text{el}} = 4\pi(a_\alpha^2 + b_\alpha^2)$  and  $K_\alpha^{\text{inel}} = (2\hbar/\mu)g_\alpha b_\alpha$ , such that both quantities tend towards constant values at small energies. The occurrence of a scattering resonance is signified by a rapid change of the phase shift by about  $\pi$  radians over a narrow range of energies. As was pointed out earlier, this is caused by the presence of a quasi-bound state which is located behind a potential barrier in the entrance channel (shape resonance) or in a completely different channel (Feshbach resonance). The coupling between the two channels causes mixing between the two states and, as a result, the scattering phase picks up a resonant contribution in addition to the background phase shift:

$$\eta_\alpha(E) = \eta_{\text{bg}}(E) + \eta_{\text{res}}(E) \quad , \quad \eta_{\text{res}}(E) = -\tan\left(\frac{\Gamma(E)/2}{E - E_\beta - \delta E(E)}\right)$$

The second term  $\eta_{\text{bg}}$  has a Breit-Wigner form and vanishes for large interatomic distances  $r$  [41].  $E_\beta$  denotes the closed channel energy,  $\Gamma(E)$  represents the resonance width and  $\delta E(E)$  the resonance shift. In the case of threshold scattering where  $E_\beta$  approaches the entrance channel energy with  $E \simeq 0$ , the threshold laws for s-wave collisions read  $\Gamma(E)/2 \rightarrow k a_{\text{bg}} \Gamma_0$  and  $E_\beta + \delta E(E) \rightarrow E_0$  as  $k \rightarrow 0$ . The complex scattering length thus takes on the form

$$\hat{a}_\alpha = a_{\text{bg}} \left(1 + \frac{\Gamma_0}{-E_0 + i\gamma/2}\right)$$

where  $\gamma$  captures the decay into other channels. The position of the resonance threshold  $E_0$  can be tuned by varying an external magnetic field as there is a difference in magnetic moments  $\Delta\mu = \mu_\alpha - \mu_\beta$  between the free atoms in the entrance channel and the quasi-bound state in the closed channel. The energy of the latter with respect to the free atoms then scales as  $E_\beta = \Delta\mu(B - B_c)$  and crosses the threshold at  $B = B_c$ .

## 4.2. Initial experimental findings

A past experimental study of the evaporation efficiency of the positive states of  $^{40}\text{K}$  revealed two previously unreported loss resonances at  $B_1 = 9\text{ G}$  and  $B_2 = 160\text{ G}$  [63]. An imbalanced mixture of  $m_F = +9/2, +7/2$  with a small fraction of  $5/2$  was evaporated for 5 s in a crossed optical dipole trap and its final remaining atom number recorded as a function of magnetic field. The corresponding loss spectrum is shown in abridged form in fig. 4.2. Given the spin composition of the sample<sup>1</sup> and the magnitude of the losses, these two features are most likely caused by the presence of Feshbach resonances between the states  $+9/2$  and  $+7/2$ . The reduction of the remaining number of atoms may be caused by inelastic losses or by an increased evaporation rate due to the resonantly enhanced elastic collision rate.

A more detailed measurement of the losses occurring near the first resonance around 8 G is shown in fig. 4.3. Here, a spin mixture of  $^{40}\text{K}$  containing the same states was first evaporated at a magnetic field of 18 G, which was then jumped to its target value and held there for 4 s. The remaining fraction of atoms was recorded via absorption imaging after a short time-of-flight to reduce the optical density of the sample. The resulting spectrum shows three distinct loss features, with the first one occurring at 8.1 G being considerably more pronounced. Given that the depth of the dipole trap was not increased after the preceding evaporation ramp,  $\eta$  is comparatively low and, consequently, enhanced evaporation may still contribute to the losses to some degree. In this context, cooling effects are not necessarily observable since they might be obscured by density dependent heating arising from inelastic losses. The evaporation rate will thus have to be addressed later on to extract the true inelastic loss rate. The presence of the three additional loss features can be explained in a number of ways. They might stem from the multiplet structure of one single higher partial wave Feshbach resonance [125], or they may be due to several independent scattering resonances. As will be detailed further below, the latter case applies in this situation.

In order to further characterize the Feshbach resonance at 8 G, the following aspects must be addressed experimentally or numerically: 1) What is the value of the resonant magnetic field  $B_0$  and the resonance width  $\Delta B$ ? 2) Are inelastic losses due to two- or three body processes? 3) In which partial waves do the atoms collide in the entrance- and exit channels? Does the resonance display a dependence on the sample temperature? 4) Is the resonance entrance- or closed channel dominated? 5) Where is the molecular side of the Feshbach resonance? A preliminary numerical simulation was kindly provided by E. Tiesinga [129], which identified the two resonances at 8 G and 160 G as  $d$ -wave in nature.

<sup>1</sup>Note that the spin composition provided in [63] was revised from 70:30 to the more accurate ratio 55:33:12 due to the recent implementation of optical pumping in the science cell (see sec. 3.1 for details).

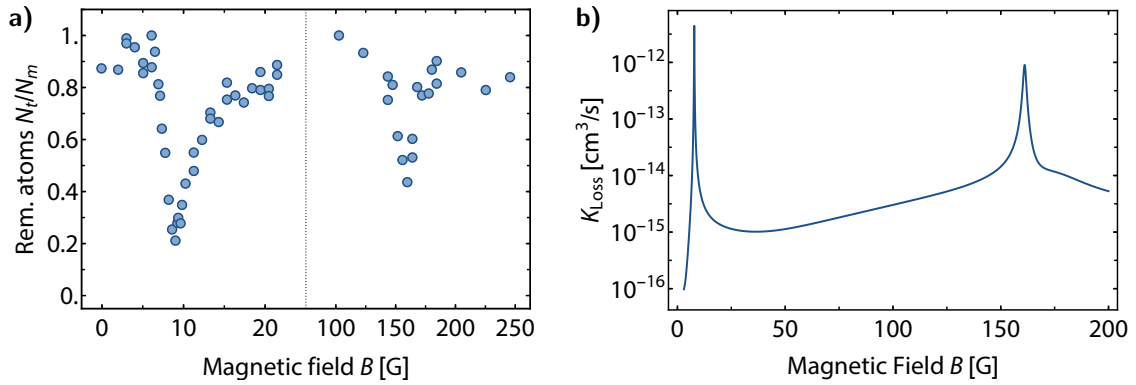


**Figure 4.2.: Two previously unreported loss resonances in  $^{40}\text{K}$ .** a) The total remaining atom number was observed after 5 s of evaporation in a crossed optical dipole trap using a mixture of the spin states  $m_F = +9/2, +7/2, +5/2$  with initial spin composition 55:33:12 at various magnetic fields. The loss features occur at magnetic fields of  $B_1 = 9$  G and  $B_2 = 160$  G. Data adapted from [63]. b) Numerical simulation by E. Tiesinga of the two-body inelastic scattering rate between  $m_F = +9/2$  and  $7/2$  at a collision energy of 60 nK [129].

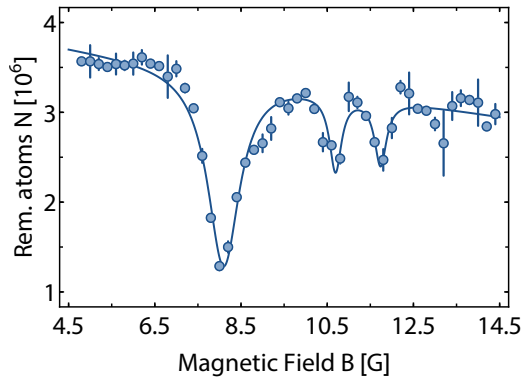


**Figure 4.3.: Inelastic losses of atoms at low magnetic fields.** The scan shows a close-up of the first resonance feature shown in fig. 4.2. After optical evaporation the magnetic field is jumped from 18 G to its target value. The 55:33:12 mixture of  $m_F = +9/2, +7/2$  and  $+5/2$  is then held in the dipole trap for 4 s after which the total remaining atom number is recorded. Solid lines are Lorentzian fits to guide the eye.

The corresponding inelastic loss rate is shown in fig. 4.2b.

A better understanding of the resonance properties at hand can be obtained through a systematic study of the two- and three-body inelastic loss rates as function of magnetic field and temperature. These rate coefficients can be extracted from lifetime measurements, whose analysis must be carried out using an appropriate mathematical framework which will be described in the following section. Moreover, because of the low Zeeman energy of  $\sim k_B \times 100 \mu\text{K}$  at the magnetic fields around 7 G, recapture after inelastic events is possible and therefore the resonant spin dynamics can be studied in deep traps. The experimental methods for spin selective detection described in section 3 were devised and implemented particularly for this study in order to be able to study these dynamics at elevated temperatures of up to 30  $\mu\text{K}$ .

### 4.3. Characterization of the resonance via inelastic loss spectroscopy

Feshbach resonances are usually observed in cold atom systems through the accompanying resonantly enhanced losses. Atoms are expelled from the trap due to the release of kinetic energy when collision partners end up in lower internal (two-body process) or molecular states (three-body process). Depending on which outgoing inelastic channel is enhanced by the Feshbach resonance, the released energy can be on the order of the Zeeman-, hyperfine- or molecular vibrational energy. In most cases, the trap depth is lower than the implied energy scales so that any inelastic collision leads to immediate loss. However, at low magnetic fields the Zeeman energy can become comparable to the trap depth and atoms may remain trapped even after undergoing inelastic collision events.

#### 4.3.1. Derivation of the loss rate equations for the shallow trap limit

In the simple case of a single component gas, two- and three body collisional losses can be described by a loss rate equation of the form [41]:

$$\dot{N}(t) = -L^{(1)}N(t) - \int d^3r \left[ L^{(2)}n^2(\mathbf{r}, t) + L^{(3)}n^3(\mathbf{r}, t) \right]. \quad (4.2)$$

Here  $L^{(1)} = 1/\tau$  is the inverse one-body lifetime set by the rate of background collisions with the impurities of the vacuum.  $n(\mathbf{r}, t)$  denotes the spatial density distribution of the trapped gas and  $L^{(2)}$  as well as  $L^{(3)}$  represent the trap loss coefficients belonging to two- and three body collisions, respectively. Considering that higher-order loss processes  $L^{(i)}$  scale as  $n^i$ , they will predominantly occur in regions of elevated atomic densities. For a given trapping potential this implies a targeted depletion of the coldest atoms of the cloud which, in turn, gives rise to heating provided rethermalization of the gas occurs faster than the inelastic loss. Assuming thermal equilibrium at any given time, the coupled differential equations for atom number and sample temperature are given by [130]:

$$\frac{\dot{N}}{N} = - \sum_{i=1}^{\infty} L^{(i)} \langle n^{i-1} \rangle_{\mathbf{v}}, \quad (4.3)$$

$$\frac{\dot{T}}{T} = + \sum_{i=1}^{\infty} \varepsilon_i L^{(i)} \langle n^{i-1} \rangle_{\mathbf{v}}. \quad (4.4)$$

In the second equation describing the anti-evaporation heating, we have  $\varepsilon_i = (1 - i^{-1})/2$ . Note that one-body losses do not give rise to any heating because they do not scale with density. The mean  $n$ -body atomic densities are given in the form of averages over the trap

assuming a thermal distribution and a harmonic potential:

$$\langle n^{i-1} \rangle_V = \int d^3n^i(\mathbf{r}) = \frac{N^{i-1}}{i^{3/2}} \left( \frac{m\bar{\omega}^2}{2\pi k_B T} \right)^{3(i-1)/2} \quad (4.5)$$

Here,  $\bar{\omega} = (\omega_x \omega_y \omega_z)^{1/3}$  denotes the mean trap oscillation frequency. In the following, the generic formalism outlined so far will be explained in more detail and adapted to our specific experimental situation to include all of the partaking spin states.

### One-body losses

Collisions with background gases present in the vacuum chamber always lead to trap loss. This can be understood from the fact that the collisional partner carries extremely high kinetic energies on the order of the room temperature, because the gaseous background phase is in thermal equilibrium with the walls of the vacuum chamber. The contribution of these collisions to the change in trapped atom number is given by

$$\dot{N}_t^{(1)} = \sum_k \dot{N}_k^{(1)} = -L^{(1)} \sum_k N_k = -L^{(1)} N_t, \quad (4.6)$$

with the sum comprising all of the spin components present in the mixture. At non-resonant magnetic fields of up to 4 G, we find experimentally that in the fully recompressed single beam dipole trap with  $\eta \simeq 16$  the lifetime of the samples is  $\tau = 1/L^{(1)} > 120$  s. When working at background fields of 18 G this figure was found to drop to  $\tau = 47$  s.

### Two-body losses

Assuming that the trap is sufficiently shallow so that any inelastic two-body collision event between  $m_F = +9/2$  and  $m_F = +7/2$  leads to the loss of both atoms, the change of the respective atom numbers  $\dot{N}_k^{(2)}$  will be given directly by the inelastic collision rate  $\Gamma_{\text{inel}}^{(2)}$ . One can write for the variation of  $N_{9/2}$ :

$$\frac{d}{dt}(\delta N_{9/2})^{(2)} = \frac{d}{dt}(n_{9/2} \delta V)^{(2)} = -L^{(2)} n_{7/2} \delta N_{9/2}, \quad (4.7)$$

where we have used that  $\delta N_{9/2}(\mathbf{r}, t) = n_{9/2}(\mathbf{r}, t) \delta V$ . Integration then yields the two-body decay rates for the two spin states,

$$\dot{N}_{9/2}^{(2)} = \dot{N}_{7/2}^{(2)} = -L^{(2)} \langle N_{9/2} N_{7/2} \rangle_V = -\Gamma_{\text{inel}}^{(2)}, \quad (4.8)$$

In general, the loss rate constant  $L^{(2)}$  may depend on temperature, which is for instance the case when interactions occur in a partial wave higher than  $s$ . In such cases, the centrifugal

barrier present in the entrance channel will introduce a dependency of the rate constants on the collision energy. In a given sample, the accessible range of energies is set by the temperature and, consequently, higher partial wave scattering can become suppressed at low temperatures. As will be detailed further below, the entrance channel is  $s$ -wave in our case implying that this effect can be neglected. The spatially averaged two-body densities in the volume  $V$  defined as

$$\langle N_{9/2}N_{7/2} \rangle_v = \int \delta V n_{7/2}(\mathbf{r}, t) n_{9/2}(\mathbf{r}, t), \quad (4.9)$$

which is the equivalent of (4.5) for two spin states. Note that this quantity depends on the sample temperature  $T = 1/k_B\beta$ . Assuming that the gas can always be taken to be in thermal equilibrium by reason that the inelastic losses occur on a much slower timescale than elastic collisions, the density will always be given by the remaining atom number and the temperature as per  $n_k(\mathbf{r}) = n_{k,0}e^{-\beta U(\mathbf{r})}$  with  $n_{k,0} = N_k/V_e$  denoting the peak density. By approximating the trap  $U(\mathbf{r})$  to be harmonic with oscillations frequencies  $\omega_i$ , the density can be written as product of Gaussians with temperature dependent radii:

$$n_k(\mathbf{r}) = \frac{N_k}{V_e} \prod_{i=1}^3 e^{-(r_i/R_i)^2}, \quad R_i = \sqrt{\frac{2}{\beta m \omega_i^2}}. \quad (4.10)$$

Correspondingly, the trap volume  $V_e$  is easily calculated as well, yielding

$$V_e = \int d^3r e^{-\beta U(\mathbf{r})} = \prod_{i=1}^3 \int dr_i e^{-\beta m \omega_i^2 r_i^2 / 2} = \sqrt{\frac{2\pi k_B T}{m \bar{\omega}^2}}^3 \quad (4.11)$$

in the case of harmonic confinement with  $\bar{\omega} = (\omega_x \omega_y \omega_z)^{1/3}$  denoting again the average oscillation frequency. Using (4.9), the final loss rate equations for the two spin states including one-body decay as defined in 4.6 can therefore be written as:

$$\dot{N}_{9/2} = -L^{(2)} \frac{N_{9/2}N_{7/2}}{2\sqrt{2}V_e} - L^{(1)}N_{9/2} \quad (4.12)$$

$$\dot{N}_{7/2} = -L^{(2)} \frac{N_{9/2}N_{7/2}}{2\sqrt{2}V_e} - L^{(1)}N_{7/2} \quad (4.13)$$

### Three-body losses

Inelastic collisions involving three constituents can be understood as a two-step process [131, 132]. At first, two atoms collide and couple to the resonant excited molecular state  $A + A \leftrightarrow A_2^*$ . This process is reversible as the molecule can then dissociate again without the release large amounts of energy. However, while occupying the virtual bound state, the excited dimer can collide with a third atom which causes the molecule to irreversibly

decay to a lower-lying vibrational (ground) state  $A_2^* + A \rightarrow A_2 + A$ . Except in the case of spontaneous radiative decay, the deactivation of the vibrationally excited molecule cannot occur on its own and requires the presence of a third atom, which then carries away part of the energy. The released energies are typically very large and lead to the simultaneous loss of all three atoms. Alternatively, three-body recombination can also be modeled as a compound process [133, 134] (see also chapter 7).

It is a priori not clear whether two- or three-body losses will dominate in a given experimental setting, especially considering that up to three different spin states may contribute to the loss dynamics of the resonance at hand. For the latter, we would have to consider loss terms of the form:

$$L_{997}^{(3)} \langle N_{9/2}^2 N_{7/2} \rangle_v + L_{977}^{(3)} \langle N_{9/2} N_{7/2}^2 \rangle_v + L_{975}^{(3)} \langle N_{9/2} N_{7/2} N_{5/2} \rangle_v + \dots$$

As will be justified later on, our situation can be well described by restricting the mathematical framework to two-body losses. The discussion of the role of three-body processes will be given alongside the interpretation of the experimental findings in sec. 4.3.3.

#### Rate equation for the total atom number

Using the relations derived so far, one is now in the position to formulate the rate equation for the total atom number  $N_t = N_{9/2} + N_{7/2} + N_{5/2}$ . Using equations (4.12) and (4.13), one can write for the change of total atom number per unit time:

$$\dot{N}_t = \dot{N}_{9/2} + \dot{N}_{7/2} + \dot{N}_{5/2} = -L^{(2)} \frac{N_{9/2} N_{7/2}}{\sqrt{2V_e}} - L^{(1)} N_t, \quad (4.14)$$

where we have restricted ourselves to two- and one-body losses. In order to deal with the product  $N_{9/2} N_{7/2}$  we introduce the two-body imbalance  $\Delta N_{97} = N_{9/2} - N_{7/2}$ , for which the following rate equation holds:

$$\Delta \dot{N}_{97} = \dot{N}_{9/2} - \dot{N}_{7/2} = -L^{(1)} \Delta N_{97}. \quad (4.15)$$

It has the straightforward solution of the form

$$\Delta N_{97} = \Delta N_{97}(0) e^{-L^{(1)} t}, \quad \text{with} \quad \Delta N_{97}(0) = [x_{9/2}(0) - x_{7/2}(0)] N_t(0) \quad (4.16)$$

denoting the initial imbalance between the two majority spin states. Here we have introduced the fractional initial populations as per  $N_k(0) = x_k(0) N_t(0)$  with  $\sum x_k(0) = 1$ . Since the spin state  $m_F = 5/2$  does not undergo any two-body collisions leading to trap loss, its evolution over time is simply given by one-body decay as per  $N_{5/2} = N_{5/2}(0) \exp(-L^{(1)} t)$ . Then, noting that  $N_{9/2} = N_t - N_{5/2} + \Delta N_{97}$  and  $N_{7/2} = N_t -$

$N_{5/2} - \Delta N_{97}$ , we find for the majority populations:

$$N_k = N_t - (f_{5/2} \pm \Delta f_0) N_0 e^{-L^{(1)}t}, \quad k = 9/2, 7/2. \quad (4.17)$$

Here we have introduced the shorthand notations  $N_t(0) = N_0$ ,  $\Delta N_{97}(0) = \Delta f_0 N_0$  with  $x_k(0) = f_k$  and  $\Delta f_0 = f_{9/2} - f_{7/2}$ . Inserting the above results into eqn. (4.14) one finds for the rate equation of the total atom number:

$$\dot{N}_t = -\frac{L^{(2)}}{2\sqrt{2}V_e} \left[ N_t^2 + (f_{5/2}^2 - \Delta f_0^2) N_0^2 e^{-2L^{(1)}t} - N_t f_{5/2} N_0 e^{-L^{(1)}t} \right] - L^{(1)} N_t. \quad (4.18)$$

Note that a dependence on temperature is contained in the trap volume  $V_e \sim 1/T^{3/2}$ . Moreover, the density-dependent anti-evaporation heating presented in eqn. (4.4) must also be taken into account. Neglecting all higher-order processes beyond  $i = 2$ , the corresponding heating rate is then given by

$$\dot{T} = \frac{T}{4} \left( \frac{\dot{N}_t - \dot{N}_{5/2}}{N_t - N_{5/2}} \right). \quad (4.19)$$

By reason that the atoms in  $m_F = 5/2$  only experience one-body collisions with the background gases, their population has to be removed from the total atom number in the above expression as it does not contribute to the density-dependent heating. In combination with (4.18), the two differential equations can now be fitted to experimental data with the two-body loss rate entering as a fit parameter. Provided the initial imbalance  $\Delta N_0$  as well as  $f_{5/2}$  are known,  $L^{(2)}$  can be extracted from lifetime measurements under the condition that no other loss mechanisms are present.

### Evaporative losses

Apart from the inelastic processes considered so far, atoms can also be expelled from the trap due to the onset of evaporation in the presence of the Feshbach resonance. Since a resonant enhancement of the inelastic collision rate invariably implies an increase of its elastic counterpart, the scattering length may increase to the extent that hot atoms begin to leave the trap carrying away excess energy. In our case, this concern applies mostly to the s-wave scattering length between the states  $m_F = +9/2$  and  $m_F = +7/2$ , which ordinarily has a background value of  $a_{\text{bg}} = 168a_0$ . As will be detailed later, the scattering length is expected to increase to  $a_{\text{res}} = 275a_0$  on resonance, implying approximately a three-fold increase of the scattering cross-section. Any evaporative losses that could occur as a result effectively increase the observed two-body loss rate of the resonance and the implied cooling counteracts the density-dependent heating arising from inelastic two- or

three-body losses. To which degree this effect is relevant in the experimental situation depends on several factors, most importantly the trap compression factor  $\eta = U_0/k_B T$ . The latter can be increased to suppress evaporation, however an upper bound is naturally given by the released energy  $E_{\text{rel}}$  of the inelastic collision events. As soon as  $U_0 \sim E_{\text{rel}}$  holds, collisional partners may (both) remain in the trap as the released energy is no longer sufficient to escape, rendering the loss rate models derived so far invalid. Moreover, evaporation can also be triggered by density dependent heating, which decreases  $\eta$  the more atoms are lost from the trap.

In order to model inelastic losses correctly, evaporative processes have to be taken into account if they cannot be suppressed. More quantitatively, the corresponding rate equation for a single species in a harmonic potential is given by [135]:

$$\dot{N} = -\Gamma_{\text{ev}} N \quad \text{with} \quad \Gamma_{\text{ev}} = n_0 \sigma(a) \bar{v} e^{-\eta} V_{\text{ev}}/V_e. \quad (4.20)$$

Here,  $\bar{v} = 8k_B T/\pi m$  represents the average quadratic velocity and  $\sigma(a) = 4\pi a^2$  the elastic s-wave scattering cross section. The evaporation volume  $V_{\text{ev}}$  is defined as

$$\frac{V_{\text{ev}}}{V_e} = \eta - 4 \frac{\Gamma(4, \eta)}{\Gamma(3, \eta)},$$

where  $\Gamma(x, y)$  denotes the incomplete Gamma-function. The evolution of the temperature in this case can be written as

$$\frac{\dot{T}}{T} = \frac{1}{3}(\eta + \kappa - 3) \frac{\dot{N}}{N}, \quad \text{where} \quad \kappa = 1 - \frac{\Gamma(5, \eta)}{\Gamma(3, \eta)} \frac{V_e}{V_{\text{ev}}} \quad (4.21)$$

denotes the mean excess energy carried away by an atom in addition to the trap depth. Together with the loss rate equations derived in the preceding sections, we are now in a position to properly analyze atom number trajectories originating from inelastic two-body losses in a given trap geometry. The corresponding lifetime measurements from which one can extract the magnetic field dependence of the resonance's loss rate will be presented in the following section. To reduce the effect of evaporation while ensuring efficient inelastic loss, we monitor atom number trajectories as function of time while holding the ensemble in a mildly recompressed dipole trap such that  $T \ll U_0 \ll E_z$ .

#### 4.3.2. Extraction of the loss rate coefficients from life time measurements

In order to determine the characteristic loss rate spectrum of the resonance  $L^{(2)}(B, T)$ , the atom number trajectories have to be recorded for various values of the magnetic field. If the resonance happens to have an entrance channel with angular momentum larger than zero (i.e. s-wave), the loss rate will also acquire a dependency on temperature as it sets

the average collisional energy available to the atoms. This modification of the loss rate is caused by the presence of a centrifugal barrier in the interaction potential, which prevents the atoms from approaching one-another if their respective kinetic energies are too low. Atom number trajectories are recorded in the form of lifetime measurements performed at different values of the magnetic bias field and initial sample temperatures with  $\eta$  being identical in each case. Experimentally, we evaporate the positive state mixture in the single beam dipole trap until reaching an intermediate trap depth before recompressing to the final potential depth well below the Zeeman energy. By varying these two trap depths, we keep the same  $\eta$  for all measurements, but vary the temperature of the atomic ensemble and hence its density as well as the mean collisional energy. The latter is important insofar as it may allow to infer the partial wave of the entrance channel from the scaling of  $L^{(2)}$  with temperature. For example, for an s-wave open channel one would expect that the shape of the curve remains the same for all temperatures while in the case of d-wave its width and height are supposed to increase [136]. Following trap recompression and spin state preparation, the magnetic field is jumped to the target value and the remaining atom numbers are recorded after varying hold times.

A set of three atom number- and temperature trajectories measured in this way is depicted in fig. 4.4a and b. They correspond to resonant and off-resonant magnetic field setpoints of 7.1 G, 7.2 G and 7.3 G, respectively, with typical initial sample sizes of  $N_0 \sim 1 \times 10^6$  atoms at a temperature of  $T_0 = 2.8 \mu\text{K}$  after recompression. The spin composition at this stage consists of roughly 60 %  $9/2$ , 28 %  $7/2$  and 12 %  $5/2$ . The recompressed trap depth is equal to  $U_0 = k_B \times 23.6 \mu\text{K}$ , implying that  $\eta_0 = 8.4$ . For reference, the Zeeman splitting between the relevant states  $m_F = 9/2$  and  $m_F = 7/2$  amounts to  $\Delta E_Z = k_B \times 111 \mu\text{K} \gg U_0$  at  $B = 7.3 \text{ G}$ . The remaining total atom number after a given hold time on resonance is recorded via absorption imaging following 5 ms of ballistic expansion.

As is evident from fig. 4.4a, we observe strong losses in the vicinity of the resonance that rapidly deplete the sample, decreasing the atom number by 70 % over the course of three seconds at  $B = 7.3 \text{ G}$ . For comparison, the one-body lifetime in this setting is usually 47 s. Turning to fig. 4.4b, relatively strong heating is observed to occur on top of the resonance, increasing the temperature by about 43 % over the course of the measurement. This causes additional complications when fitting the rate equation (4.18) to the atom number trajectories since the trap volume  $V_e \sim 1/T^{3/2}$  cannot be assumed to remain constant throughout the evolution. In order to obtain a high fidelity fit of the two-body loss rate, the differential equation system (4.18) and (4.19) is solved numerically and parametrically fitted to the total atom numbers and the corresponding temperatures at the same time. The two-body loss rates  $L^{(2)}$  and initial imbalance  $\Delta f_0 = (N_{9/2}(0) - N_{7/2}(0))/N_0$  are then obtained as fit parameters subjected to the constraint  $f_{5/2} - 1 \leq \Delta f_0 \leq 1 - f_{5/2}$ . The latter condition contains the three extreme configurations  $f_{9/2} = 0$ ,  $f_{9/2} = f_{7/2}$  and  $f_{7/2} = 0$ ,

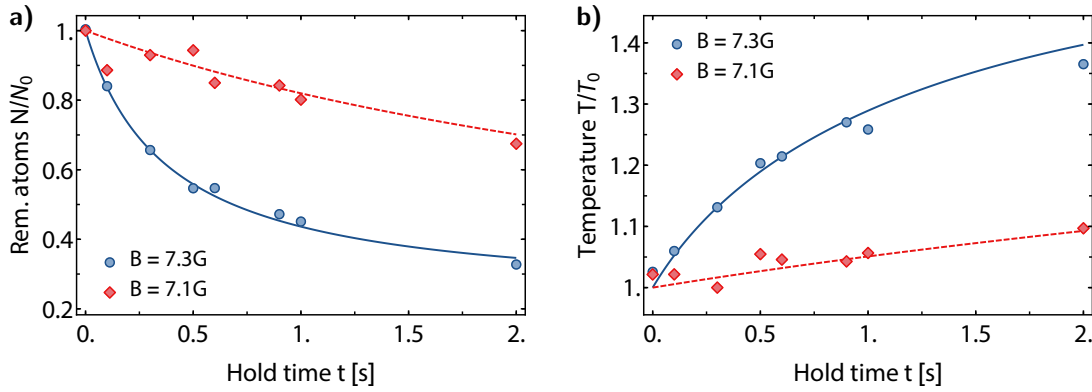


**Figure 4.4:** Inelastic losses and heating for different values of the magnetic field. a,b) Total atom number and cloud temperature as a function of wait time for  $B = 7.3$  G and 7.1 G with  $N_0 = 1.2 \times 10^6$  and  $T_0 = 2.8$   $\mu$ K. The dipole trap was recompressed after evaporation to  $\eta_0 = 8.4$  to reduce losses due to enhanced evaporation. Lines are parametric fits using the differential equations for  $\dot{N}$  and  $\dot{T}$ .

respectively, and ensures that the fitting routine respects atom number conservation at  $t = 0$ . However, one must ensure that the best fit parameters do not get stuck exactly at either boundary as this would imply some inconsistency in the data or the model. Note as well that evaporation is not included in this model.

On top of the resonance at  $B = 7.3$  G and setting  $f_{5/2} = 0.12$  (natural population of 5/2 after evaporation), we find  $L_{\text{fit}}^{(2)} = 3.25(10) \times 10^{-12} \text{ cm}^3 \text{ s}^{-1}$  and  $\Delta N_{0,\text{fit}} = 0.26(2)$ . The latter figure is in excellent agreement with the expected initial spin population (see fig. 3.3). Note that the inclusion of the small population in  $m_F = 5/2$  is important insofar as one would otherwise underestimate the loss rate or overestimate the imbalance.

While the fit is quite sensitive to the imbalance and even benefits from its inclusion as parameter, it quickly becomes insensitive to it when the magnitude of the losses decreases on either side of the resonance. We therefore fixed it at the value given before for the less resonant data sets. The fact that the temperatures can also be fitted well with this model seems to indicate that evaporation does not play a major role over the course of the measurement. To substantiate this observation, one can estimate an upper bound for the evaporation rate between the states  $m_F = 9/2$  and  $m_F = 7/2$  using equation 4.20. A numerical simulation by E. Tiesinga of the scaling of the scattering length as function of magnetic field predicts a maximum value of  $a \sim 275a_0$  [129]. One thus infers an evaporation rate of  $2.68 \times 10^{-14} \text{ cm}^3 \text{ s}^{-1}$  at the beginning of the measurement, which increases to  $3.66 \times 10^{-13} \text{ cm}^3 \text{ s}^{-1}$  for hold time of 3 s. Being at least an order of magnitude smaller than the fitted inelastic two-body loss rate, this estimate for the evaporation rate corroborates the initial assumption that it can be neglected for the trap configuration at hand.

The full scaling of the two-body loss rate with magnetic field and temperature was determined from a large number of such lifetime measurements as described above. An overview and discussion of the implied properties of the Feshbach resonance will be the subjects of the following section.

### 4.3.3. Loss rate spectrum and resonance structure

The two-body loss rate spectrum  $L^{(2)}(B)$  around the resonance at 9 G is shown in fig. 4.5a. The behavior at larger magnetic fields will be discussed later on. Using the methods described in the previous section, the two-body loss rates were measured for four distinct initial temperatures ranging from 2.8  $\mu\text{K}$  to 30  $\mu\text{K}$ . In order to prepare the ensembles of  $^{40}\text{K}$  at one of the intended sample temperatures, the evaporation in the optical dipole trap was interrupted at a given moment, to be followed by a slow recompression ramp to the final trap depth. The parameters were chosen such that  $\eta_0 \simeq 8$  holds for all measurements with the potential depth ranging from  $U_0 = k_B \times 23.6 \mu\text{K}$  to 222  $\mu\text{K}$ . The spin composition of the 2.8  $\mu\text{K}$ -set corresponds to the well calibrated ratio of 60:28:12, however the situation for the other sets may be different because the evaporation is stopped at different trap depths to achieve the sample temperatures mentioned above while keeping  $\eta$  constant. Given that the three spin states  $9/2$ ,  $7/2$ ,  $5/2$  of comparable but unequal populations and scattering lengths are present in the dipole trap at the moment of loading [61], the ensuing evaporation dynamics will cause the sample to polarize to some extent. Therefore, when fitting the loss rate sets for the temperatures larger than 2.8  $\mu\text{K}$ , the parameter  $f_{5/2}$  and the imbalance  $\Delta N_0$  are therefore set to the experimentally plausible upper bounds for the populations. The obtained results for the rate constants can be then considered to represent upper bounds as well.

### Origin of the inelastic losses

The obtained loss spectrum displays some intriguing properties. First, for increasing temperatures the strength of the observed losses decreases, which manifests itself as a drop of the peak two-body loss rate extracted from the atom number trajectories. Second, the center position appears to be shifted slightly towards lower magnetic fields. Third, the width appears to increase at higher sample temperatures.

Several conclusions about the nature of the inelastic losses can already be drawn from these observations. Contrary to the negative Zeeman levels for which inelastic two-body collisions are energetically forbidden since  $k_B T \ll \Delta E_Z$ , the energetically higher lying positive ones can undergo exothermic spin flips to lower states. The fact that inelastic losses are reduced with increasing sample temperature and trap depth suggests that the underlying mechanism is most likely a two-body process. 3-body losses should occur

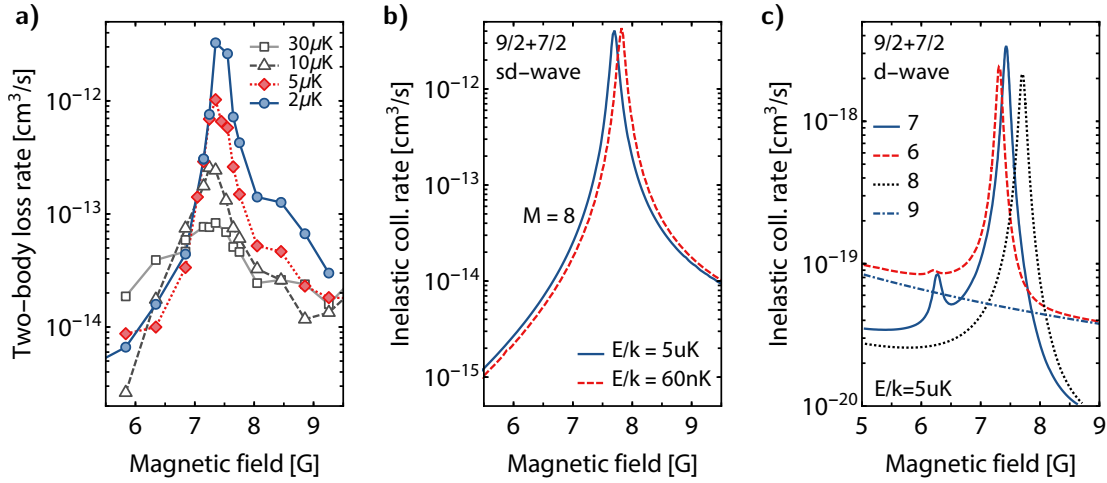


**Figure 4.5.: Two-body loss rate spectrum.** a) Experimental determination of the loss rate as a function of magnetic field  $B$  and average collisional energy as given by the sample temperature  $T_0$ . b,c) Numerical simulations by E. Tiesinga of the inelastic collision rates of the possible entrance channels at various magnetic fields [137].

irregardless of the trap depth because the released energy usually corresponds to the binding energy of a deeply bound dimer, which is not consistent with the experimental observations in this case.<sup>2</sup> However, this line of reasoning is only valid as long as there is no shallow bound state close to the threshold of the background scattering potential. If such a state is present, the enhancement of the elastic scattering length due to the Feshbach resonance will cause atoms to spend more time at close range, which in turn entails an increase of the overlap of the wave functions with the weakly bound state. As a result, the probability for three atoms to undergo recombination is enhanced as well. In the case of  $^{40}\text{K}$ , the background scattering properties are indeed strongly influenced by the presence of weakly bound states in the singlet and triplet potentials [83]. The associated background scattering lengths are enhanced due to these potential resonances, taking on the values  $a_s \simeq 104a_0$  as well as  $a_t \simeq 170a_0$ . With the scattering lengths being much larger than the van-der-Waals range of  $r_0 \simeq 65a_0$ , the corresponding wave functions of the least bound states extend far into the asymptotic region of the van-der-Waals tail of the inter-atomic potential. The binding energy of these s-wave bound states will be correspondingly small with  $E_b \sim \hbar^2/2ma_{\text{bg}}^2 \sim U_{0,\text{max}}/3$ , which implies that atoms recombining into them are not necessarily lost after a recombination event, especially considering that such dimers can be long-lived. In order to be certain that we indeed observe inelastic two-body losses, one has to invoke additional arguments to exclude the presence of comparatively strong three-body processes. One option could be to fit the lifetime data with two- and three-body

<sup>2</sup>By the same reasoning, we can also exclude inelastic hyperfine changing collisions as they would release enormous amounts of energy of roughly  $k_B \times 61 \text{ mK} \gg U_0$ .

models and compare the obtained fidelities of the fits. However, this approach may not provide reliable results as two-body losses with spin imbalance may resemble three-body losses at longer times. One can, however, calculate the three-body recombination rate for fermions to form a dimer and a free atom  $\uparrow + \uparrow + \downarrow \longrightarrow (\uparrow\downarrow)^* + \uparrow$  in the low energy limit, which is given by

$$\frac{\dot{n}}{n} = -L^{(3)}n^2 \simeq -111(na^3)^2 E/\hbar,$$

for a balanced gas [138, 139]. The above expression is valid as long as the condition  $E \ll \hbar^2/ma^2 \ll \hbar^2/mR_c^2$  holds. Taking the predicted value of the resonant scattering length of  $a \sim 275a_0$  [129], one would obtain rate coefficients of  $L_{\min}^{(3)} = 3.9 \times 10^{-28} \text{ cm}^6 \text{ s}^{-1}$  and  $L_{\max}^{(3)} = 4.1 \times 10^{-27} \text{ cm}^6 \text{ s}^{-1}$  for the two sets with initial temperatures of  $T_0 = 2.8 \text{ } \mu\text{K}$  and  $T_0 = 30 \text{ } \mu\text{K}$ , respectively. One can convert these rates into effective two-body rate constants by multiplying with the initial peak density, which yields  $L_{\text{eff},\min}^{(2)} = 1.7 \times 10^{-15} \text{ cm}^3 \text{ s}^{-1}$  and  $L_{\text{eff},\max}^{(2)} = 2.3 \times 10^{-14} \text{ cm}^3 \text{ s}^{-1}$ . One can therefore see that in the worst case scenario of balanced populations (even neglecting 5/2) interacting via the predicted resonant scattering length, the initial formation rates of dimers are between three and one order of magnitude lower than the measured peak two-body loss rates, which puts them firmly in the background. These estimates suggest that the three-body recombination to the weakly bound s-level can most likely be neglected in our situation. This conclusion is further corroborated by the following additional observation: when atoms are trapped with  $\eta$  being very large, one observes strong resonant heating in the absence of inelastic losses and a significant change of the spin populations. These dynamics will be studied in greater detail in sec. 4.4.4. Finally, the observed two-body loss rate 4.5a is reproduced very well, both in magnitude and scaling with magnetic field, by the numerically determined two-body inelastic collision rate shown in fig 4.5b. Additional details and comments regarding the theoretical analysis will be given further below.

Taking all of the arguments raised so far, one can safely conclude that the losses are indeed two-body in nature. Under this condition, the average released energy per atom must then be on the order of half of the Zeeman splitting  $\Delta E_Z(B = 7.4 \text{ G})/2k_B \sim 55 \text{ } \mu\text{K}$ . The underlying reasoning is that  $\Delta E_Z$  corresponds exactly to the released energy arising from an inelastic collision in which one of the partners undergoes a spin flip to another Zeeman state. Since the states partaking in the resonance are the energetically highest-lying Zeeman levels of the ground state manifold, the spin-exchange process will necessarily be exothermic. The trap depths for the measurements with  $T_0 = 2.8 \text{ } \mu\text{K}$ ,  $5 \text{ } \mu\text{K}$ ,  $10 \text{ } \mu\text{K}$  and  $30 \text{ } \mu\text{K}$  evolve according to  $U_0/k_B = 23 \text{ } \mu\text{K}$ ,  $48 \text{ } \mu\text{K}$ ,  $108 \text{ } \mu\text{K}$  and  $222 \text{ } \mu\text{K}$ , respectively. When comparing these potential depths with the released energy, one can attribute the reduction of the losses seen in 4.5a to the increased likelihood for atoms to remain in the trap after an inelastic two-body collision. The elevated baseline of the 30  $\mu\text{K}$ -set's loss rate may be attributed to the higher levels of remaining evaporation.

Higher-partial wave entrance channels do typically display a dependence on temperature due to the presence of a centrifugal barrier. As the average kinetic energy of the trapped atoms increases they are more likely to overcome the barrier, which introduces a dependence on the sample temperature into the loss rate. In the case of p-wave collisions, the center position and width of  $L^{(2)}(B, T)$  increases with  $T$ , but the height remains unchanged [127]. For d-wave collisions, also the height of the loss rate curve increases with temperature [125, 136]. We can see from the spectrum in fig. 4.5 that the resonance at hand does not fall into either category, which implies that the entrance channel is s-wave.

### Structure of the resonance

Theoretical insight into the nature of the closed channel was kindly provided by E. Tiesinga [137]. The bound state giving rise to this Feshbach resonance is d-wave in nature with orbital angular momentum of  $l = 2$ . At zero magnetic field, the molecular state has furthermore an internal spin of  $f = f_1 + f_2 = 6$ . Together with the orbital angular momentum, this gives rise to multiple bound states according to the possible configurations of the total angular momentum  $f_t = f + l = 6, 7, 8$ . They are located at an energy of  $k_B \times 450 \mu\text{K}$  above the threshold at zero field and cross it around  $B = 8 \text{ G}$ . The energy splittings between the bound states are created by the magnetic dipole interaction. The predicted height of the centrifugal barrier amounts to  $k_B \times 1.5 \text{ mK}$ .

The entrance channel has a spin angular momentum projection number of  $m = 9/2 + 7/2 = 8$ . For collisions in s-wave with  $l = 0$ , one thus has total angular momentum projection of  $M_t = m + l = 8$ . As soon as  $M_t \neq 8$ , the entrance channel is predicted to be d-wave with  $l = 2$ . The numerically simulated inelastic collision rates arising from these various channels at a collision energy of  $k_B \times 5 \mu\text{K}$  are shown in figures 4.5b and c, corresponding to s- and d-wave entrance channels, respectively. As is evident, the inelastic rate associated to incoming s-wave collisions exceed by several orders of magnitude the ones originating from the different higher partial wave channels at the temperatures under consideration. Consequently, the inelastic two-body loss rate should not display a strong dependence on temperature, which is consistent with the experimental observation except for the effects arising from recapture, as discussed above. The comparatively weak nature of the d-wave contributions precludes the observation of the associated multiplet structure in the entrance channel. The observed overall shape and magnitude of  $L_2(B)$  are well reproduced by the numerical simulations, with the measured peak loss rate of  $L_{\text{fit}}^{(2)} = 3.25(10) \times 10^{-12} \text{ cm}^3 \text{ s}^{-1}$  agreeing to within 20 % with the predicted value of  $4.05 \times 10^{-12} \text{ cm}^3 \text{ s}^{-1}$ . The discrepancy is caused by the fact that the measured value is most likely not exactly on top of the  $L_2(B)$  curve. The resonance position itself appears to be shifted by roughly  $-0.45 \text{ G}$ . This deviation is within the prescribed uncertainty of the numerical predictions of  $\pm 0.5 \text{ G}$  [137]. Moreover, it was later discovered that an additional

DC magnetic offset field *might* have been present during the loss rate measurements, which could have shifted the resonance position by up to 0.2 G. These systematic errors do not affect any of the conclusions about the properties of the resonance and can be reprimanded easily by a future recalibration of the  $L^{(2)}$  spectrum.

#### 4.4. Resonant spin dynamics in (s,d)-wave collisions

The apparent absence of three-body recombination and the ability to keep atoms trapped even after they have undergone inelastic two-body collisions makes it possible to study the time evolution of the spin populations. This dynamical system is driven by the resonant coupling between the  $s$ -wave entrance channel ( $l_{\text{in}} = 0$ ) with  $M_{\text{in}} = 9/2 + 7/2 + l_{\text{in}} = 8$ , and the  $d$ -wave molecular bound states with  $M_{\text{out}}$  and  $l_{\text{out}} = 0, 1, 2$ . Because the spin-spin interaction is of tensor form, it breaks the spatial spherical symmetry and facilitates the redistribution of angular momentum between the spin- and spatial degrees of freedom [112]. In particular, the magnetic dipole interaction  $\hat{H}_{\text{ss}}$  mixes  $L = 0$  with  $L = 2$  channels, which gives rise to narrow  $s$ -wave Feshbach resonances<sup>3</sup> with weak inter-channel coupling [107, 113, 114, 121–123, 140–142]. The projections of total angular momentum are the only conserved quantities, i.e.  $M_{\text{in}} = M_{\text{out}}$ .

One interesting question is whether this system, consisting of the spin degrees of freedom, will converge towards a steady state and, if so, whether it corresponds to a thermal Boltzmann equilibrium or something else. In this context, it is a-priori not clear if this quantum system is open or closed since additional loss channels may become relevant at long times. In order to address these issues experimentally, the relaxation dynamics have to be observed in the absence of losses, necessitating the use of a very deep trap with large  $\eta$ . Apart from the spin populations, the heating experienced by the ensemble represents a potential observable as it will originate directly from the energy released during inelastic collisions. The theoretical framework to relate these quantities to the underlying microscopic processes will be developed in the ensuing sections.

##### 4.4.1. Calculation of the collision channels' branching ratio

In order to determine at what rate the Zeeman energy is released into the system, one must know the branching ratio to the available inelastic exit channels. The underlying transition probabilities are given by the matrix elements of the magnetic dipole interaction, which will be considered in the following. The inelastic scattering rate is dominant for atoms colliding in the  $s$ -wave channel. Therefore, we can restrict this discussion to one

<sup>3</sup>By contrast, the exchange interaction contained in  $\hat{H}_{\text{c}}$  can mix different hyperfine states because it is not diagonal in the hyperfine basis  $\{F, m_F\}$  at short range. However, for incoming  $s$ -waves the orbital angular momentum  $L, m_l$  is conserved since the exchange interaction is spherically symmetric. Consequently, Feshbach resonances mediated by this interaction can only occur if the molecular state is also  $s$ -wave [112].

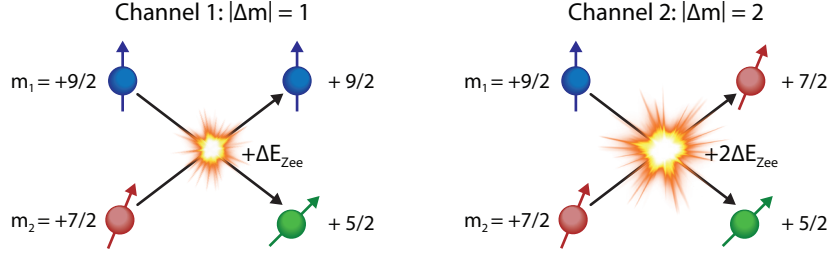


**Figure 4.6.: Possible inelastic collision channels due to the (s,d)-wave Feshbach Resonance.** Left: First collision channel  $9/2 + 7/2$  with  $\Delta m = 1$ , in which only the colliding atom with  $m_F = 7/2$  undergoes an exothermic spin flip to the lower lying spin state  $m_F = 5/2$ . The released energy corresponds exactly to the Zeeman splitting between the two states at the given ambient magnetic field. Right: Second collision channel with  $\Delta m = 2$ . Both colliding atoms flip their spin, releasing twice as much energy into the cloud.

entrance channel with  $l = 0$  and consider the possible outcomes given that the change of angular momentum projection can be 0, 1 or 2 by virtue of the exit channel being d-wave in nature. As was discussed earlier, the angular momentum projection of the incoming channel amounts to  $M = l + 9/2 + 7/2 = 8$ , which has to be conserved throughout the collision (see sec. 4.1). Based on the fact that we can at most change the internal angular momentum by  $\Delta m_F = 2$ , we are thus left with the following reactions,

$$|9/2\rangle + |7/2\rangle \rightarrow |9/2\rangle + |5/2\rangle + 1\Delta E_Z \quad , \quad \Delta m_F = -1, \quad (4.22)$$

$$|9/2\rangle + |7/2\rangle \rightarrow |7/2\rangle + |5/2\rangle + 2\Delta E_Z \quad , \quad \Delta m_F = -2, \quad (4.23)$$

which are depicted schematically in fig. 4.6. Because the atoms obey fermionic statistics, the corresponding incoming  $|i\rangle$  and outgoing two-particle states  $|f\rangle$  are given by antisymmetric superpositions of the Zeeman levels as per:

$$|i\rangle = \frac{1}{\sqrt{2}} |L = 0, m_L = 0\rangle \otimes (|9/2, 7/2\rangle - |7/2, 9/2\rangle), \quad (4.24)$$

$$|f_1\rangle = \frac{1}{\sqrt{2}} |L = 2, m_L = 1\rangle \otimes (|9/2, 5/2\rangle - |5/2, 9/2\rangle), \quad (4.25)$$

$$|f_2\rangle = \frac{1}{\sqrt{2}} |L = 2, m_L = 2\rangle \otimes (|7/2, 5/2\rangle - |5/2, 7/2\rangle). \quad (4.26)$$

We can define the branching ratio  $\rho$  with respect to the total loss rate  $L_t^{(2)} = L_1^{(2)} + L_2^{(2)}$  as per

$$L_1^{(2)} = \rho L_t^{(2)} \quad \text{and} \quad L_2^{(2)} = (1 - \rho) L_t^{(2)}, \quad (4.27)$$

with  $0 \leq \rho \leq 1$ . Based on the theoretically predicted structure of the resonance, the bound state has internal spin of  $m_F = 6$ . As the dominant entrance channel is s-wave with

$M_t = 8$ , we thus expect that only reaction (4.23) occurs in practice due to the conservation of angular momentum projection. This implies that  $\rho = 0$ , which will need to be confirmed experimentally.

By using the experimentally determined inelastic loss rate of the Feshbach resonance, we can infer the rates at which population is transferred to the target spin states. For the sake of generality, we will keep  $\rho$  as a potentially needed modification to the model in the ensuing discussion.

#### 4.4.2. Rate equations in the limit of deep trapping potentials

In order to model the dynamics of the spin populations, we assume that the trap depth is much larger than the Zeeman splitting so that inelastic collisions no longer lead to trap loss. Rather, the released energy of  $E_{\text{rel}}/k_B = 2 \times 111 \mu\text{K}$  (reaction (4.23) at  $B = 7.3 \text{ G}$ ) is retained in the sample in the form of kinetic energy, resulting in an overall increase of the temperature after thermalization through elastic collisions. This continuous increase of thermal energy may eventually cause spilling and the onset of evaporation as the atoms begin to approach the threshold of the trap. For now, however, we assume that the atom number is constant throughout the evolution.

Using energy- and number conservation, the rate equations for the spin populations and temperature can then be written as:

$$\dot{N}_{7/2} = -\Gamma_1^{(2)}, \quad \dot{N}_{9/2} = -\Gamma_2^{(2)}, \quad \dot{N}_{5/2} = \Gamma_1^{(2)} + \Gamma_2^{(2)}, \quad (4.28)$$

$$3Nk_B\dot{T} = \Delta E_Z\Gamma_1^{(2)} + 2\Delta E_Z\Gamma_2^{(2)}, \quad (4.29)$$

with  $\Gamma_n^{(2)}$  representing the inelastic collision rate of channel  $n = 1, 2$ , as discussed earlier. The total inelastic rate would be given by the sum over the two available channels as per  $\Gamma_t^{(2)} = \Gamma_1^{(2)} + \Gamma_2^{(2)}$ . Neglecting one-body losses, we recall that

$$\dot{N}_{7/2} = -L_1^{(2)} \frac{N_{7/2}N_{9/2}}{2\sqrt{2}V_e}, \quad (4.30)$$

$$\dot{N}_{9/2} = -L_2^{(2)} \frac{N_{7/2}N_{9/2}}{2\sqrt{2}V_e}, \quad (4.31)$$

hold for the two-body collisions at hand. Based on the considerations of the previous section we set again  $L_1^{(2)} = \rho L_t^{(2)}$  as well as  $L_2^{(2)} = (1 - \rho)L_t^{(2)}$  for the two channels and introduce the dimensionless variables

$$x_k = \frac{N_k}{N_t}, \quad \tau = \frac{k_B T}{\Delta E_Z}, \quad u = \frac{LN_t}{2\sqrt{2}V_e(T_Z)}t, \quad (4.32)$$

with  $k_B T_Z = \Delta E_Z$  denoting the Zeeman splitting at a given magnetic field and  $N_t$  the total

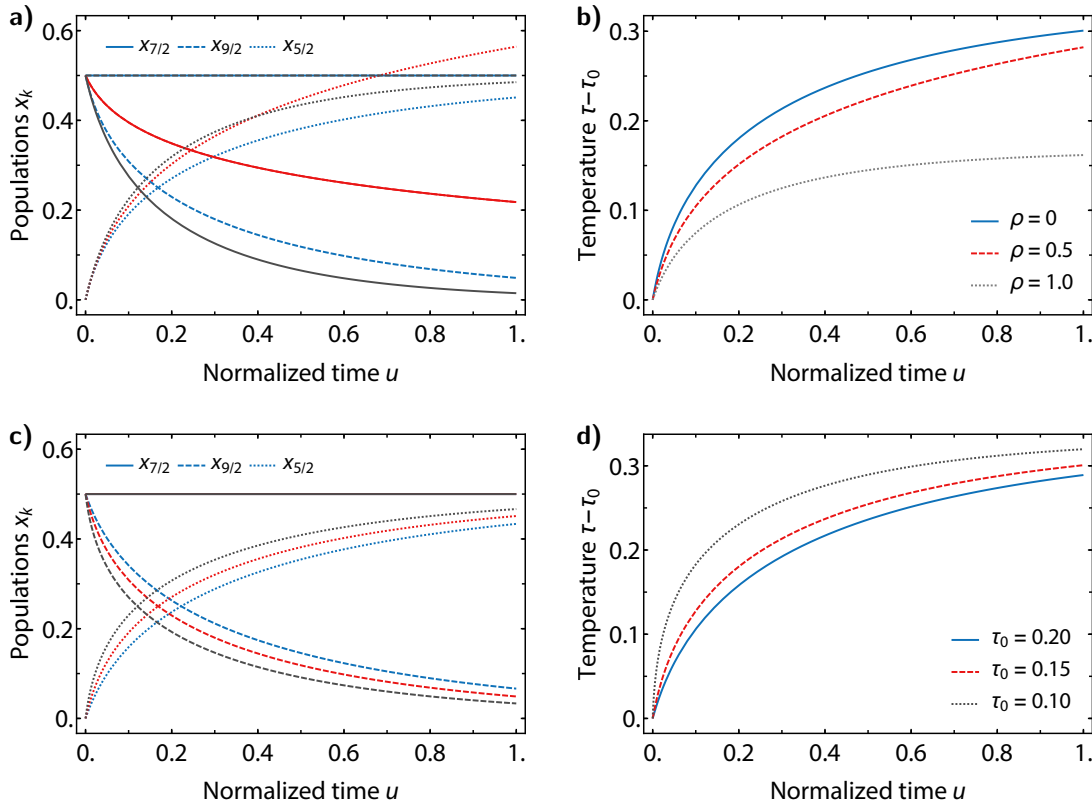


**Figure 4.7.:** Numerical simulation of the rate equations in dimensionless units. a) Time evolution of the spin populations with the initial conditions  $x_{7/2}(0) = x_{9/2}(0) = 0.5$ ,  $x_{5/2}(0) = 0$  and  $\tau(0) = 0.15$  for  $\rho = 0, 0.5, 1$ . b) Heating as function of time for different branching ratios with  $\tau(0) = 0.15$ . c) Spin dynamics as in a) for different temperatures  $\tau(0) = \{0.05, 0.15, 0.20\}$  and  $\rho = 0$ . d) Evolution of the temperature for the curves shown in c).

atom number. The rate equations can then be recast in the more convenient form:

$$\frac{dx_{7/2}}{du} = -\rho \frac{x_{7/2}x_{9/2}}{\tau^{3/2}}, \quad (4.33)$$

$$\frac{dx_{9/2}}{du} = -(1 - \rho) \frac{x_{7/2}x_{9/2}}{\tau^{3/2}}, \quad (4.34)$$

$$\frac{dx_{5/2}}{du} = -\frac{dx_{7/2}}{du} - \frac{dx_{9/2}}{du}, \quad (4.35)$$

$$\frac{d\tau}{du} = (2 - \rho) \frac{x_{7/2}x_{9/2}}{3\tau^{3/2}}. \quad (4.36)$$

This set of coupled differential equations can be solved numerically, with an example being given in fig. 4.7. For  $\rho = 0$  and balanced initial populations  $x_{7/2}(0) = x_{9/2}(0)$  as well as  $x_{5/2}(0) = 0$ , the inelastic collisions will deplete 9/2 while building up population in 5/2. As this process continues, the temperature of the sample increases until the system

reaches an asymptotic steady state at long times where  $x_{9/2} \rightarrow 0$  and  $\dot{\tau} = \dot{x}_{5/2} = 0$ . The population of  $7/2$  stays constant throughout the entire dynamics. In general, for otherwise identical initial conditions, the timescale of the dynamics becomes faster with decreasing initial temperature  $\tau_0$ .

The situation is quite different if  $\rho \neq 0$ . Due to the presence of the second channel, the average released energy per atom is lower with  $E_{\text{rel}} = (2 - \rho)\Delta E_Z/2k_B$  and therefore the timescale of the heating is reduced. Moreover,  $7/2$  is now being depleted as well, which provides a clear experimental signature to distinguish between the expected scenario where  $\rho = 0$ . If the  $7/2$  population is observed to be constant to within the experimental noise, this will amount to stating an upper bound for  $\rho$ .

#### 4.4.3. Spectrum of the initial heating rates

The initial heating rate itself represents an alternative means to characterize the resonance and, more importantly, it can be used as a first *qualitative* confirmation of the validity of the kinetic model provided the scaling with initial temperature can be reproduced experimentally. To that end, we performed measurements similar to the lifetime measurements described in sec. 4.3.2. However, the trap is now always recompressed to its full strength of  $U_0/k_B = 222 \mu\text{K}$  after evaporation to suppress inelastic losses. To prepare the sample in different initial temperatures, the end point of the evaporation ramp is varied implying that  $\eta_0$  will not be the same for all of the measurements as is the case for the spin populations. After the magnetic field is jumped to its target value, the size of the cloud is recorded via absorption imaging after various (short) hold times and converted into temperature using the trapping frequencies. The heating rate is then obtained from a linear fit to the data. The corresponding spectrum is shown in fig. 4.8a for the three initial temperatures  $T_0 = 12 \mu\text{K}$ ,  $16 \mu\text{K}$  and  $25 \mu\text{K}$ , which resembles the equivalent curve of the two-body loss rate seen in fig. 4.5. The peak heat rates given in  $\mu\text{K s}^{-1}$  decrease with increasing sample temperature. However, in order to compare these findings with the kinetic model devised above, the data has to be converted into dimensionless units to account for the differences in atom number, which alter the timescale of the heating.

In fig. 4.8b the long-time evolution of the cloud temperature on resonance at  $7.3 \text{ G}$  with  $T_0 = 16 \mu\text{K}$  is shown in the corresponding dimensionless units (4.32) using the experimentally determined peak loss rate of  $L_t^{(2)} = 3.25(10) \times 10^{-12} \text{ cm}^3 \text{ s}^{-1}$  for the conversion. The data is fitted using the rate equations (4.36) with  $\rho = 0$  and the initial spin populations as free parameters, which assume realistic values in the process.

While these measurements establish overall consistency between the kinetic model and the experimental findings, a spin resolved measurement is nevertheless needed to confirm the validity of the model in a quantitative fashion. The experimental procedure will be described in the following section.

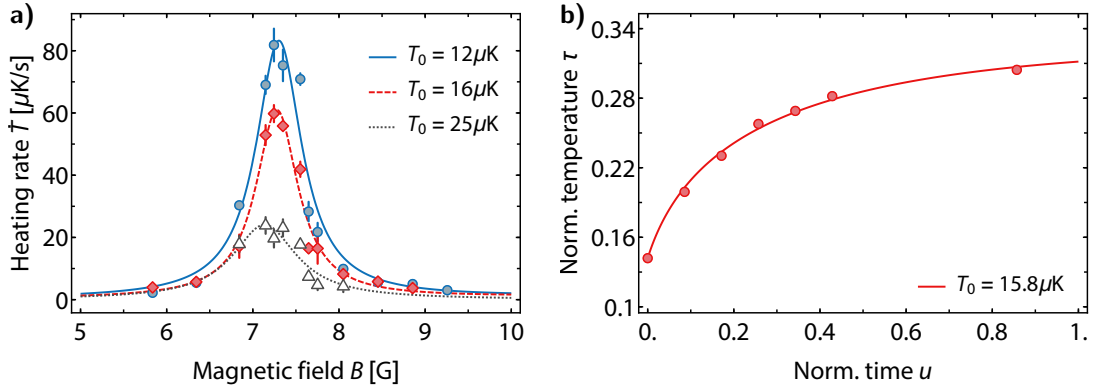


**Figure 4.8.: Heating dynamics in a strongly recompressed trap.** a) Heat rate spectrum around the first Feshbach resonance. The sample was held for various wait times of up to 0.1 s (on resonance) or 0.5 s (off-resonant) and the heat rate was extracted from a linear fit to the recorded temperatures. b) Resonant long-term heating in dimensionless units, where the peak loss rate of  $L^{(2)} = 3.25 \times 10^{-12} \text{ cm}^3 \text{ s}^{-1}$  was used for the conversion. Solid line: Fit of (4.36) to the data with spin populations as free parameters.

#### 4.4.4. Spin dynamics and verification of the branching ratio

Since the temperatures in the recompressed dipole trap are rather high with  $T_0 \sim 25 \mu\text{K}$ , Stern-Gerlach separation cannot be used for spin-selective imaging, as was already elaborated upon in sec. 3.1. We therefore employ calibrated microwave probing (see sec. 3.3 for details) in combination with optical pumping to detect changes among the spin state populations. Just like during the heating rate measurements described in the previous section, the optical dipole trap is recompressed to its maximum strength of  $U_0/k_B = 222 \mu\text{K}$  after evaporation. After an intermediate hold time at 4 G to let the atoms settle, one obtains a sample of  $2.10(19) \times 10^6$  atoms at a temperature of  $T_0 = 21.50(16) \mu\text{K}$ . This corresponds to  $\eta_0 = 12.4$  and a peak density of  $7.2 \times 10^{12} \text{ cm}^{-3}$ . The magnetic field is then jumped to its near-resonant target value of  $B = 7.80(2) \text{ G}$ <sup>4</sup> for various hold times, before being dropped to 3 G where the atoms are subjected to short microwave pulses that are tuned to be resonant with a given Zeeman level and its counterpart in the upper hyperfine manifold. After this spin-selective depletion, the remaining atoms are optically pumped into the stretched state  $m_F = 9/2$  before their total atom number is recorded via absorption imaging. The population of a given spin state  $N_k$  is then calculated by comparing the remaining number of atoms  $(N)_k$  after the application of a probe pulse resonant with  $|m_F = k\rangle$  to the case where none were removed  $(N)_0$ ,

$$N_k = \frac{(N)_0 - (N)_k}{1 - \beta_k}.$$

<sup>4</sup>Note that the calibration has changed with respect to the measurements presented so far. See sec. 4.3.3 for details.

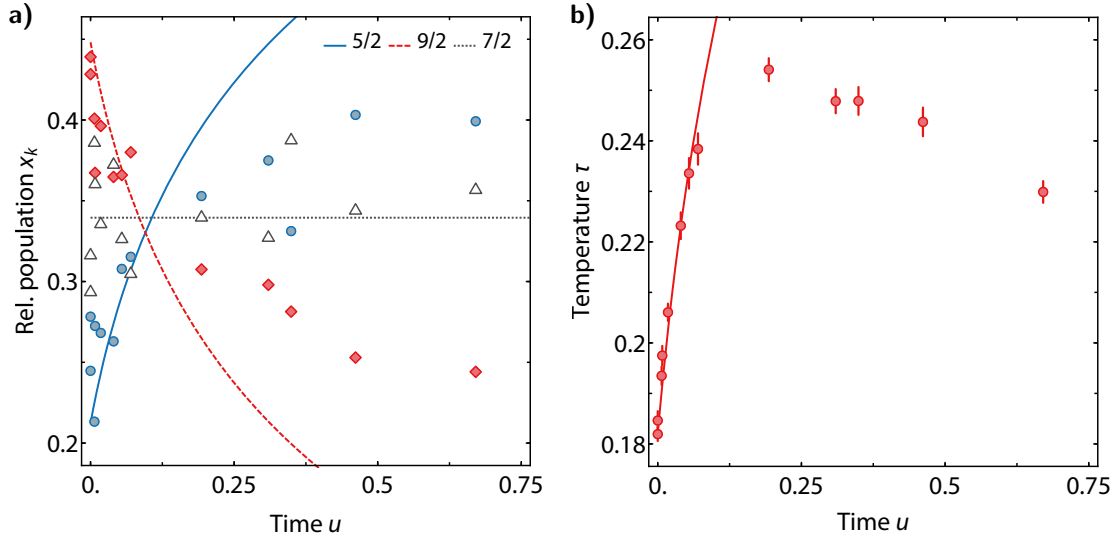


**Figure 4.9.: Spin dynamics close to resonance.** a) Fractional spin populations of the states  $m_F = 9/2, 7/2$  and  $5/2$  vs. rescaled time as detected by MW-probing. b) Sample temperature vs. time in dimensionless units. All lines in a) and the solid line in b) correspond to simultaneous parametric fits of the differential equation system (4.36) to all four experiment data sets. The initial spin populations are left as free parameters. The conversion into dimensionless time is done using the loss rate constant  $L^{(2)} = 7.5 \times 10^{-13} \text{ cm}^3 \text{ s}^{-1}$  and the detected atom numbers at each time. The longest hold time depicted here corresponds to  $t = 20 \text{ s}$ .

The depletion efficiency  $\beta_k$  for a given spin state is defined as  $N'_k = \beta_k N_k$ , which depends on the chosen parameters of the Landau-Zener ramp such as its duration and bandwidth. In this case we have 10 ms and 0.35 MHz, respectively, which entails  $1 - \beta = \{0.894, 0.377, 0.588\}$  for  $9/2, 7/2$ , and  $5/2$ . These efficiencies were previously calibrated using Stern-Gerlach imaging in conjunction with the MW-probes in a colder trap setting, ensuring that only one state is addressed at a time. Moreover, the depletion probability is assumed to not depend on sample density<sup>5</sup>, which is the basic prerequisite to be able to use this technique reliably on its own with hotter samples once SG separation becomes unfeasible. Experimentally, we determine  $\Delta N = (N)_0 - (N)_k$  as averages over multiple measurements and infer the spin populations using the above relation. Using this technique, the initial spin populations after the preparation sequence outlined above were determined to be  $x_{9/2}(0) = 41.9(35)$ ,  $x_{7/2}(0) = 33.2(38)$  and  $x_{5/2}(0) = 25.0(22)$ .

A measurement of the ensuing short- and long-term spin dynamics as well as of the accompanying heating is shown in fig. 4.9, where the experimental data has already been converted into dimensionless variables as per (4.32). At short times  $t \leq 0.1u$  ( $\sim 1 \text{ s}$ ) one can guarantee the absence of evaporative losses. Apart from the relatively strong heating, one indeed observes the theoretically expected increase of population in  $5/2$  as well as the

<sup>5</sup>At least over the range of values we are dealing with here

decrease of  $9/2$  and the constance of  $7/2$ . Since the spin populations are determined from multiple measurements of the total atom number, the shot-to-shot fluctuations of  $\sim 20\%$  of the experiment directly enters as errors of  $N_k$  and render the detection of small changes challenging. To compensate for these fluctuations, every data point is taken six times to obtain a stable average value. We then parametrically fit the differential equation system (4.36) simultaneously to the four obtained data sets  $\{x_{9/2}, x_{7/2}, x_{5/2}, \tau\}$  with the branching ratio  $\rho = 0$  and the initial temperature  $\tau_0$  a fixed parameters. Leaving the three initial spin populations as free parameters, one obtains a good fit for  $L^{(2)} = 7.5 \times 10^{-13} \text{ cm}^3 \text{ s}^{-1}$  for the first 8 data points, which is in good agreement with the expected rate. At times larger than  $0.1u$  the dynamics of  $9/2$  and  $5/2$  follow the same trend, but appear to slow down with  $x_{7/2}$  still remaining at a constant level.

The heating dynamics are displayed in fig. 4.9b. After a fast and strong increase of the sample temperature by roughly  $40\%$  over the course of  $0.07u$ , one can clearly see the onset of evaporation that lead to a slow cooling of the sample at longer times. At this stage, the atom number begins to decrease exponentially with a timescale of roughly  $32.0 \text{ s}$ , which is much faster than the one-body lifetime of  $> 120 \text{ s}$ . Note that the conversion of time into dimensionless units did incorporate these changes in total atom number.

While the findings are well reproduced by the kinetic model at short times, the eventual onset of evaporation and loss of atoms makes the description of the entire dynamics more challenging. The observed increase of  $5/2$  and decrease of  $9/2$  slow down considerably as a result of the losses, and the steady state will thus be given by an equilibrium of evaporation and resonant inelastic collisions. Moreover, at long times the collisions may also occur in the opposite fashion as a result of detailed balance. The steady state observed here is not thermal as evidenced by the fact that the ratios of the populations are clearly not given by their expected Boltzmann weights of  $e^{-\Delta E_z/k_B T_\infty} \simeq 0.01$ . The system is open due to the presence of evaporation and spilling losses, and the nature of the steady state thus needs to be modeled by incorporating these effects for the three involved spin states in the rate equation model.

#### 4.5. Summary and additional resonances

So far, the analysis of the Feshbach resonance has established the 2-body nature of the losses and confirmed the numerically determined inelastic collision rate [137]. The spin dynamics near the resonance clearly show a proliferation of the population in the state  $m_F = 5/2$  at the expense of  $9/2$ , while  $7/2$  remains at a constant level. Besides this inelastic process for which  $\Delta m = 2$ , there is no discernible signature of an additional channel with  $\Delta m = 1$ . The latter would be signified by a depletion of the  $m_F = 7/2$  population, which was not observed up to the error bars. This confirms qualitatively the prediction that, for incoming s-waves, only one of the bound states in the closed channel is accessible by

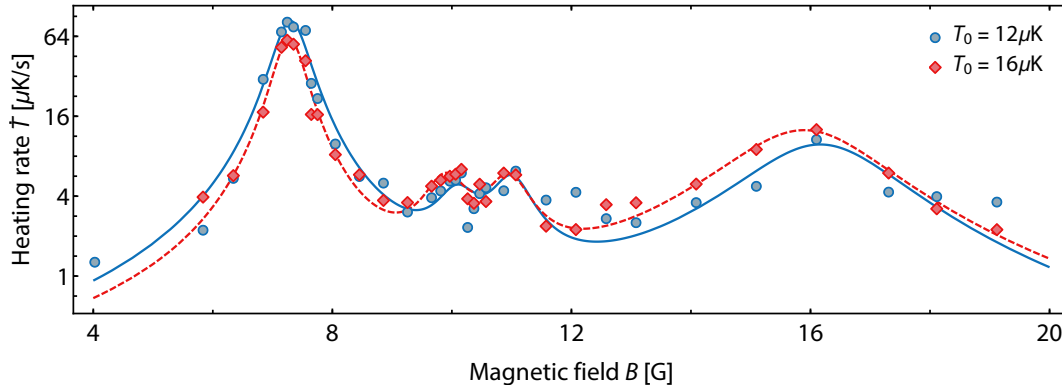


**Figure 4.10.: Full spectrum of the heating rates versus magnetic field.** The data points of the first resonance around 7.3 G correspond to the ones shown in fig. 4.8. The spectrum shows additional resonances at 10 G, 11 G and 16 G, which were not predicted by the numerical simulations [129, 137] used to describe the first (s,d)-wave peak on the left. Solid lines are guides to the eye.

virtue of angular momentum conservation.

In order to further study the resonance, several steps can be taken. Apart from the full characterization of the steady state as outlined above, a more precise measurement of the two-body loss rate is required to pinpoint the resonance position more accurately. This can be done by directly fitting the corresponding numerical simulation for  $L_2$  to the data. The second resonance predicted at 160 G may also be studied in a similar manner. Moreover, the binding energy can be measured via RF association spectroscopy in order to confirm the numerically predicted scalings in [137]. Finally, the controlled creation of molecules via magneto-association represents another interesting avenue to pursue.

During the course of this study, additional resonances were found in the range of magnetic fields under consideration. In fig. 4.10 we show the full spectrum of the short-term heating rates recorded for magnetic fields of up to 20 G. Apart from the main resonance located between 7 G and 8 G, three smaller peaks at 10 G, 11 G and 16 G are clearly visible. They also appear in the corresponding spectrum of the two-body loss rate for  $7/2$  and  $9/2$ , which may not provide the correct scaling since the losses may be three-body in nature. Given that the mixture used to obtain this data contains also small amounts of  $m_F = 5/2$ , it is not a-priori clear which combinations of spin states contribute to these loss features. The processes may also correspond to higher-partial wave resonances between identical spin states. These features were not present in the numerical simulations provided by E. Tiesgina [129, 137]. Additional simulations suggest that no p-wave Feshbach resonances between  $9/2, 9/2$  and  $7/2, 7/2$  are expected at these magnetic fields [143].

The detailed experimental and numerical analysis of these loss features will be the subject of future study.

**Towards 3D-1D dimensional crossovers in strongly  
interacting Fermi gases**



## Chapter 5

### From Fermi- to Luttinger liquids

---

5.1. Landau Fermi-liquid theory . . . . .	111
5.2. Tomonaga-Luttinger theory . . . . .	114
5.3. Momentum-resolved RF spectroscopy . . . . .	117
5.4. Mapping of the momentum distribution . . . . .	118
5.5. Dimensional crossovers between normal states in 3D and 1D . . . . .	120

---

In chapter 1 we have emphasized the role of ultracold Fermi gases as versatile platforms for quantum simulation. Feshbach resonances make it possible to create scale invariant systems and strong interactions in spin mixtures reaching even the unitary regime, which gives rise to thermodynamical behavior that depends only on the density and temperature of the gas [52]. The efforts described so far were directed at system with equal spin populations. Partially polarized gases enable the study of exotic phases of fermionic superfluidity in situations, where only partial pairing can occur [36, 144, 145]. Spin imbalance introduces an effective magnetic field into the thermodynamical description of the gas, which corresponds to the difference of the two underlying chemical potentials. Strongly interacting Fermi gases with tailored spin populations can be prepared in a straightforward manner, which is not possible with condensed matter systems.

The phase diagram of the imbalanced Fermi gas is by definition richer than the one of the balanced case and contains, for example, the elusive Fulde-Ferrel-Ovchinnikov state [146, 147]. The latter corresponds to an inhomogeneous superfluid state made up of mobile Cooper pairs, the observation of which represents one of the major goals of currently ongoing experimental research [52].

The mean field phase diagrams of the three-dimensional Fermi gas with imbalance are shown in fig. 5.1. Below the tricritical point one observes, depending on the degree of polarization  $P = N_{\uparrow} - N_{\downarrow} / N_{\uparrow} + N_{\downarrow}$ , a separation between the paired superfluid and the mixed normal phase consisting of polarons, and the eventual collapse of superfluidity at a critical imbalance [52]. This threshold is known as the Chandrasekhar-Clogston- or Pauli-limit and signifies the onset of the first-order (2nd order above the tricritical temperature) superfluid to normal phase-transition [148, 149]. In typical inhomogeneous

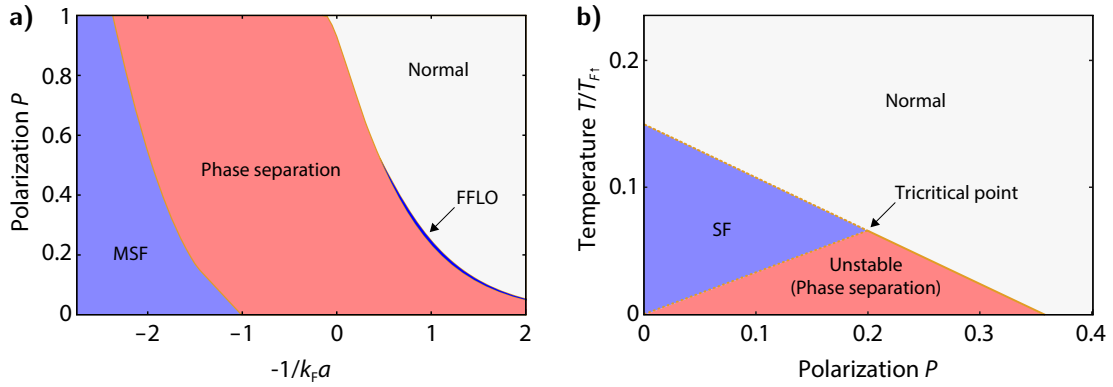


**Figure 5.1.: 3D Phase diagrams of imbalanced Fermi gases.** a) Mean-field phase diagram depicting the ground state as function of interaction strength and population imbalance  $P = N_{\uparrow} - N_{\downarrow} / N_{\uparrow} + N_{\downarrow}$ . Figure adapted from [156]. b) Phase diagram of a homogeneous Fermi gas with resonant interactions. Figure adapted from [157].

cold atom systems, the pairing gap  $\Delta(\mathbf{r})$  depends on the local density while the imbalance of the chemical potentials  $2h = \mu_{\uparrow} - \mu_{\downarrow}$  is constant throughout the trapping potential. Since the critical imbalance is given as per  $h_c = \Delta/\sqrt{2}$ , the transition will thus occur at a given equipotential shell in the cloud [52]. It was found experimentally that superfluidity persists up to a critical imbalance and, beyond the CC-limit, the system behaves like a normal Fermi liquid [34, 150–155]. In the extreme case of very high imbalance, there is only one impurity atom surrounded by the majority Fermi sea. This is the so-called Fermi polaron that has a well-defined energy and effective mass [48].

Over the course of the discussion in chapter 1, we have emphasized as well the role of reduced dimensionality. Lower-dimensional bosonic gases, on the one hand, have received a lot of experimental and theoretical attention [36, 158]. Fermi gases, on the other hand, have been studied predominantly in 3D, as described above, and in 2D [159–164]. Research of 1D Fermi gases remains scarce, and has been focused mainly on the observation of (superfluid) pairing and phase separation [165–170]. Recently, first experimental observations of Luttinger like behavior of Fermions has been reported [58, 171]. In part, the increased interest in (quasi-)1D systems is due to the fact that the FFLO state is predicted to occupy a larger area of the phase diagram [172–177] in comparison to 3D.

In the absence of superfluidity, however, very little is known about the dimensional crossover behavior between the two limiting normal states in 3D and 1D. They correspond to the well-known Fermi- and Luttinger liquids, respectively. In the following, the salient properties of these two regimes will be summarized before moving on to elaborate on how the interpolating physics can be studied experimentally, which constitutes one of the major aims of this thesis.

## 5.1. Landau Fermi-liquid theory

The macroscopic properties of many metals, like for example their specific heat and susceptibility, can be explained at low temperature using the model of weakly interacting Fermi gases despite the presence of strong interactions. The underlying model is the much celebrated Fermi-liquid theory by L. Landau [10], which is valid provided that phonon-mediated pairing can be neglected. The essential idea is that properties on a macroscopic scale are due only to excitations with energies small compared to the Fermi energy. The overall state of the many body system can then be given in terms of the ground state corresponding to the Fermi surface, and the elementary excitations that form a gas of quasi-particles with finite lifetimes and increased effective mass. Loosely speaking, one can say that the quasi-particle consists of a particle that is dressed by other particles around it [178], as is illustrated in fig. 5.2a. There is adiabatic continuity between the quasi-particles and the bare fermions in the sense that the former can be mapped onto the latter as the interactions are switched on slowly. The quantum numbers of the quasi-particles are identical, however their dynamical properties are rescaled by the interactions [12]. The ground state of free fermions is given by its momentum distribution  $n_0(\mathbf{k})$ . The corresponding distribution of the interacting system can be obtained via the distribution function of the quasi-particles. Excitations are given by the deviation with respect to the ground state as per  $\delta n(\mathbf{k}) = n(\mathbf{k}) - n_0(\mathbf{k})$ . In the limit of few excitations, the change in energy can be expressed in powers of  $\delta n(\mathbf{k})$  [179]:

$$\delta E = \sum_{\mathbf{k}} (\zeta(\mathbf{k}) - \mu) \delta n(\mathbf{k}) + \frac{1}{2} \sum_{\mathbf{k}, \mathbf{k}'} \delta n(\mathbf{k}) f(\mathbf{k}, \mathbf{k}') \delta n(\mathbf{k}') + \dots \quad (5.1)$$

Here  $f(\mathbf{k}, \mathbf{k}')$  denote the residual interactions between the quasi-particles, which give rise to the so-called Landau parameters. They, in turn, define the thermodynamical behavior of the system. The low lying excitations of a Fermi liquid correspond to single quasi-particle excitations (particle-hole excitations) as well as collective excitations between interacting quasi-particles. The latter are given in the form of density oscillations (plasmons for electron gases and sound waves for neutral Fermi liquid) and dampened spin waves (paramagnons) [178].

### The spectral function

Following [180], the single particle Green function of an interacting system is given by:

$$G(\mathbf{k}, \omega) = \frac{1}{\omega - \zeta(\mathbf{k}) - \Sigma(\mathbf{k}, \omega)},$$

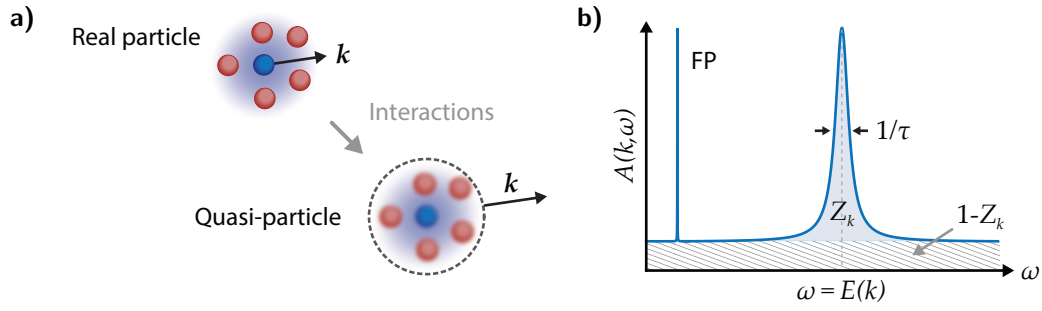


**Figure 5.2.: Fermi-liquid description of interacting particles.** a) Formation of fermionic quasi-particles in the presence of interactions. b) Schematic plot of the spectral function  $A(\mathbf{k}, \omega)$  consisting of the quasi-particle peak and the incoherent background incorporating the excitations that do not resemble quasi-free particles. FP corresponds to the delta-shaped spectral function of free particles.

with  $\zeta(\mathbf{k})$  denoting the bare dispersion relation and  $\Sigma(\mathbf{k}, \omega)$  the self-energy incorporating all of the many-body effects. The latter is equal to zero when interactions are absent. The poles of  $G$  correspond to the single-particle excitation energies, i.e. the spectrum of elementary excitations. The imaginary part of the Green function is referred to as the spectral function  $A(\mathbf{k}, \omega) = -2\Im[G(\mathbf{k}, \omega)]$ . It gives the probability to find a single particle excitation at momentum  $\mathbf{k} > \mathbf{k}_F$  and energy  $\omega$  or a hole with  $\mathbf{k} < \mathbf{k}_F$ , and is thus normalized as per  $\int A(\mathbf{k}, \omega) d\omega = 1$ . For a free particle (no interactions) the spectral function consequently takes on the simple form  $A_0(\mathbf{k}, \omega) = \delta(\omega - \zeta(\mathbf{k}))$  with  $\zeta(\mathbf{k}) = \epsilon(\mathbf{k}) - \mu$ , which is only non-zero when the frequency corresponds exactly to the dispersion relation  $\epsilon(\mathbf{k}) = \hbar^2 k^2 / 2m$ . In general, the spectral function can be written as,

$$A(\mathbf{k}, \omega) = -\frac{1}{\pi} \frac{\Im[\Sigma(\mathbf{k}, \omega)]}{(\omega - \zeta(\mathbf{k}) - \Re[\Sigma(\mathbf{k}, \omega)])^2 + (\Im[\Sigma(\mathbf{k}, \omega)])^2},$$

and in the case of quasi-particles, it has only one pole. The self-energy defines the nature of the spectral function via its real- and imaginary parts [181]. The imaginary part  $\Im[\Sigma(\mathbf{k}, \omega)] < 0$  imparts a finite width and height onto  $A(\mathbf{k}, \omega)$ . The delta-function of the free particle limit is thus converted into a Lorentzian centered around  $\omega = \zeta(\mathbf{k}) + \Re[\Sigma(\mathbf{k}, \omega)]$ . This spread in energy can be interpreted as the lifetime of the quasi-particles, which is inversely proportional to the imaginary part of  $\Sigma$  and thus depends on the underlying interactions. Well above the Fermi level, particles can scatter freely while close to the Fermi sea the phase space is strongly reduced and one can show that in this limit  $\tau \sim 1/E(\mathbf{k})^2$  holds. As a result, the lifetime of quasiparticles can become quite long and quasi-particles near the Fermi level are thus well-defined [178]. One can furthermore show that  $\tau \sim 1/T^2$  as long as  $k_B T \ll E_F$  [182].

The real part  $\Re[\Sigma(\mathbf{k}, \omega)]$  of the self energy modifies the position of the spectral function.

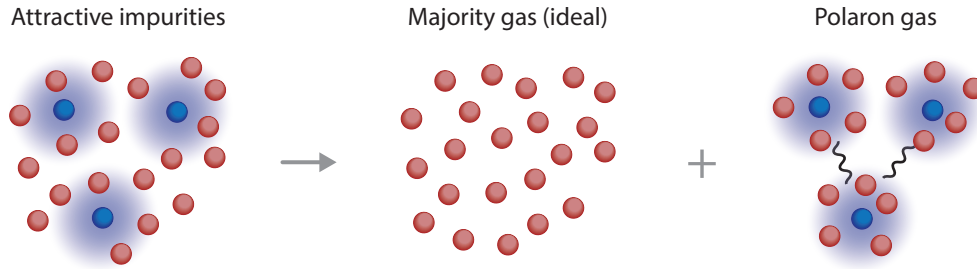


**Figure 5.3.: Fermi-liquid of weakly interacting polarons.** Atoms belonging to the minority spin component are dressed by the surrounding majority atoms due to attractive interactions, thereby forming Polaron quasi-particles. The entire gas can be understood as a Fermi liquid consisting of an ideal Fermi gas made up of the majority spin component and a weakly interacting Fermi gas of Polarons.

The interactions give rise to a modification of the dispersion relation of the single particle excitations as per  $E(k) = \zeta(k) + \Re\epsilon[\Sigma(k, \omega = E(k))]$ . For low energy excitations near the Fermi surface, one can expand this expression in powers of  $k$  and finds a similar relation as for free particles, however with an effective mass  $m^*$  due to the interactions. In addition, the frequency dependence of the real part also alters the total spectral weight  $Z_k$  of the excitation peak, reducing it below 1 as in comparison to the free-particle limit. In essence, this weight quantifies the proportion of the liquid that can be considered to be free quasi-particles and also manifests itself in the momentum distribution. For an ideal Fermi gas at zero temperature,  $n(k)$  has a sharp drop of magnitude 1 exactly at the Fermi level  $k_F$ . The presence of long-lived quasi-particles near the Fermi surface reduces the height of the discontinuity in the case of the Fermi liquid, which is then given exactly by the weight  $Z_{k_F} < 1$  [178]. Apart from the quasi-particle peak, there is in general an incoherent continuous background carrying the total spectral weight  $1 - Z_k$ , which contains excitations not resembling free particles. The full spectral function can be represented as  $A(k, \omega) = Z_k \delta(\omega - E(k)) + (1 - Z_k) A_{\text{inc}}(k, \omega)$ .

### Realizing Fermi-liquid behavior in cold atomic gases

In Fermi gases with tunable interactions, Fermi liquid behavior is most easily achieved by preparing spin-imbalanced mixtures above the Clogston-Chandrasekhar (CC) limit of superfluidity [52]. The case of extreme imbalance with  $P$  approaching unity gives rise to the Fermi Polaron, which was already discussed earlier. In this limit, one minority atom is suspended in the Fermi sea of the majority component and thus represents a dressed impurity with well-defined energy and effective mass. For the more relevant situation of lower imbalance, i.e. higher concentration of minority spins, it was found that the energy of the minority species does not change significantly when staying above the CC-limit [150]. The quasi-particles are polarons and only interact weakly with one

another, thus forming a Fermi liquid. Due to the attractive interactions between the two spin components, each impurity will then be dressed by many majority atoms and, consequently, polarons will not overlap and thus form a weakly interacting Fermi gas (see fig. 5.3). As long as the concentration of impurities remains small, the gas can be described as a mixture of a Fermi sea of majority spins and a Fermi sea of polarons with rescaled energy and mass, equal to the ones of the single impurity [48].

Fermi liquid behavior of this type has been observed experimentally in ultracold Fermi gases [151, 153, 154]. The properties of the quasi-particles can be probed via RF spectroscopy [150, 183–192], which is reminiscent of photo-emission spectroscopy used in condensed matter physics as will be described later on.

## 5.2. Tomonaga-Luttinger theory

Reducing the dimensionality of a system can strongly alter its properties on a fundamental level. For quantum systems, low dimensions tend to enhance the role of fluctuations and correlations for both the ground state as well as its excitations. Fractional statistics are a prominent example for an exotic property arising as a result. Moreover, one-dimensional quantum liquids in particular possess a number of exactly solvable models. The most prominent example is the Tomonaga-Luttinger liquid that can be thought of as the 1D-equivalent of the Landau Fermi-liquid in 3D, which is not applicable in one dimension [193]. It describes the low-energy properties of gapless 1D and quasi-1D Fermi gases [194]. The elementary excitations are always collective and obey bosonic commutation relations, with the most striking feature being the separation of spin- and charge (mass) degrees of freedom. Their dynamics are sound-like and have different propagation velocities [195]. In practice, an effectively one-dimensional trapping potential can be implemented with cold atoms, for example, by working with an elongated harmonic trap whose transverse confinement  $\hbar\omega_{\perp}$  exceeds by far the energy scale of the longitudinal motion  $\hbar\omega_z$  [196]. For a Fermi gas at temperature  $T/T_F \ll 1$ , this corresponds to the condition  $E_{F\uparrow} = N_{\uparrow}\hbar\omega_z \ll \hbar\omega_{\perp}$  with  $N_{\uparrow}$  denoting the number of majority atoms [195]. Assuming a 3D s-wave scattering length  $a_{3D}$ , the 1D collisions can be modeled as contact interactions via the zero-range potential  $U_{1D}(z) = g_{1D}\delta(z)$ . They are characterized by the ratio of the kinetic and interaction energy,  $\gamma = E_{\text{int}}/E_{\text{kin}} = mg_{1D}/\hbar^2 n_{1D}$ , where  $n_{1D}$  and  $g_{1D}$  denote the number density and coupling constant, respectively [197]. The latter is determined by the 3D scattering length and the transverse extension of the wave function:

$$g_{1D} = -\frac{2\hbar^2}{ma_{1D}} = \frac{2\hbar^2 a_{3D}}{ml_{\perp}^2} \frac{1}{1 - Aa_{3D}/l_{\perp}},$$

where  $A = 1.0326$  is a constant and  $l_{\perp} = \sqrt{\hbar/m\omega_{\perp}}$  the transverse oscillator length

[198]. In the limit where  $l_{\perp} = \sqrt{\hbar/m\omega_{\perp}}$  is much larger than the 3D scattering length,  $|a| \ll l_{\perp}$ , the inter-atomic interactions take on a 3D character. By changing their strength via  $g_{1D}(a)$ , one can implement the transition from the quasi-BEC to the Tonks-Girardeau gas in bosonic gases in 1D, and the BEC-BCS-like crossover in the case of two-component Fermi gases [199]. In this context one should point out a peculiarity of 1D, in that a bound states exists even when the scattering length is tuned to the negative side of the Feshbach resonance. This behavior is quite different from the conventional 3D case and is known as confinement-induced resonances [165].

### Luttinger parameters

Following [195], we will assume for the moment a homogeneous system of size  $L$ . In the absence of interactions the Fermi sea consists of only two points, which are given exactly by the Fermi momenta  $\pm k_F = \pm \pi \hbar (N_{\uparrow} + N_{\downarrow}) / 2L$ . The momentum representation of the Hamiltonian incorporating the aforementioned effective 1D interaction is given by

$$H = \sum_{k,\sigma} \epsilon_k c_{k,\sigma}^{\dagger} c_{k,\sigma} + \frac{g}{L} \sum_{k_1, k_2, q} c_{k_1, \uparrow}^{\dagger} c_{k_1 - q, \uparrow} c_{k_2, \downarrow}^{\dagger} c_{k_2 + q, \downarrow}$$

with  $\epsilon_k = \hbar^2 k^2 / 2m - \mu$ . One can introduce fermionic creation-  $c_{r,\sigma}^{\dagger}(k)$  and annihilation operators  $c_{r,\sigma}(k)$  for left- and right-moving particles, corresponding to  $r = R$  and  $L$ , respectively. The four types of particles are thus  $\{R\uparrow, R\downarrow, L\uparrow, L\downarrow\}$  and have the dispersion relation  $\epsilon_{r,q} = a_r \hbar v_F q$ . The Fermi velocity is given by  $v_F = k_F / m$  and  $a_{R,L} = \pm 1$ . As all of the states up to the Fermi level are occupied, one is left with two branches with unbounded momentum and energy. The densities  $\rho_{r,s}(q) = \sum_k c_{r,\sigma}^{\dagger}(k+q) c_{r,\sigma}(k)$  are subject to bosonic commutation relations [193].

Several different kinds of scattering processes can occur. Forward scattering refers to the process  $(R\sigma)(L, -\sigma) \rightarrow (R\sigma)(L, -\sigma)$  while backward scattering corresponds to  $(R\sigma)(L, -\sigma) \rightarrow (L\sigma)(R, -\sigma)$ . By definition, atoms of the same spin do not interact with one another. One can now introduce four new bosonic fields  $\Phi_i$  and  $\Pi_i$  with  $i = c, s$  (charge and spin, respectively), such that  $\rho_{r,s}(z) = [\partial_z \Phi_c - a_r \Pi_c + \sigma(\partial_z \Phi_s - a_r \Pi_s)] / \sqrt{8\pi}$  holds in real space. These fields correspond to fluctuations of the (charge) density  $\rho_c = \partial_z \Phi_c / \sqrt{\pi}$ , the spin density  $\rho_s = \partial_z \Phi_s / \sqrt{\pi}$ , the current density  $j_c = \Pi_c / \sqrt{\pi}$  and the spin current density  $j_s = \Pi_s / \sqrt{\pi}$ . One thus finds the bosonized Hamiltonian

$$H = \sum_{i=c,s} \frac{u_i}{2} \int dz \left( K_i \Pi_i^2 + \frac{1}{K_i} (\partial_z \Phi_i)^2 \right),$$

which contains two independent 'elastic strings'. Their eigenmodes corresponds to collective number density and spin density fluctuations of the quantum liquid. The two

quantities  $u_i$  and  $K_i$  are referred to as the Luttinger parameters and correspond to the speed of sound and the behavior of the correlation function at low energy, respectively. In general  $u_c \neq u_s$ , which implies that mass- and spin-density waves propagate with different velocities (spin-charge separation, see e.g. [200]), except in the non-interacting system where they are equal [193]. The latter case is signified by  $K = 0$  and attractive/repulsive interactions corresponds to  $K > 0$  and  $K < 0$ , respectively.

The identities presented so far can be applied to the inhomogeneous case via the local density approximation (LDA). Provided the sample is large with respect to the inter particle spacing as per  $k_F \ll 1/R$ , the identity  $\mu - U(z) = dE_0/dn$  must hold.  $E_0(n)$  represents the internal ground state energy per unit length and  $n$  the density. The external longitudinal potential is given by  $U(z) = 1/2m\omega_z^2 z^2$ . The underlying assumption is that the Luttinger parameters vary with space only through the density, so that one can make the substitutions  $K_i = K_i[n(x)]$  and  $u_i = u_i[n(x)]$ . The values of the parameters then depend on the strength of the interactions  $g$ . The density profile is always given by a Thomas-Fermi profile,

$$n = n_0 \sqrt{1 - \frac{z^2}{R^2}} \quad , \quad |z| < R$$

where the Radius  $R$  and the central density  $n_0$  depend on  $g$ . A summary of the corresponding profiles and Luttinger parameters for different regimes can be found in [195].

### Spectral functions in 1D

In one dimension, the spectral function  $A(k, \omega) = -\Im[G(k, \omega)]\text{sgn}[\omega]/\pi$  can be viewed as a tunneling density of states [201]. It gives the probability for a particle (hole) with momentum  $k$  and energy  $\omega > 0$  ( $\omega < 0$ ) to tunnel into the system. For right-moving fermions with no interactions, the spectral function reads  $A(k, \omega) = \delta(\omega - u(k - k_F))$ . The momentum distribution of a Luttinger liquid is different from the Fermi-liquid case. For any non-zero interaction strength  $K_c \neq 1$  one finds that  $n(k) = n_{k_F} - \text{const.} \times \text{sgn}[k - k_F] |k - k_F|^\delta$  in the vicinity of  $k = k_F$ , with  $\delta = (K_c + 1/K_c - 2)/4$ . The power-law singularities occurring at the Fermi level are quite different from the step-like singularity akin to the Landau Fermi-liquid. This implies the absence of a quasi-particle pole in the single particle Green function and thus a qualitatively different spectral function. The quasi-particle peak typically seen in the Fermi-liquid is replaced by a continuum with a lower threshold at  $\min_i[u_i(k - k_F)]$  and singularities on the mass shell [193]:

$$A(k, \omega) = \begin{cases} (\omega - u_s(k - k_F))^{\delta-1/2} |(\omega - u_c(k - k_F))|^{(\delta-1)/2} , & u_c > u_s \\ (\omega - u_c(k - k_F))^{\delta-1/2} |(\omega - u_s(k - k_F))|^{(\delta-1)/2} , & u_c < u_s \end{cases}$$

A schematic illustration is given in fig. 5.4. Since there is particle-hole symmetry in the

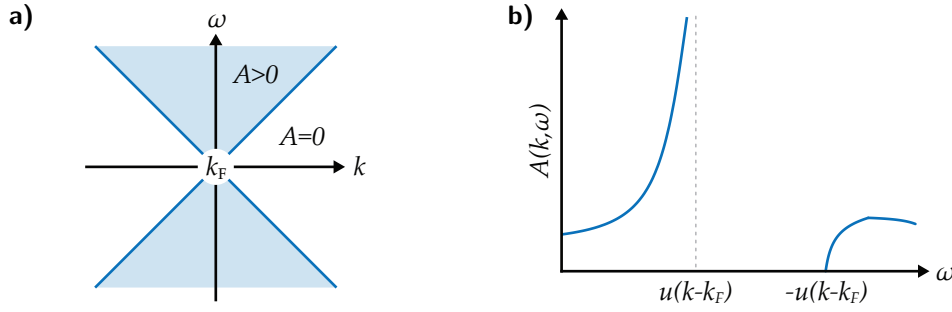


**Figure 5.4.: Spectral function of the Luttinger-liquid.** a)  $A(k \simeq k_F, \omega)$  for the linear part of the dispersion. b) Spectral function for a fixed momentum  $k \leq k_F$ . Interactions cause the divergence at the mass shell and a convergent power-law cusp at the inverted mass shell.

Tomonaga-Luttinger model, the spectral function in the particle region (pos. energy) is identical to the one in the hole region (neg. energy) for a given  $k$ . The fundamental assumption made so far is that the dispersion relation is linear, which entails the exact solvability of the Tomonaga-Luttinger model. This way, all of the dynamic response functions for weakly interacting Fermions can be calculated for arbitrary momenta. This is valid only if the interaction energy is not on the same order as the kinetic energy [201]. Non-linearities in the dispersion relation can dramatically alter the shape of the spectral function, for example by re-introducing a Lorentzian-type peak reminiscent of the Fermi liquid on the particle mass shell [202].

### 5.3. Momentum-resolved RF spectroscopy

The spectral function of an ultracold Fermi gas can be measured via momentum-resolved RF spectroscopy [128, 203, 204]. The basic mechanism of this technique is illustrated in fig. 5.5. Electromagnetic radiation in the radio-frequency domain is shone onto the ensemble, the atoms of which initially occupy two (strongly) interacting spin states  $|1\rangle$  and  $|2\rangle$ . By absorbing a photon, one of the atoms can change its internal state to a third target state  $|3\rangle$  that does only interact weakly or not at all. In absence of the (strong) interactions, the energy difference between the initial and target state is simply given by the Zeeman splitting for the given ambient magnetic field. Interactions between  $|1\rangle$  and  $|2\rangle$  give rise to spectral shifts as well as broadening in the RF response, which in turn can be used to infer the properties of the many-body system at hand [205–208]. Note that in fermionic gases one has to use a scheme involving three states due to the absence of clock shifts in two-level systems [184]. The wavelength of the RF field is usually large with respect to the size of the atomic cloud. Therefore, the spatial dependence can be neglected and the intensity can be taken to be constant. The momentum of the RF photon is thus negligible with respect to the Fermi momentum.

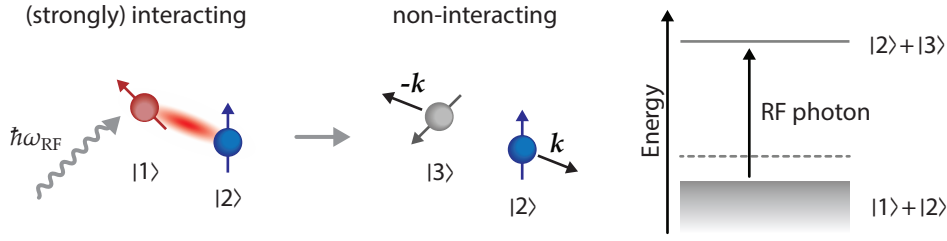


**Figure 5.5.: RF spectroscopy in interacting systems.** Two fermions with different spin states  $|1\rangle$  and  $|2\rangle$  interact (strongly) in the vicinity of a Feshbach resonance (left). A photon of energy  $\hbar\omega_{\text{RF}}$  is absorbed by one atom, which changes its internal state into  $|3\rangle$ . The resulting combination of states is no longer interacting with one another (middle). Due to the presence of interactions between  $|1\rangle$  and  $|2\rangle$ , the required energy to transfer  $|1\rangle$  to  $|3\rangle$  is shifted with respect to the bare energy difference between the two internal states.

If the spectroscopy is realized in a momentum-resolved manner [154, 209, 210], the peak of the resulting spectrum corresponds to the underlying dispersion relation. This way, one gains direct experimental access to the spectral function  $A(k, \omega) = -2\text{Im}[G_{\text{ret}}(k, \omega)]$  of the many-body system. In this form, momentum-resolved RF spectroscopy is equivalent to photo-emission spectroscopy commonly used in condensed matter physics.

Degenerate gases of  $^{40}\text{K}$  with tunable interaction strength are realized using the two lowest lying Zeeman ground states  $|-9/2\rangle$  and  $|-7/2\rangle$ , which possess a Feshbach resonance at 202.1 G. The straightforward choice for target state for RF spectroscopy is the neighboring Zeeman state  $|-5/2\rangle$ , whose background scattering length with the other two states amounts to only  $a \simeq 200a_0$ . However, care has to be taken as it has two additional narrow resonances with  $|-9/2\rangle$  and  $|-7/2\rangle$  located at 224.21 G and 228.7 G, respectively (see sec. 2.11.4 for details). A high degree of magnetic field stability is a crucial requirement in order to be able to record well resolved RF spectra. A detailed discussion of the experiment's performance (and compliance) in this regard can be found in appendix B.2.

The reconstruction of the spectral function requires the simultaneous observation of the momentum distribution for a given probe energy. As we aim on working with closely placed arrays of microtraps, the appropriate measurement procedure is not obvious and will be discussed in the following.

#### 5.4. Mapping of the momentum distribution

Access to the momentum distribution of an ultracold gas is typically obtained through free ballistic expansion. After all trapping potentials are switched off, the atoms move about freely according to their initial momentum and after a certain time of flight the momentum distribution can be obtained from the imaged spatial density. The implied

mapping is, strictly speaking, only valid in the far-field limit as  $t \rightarrow \infty$ . The underlying reason is that the influence of the initial in-situ density must become asymptotically small. This conventional time-of-flight method suffers from two main limitations. First, the expansion must take place in the absence of interactions in order to avoid redistribution of momentum among the atoms. Given that interactions are controlled via a Feshbach resonance, this problem can be addressed by quickly ramping the magnetic field to the zero-crossing of the scattering length. This is only possible if the resonance width is sufficiently small, as is the case for  $^{40}\text{K}$ . Moreover, when performing RF spectroscopy the target state can be chosen such that it is only weakly interacting. In this scenario, the strong interactions between the probed states do not play a role during time-of-flight. Second, the maximum expansion time is limited by the detection threshold of the imaging system since increasing cloud sizes entail a reduction of the signal-to-noise ratio. In addition, when working with systems consisting of multiple macroscopically populated microtraps as in our situation, the free expansion of neighboring ensembles may cause unwanted overlap between the density distributions.

The problem of long expansion times can be overcome by momentum refocusing [211–215]. By letting the atoms evolve in a harmonic potential  $U(z) = 1/2m\omega_{\text{osc}}^2 z^2$  rather than in free space, the far-field limit of TOF is obtained after exactly a quarter period. This can be understood using a classical picture, where each particle  $i$  starts at some initial position and momentum. In the absence of interactions, the ensuing single particle trajectories  $\{z_i(t), p_i(t)\}$  are governed by the differential equation  $\ddot{z}_i(t) = -\partial_{z_i}U(z_i)$ , with the general solutions

$$z_i(t) = z_{i,0} \cos(\omega_{\text{osc}}t) + \frac{p_{i,0}}{m\omega_{\text{osc}}} \sin(\omega_{\text{osc}}t) \quad \text{and} \quad p_i(t) = m\dot{z}_i(t). \quad (5.2)$$

After a quarter period the position becomes equal to the initial momentum up to a constant factor,  $z_i(\tilde{t}) = p_{i,0}/m\omega_{\text{osc}}$  with  $\tilde{t} = \tau/4 = \pi/2\omega_{\text{osc}}$ . The oscillation period  $\tau$  is shared by all single particle orbits and since the phase retardation between the trajectories' position and momentum remains always constant, one can infer the past momentum distribution of  $t - \tau/4$  from the instantaneous position distribution at any time  $t$  as per

$$\{z_1(t), \dots, z_N(t)\} = \frac{\tau}{2\pi m} \{p_1(t - \tau/4), \dots, p_N(t - \tau/4)\} \quad \forall t. \quad (5.3)$$

This unique correspondence is illustrated in fig. 5.6a. As soon as the potential becomes anharmonic, the nature of the orbits change. Typically, the temporal synchronization between the trajectories is lost as the oscillation periods can now depend on the initial position and momentum. This situation is shown in fig. 5.6b. This detrimental effect will become important in the experimental context of the next chapter.

In practice, one does not have direct access to the single particle orbits in phase space, but

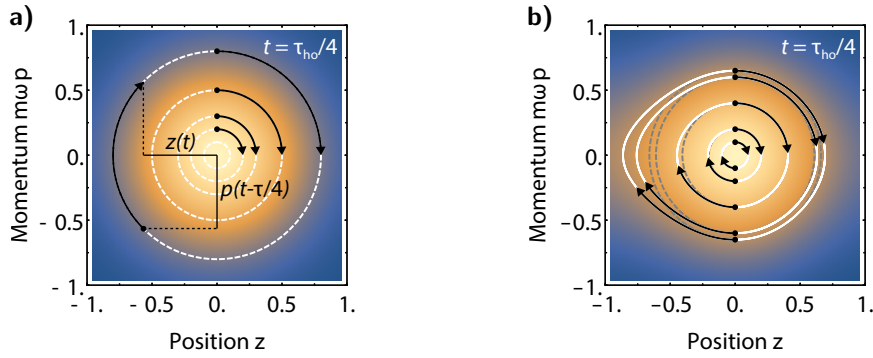


**Figure 5.6: Mapping of momentum onto real space in a harmonic trap.** a) Rescaled single particle orbits in an infinitely high harmonic potential. b) Dephasing of low- and high energy orbits in a finite trapping potential of the form  $-a \exp(-bz^2) + cz$ . The black lines indicate the distance covered during a quarter harmonic period.

rather to the density distribution measured through absorption imaging. The relationship (5.3) can be reformulated in terms of the probability distribution function in phase space. As long as the potential is harmonic, the phase-space distribution will undergo a rotation of  $\pi/2$  after a quarter period. As a result, the position- and momentum distributions will exchange their roles, which is easily verified using classical expressions for the phase space distribution [86]. In the more relevant case of a quantum gas, these distributions are given via field operators as per  $f(z) = \langle \hat{\psi}^\dagger(z) \hat{\psi}(z) \rangle$  and  $f(p) = \langle \hat{\psi}^\dagger(p) \hat{\psi}(p) \rangle$ . Following [214], the time evolution can be determined in the Heisenberg picture, which yields a Schrödinger equation reminiscent of the paraxial wave equation in optics. One thus finds the identity  $\langle \hat{\psi}^\dagger(z, \tau/4) \hat{\psi}(z, \tau/4) \rangle = \langle \hat{\psi}^\dagger(p, 0) \hat{\psi}(p, 0) \rangle$ , which implies that  $f(z, t = \tau/4) = f(p, t = 0)$  with  $p = m\omega_{\text{osc}}z$ . The density distribution at  $t = \tau/4$  gives therefore direct access to the momentum distribution at  $t = 0$ .

Momentum refocusing can be interpreted as a matter-wave analogy to optical lenses, which map the far-field Fraunhofer diffraction pattern onto their focal plane by imprinting a quadratic phase shift on the incoming electric field [214]. By combining momentum mapping with RF spectroscopy, one can thus reconstruct the spectral function  $A(k, \omega)$  of an interacting system and avoid the aforementioned detrimental effects arising from long times of expansion. To that end, harmonic confinement must be provided during time-of-flight, as will be discussed in sec. 6.2.7.

## 5.5. Dimensional crossovers between normal states in 3D and 1D

The nature of the normal states of Fermi gases in three and in one dimension is very different on a fundamental level. On the one hand, one has single-particle excitations forming a weakly interacting gas of polarons with an effective mass. On the other hand,

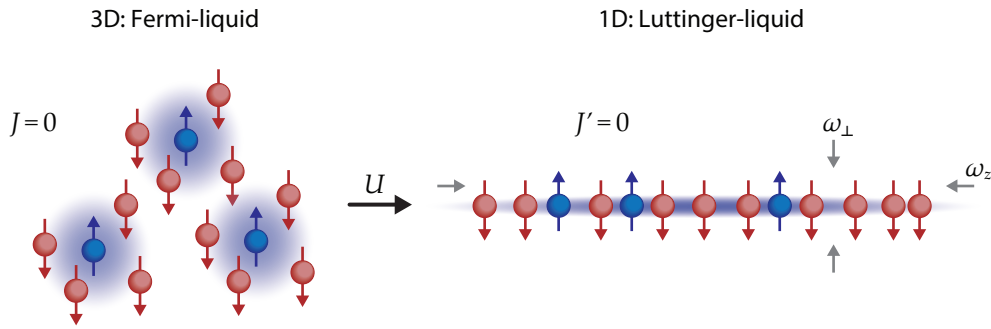


**Figure 5.7.: Dimensional crossover in a large spacing optical lattice.** Left: The dynamics in the microtraps located at each lattice site are three-dimensional due to the weak degree of confinement. The large lattice spacing nevertheless causes site-to-site tunneling to be negligible. Right: Increasing the optical power increases the trap depth, eventually freezing out the transverse degrees of freedom.

there are no single particle excitations, but only collective ones in the form of density- and spin waves. Both limits are characterized by their respective spectral functions, which reflect the contrast between the two regimes. For a Fermi-liquid there is a well-defined quasi-particle peak while for a Tomonaga-Luttinger liquid one expects a continuum with singularities. The dimensional crossover between these two seemingly opposite types of quantum liquids remains largely unexplored.

Cold atoms offer the possibility to tune the dimensionality of the trapping potential in-situ [158, 165, 170]. So far, theoretical and experimental efforts to study Fermi systems in their normal state have been focused on 3D or 1D systems. Dimensional crossovers between one and three dimensions have been realized, but with the aim to study the phase diagrams in the presence of (superfluid) pairing [170]. Moreover, the 3D side of the crossover was realized via weak site-to-site hopping in a 2D optical lattice, which has also been the main focus of theoretical inquiry [216, 217].

In order to study the dimensional transition of one independent normal Fermi-liquid to a Luttinger-liquid [218], we employ a 2D optical lattice with large spacing. This enables the tuning of the dimensionality from 3D to 1D on each lattice site by increasing the potential depth while, at the same time, suppressing nearest neighbor tunneling at low trap depths. This way, the lattice effectively forms an array of independent, macroscopically populated microtraps, which can be analyzed in terms of their excitation spectrum and momentum distribution. Since this configuration naturally precludes long time-of-flight measurements, momentum refocusing will be used to reconstruct the momentum distribution in order to recover the full spectral function via RF spectroscopy. In the next chapter, the progress towards the experimental implementation of this system will be described in detail.



## Chapter 6

### Experimental realization of dimensional crossovers with Potassium-40

---

6.1. Fundamental design considerations and physical requirements . . . . .	124
6.1.1. Creation of optical lattices with large spacings . . . . .	124
6.1.2. Tuning the dimensionality of the atomic dynamics . . . . .	127
6.2. Preparation and detection of a single row of tubes . . . . .	131
6.2.1. High power laser system . . . . .	131
6.2.2. Generation of the tube lattice . . . . .	132
6.2.3. Calibration of the lattice spacing via matter wave diffraction . . . . .	134
6.2.4. Site-resolved imaging system . . . . .	135
6.2.5. Spin selective imaging at high magnetic fields . . . . .	137
6.2.6. Isolation of a single row of tubes . . . . .	141
6.2.7. Harmonic confinement for momentum refocusing . . . . .	143
6.2.8. Optical compensation of gravity . . . . .	150

---

The study of the dimensional crossover between Fermi- and Luttinger liquids is difficult to realize in conventional condensed matter systems. One requires a means to tune the dimensionality, the interactions as well as the population imbalance between spin-up and spin-down fermions. None of these conditions can be met easily within the scope of classical condensed matter physics. By contrast, many-body systems realized using cold atoms do offer the necessary means of control in terms of interactions (see secs. 2.11.4, 4.1, C.5) and spin populations (sec. 2.11.3). Moreover, the spectral function can be probed directly via momentum resolved RF spectroscopy, in analogy to the ‘photo-emission spectrum’ akin to condensed matter systems. In sec. 5.5 we have already outlined the proposed experimental platform, which is based on large-spacing 2D optical lattices. In the following, its experimental implementation will be described in detail.

## 6.1. Fundamental design considerations and physical requirements

### 6.1.1. Creation of optical lattices with large spacings

Conservative potentials for neutral atoms can be tailored with off-resonant light. A fundamental example of this context was already discussed in sec. 2.11.2 in the form of optical dipole traps created by tightly focused Gaussian beams. Provided the laser source is sufficiently phase-coherent, one can create periodic potentials by interfering two beams. Ordinarily, such optical lattices [219] are generated by retro-reflecting a TEM<sub>00</sub> beam of trap depth  $U_0$ , which results in an approximately harmonic potential of the form:

$$U(x, r) = 4U_0 \left( 1 - \frac{2r^2}{\omega_0^2} \right) \sin^2(k_\lambda x).$$

The corresponding spacing of the intensity modulation is given by  $d = \lambda/2 = 2\pi/k_\lambda$  and atoms are trapped at its nodes or anti-nodes for red and blue detuning of the laser wavelength, respectively. The total potential depth of the lattice is four times larger than the single beam trap depth, i.e.  $U_{\text{lat}} = 4U_0$ . Note that here we have neglected the intensity envelope of the Gaussian beam along its longitudinal axis  $x$ . Along the transverse directions  $y$  and  $z$ , the confinement is set by the radial trapping frequencies  $\omega_R$  of the two underlying dipole traps to  $\sqrt{2}\omega_R$ . As a result, the density distribution of atoms will have a pancake-like shape, as is shown in fig. 6.1a. The harmonic trapping frequency at the center of each lattice site is given by

$$\omega_{\text{lat}} = \sqrt{\frac{U_{\text{lat}} \hbar^2 k_\lambda^4}{E_{\text{rec}} m^2}}, \quad (6.1)$$

where we have introduced the recoil energy of the trapping light as per  $E_{\text{rec}} = \hbar^2 k_\lambda^2 / 2m$ . It should be pointed out that the harmonic approximation is valid only as long as the lattice is sufficiently deep. In this case, each well of the lattice is sufficiently deep to support several vibrational levels with spacings  $\hbar\omega_{\text{lat}}$ . The other important energy scale  $J$  is associated with tunneling between adjacent sites, which corresponds to a gain of kinetic energy. For deep lattices, it can be calculated, for example, using the Mathieu equation [36]. Atomic dynamics can be constrained to one lattice site if  $J$  is small, or they can extend over the entire lattice.

When incoherently superimposing two lattices, one obtains a 2D array of elongated microtraps, as depicted in fig. 6.1b. The trapping frequencies along the non-modulated, vertical direction  $z$  is given by the radial confinement of the partaking Gaussian beams. Due to the absence of cross-interference, the tunneling energy scales of each partaking lattice are independent. Here again, the atomic dynamics can extend over the entire lattice

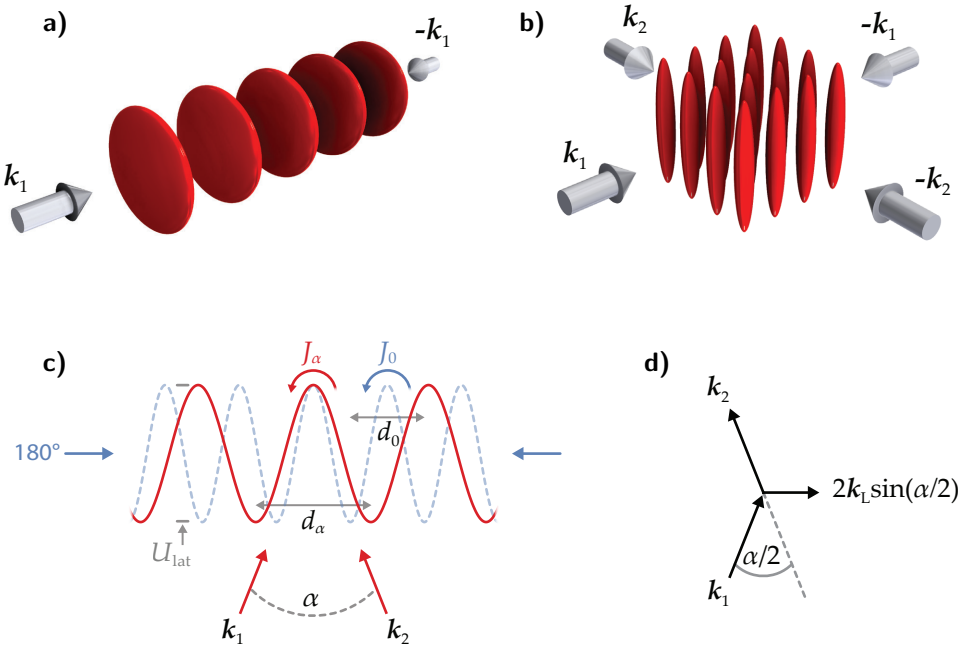


**Figure 6.1.: Generation of optical lattices with large spacings.** a,b) Cubic optical lattices created by one and two pairs of counter-propagating beams, respectively. c) Interference pattern along  $x$  of two running waves intersecting under an angle  $\alpha$ .  $U_{\text{lat}}(\alpha)$  denotes the lattice depth and  $d(\alpha)$  the spacing between successive sites. d) Wave number of the intensity modulation along  $x$  as function of the difference of the interfering wave vectors.

structure if  $J_1$  and  $J_2$  are small, or be confined to a single site (or lattice). As the lattice depths become deeper, it will be less likely for atoms to tunnel to adjacent sites, which eventually turns the lattice into an array of (macroscopically populated) microtraps. The dynamics within the 'tubes' may then be considered either three- or one-dimensional (along  $z$ ) depending on whether transverse motion is still possible. The latter limit can be reached if the confinement within the  $xy$ -plane containing the intensity modulation is increased further. The straightforward way to tune the dynamics in this manner is the optical power of the lattice beams. For the study of dimensional crossovers within a given tube, one must thus be in a position to tune the dynamics from 3D to 1D while maintaining negligible site-to-site tunneling rates at all times. The tunneling rate  $J(U_0)$  then determines whether tubes are independent many-body systems while the transverse trapping frequency  $\omega_{\perp}(U_0)$  sets the dimensionality of the atomic dynamics inside of each tube.

As will be discussed in more detail later on, the scaling of the tunneling rate with trap depth is very slow in the case of the retro-reflected lattice. Using large optical powers one can then still suppress tunneling and reach the 1D regime in each tube. In the 3D limit, however, the tubes will no longer be independent due to the onset of tunneling. A

straightforward solution is to increase the spacing  $d$  of the lattice, which quickly suppresses the tunneling as per  $J \sim \exp(-4d/\lambda)/\sqrt{d}$ , and facilitates in-situ imaging of individual sites due to the reduced need for optical resolution [220]. However, this strategy comes at the expense of reduced trapping frequencies, which, as will be detailed below, scale much slower with  $\omega_{\perp} \sim 1/d$ . A decrease of trapping frequency at fixed trap depth also implies that the number of transverse vibrational states per site increases, which makes it more difficult to achieve 1D dynamics along the vertical direction  $z$ . As was already pointed out in sec. 5.2, in order to be quasi-1D along  $z$  the conditions  $\omega_z/\omega_{\perp} \ll 1$  and  $E_{F,z} = N_{\uparrow}\hbar\omega_z \ll \hbar\omega_{\perp}$  as well as  $k_B T \ll \hbar\omega_{\perp}$  must hold. A low value for  $\omega_{\perp}$  thus necessitates to compensate by either reducing the majority population  $N_{\uparrow}$  or the vertical trapping frequency  $\omega_z$ , which can cause SNR issues due to low atom numbers or loss of vertical trapping with respect to gravity. Finding the appropriate set of parameters for  $d$  and  $U_0$  will be the subject of the ensuing section 6.1.2.

The lattice constant can be tuned by bringing the beams to interference under an angle  $\alpha < 180^\circ$ , which results in a larger spacing  $d_{\alpha} > d_0 = \lambda/2$  as will be derived below. Since the light polarization is always transverse with respect to the direction of propagation  $k_i$ , interference will occur only along the axis containing the mutually parallel projections of the two polarization vectors. The mutually orthogonal components, naturally, do not interfere. This situation is illustrated in more detail in fig. 6.1c and d. The wave vectors of the two beams are given by

$$\begin{aligned} \mathbf{k}_1 &= k_{\lambda} \left( \mathbf{e}_x \sin \frac{\alpha}{2} + \mathbf{e}_y \cos \frac{\alpha}{2} \right), \\ \mathbf{k}_2 &= k_{\lambda} \left( \mathbf{e}_y \cos \frac{\alpha}{2} - \mathbf{e}_x \sin \frac{\alpha}{2} \right), \end{aligned}$$

where  $k_{\lambda} = 2\pi/\lambda$ . We are interested in the intensity modulation along the  $x$  axis, which can be calculated via the square modulus of the total electric field:

$$I_{\alpha}(x) = I_0 \left| e^{ik_1 r} + e^{ik_2 r} \right|^2 = 2I_0 (1 + \cos(\Delta \mathbf{k} \mathbf{r})), \quad (6.2)$$

with  $\Delta \mathbf{k} \mathbf{r} = 2k_{\lambda} \sin(\alpha/2)x$ . The corresponding AC Stark shift is given via the polarizability of the atoms as per  $U(x) = \Re[\alpha_{\lambda}] I(y, z)/(2\epsilon_0 c)$ . More importantly, the lattice spacing can be calculated as function of the angle of intersection  $\alpha$  as per

$$d_{\alpha} = \frac{\pi}{k_{\lambda} \sin(\alpha/2)}, \quad (6.3)$$

which takes on the usual value of  $d_0 = \pi k_{\lambda} = \lambda/2$  for a retro-reflected lattice where  $\alpha = 180^\circ$ . The trapping frequencies at the individual sites as a function of  $\alpha$  can be found

by applying a series expansion up to second order to the antinodes of the potential (6.2):

$$U_\alpha(0) + U'_\alpha(0)x + U''_\alpha(0)x^2 + \mathcal{O}(x^3) \simeq U_\alpha(0) + \frac{1}{2}m\omega_\alpha^2 x^2.$$

One then readily finds the non-angular oscillation frequencies,

$$\nu_\alpha = \sqrt{\frac{2|U_0|}{m} \frac{1}{d_\alpha}} = \frac{h}{md_0} \sqrt{\frac{|U_0|}{E_r} \frac{1}{d_\alpha}}. \quad (6.4)$$

For a given trap depth or optical power, the angle  $\alpha$  will define both the maximum transverse trapping frequency  $\omega_\perp = 2\pi\nu_\alpha$  and to which degree tunneling plays a role. In order to make a sensible choice, the resulting band structure has to be calculated in order to determine the exact value of  $J_\alpha$ .

### 6.1.2. Tuning the dimensionality of the atomic dynamics

In order to calculate the nearest neighbor tunneling rates between the lattice sites (tubes), one has to solve the Schrödinger equation describing the underlying two-dimensional periodic potential. However, since the tube lattice is made up of two independent lattices, one can treat them separately and restrict the calculation to the one-dimensional Hamiltonian  $\hat{H}\phi_n(x) = E_n\phi_n(x)$  with  $U(x) = U(x + nd)$  with  $n \in \mathbb{Z}$ . In general, the eigenstates correspond to functions  $\phi_q^n(x)$  characterized by a discrete band index  $n$  and quasi-momentum  $q$  [221]. These eigenstates can be determined by using the Bloch theorem's well-known Ansatz,

$$\phi_q^n(x) = e^{iqx} u_q^n(x) \quad \text{with} \quad u_q^n(x) = u_q^n(x + nd),$$

with which one then readily finds the modified Schrödinger equation for the Bloch states  $u_q^n(x)$ :

$$\hat{H}_b u_q^n(x) = E_\alpha^n(q) u_q^n(x) \quad , \quad \hat{H} = \frac{\hbar^2}{2m} \left( -i \frac{d}{dx} + q \right)^2 + U_\alpha(x).$$

Considering that  $u(x)$  and the potential  $U_\alpha(x)$  are both periodic functions of the lattice constant, we can expand them into Fourier series:

$$u_q^n(x) = \sum_i c_i^n(q) e^{i2\pi i x/d} \quad , \quad U_\alpha(x) = \sum_j d_j e^{i2\pi j x/d}.$$

Since  $U_\alpha(x) = 2U_0 (1 + \cos(2\pi x/d_\alpha))$  holds, the latter expansion must have only three contributing terms with  $d_0 = 2U_0$ ,  $d_1 = U_0$  and  $d_{-1} = U_0$ . In combination with the above

Schrödinger equation, one finds for the coefficients of the Bloch states:

$$\hat{H}u_q^n(x) = E_\alpha^n(q) \sum_j c_j^n(q) e^{i2\pi jx/d},$$

which can be recast in a more compact form as

$$\sum_i c_i^n(q) H_{ij} = E_\alpha^n(q) c_j^n(q). \quad (6.5)$$

The matrix elements of the Bloch band Hamiltonian as a function of lattice spacing  $d_\alpha$  and potential depth  $U_0$  are then given by the expression

$$H_{ij} = \begin{cases} (\hbar^2/2m)(2\pi i/d_\alpha + q)^2 + 2U_0, & , i = j \\ U_0 & , |i - j| = 1 \\ 0 & , \text{else} \end{cases} \quad (6.6)$$

which can be rewritten in a more convenient form by renormalizing with the recoil energy  $E_{\text{rec}}$  and the wave vector  $k_d$  of the lattice:

$$\frac{H_{ij}}{E_{\text{rec}}} = \begin{cases} (d_\alpha/d_0)^2(2i + 2q/k_d)^2 + 2U_0/E_{\text{rec}}, & , i = j \\ U_0/E_{\text{rec}} & , |i - j| = 1 \\ 0 & , \text{else} \end{cases} \quad (6.7)$$

After diagonalization of the above Hamiltonian, the nearest neighbor tunneling rate in the tight binding limit is given via the bandwidth  $\Delta E_\alpha^1$  of the lowest Bloch band  $E_\alpha^1(q)$  as per

$$J_\alpha = \frac{1}{2} \left( \max [E_\alpha^1(q)] - \min [E_\alpha^1(q)] \right), \quad (6.8)$$

where  $\max [E_\alpha^1(q)] = E_\alpha^1(q = \pm k_d/2)$  and  $\min [E_\alpha^1(q)] = E_\alpha^1(q = 0)$  are the eigenenergies at the edge and center of the first Brillouin zone, respectively. As was mentioned earlier, when superimposing in an incoherent fashion two optical lattices along  $x$  and  $y$  to form the tube lattice, one will, correspondingly, end up with two independent tunneling rates  $(J_{x,\alpha_x}, J_{y,\alpha_y})$ .

The aim is now to find a configuration in which the atomic dynamics of each site are independent, which requires the suppression of tunneling between the tubes over long timescales  $\hbar/J_{k,\alpha} \rightarrow \infty$ . A related, but more intuitive, quantity to address this issue is the effective mass  $m^*$ . Within classical band theory, the dynamics of (non-interacting) electrons in solids can be described in a semi-classical fashion by considering the change of the group velocity  $v_g(q) = (dE/dq)/\hbar$  under the action of an external force and comparing the result to Newton's equation of motion [8]. One then finds a formally equivalent

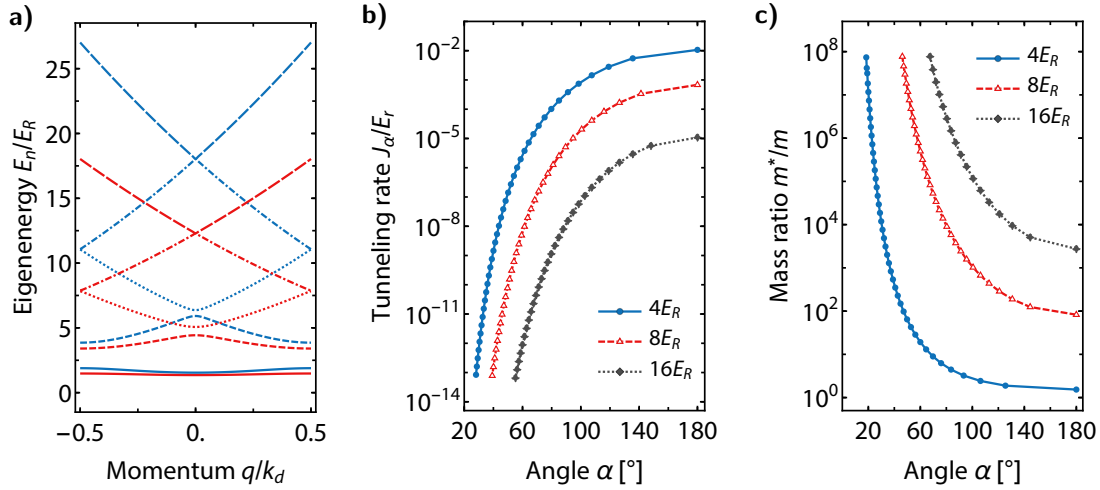


**Figure 6.2.: Bandstructure, tunneling rates and effective mass of a large spacing 1D optical lattice.** a) Eigenenergies of the first five bands  $n = \{1, \dots, 5\}$  for  $d_0/d_\alpha = 1, 0.8$  (blue and red lines, respectively). Note that  $q$  is renormalized by  $k_d$ . b) Tunneling rates  $J_\alpha$  as function of the angle of intersection  $\alpha = 2 \arcsin(d_0/d_\alpha)$  for different trap depths  $U_0$  given in units of the recoil energy  $E_r$ . The data points are obtained using (6.8) in conjunction with the numerical solutions for the Bloch bands. c) Numerical calculation of  $m^*/m$  as function of the angle of intersection  $\alpha$  for three different trap depths  $U_0$ .

expression, but with a modified mass of the form

$$\frac{1}{m^*} = \frac{1}{\hbar^2} \left( \frac{\partial^2 E_0}{\partial q^2} \right),$$

for which  $m^* = m$  holds in the free-particle limit  $U_0 = 0$ . As the potential becomes deeper, the lowest band  $E_0(q)$  is shifted towards higher energies but also becomes flatter, resulting in a reduced group velocity and band curvature. Consequently, the effective mass increases accordingly, which reflects the fact that trapped particles are less likely to move about the lattice and respond less strong a external forces. For our purpose, we can thus compare the effective mass at the center of the lowest band as a function of  $\alpha$  to the bare mass of  $^{40}\text{K}$ . We are interested in the limit where the effective mass of the transverse dynamics becomes infinite, i.e.  $m^*(q=0)/m \rightarrow \infty$  implying that the dispersion relation of the lattice is flat in comparison to the vertical direction. In dimensionless units, the corresponding ratio is given by

$$\frac{m^*}{m} = 8 \left( \frac{d_0}{d} \right)^2 \left( \frac{\partial^2 E_0(k_d \tilde{q})}{\partial \tilde{q}^2} \right)_{\tilde{q}=0}^{-1} \quad (6.9)$$

Using (6.7) the bandstructure  $E_\alpha^n(q)$ , and hence  $J$  and  $m^*$ , can be calculated by solving the eigenvalue problem numerically using a truncated basis  $|i| \leq i_{\max}$ . The precision of

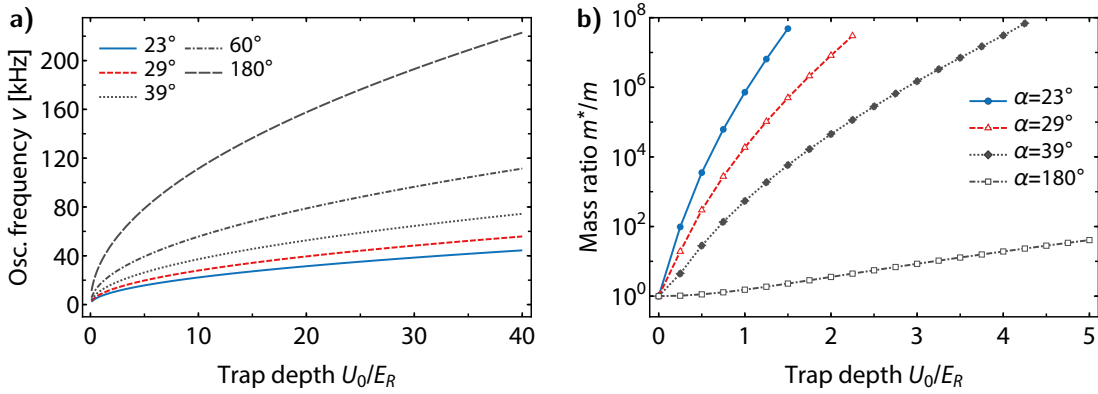


**Figure 6.3.: Scaling of the effective mass and trapping frequency of a large-spacing optical lattice.** a) Tuning of the dimensionality of the dynamics via the single beam trap depth for the range of ideal angles between  $20^\circ$  and  $30^\circ$ . The curve corresponding to  $\alpha = 180^\circ$  is drawn for reference. b) Harmonic oscillation frequencies  $\nu_\alpha$  vs.  $U_0$  for various values of  $\alpha$ .

the calculated tunneling rate is directly linked to the chosen cutoff for a given trap depth  $U_0$ . The deeper the trap, the higher the cutoff that needs to be set. Fig. 6.2 depicts the results for various choices of the angle of intersection as parametrized by  $d_0/d_\alpha$ , with  $d_0/d_\alpha = 1$  corresponding to the ordinary retro-reflected configuration  $\alpha = 180^\circ$ . Since the size of the first Brillouin zone increases with  $d_\alpha$ , the bands are plotted for the normalized quasi-momentum  $q/k_d$ .

The scaling of the tunneling probability between neighboring lattice sites with the angle of intersection  $\alpha$  is shown in fig. 6.2b for various trap depths. For a given single beam potential depth  $U_0$ , the corresponding hopping rate decreases as the lattice spacing becomes larger with  $d_\alpha \sim 1/\sin(\alpha/2)$ . Already for a modest trap depth of  $U_0 = 4E_{\text{rec}}$ , the corresponding energy scale for nearest neighbor hopping is reduced by more than ten orders of magnitude when going from the retro-reflected configuration to  $\alpha = 30^\circ$ .

The numerical calculation of the ratio  $m_\alpha^*/m$  is shown in figs. 6.2c and 6.3b for different angles and trap depths, respectively. In general, the dynamics start to slowly freeze out as the lattice depth increases and, more importantly, becomes increasingly suppressed as  $\alpha$  is decreased. For conservative values of the trap depths of  $U_0 = 1E_R$  one already obtains that  $m_\alpha^*/m > 10^7$  when the angle of intersection is chosen smaller than  $30^\circ$ . However, intersecting two beams under a small angle in a well-controlled way becomes more challenging from a technical point of view the smaller one sets the angle. Therefore, the ideal parameter range for  $\alpha$  is then given between  $20^\circ$  and  $30^\circ$ . In 6.3b the scaling of the effective mass with optical power is shown for this selection of angles. As expected, all of the curves converge at  $m_\alpha^*/m = 1$  when the trap depth becomes zero. In stark contrast to the retro-reflected case, this range of angles enables the tuning of the ratio  $m^*/m$  over eight orders of magnitude already by increasing  $U_0$  to a mere  $3E_R$  while loosing only a

factor of roughly 5 in terms of oscillation frequency (see fig. 6.3a).

Experimentally, with a waist of  $250\ \mu\text{m}$  and a reasonable optical power of  $6\ \text{W}$  one can already achieve single beam trap depths of  $U_{0,\text{max}} \simeq 33E_R$  for  $^{40}\text{K}$ . This corresponds to a maximum transverse trapping frequency of  $\omega = 2\pi \times 44\ \text{kHz}$  for  $\alpha = 25^\circ$ . As four beams are needed to generate the tube lattice, a total initial power of  $\sim 40 - 50\ \text{W}$  will thus be required on the side of the laser setup since one typically loses  $\sim 40 - 50\%$  on the way to the atoms due to limited diffraction efficiencies of high power AOMs and fiber couplings. Note that a single laser source is preferable in order to ensure high levels of phase-coherence between the interfering beams. The laser setup as well as the optical systems on top of the science cell to generate the lattice will be described in sec. 6.2.1 and 6.2.2, respectively. Finally, the degree to which the sites are quasi-1D involves the axial trapping frequency  $\omega_z$ , which will be discussed in sec. 6.2.7.

Another important consequence arising from the choice of  $\alpha$  concerns the optical imaging system to be used to resolve the individual tubes. As was hinted on earlier, a larger value of  $d_\alpha$  is beneficial since it reduces the required optical resolving power. With  $\alpha = 25^\circ$  and  $\lambda = 1064\ \text{nm}$  we obtain a spacing of  $d \simeq 2.5\ \mu\text{m}$ . Using Rayleigh's criterion [222] the minimum numerical aperture necessary to resolve this length scale corresponds to  $\text{NA}_{\text{min}} = 0.61\lambda_{\text{D2}}/d_\alpha = 0.19$ . This level of performance is still within the capabilities of standard optics, as will be described in greater detail in sec. 6.2.4. For comparison, in the retro-reflected case one would have  $d \simeq 0.53\ \mu\text{m}$  and thus a minimum resolution of  $\text{NA}_{\text{min}} = 0.88$ ! From a mere technical point of view, achieving this level of resolution is challenging and not realistic given the geometrical constraints of the FerMix experiment.

## 6.2. Preparation and detection of a single row of tubes

Over the course of the previous section we have identified the physical parameters to facilitate the study of 3D-1D crossovers in an optical tube lattice. In the following, the technical realization of the suitable experimental platform will be described in detail. This includes the laser- and optical setup to generate the large spacing 2D optical lattice as well as the imaging system to resolve the tubes. Moreover, we will elaborate on the implementation of spin selective imaging at high magnetic fields as well as on the related spatially resolved optical pumping to isolate a single row of tubes. Finally, the means devised to compensate gravity and to provide axial confinement along the vertical axis of the lattice will be presented.

### 6.2.1. High power laser system

As was discussed previously in sec. 6.1.2, the generation of a tube lattice with four beams intersecting at  $25^\circ$  requires total optical powers in excess of  $40\ \text{W}$  (at  $\lambda = 1064\ \text{nm}$ )

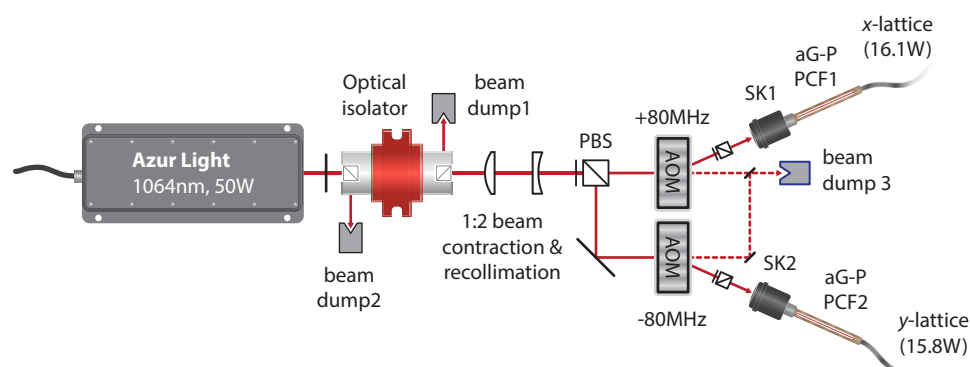


**Figure 6.4.: Schematic overview of the high power IR laser system.** The laser head’s output of 50 W at a wavelength of 1064 nm is split via a PBS and coupled into two high power optical fibers via acousto-optical modulators with high damage thresholds. The light intensity after the cleaning fibers is controlled with a PID circuit, which provides feedback to the RF power of the AOMs (see. sec. 2.11.2). Excess heat is removed from the setup via water cooled beam dumps. Laser: single frequency Yb<sup>3+</sup> fiber laser amplifier (Azurlight Systems ALS-IR-AMP 1064 nm 50 W), Optical isolator: EOT Tech, AOM: Gooch & Housego 3110-197, SK1/2: fiber collimator  $f = 11$  mm (Schäfter-Kirchoff 60FC-SMA-T-23-A11-03), aG-P PCF: broadband single mode photonic crystal fiber (NKT Photonics aeroGuide Power-15-PM), beam dump 3: water cooled beam dump (Eksma Optics 990-0820).

provided by a single laser source. To that end we are using an Yb<sup>3+</sup> fiber laser amplifier by Azurlight Systems, which offers high optical output powers at low RIN performance and spectral linewidth. A schematic overview of the laser setup is depicted in fig. 6.4. The output of up to 45 W of the ALS laser head is passed through a high power optical isolator that protects the fibered amplification stage from harmful back reflections. Afterwards the beam is de-magnified and re-collimated<sup>1</sup> by a 1:2 telescope, which optimizes the mode matching with the ensuing acousto-optical modulators and, by extension, the diffraction efficiency. After being split into two beams corresponding to the x- and y lattice, respectively, the light is coupled into high power optical fibers via large aperture beam collimators. At the outputs of the respective fibers, both axes have maximum optical powers in excess of 15 W.

The intensity stabilization is analogous to the one used for the main dipole trap of the experiment, which was already described in sec. 2.11.2. Technical details regarding the custom electronics used to drive the AOMs can be found in appendix B.4.3.

### 6.2.2. Generation of the tube lattice

To generate the two dimensional tube lattice, a total of four beams are brought to intersection at the position of the atoms under a full angle of 23°-30°. To realize experimentally

<sup>1</sup>The output mode of the ALS laser head is by design slightly converging.

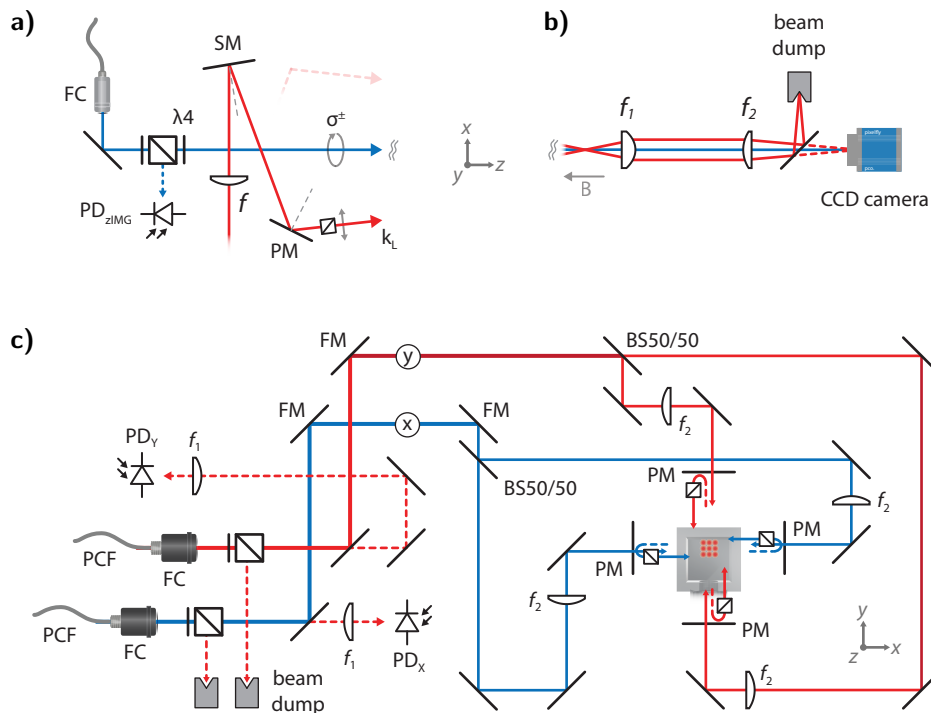


**Figure 6.5.: Optical setup to project the lattice onto the atoms.** a) Vertical cross section of the beam geometry of one lattice axis and the  $z$ -imaging/optical pumping. b) Imaging stage after passage through the science cell. c) Top view of the entire lattice setup mounted on a custom breadboard (not shown here) located above the science cell. Four narrow, slot-shaped openings allow the lattice beams to pass through the breadboard under various angles and facilitate alignment. A larger opening at the center gives direct vertical access to the atoms, which is used for imaging and optical pumping. SK: fiber collimator  $f = 7.5$  mm (Schäfer-Kirchoff 60FC-SMA-T-23-A7.5-03), aG-P PCF: broadband single mode photonic crystal fiber (NKT Photonics aeroGuide power), BS80/50: non-polarizing beam splitter cube, PM: precision motorized Piezo mirror mount (Newport Picomotor 8816-6), LRO VAR2-R1064-PCX-25.4U-400.

the entire range of lattice depths and tunneling rates calculated earlier, each beam has a waist of  $250 \mu\text{m}$  and a maximum optical power of  $8 \text{ W}$ . The optical setup used to generate the beams and redirect them vertically towards the atoms is depicted in fig. 6.5. It is assembled on a custom breadboard mounted at a specific distance above the science cell, which was chosen to use as little optical access as necessary and at the same time prevent the occurrence of optically undesirable angles.

The outputs of the two high power fibers arriving from the ALS laser setup ( $x$ - and  $y$ -lattice) are divided by high power non-polarizing plate beam splitters and guided to the cross-shaped opening of the breadboard located above the science cell. In order to direct the beams downwards, the cross shaped mirror geometry shown in fig. 6.5a is used, which keeps the reflection angles off mirrors below  $45^\circ$ . The final inclination of the lattice beams

can be controlled individually via piezo mirror mounts. Additional PBS cleaning cubes are mounted on the bottom of the breadboard to restore horizontal polarization of the light, which might have picked up vertical or circular components due to the preceding oblique reflection angles.

After passing through the science cell the lattice beams are captured by the z-axis imaging system (see fig. 6.5b), from which they are extracted and dumped by a reflective dichroic element. The small portion transmitted through the dichroic gets imaged onto the CCD camera and can be used to check the alignment of the lattice with respect to the atoms since all beams have to overlap perfectly in the object plane. The calibration of the angle of intersection is performed via matter-wave diffraction in the Bragg- or Kapitza-Dirac limit, the experimental procedure of which is described in greater detail in the following sec. 6.2.3.

The lattice breadboard is also used to deliver circularly polarized imaging- and optical pumping light with respect to the quantization axis  $z$ . The optical components are depicted in fig. 6.2.3a. Depending on whether one works with positive or negative Zeeman states, the polarization of the light can be tuned between  $\sigma^+$  and  $\sigma^-$  using a  $\lambda/4$  waveplate.

### 6.2.3. Calibration of the lattice spacing via matter wave diffraction

The precise alignment of the four beams is essential to guarantee that a homogeneous lattice potential is formed at the center of the partaking Gaussian beams. As will be detailed in the next section, along the transport direction  $y$  the lattice can be imaged directly by using a site-resolved imaging system in combination with a highly sensitive CCD camera. However, this gives only access to the lattice formed along  $x$ . The vertical axis  $z$  does in principle give access to both degrees of freedom, however it can only be used to confirm that the laser beams overlap in the focal place due to limited optical resolution, as was detailed in the previous section.

Another way to measure the lattice spacing  $d_\alpha$  is by taking advantage of matter-wave interference created by the periodic potential [223]. In essence, the optical standing wave can act as a diffraction grating if it is pulsed on for a short time. The implied non-adiabatic nature of this process will cause atoms to be projected onto higher momentum states, the population of which will depend on the area of the pulse [224]. Afterwards, the atoms are left to expand freely resulting in characteristic types of interference patterns, which can be either given by Kapitza-Dirac- (Raman-Nath-) [225] or Bragg scattering [226]. The main difference between these two limits is the number of populated momentum states. For the former, one generally works with short pulses<sup>2</sup> (i.e. with a large Fourier-width) and thus observes a large number of symmetric interference orders while for the latter, only one non-zero order is populated. An equivalent way of putting this is that Bragg scattering

<sup>2</sup>Whether the duration is short or long depends also on the pulse area.

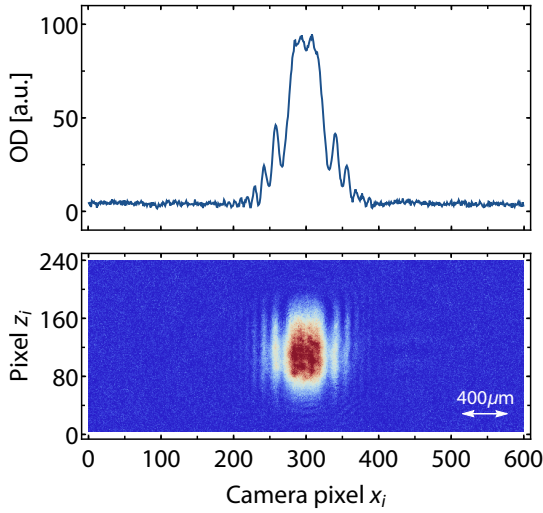


**Figure 6.6.: Matter-wave diffraction pattern created by one optical lattice.** After evaporation of a positive state mixture in the crossed optical dipole trap, the lattice was pulsed on before letting the atoms expand freely for 6 ms. In stark contrast to BECs that have only one initially populated momentum state, Fermi gases tend to be larger and consequently the observation of clear signatures of matter-wave interference is more challenging. The pattern seen here is reminiscent of a Kapitza-Dirac type interference structure.

occurs when the optical grating is thin while Kapitza-Dirac scattering occurs when the grating is thick [227].

Atoms pick up momentum in units of  $2\hbar k_d$  via 2-photon Raman coupling, during which they undergo absorption and stimulated emission between the two travelling waves of the lattice. An example of a measurement of the  $y$ -lattice spacing is shown in fig. 6.6. Here, multiple orders were populated after one of the lattices was pulsed onto the atoms after evaporation in the crossed optical dipole trap. During time-of-flight of duration  $\tau$  atoms of a certain momentum class will cover a certain distance, with the spacing between two interference orders  $n_1$  and  $n_2$  being given by  $\Delta y / \Delta n = 2\hbar k_d \times \tau / m$ . One can thus infer the angle of intersection  $\alpha$  of the lattice from the observed distance between neighboring peaks as per  $\alpha = 2 \arcsin(\Delta y \times d_0 m / 2h\tau)$ . For the measurement shown here, we find  $\alpha = 28.8^\circ$  corresponding to a lattice spacing of  $d_y = 2.14 \mu\text{m}$ . This result matches well the expected value based on the purley geometric prealignment of the lattice beams.

#### 6.2.4. Site-resolved imaging system

The tube-shaped microtraps represent *mutually independent* many-body ensembles. Therefore, site-resolved imaging is required in order to access their thermodynamic quantities via in-situ density distributions or for momentum refocusing (see sec. 5.4 for details). The resolution of the imaging system as well as its overall sensitivity must be sufficiently high to resolve the elongated lattice sites. Taking for example the aforementioned angle of intersection of  $28.8^\circ$ , the lattice will have a spacing of  $2.14 \mu\text{m}$ . To be able to resolve this length scale, the imaging system shown in 6.7 was installed along the transport axis of the experiment ( $y$ -axis, see also fig. 2.12). The lens system is made up of two telescopes in 8-f configuration which have magnifications of  $M_1 = 5$  and  $M_2 = 3.75$ . After having passed through the atoms (object plane, OP), the modulated absorption light is imaged by the

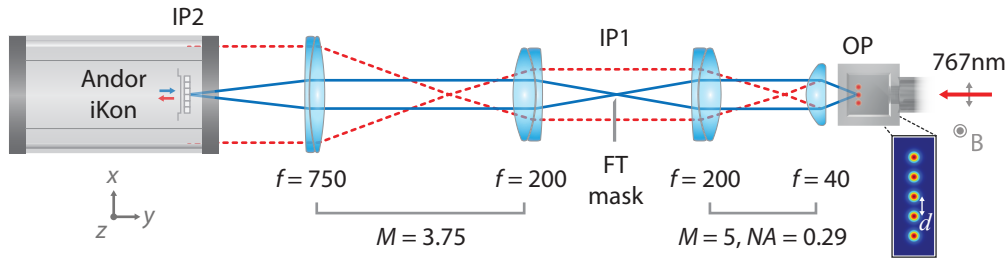


**Figure 6.7.: High resolution imaging system.** The two telescopes with total magnification of  $M = 18.75$  are arranged in  $8f$ -configuration in order to image sharply both the imaging light as well as the ‘shadow field’. The probe light at  $\lambda_{D2} = 767$  nm is sent along the transport tube of the vacuum assembly and consists of  $\sigma^+$  and  $\sigma^-$  polarization with respect to the quantization axis. Optical components: Asphericon AFL-25-40-B, 2x Edmund Optics 50x200 VIS-MIR 200mm, Thorlabs AC508-750-B-ML 750mm; Camera: Andor iKon-M 934.

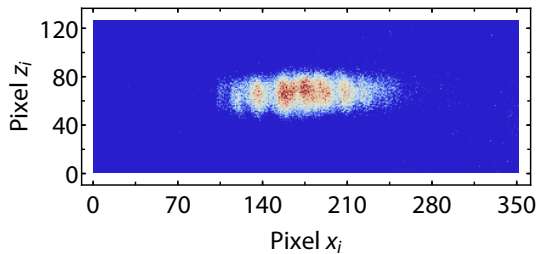


**Figure 6.8.: First signature of the x-lattice.** A positive state mixture close to the degenerate regime is held in the cODT after evaporation. Prior to absorption imaging, the  $x$ -lattice was ramped up on top of the cODT and left on until the end of the ensuing short time-of-flight.

first  $4f$ -telescope onto the conjugated image plane (IP1), where a frame transfer mask can be installed later on. This intermediate image is then processed by the second  $4f$ -telescope, which creates the final,  $19\times$ enlarged image in the plane of the camera’s CCD chip (IP2). The most crucial first element of the imaging is an aspheric lens with a numerical aperture of  $NA = 0.29$ . It is placed in close proximity to the science cell, having a short effective focal length of 40 mm. Given the geometrical constraints of the surrounding coils and the dimensions of the glass cell, achieving a higher NA along this direction is challenging since optical elements can at most have a diameter of 25 mm. The second lens is an achromatic doublet with a focal length of 200 mm, which, together with the asphere, reduces the amount of spherical aberrations. As of the focal plane of the asphere the imaging light expands very quickly as it propagates along the  $y$ -axis. While the surrounding tube is large enough to preclude clipping and thus loss of information, the ensuing achromat was chosen to be large with a diameter of 50 mm to reduce imaging aberrations. The expected resolving power of the complete imaging setup was verified prior to installation using a 1951-USAF resolution target.

In practice the fidelity of the absorption images are oftentimes compromised by temporal fluctuations of the imaging light’s intensity and frequency. In addition, interference between optical elements of the imaging system is usually present and introduces fringes

into the images, the structure of which can also vary slightly over time. One main source of interference is the CCD chip of the camera itself, because it can act as an etalon. To detect (very) low atom numbers the camera has to distinguish small differences between  $I_{\text{abs}}$  and  $I_{\text{ref}}$ , assuming the absence of other fluctuations. This is a concern, especially in the case of imaging systems with high magnification which decrease the SNR further.<sup>3</sup> To address these problems for the lattice imaging system, we use an Andor iKon-M 934 as camera, which has high quantum efficiencies at 767 nm of roughly 95 % and extremely low levels of (readout-) noise.<sup>4</sup> Etaloning of the CCD chip is reduced by means of a specialized AR coating for the NIR spectral range and the problem of unstable imaging light intensity can be addressed by taking advantage of the camera's frame-transfer functionality ('Fast kinetics').

One of the first images showing a modulation effect of the  $x$ -lattice taken with the complete imaging system is shown in 6.8. So far, all of the tests have been performed using the positive Zeeman states at low magnetic fields held in a crossed dipole trap to hold the atoms against gravity. In the following, we will describe the corresponding imaging scheme for negative states (see 2.11.3) at high magnetic fields and how to isolate a single row of tubes at the focal plane of the object lens. Afterwards, the techniques for gravity compensation and momentum refocusing will be described.

### 6.2.5. Spin selective imaging at high magnetic fields

At magnetic fields of about 200 G - 230 G, the Zeeman splitting in the ground state of  $^{40}\text{K}$  is sufficiently large with respect to the natural linewidth to allow for spin-selective imaging. However, owing to the decoupling of the electronic and nuclear angular momenta at high magnetic fields, the total angular momentum  $\hat{F}$  does no longer represents a good quantum number. The approximate level structure at 230 G is shown in fig. 6.9.

In the Paschen-Back limit ( $B \rightarrow \infty$ ) the lowest energy levels of the ground state are  $|1\rangle = |m_I = -4, m_J = -1/2\rangle$  (stretched state),  $|2\rangle = |-3, -1/2\rangle$  and  $|3\rangle = |-2, -1/2\rangle$ , which adiabatically connect to the Zeeman levels  $|m_F = -9/2\rangle$ ,  $|-7/2\rangle$  and  $|-5/2\rangle$ , respectively, as  $B \rightarrow 0$ . The natural choices for the imaging transitions along the D2 line correspond to the target states  $|1'\rangle = |-4, -3/2\rangle$  (stretched state),  $|2'\rangle = |-3, -3/2\rangle$  and  $|3'\rangle = |-2, -3/2\rangle$ , which correspond to the three lowest lying states in the  $F = 11/2$  manifold of  $4^2P_{3/2}$  at low magnetic fields. The selection rules at high magnetic fields for electric dipole

<sup>3</sup>One could counteract this issue by increasing the imaging light's intensity or its exposure time to scatter more photons. However, this solution causes other detrimental effects such as Doppler-shifts and non-zero acceleration due to radiation pressure, because the imaging no longer takes place in the low-saturation limit.

<sup>4</sup>For comparison, the standard PixelFly QE cameras used otherwise are only in excess of 25 %, which essentially amounts to losing about 75 % of the atomic signal!

transitions are given by

$$\Delta J = 0, \pm 1, \Delta L = \pm 1, \Delta m_J = 0, \pm 1, \Delta m_I = 0. \quad (6.10)$$

Therefore, for the transitions between the intended pairs of states left-handed circular polarization carrying angular momentum  $-\hbar$  is required as one needs to change the total electronic angular momentum projection  $J_z$  from  $m_J = -1/2$  to  $m'_J = -3/2$ . As was mentioned earlier, the imaging light to perform absorption imaging on the lattice tubes must propagate orthogonally with respect to the quantization axis (see sec. 6.7), which means that it is in principle capable of driving all types of electronic transitions with  $\Delta m_J = 0$  ( $\pi$ ) and  $\Delta m_J = \pm 1$  ( $\sigma^\pm$ ) at the same time. This can be understood by decomposing the polarization vector of the electric field into the spherical basis. Moreover, the energy splitting between the target states amounts to only  $\sim 11$  MHz, which is less than twice the natural line width. Such narrow energy splittings immediately preclude the energetic isolation of the lines. At low magnetic fields, one would have to use pure  $\sigma^-$  polarization to drive the above transitions without exciting along  $\pi$  or  $\sigma^+$  channels (the role of subsequent spontaneous decay will be discussed further below), which is not possible for our imaging light configuration as it cannot be sent along the quantization axis if the tubes are to be imaged along their radial direction. However, at high magnetic fields the situation is rather different since the electric dipole interaction, while changing the parity of the orbital wavefunction and hence  $m_J$ , cannot alter the nuclear spin  $m_I$ . As is shown in fig. 6.9, the other excited states with  $m'_J = \pm 1/2$  are energetically well separated from the targeted ones with  $m'_J = -3/2$  and  $m'_I = -4, -3, -2$ , which means that imaging light of mixed polarization will only be resonant with its  $\sigma^-$  component. Spontaneous decay back to the ground states can occur along any channel that is allowed according to the selection rules. Given that  $m_I$  needs to be conserved during the decay and since  $m'_J = -3/2$ , the only available decay channels are  $1' \rightarrow 1$ ,  $2' \rightarrow 2$  and  $3' \rightarrow 3$ . By that reason, the three imaging lines cannot mix during excitation or spontaneous decay and therefore can be considered as cycling transitions. However, this picture relies on validity of the notion that the atoms are indeed deep inside the Paschen-Back regime. Any deviation from this limit implies mixing as the transitions become partially open. In the experimental context, this parasitic pumping effect has to be kept small with respect to the number of scattered photons during imaging.

In order to determine to which extent  $^{40}\text{K}$  is affected by this issue around the magnetic fields of interest between 202 G and 230 G, one has to calculate numerically the energy eigenstates of the hyperfine Hamiltonian (see appendix C.4 for additional details) and express them in the  $\{I, m_I; J, m_J\}$  basis. At  $B = 230$  G, the decomposition of the ground

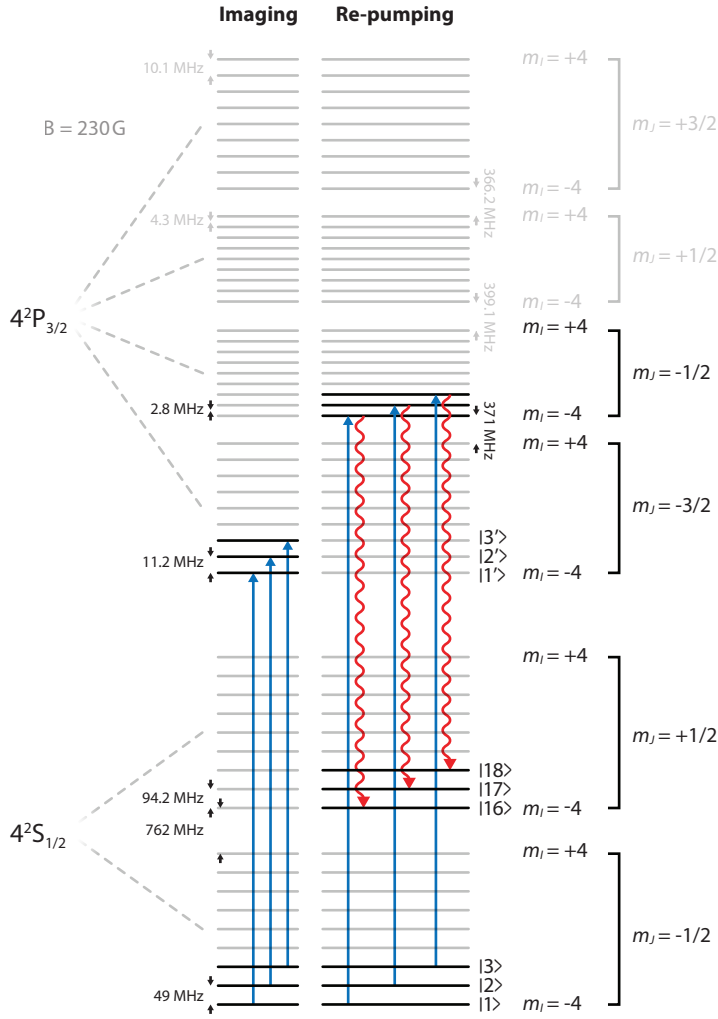


**Figure 6.9.: Level structure of the ground- and second excited state of  $^{40}\text{K}$  in the Paschen-Pack limit.** Left: transition scheme for optical pumping into the upper hyperfine ground states. Right: Cycling transitions used for high-field imaging of the three lowest lying negative spin states. The cycling and spin-selective nature of the imaging process results solely from the conservation of the nuclear spin projection. The indicated splittings are given for a magnetic field of 230 G. Note that for these field strengths the depicted level scheme represents an idealization as the ground state is entering the high-field limit much slower than the D2 excited state  $4^2P_{3/2}$ . Consequently, additional basis states are mixed in and modify the branching ratios of stimulated optical transitions and spontaneous decay.

states reads explicitly

$$|1\rangle = |m_I = -4, m_J = -1/2\rangle = |m_F = -9/2\rangle, \quad (6.11)$$

$$|2\rangle = \sqrt{0.95} |m_I = -3, m_J = -1/2\rangle + \sqrt{0.05} |m_I = -4, m_J = +1/2\rangle, \quad (6.12)$$

$$|3\rangle = \sqrt{0.89} |m_I = -2, m_J = -1/2\rangle + \sqrt{0.11} |m_I = -3, m_J = +1/2\rangle, \quad (6.13)$$

with  $I = 4$ ,  $J = 1/2$  and  $F = 9/2$  at zero field. For the excited states of  $4^2P_{3/2}$  with  $I = 4$  and  $J = 3/2$  ( $F = 11/2$  at zero field) one finds similarly that

$$|1'\rangle = |m_I = -4, m_J = -3/2\rangle = |m_F = -11/2\rangle, \quad (6.14)$$

$$|2'\rangle = \sqrt{0.998} |m_I = -3, m_J = -3/2\rangle + \sqrt{0.002} |m_I = -4, m_J = -1/2\rangle, \quad (6.15)$$

$$|3'\rangle = \sqrt{0.997} |m_I = -2, m_J = -3/2\rangle + \sqrt{0.003} |m_I = -3, m_J = -1/2\rangle. \quad (6.16)$$

Evidently, there is a considerable amount of admixing of additional basis vectors at the magnetic fields of interest, especially in the ground state where the nuclear spin stays coupled to the electronic angular momentum longer than in the excited state. This does have a few important consequences for the experimental implementation of spin selective high field imaging, which become apparent when considering the matrix elements of the dipole operator.

As was detailed earlier, the polarization of the imaging light is always mixed.  $\sigma^-$  polarization is needed to drive the main imaging transitions with  $\Delta m_J = -1$ , and all  $\sigma^+$  lines are energetically suppressed. However, the occurrence of other basis states may enable  $\pi$  components to cause mixing and parasitic pumping to other states because the energy splittings in the excited states are similar to the natural linewidth. When considering the crosswise dipole matrix elements of the states given above, one finds indeed that  $\langle 1|\hat{d}|2'\rangle \sim \langle -1/2|\hat{d}| - 1/2\rangle \neq 0$  and  $\langle 2|\hat{d}|3'\rangle \sim \langle -1/2|\hat{d}| - 1/2\rangle \neq 0$ . While these couplings are small, they should nevertheless be avoided. This can be achieved by ensuring that the imaging light has horizontal polarization, which corresponds to an equal superposition of  $\sigma^+$  and  $\sigma^-$ . Contrarily, in the case of spontaneous emission these two parasitic decay channels cannot be avoided by technical means. As a result, population can in principle decay to the 'wrong' ground state, but the related branching ratios are negligible in view of the fact that the number of scattered photons during imaging is expected to be small.

Spontaneous emission back to the ground states can occur along any path with non-zero matrix elements. To be certain that there are no additional decay channels at 230 G, the basis representation of all ground states has to be considered, which is given in table B.1. While the stretched state  $|1'\rangle$  can only decay back to  $|1\rangle$ , the two states  $|2'\rangle$  and  $|3'\rangle$  do have additional decay channels apart from the ones mentioned so far. They target the two highest energy levels of the upper ground state hyperfine manifold  $m_J = +1/2$ :

$$|18\rangle = a_{18} |-4, +1/2\rangle + b_{18} |-3, -1/2\rangle, \quad (6.17)$$

$$|17\rangle = a_{17} |-3, +1/2\rangle + b_{17} |-2, -1/2\rangle. \quad (6.18)$$

The corresponding transition matrix elements with the excited states are given by

$$\langle 2'|\hat{d}|17\rangle = 0, \quad (6.19)$$

$$\langle 3'|\hat{d}|18\rangle = d_3 b_{18}^* \langle -1/2|\hat{d}| - 1/2\rangle \simeq 0, \quad (6.20)$$

$$\langle 3'|\hat{d}|17\rangle = d_3 a_{18}^* \langle -1/2|\hat{d}| + 1/2\rangle + c_3 b_{18}^* \langle -3/2|\hat{d}| - 1/2\rangle \quad (6.21)$$

$$\simeq 0 + c_3 b_{18}^* \langle -3/2|\hat{d}| - 1/2\rangle, \quad (6.22)$$

$$\langle 2'|\hat{d}|18\rangle = c_2 b_{18}^* \langle -3/2|\hat{d}| - 1/2\rangle. \quad (6.23)$$

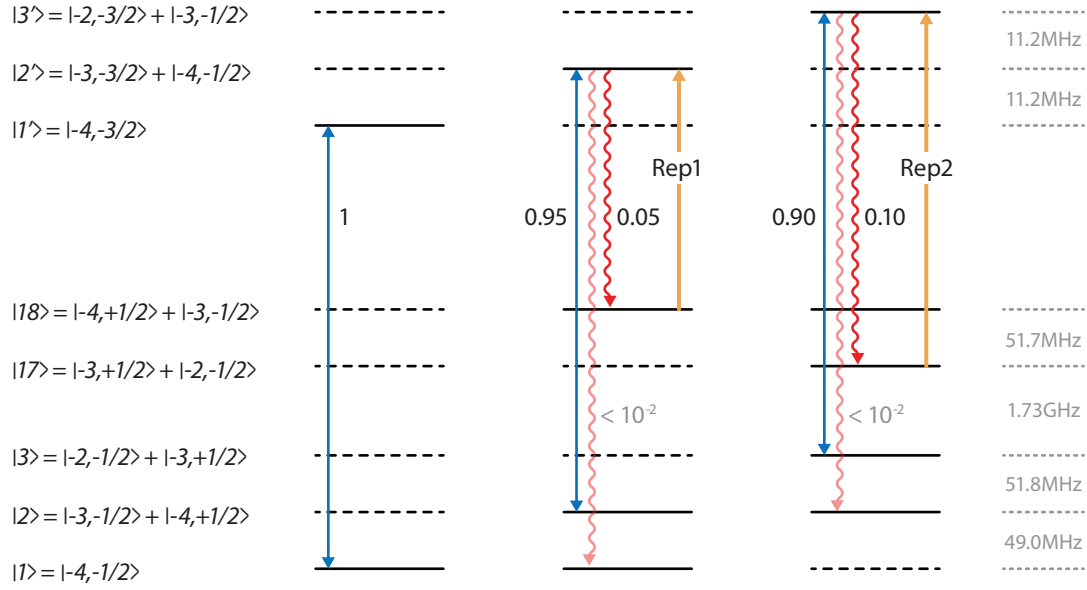


**Figure 6.10.: Branching ratios for spontaneous decay during high-field imaging of  $^{40}\text{K}$ .** The magnetic field is set to the background value of  $B = 230$  G. Note that the exact values of the basis expansion coefficients in  $|1\rangle$ ,  $|2\rangle$ , etc. were omitted here for clarity. They can be found in table B.1 and in equations (6.13) and (6.16).

The two matrix elements  $\langle 3'|\hat{d}|17\rangle$  and  $\langle 2'|\hat{d}|18\rangle$  are not negligible, which is due to the fact that the admixing is more pronounced in the ground state than in the excited state because of the stronger spin-orbit coupling. As a result, already after 10 scattered photons only 50 % of the population will remain in the imaging cycle  $2 \leftrightarrow 2'$  and in the case of  $3 \leftrightarrow 3'$  this number decreases to 30 %. An overview of the relevant branching ratios is shown in fig. 6.10. Consequently, an additional bichromatic repumper with  $\sigma^-$  polarization has to be shone in along the quantization axis to return the population accumulating in these states to their respective imaging cycles. The laser systems generating the light for high-field imaging were already described in sec. 2.3.

### 6.2.6. Isolation of a single row of tubes

Due to the absence of tunneling, the individual tubes of the 2D lattice represent independent thermodynamical systems whose parameters will vary across the lattice. For example,  $T/T_F$  may be very low for a tube located at the center, but a marginal site might be much less degenerate. During imaging one automatically averages over several sites along the line of sight of the imaging system, which can obscure potential physical signatures of interest. Moreover, the imaging system employed to resolve the lattice sites naturally has a very shallow depth of field. This will cause the rows located in front- and behind of the

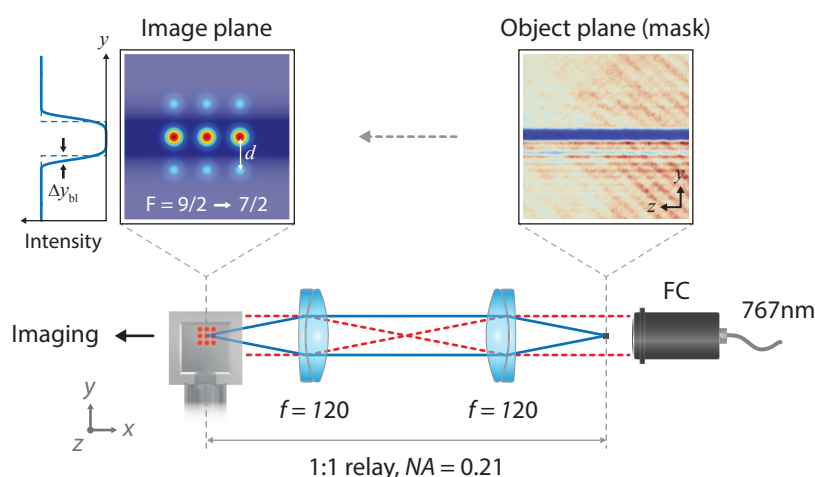


**Figure 6.11.: Optical setup providing spatially modulated optical pumping.** The object plane containing the mask is imaged onto the position of the atoms via a 1:1 telescope that matches the dimensions of the mask to the lattice constant. The alignment of the mask is done with the help of an ancillary imaging system (not shown) on the exit side of the science cell. Left: schematic illustration of the hiding process via optical pumping into dark states; Right: image of the mask taking with a high-resolution test setup.

one at the focal plane to blur as well, and thereby reduce the contrast of the absorption image.

In order to circumvent this problem, a single row of tubes has to be prepared, which is most easily achieved by removing the other ones. As there are no straightforward magnetic means available to isolate one row, the only viable option is to remove the other tubes optically. This can be achieved by pumping the concerned atoms to dark states, rendering them invisible to the imaging light. This approach requires the optical pumping light to be spatially modulated so that it leaves exactly one row of tubes unaffected. Experimentally, this can be implemented by first letting the imaging light pass through a rectangular mask before propagating it to the atoms. This will create a shadow inside of the beam, which needs to be imaged onto the atoms at high resolution to avoid blurring. The concrete optical setup is depicted in fig. 6.11. The optically thick mask is deposited on a transparent glass plate and has a width of  $5\ \mu\text{m}$  corresponding to roughly two lattice constants and a length of  $> 1\ \text{cm}$ . The light's intensity distribution at the position of the mask (object plane) is then imaged by a 1:1 telescope onto the atoms.<sup>5</sup> The relay telescope must have sufficient resolving power since excessive blurring of the mask will cause pumping light to seep into the dark region, which will cause the tube row of interest to become partially transparent to the imaging light. Yet another detrimental effect arising from stray photons incident on the central row is the potential onset of uncontrolled exothermic collisions

<sup>5</sup>Since the mask already has the correct size, no demagnification is needed.

between the ‘good’ atoms in the states  $|1\rangle$ ,  $|2\rangle$  and  $|3\rangle$  with the (parasitically) pumped ones residing in different energy levels of the ground state manifold. The telescope is made up of two 2" achromatic lenses with focal lengths of 120 mm each. The resolution of the imaging system is limited to roughly  $4\ \mu\text{m}$  due to geometrical constraints arising from the science cell coil assembly. Nevertheless, it should provide sufficient sharpness to avoid parasitic optical pumping at the center.

There are several possible choices for the re-pumping transitions. For technical reasons, the ones requiring the least amount of additional energy were chosen. These lines transfer the atoms from the states  $|1\rangle$ ,  $|2\rangle$  and  $|3\rangle$  to the  $m'_J = -1/2$  manifold of  $4^2P_{3/2}$  via  $\pi$ -transitions<sup>6</sup> as is shown in fig. 6.9. From there the atoms can decay spontaneously via  $\sigma^+$  transitions into states of the upper ground state manifold with  $m''_J = +1/2$ :

$$\begin{aligned} |1\rangle &= |-4, -1/2\rangle_{J=1/2} \rightarrow |-4, -1/2\rangle_{J'=3/2} \rightsquigarrow |-4, +1/2\rangle_{J''=1/2} = |16\rangle, \\ |2\rangle &= |-3, -1/2\rangle_{J=1/2} \rightarrow |-3, -1/2\rangle_{J'=3/2} \rightsquigarrow |-3, +1/2\rangle_{J''=1/2} = |17\rangle, \\ |3\rangle &= |-2, -1/2\rangle_{J=1/2} \rightarrow |-2, -1/2\rangle_{J'=3/2} \rightsquigarrow |-2, +1/2\rangle_{J''=1/2} = |18\rangle. \end{aligned}$$

Once an atom populates one of these states, it will no longer be resonant with respect to the imaging light due to the large detuning of several gigahertz.

The optical system generating the required light frequencies was already described in sec. 2.3. At the time this thesis was written, the above re-pumping scheme had already been confirmed to work properly in the experimental context and the imaging system adding the spatially modulated beam profile (fig. 6.11) was in the process of being implemented.

### 6.2.7. Harmonic confinement for momentum refocusing

In order to reconstruct the spectral functions  $A(k, \omega)$  of each tube, their respective momentum distributions need to be determined after performing RF spectroscopy. As was detailed in sec. 5.4, this can be done without the need for long time-of-flight expansion via momentum refocusing. To that end, an additional harmonic potential acting as a matter wave lens along the vertical axis of the tubes is required. Since this potential must not depend on the spin state of the atoms, the use of magnetic curvature is not possible in the case of  $^{40}\text{K}$  (see sec. 6.2.8 for details). This potential will also set the 1D Fermi energy for a given tube, and must therefore be weak with respect to the transverse confinement of the lattice. This condition signifies that the dynamics in a given tube are indeed quasi-1D.

In the following, we will describe how to provide harmonic confinement optically using a  $0/\pi$  phase plate to generate a blue-detuned  $\text{TEM}_{01}$ -like mode.<sup>7</sup> Apart from momentum

<sup>6</sup>The absorption imaging was making use of the energetically lower lying  $m'_J = -3/2$  manifold.

<sup>7</sup>In principle, one could also use a red-detuned optical dipole trap instead of a phase-plate. However, in order to prevent the ODT from competing with the transverse confinement of the lattice, its waist along

refocusing, this trap can also be used to support the atoms against gravity. However, the implied asymmetric deformation of the potential must then be taken into account when inferring the momentum distribution from the spatial density.

### Working principle of a phase step plate

To understand how the targeted modulation of a Gaussian beam's phase can be used to tailor unconventional intensity profiles, it is instructive to recall several basic relations from classical wave optics. The free-space propagation of an electric field  $E(y, z; x)$  along the  $x$  axis can be described for the paraxial case by making use of the Fresnel approximation. The field  $E(y', z'; x')$  at a distance  $x' = x + \Delta x$  is given as the convolution with the impulse response function of free space [228],

$$E(y', z'; x') = \frac{-i}{\lambda \Delta x} \int dy \int dz E(y, z; x) \exp [i\phi_x(y, z, y', z')], \quad (6.24)$$

with

$$\phi_x(y, z, y', z') = -\frac{k}{2\Delta x} \left( (y - y')^2 + (z - z')^2 \right). \quad (6.25)$$

An optical lens imprints a phase on the wavefront, the magnitude of which varies quadratically with the distance to the optical axis as per [228, 229]

$$E_{\text{out}}(y, z; x) = E_{\text{in}}(y, z; x) \exp \left( \frac{ik}{2f} (y^2 + z^2) \right) \quad (6.26)$$

For positive focal lengths  $f$ , this alteration of the phase transforms a plane wave into a spherically converging one. The electric field distribution at the focal plane, i.e. after a propagation distance  $x' = x + f$ , can be calculated using eqn. (6.24):

$$E(\boldsymbol{\rho}'; x') = \frac{1}{\lambda f} \exp \left( -\frac{ik}{2f} \rho'^2 \right) \int dy \int dz E(\boldsymbol{\rho}; x) \exp \left( \frac{ik}{f} \boldsymbol{\rho} \boldsymbol{\rho}' \right). \quad (6.27)$$

Here the abbreviations  $\boldsymbol{\rho} = (y, z)$  and  $\boldsymbol{\rho}' = (y', z')$  for the radial position vectors were used. The above equation embodies the fact that the electric field profile at the focal plane of a lens is proportional to the Fourier transform of the incident field. The emerging pattern can be thought of as the result of the interference of many elementary spherical waves, which carry the local amplitude and phase information of the incoming electric field. Combining these transformation properties of a lens with the ability to alter the phase front of the incoming light field  $E(x; y, z)$  locally form the basis of the beam shaping techniques described in the following.

---

this direction must be kept very large. Especially in the case when one wants to compensate gravity, this scales up the power requirements to unrealistic levels. A TEM<sub>01</sub> mode does not suffer from this problem, so that it can be shaped elliptically which substantially reduces the need for optical power.

In practice one does not work with ideal plane waves, but rather with (elliptical) Gaussian TEM<sub>00</sub> beam modes, which have an electric field (in units of  $\sqrt{W}/\text{m}$ ) of the form

$$E(\boldsymbol{\rho}; x = 0) = \sqrt{\frac{2P}{\pi\omega_y\omega_z}} \exp\left(-\frac{y^2}{\omega_y^2} - \frac{z^2}{\omega_z^2}\right) \quad (6.28)$$

in the plane of the waists  $\omega_y$  and  $\omega_z$ . Note that this beam mode usually carries a phase term that varies along the propagation axis  $x$ . However, for our purposes it can be omitted safely as it does not enter into the final intensity distribution and, consequently, bears no relevance for the resulting optical potential. Gaussian beams propagate through free space and optical elements in a more complicated fashion than plane waves which is due to the finite radius of wavefront curvature  $R$  that only becomes infinite at the waist. When such a beam is subjected to a focusing lens located at its waist, the ensuing focal plane where again  $R = \infty$  will not exactly be located at a distance  $f$  from the lens, but rather at  $f' = f / (1 + (f/z_R)^2)$ . This shift becomes negligible when  $z_R \gg f$  holds, and the incoming Gaussian beam is referred to as quasi-collimated. In this case, the profile of the electric field at the position of the focal plane will correspond to the Fourier transform of the incoming one, which is again a Gaussian beam with rescaled waists and Rayleigh ranges given by

$$\omega'_i = \frac{\lambda f}{\pi\omega_i} \quad \text{with} \quad z'_R = \frac{f^2}{z_R}. \quad (6.29)$$

Now, by deliberately altering the phase of the incoming wavefronts as a function of radial position, the nature of the profile emerging at the focal plane of the lens can be altered dramatically. This can be achieved by employing a transparent diffractive optical element, which is placed at the position of the beam waist (because only here the wavefront is flat) just prior to a converging lens. The parameters are chosen such that the beam can be taken to be quasi-collimated. Depending on where the light passes through it a local phase delay is picked up, the magnitude of which can be manufactured to assume any value between 0 and  $\pi$  radians. This way, a great number of otherwise technically elusive intensity profiles can be created by using complex phase patterns. However, the obtained result is typically only an approximation to the intended, ideal target. In order to provide harmonic confinement along gravity using blue detuned light, a highly anisotropic TEM<sub>01</sub> mode would be an ideal candidate. This mode can be approximated by employing a binary 0- $\pi$  step phase distribution [230, 231], which has a complex transmittance of the form

$$\tau(y, z) = \begin{cases} 1, & z < 0 \\ \exp(-i\pi), & z > 0 \end{cases}, \quad (6.30)$$

as is shown in fig. 6.12a. With an elliptical Gaussian beam as per (6.28) as input, the intensity pattern at the focal plane can be calculated as the modulus of the electric field

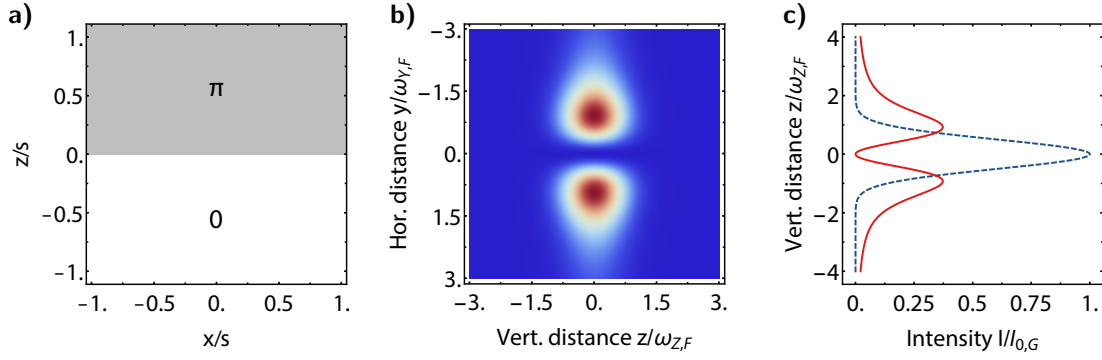


**Figure 6.12.: Generation of harmonic confinement with a step phase plate.** a) Phase distribution of the 0- $\pi$  plate. b) Normalized intensity profiles at the focal plane of the resulting TEM<sub>01</sub>-like mode  $I'(y' = 0, z')$  and of the incoming Gaussian  $I(y' = 0, z)$  when no phase plate is present prior to the FT lens. c) Density plot of  $I'(y', z')$ .

via equation (6.27), yielding

$$I'(y', z') = \frac{2P}{\pi\omega'_y\omega'_z} \operatorname{erfi}\left(\frac{z'}{\omega'_z}\right)^2 \exp\left(-\frac{2y'^2}{\omega_y'^2} - \frac{2z'^2}{\omega_z'^2}\right). \quad (6.31)$$

Here,  $\operatorname{erfi}(z) = -i \operatorname{erf}(iz) \simeq (2/\sqrt{\pi})z + \mathcal{O}(z^3)$  denotes the imaginary error function and the rescaled beam waists are given as per equation (6.29). In essence, one recovers the intensity pattern of a Gaussian beam that has been focused down and modulated by the error function. The latter is an odd in  $z$ , which causes the electric field to vanish near the origin, giving rise to an approximately harmonic intensity distribution:

$$I'(y' = 0, z') \simeq \frac{8P}{\pi^2\omega'_y\omega'_z} \left(\frac{z'}{\omega'_z}\right)^2 \quad \text{if } z' \ll \omega'_z. \quad (6.32)$$

This can be understood as consequence of the fact that due to the phase retardation of exactly  $\pi$  radians, the interference between the two halves of the beam at the origin is going to be destructive [232]. The full intensity profile described by equation (6.31) is plotted in figs. 6.12b and c. As is evident from the above relation, the waist  $\omega'_z$  is the relevant length scale that restricts the region over which the potential can be taken to be harmonic.  $\omega'_y$ , on the other hand, quantifies the rate at which the potential falls off along  $y$  (for  $z \neq 0$ ). Together with the total optical power  $P$ , these three parameters will need to be optimized to match the experimental situation at hand.

### Parameter optimization

The axial harmonic confinement is to be applied to the lattice along  $x$ , which is parallel to the orientation of the single row of tubes and perpendicular to the high resolution imaging

axis. This choice reduces the amount of required optical power and, more importantly, ensures that all tubes within the previously isolated single row are subjected to the same axial trapping potential provided the beam does not diverge too fast, as will be discussed further below. The relevant length scales based on the lattice's geometry, to which the phase plate's potential  $U(x; y, z) = \Re[\alpha_\lambda] I(x; y, z)/2\epsilon_0 c$  will need to be matched, are given by several factors.

First, the range on both sides of the focal plane over which the potential remains nearly constant must be made large with respect to the number of lattice tubes being imaged. This distance is referred to as beam-shaping longitudinal range (BSLR) [233] or, less precisely, as the depth of field (DOF). When considering only small deviations from the focal plane located at  $x' = f$ , we can insert the series expansion  $1/x' = 1/f - \delta x'/f^2 + \dots$  into the propagation integral in (6.24). Together with the phase transformation of the lens, one arrives at a more general form of eqn. (6.27), the norm of which is given by [229]

$$|E(\boldsymbol{\rho}'; \delta x')| = \frac{1}{\lambda f} \left| \int dy \int dz E(\boldsymbol{\rho}; 0) \exp \left( ik \left( \frac{\boldsymbol{\rho}\boldsymbol{\rho}'}{f + \delta x'} + \frac{\rho^2 \delta x'}{2f^2} \right) \right) \right|. \quad (6.33)$$

Second, the radial extension of a tube along  $y$  is not larger than the lattice constant  $d_{\text{lat}} = 2.5 \mu\text{m}$ . At least over this distance the harmonic potential  $U(y, z)$  should not vary too much to guarantee consistent axial trapping frequencies for all atoms, which essentially fixes  $\omega'_y$ . Increasing this size further beyond the bare minimum is advantageous since it minimizes the effect of pointing jitter and increases the depth of field. Third, along the direction of gravity  $U(y, z)$  should be harmonic to within 5% over a spatial extent of  $\Delta z = 200 \mu\text{m}$ , implying that  $\omega'_y$  will most likely have to be much larger. If the potential has to support the atoms against gravity as well, a compromise needs to be found between the harmonicity along  $z$ , the flatness along  $y$  and the available optical power  $P$ . For this worst-case scenario, we take as starting parameters for the optimization:  $\omega'_y = 2d_{\text{lat}}$ ,  $\omega'_z = \Delta z$  and  $P = P_{\text{max}} = 5 \text{ W}$ . Given its small size,  $\omega'_y$  should not be reduced further to avoid technical complications<sup>8</sup>, leaving  $\omega'_z$  as the main tuning parameter. A summary of the results is given in 6.13.

The situation can be relaxed significantly if the the gravitational field does not have to be compensated by the phase plate's potential. Choosing less stringent and more favorable starting parameters,  $\omega'_y = 10d_{\text{lat}}$ ,  $\omega'_z = \Delta z$  and  $P = 0.4P_{\text{max}} = 2 \text{ W}$ , one finds the optimization curves shown in figure 6.14. In the ensuing section, we will elaborate on how gravity can be canceled using an optical gradient field created by a spatial light modulator. While the simultaneous implementation of both and the phase plate and the gradient potential is technically more cumbersome, it greatly enhances the flexibility one

<sup>8</sup>Apart from pointing instability, such a small waist already implies a very shallow depth of field along  $x$  and is challenging to realize experimentally.

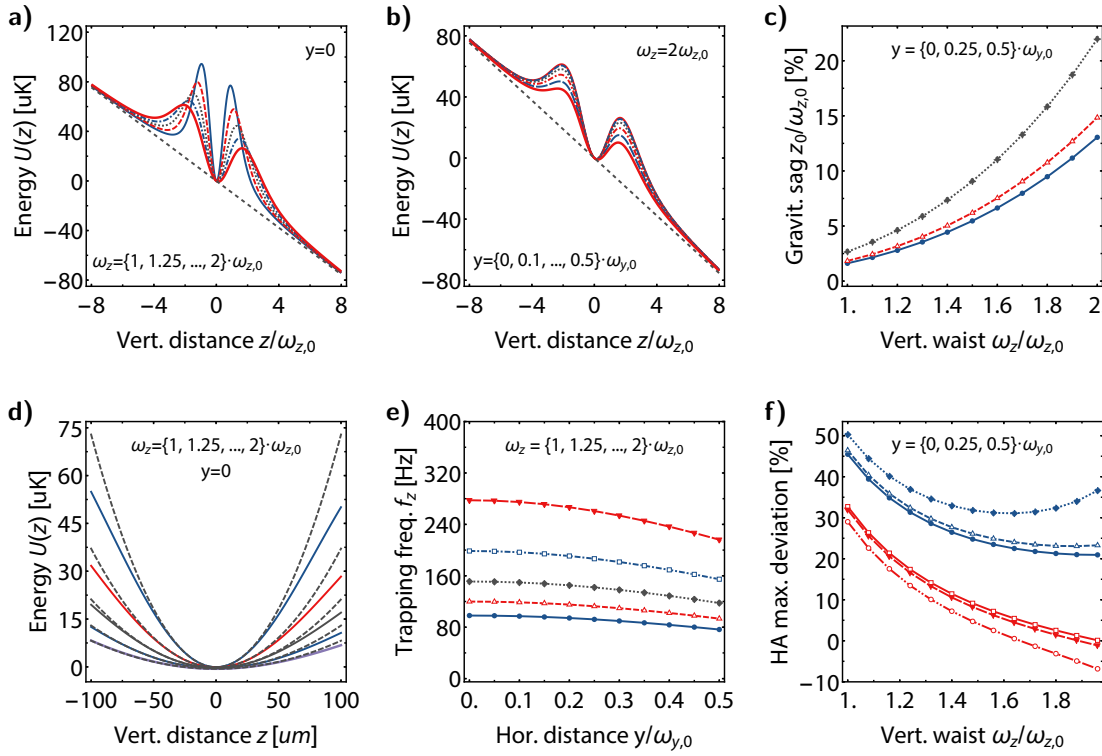


**Figure 6.13.: Case study in the presence of gravity.** Parameters:  $P = 5W$ ,  $\omega_{z,0} = 200 \mu\text{m}$ ,  $\omega_{y,0} = 2c_{\text{lat}} = 5 \mu\text{m}$ . a) Optical potentials for different increasing beam waists  $\omega_z$ . b) Fall-off of the potential for a given waist  $\omega_z$  along the transverse direction  $y$  up to a distance of  $y = c_{\text{lat}}$ . c) Gravitational sag as a function of  $\omega_z$  for several values of  $y$ . d) Harmonic approximations to the potentials in a), plotted for the region of interest  $\pm 100 \mu\text{m}$  and various choices of  $\omega_z$ . All curves were shifted by their respective gravitational sag. e) Harmonic trapping frequencies as a function of  $y$  position and for different choices of  $\omega_z$ . f) Deviation from the harmonic approximation at the outer edges of the ROI as a function of increasing  $\omega_z$  (see plot d). Solid blue and orange lines:  $z = \pm 100 \mu\text{m}$  at  $y = 0$ , Dashed and dot-dashed lines: same for  $y = 0.5, 1 d_{\text{lat}}$ .

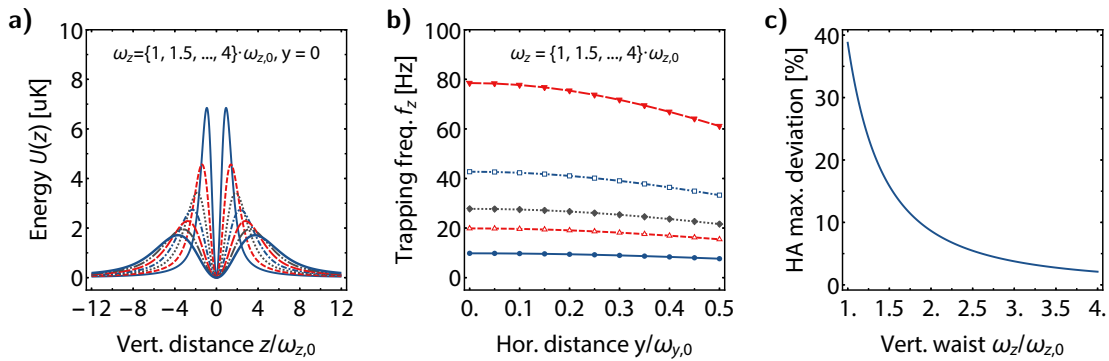


**Figure 6.14.: Case study in absence of gravity.** Parameters:  $P = 2W$ ,  $\omega_{z,0} = 200 \mu\text{m}$ ,  $\omega_{y,0} = 10d_{\text{lat}} = 10 \times 2.5 \mu\text{m}$ . a), b) similar as above. In c) only the curve at  $y = 0$  is drawn as all normalized deviations from the harmonic approximation are identical in the absence of gravity.

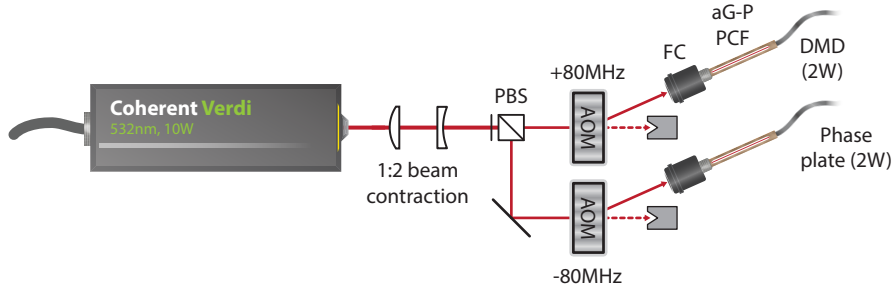


**Figure 6.15.: Schematic overview of the green high power laser system.** The Verdi laser head's output of 10 W at a wavelength of 532 nm is split via a PBS and coupled into two high power optical fibers via acousto-optical modulators. The light intensity after the cleaning fibers is controlled with a PID circuit, which provides feedback to the RF power of the AOMs (see. sec. 2.11.2).

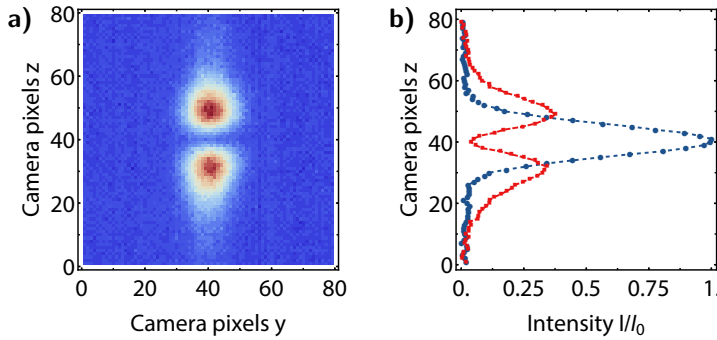


**Figure 6.16.: Preliminary result of the phase-plate.** The example depicted here was obtained using a test setup without careful alignment of the phase plate. a) Density map of the intensity profile. b) Integrated profiles of the incoming and resulting beams.

has in choosing the parameters of the harmonic confinement.

With the range of technically available trapping frequencies being established, we are now in a position to gauge to which degree to which the resulting tube is one-dimensional. As was mentioned earlier, the trapping frequency  $\omega_z$  of the harmonic confinement created by the phaseplate will define the 1D Fermi energy of a given tube as per  $E_{F\uparrow} = N_{\uparrow}\hbar\omega_z$ . In order for the gas to be quasi-1D, the condition  $E_{F\uparrow}/\hbar\omega_{\perp} \ll 1$  must hold where  $\omega_{\perp}$  denotes the transverse confinement of the lattice. Taking conservative values of  $\omega_z = 2\pi \times 30$  Hz,  $N_{\uparrow} = 5 \times 10^2$  and  $\omega_{\perp} = 2\pi \times 45$  kHz (see sec. 6.1.2) with respect to the ones reported in [58], one already has  $\hbar\omega_{\perp}/E_{F\uparrow} = 0.33$ .

### Experimental realization

The blue-detuned light is provided by a 10 W Coherent Verdi with a wavelength of 532 nm. The laser setup is depicted in fig 6.15. After some initial beamshaping of the laser head's output, the light is split into two beams and coupled into high power single mode fibers after passage through AOMs. The mode-cleaned outputs are used for the phase-plate and the DMD setup (see sec. 6.2.8), respectively. Intensity stabilization is realized by providing

feedback to the AOMs RF drivers, as described in sec. 2.11.2.

A preliminary result of a  $\text{TEM}_{01}$ -like intensity pattern created with the phase-plate is shown in fig. 6.16. As is evident, the obtained result is well described by the relation (6.31). The remaining minor deviations from the ideal behavior can be attributed to the absence of precise means of alignment in the test setup. The loss of optical power due to the passage through the substrate or other parasitic diffraction effects was found to be completely negligible. These first results show great promise for the future realization of harmonic confinement using a phaseplate, especially when gravity is compensated by an additional means.

### 6.2.8. Optical compensation of gravity

Given that the optical lattice is oriented along gravity and possesses only very weak axial confinement, the gravitational acceleration would cause the atoms to slide out of the tubes after a few milliseconds. As was discussed earlier, phase-plate is, in principle, sufficient to provide harmonic confinement for momentum refocusing and to hold the atoms against gravity. However, the fidelity of this technique is decreased by the linear gravitational potential, which introduces anharmonicities into the potential.

One can easily compensate this effect by subjecting the atoms to a linear magnetic gradient field whose slope is chosen such that it exactly cancels out gravity. However, in the case of  $^{40}\text{K}$  one typically works with the two Zeeman spin states  $m_F = -9/2, -7/2$  to take advantage of their Feshbach resonance and, in our specific case, also with  $-5/2$  as target state for RF spectroscopy (see sec. 5.3), at magnetic bias fields of  $\sim 200$  G. At these fields, the respective magnetic moments differ by roughly 10% and 20% with respect to the stretched state, as is shown in figure C.4a and b. It is this difference which prevents one from employing magnetic gradients for gravity compensation as the differential acceleration would reduce the spatial overlap of the clouds belonging to different Zeeman states. This situation could be resolved by adding sufficiently strong harmonic confinement through magnetic curvature while compensating simultaneously the gravitational pull for the stretched state with a gradient, which would partially compensate the sag of the other two states as well. As the negative Zeeman levels are high field seekers the field curvature must be negative, which is the case for the outer coils with  $B'' = -2.92 \text{ G cm}^{-2}$  at the appropriate current to obtain a bias field of 230 G. However, with this method one can only obtain trapping frequencies of about 4.55 Hz ( $-9/2$ ), 4.31 Hz ( $-7/2$ ) and 4.03 Hz ( $-5/2$ ) with the differential gravitational sags of 1.4 mm and 3.3 mm remaining intolerably large.

The fact that the dipole gradient force scales as  $U \sim I(\mathbf{r})$  with the intensity of the light field makes it possible to tailor a wide range of potentials for the atomic ensembles. The effect of gravity can thus also be counteracted by an optical gradient field as long as

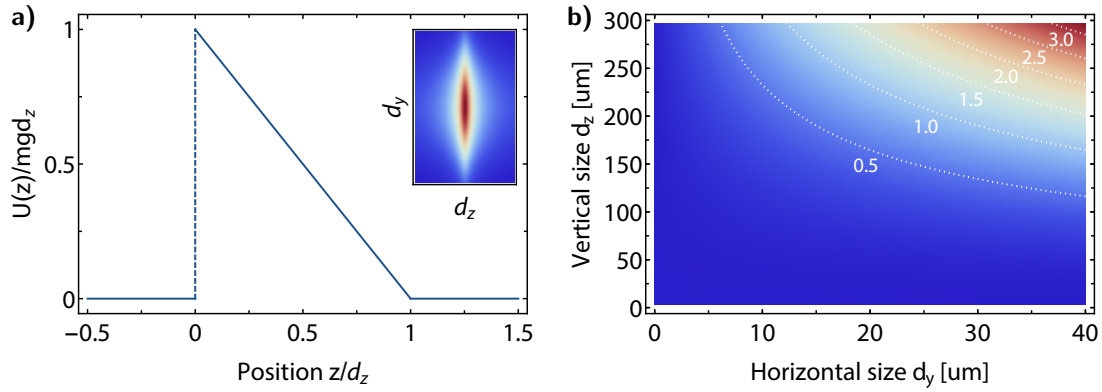


**Figure 6.17.: Gravity compensation using a linear intensity pattern.** a) Ideal potential to counteract gravity. The inset indicates the size of the lightfield with respect to the lattice tubes. b) Density plot of the total power  $P_t \times 1/0.3$  vs. box size as per equation 6.36. The additional factor is a realistic estimate of the losses occurring in the optical setup to approximate the power needed after the cleaning fiber. These losses are mostly due to the limited light utilization efficiency of the DMD, but also to transmission and reflection losses.

its polarization is linear, which implies the absence of any dependence on the atoms internal spin state. The creation of such an intensity pattern requires the use of spatial light modulators such as liquid crystal panels (LCD) or digital micromirror devices (DMD), which are commonly found in video projectors. While offering a great deal of flexibility, the main drawback of such modulators are either a low damage threshold for LCD panels or low light utilization efficiencies in the case of DMDs. Since we would like to work at far-off resonant wavelengths, which entails high optical powers, we opted for the latter. In order to gauge whether such an undertaking is feasible from a technical point of view, one needs to determine the power requirements as imposed upon by the situation of the atoms at the moment of the loading of the lattice.

### Power requirements for an optical gradient potential

For a wavelength of  $\lambda = 532$  nm the optical potential will be repulsive, that is to say that regions of high intensity will shift the energy toward larger values. The lightfield  $I(y, z)$  should have a width  $d_y$  of at least a few lattice constants  $d_L = 2.5 \mu\text{m}$  and a height  $d_z$  that is slightly larger than the extent of the crossed optical dipole trap before loading the lattice. To counteract gravity, the potential energy must be of the form

$$U(y, z) = \frac{1}{2\epsilon_0 c} \Re[\alpha_\lambda] I(y, z) = \begin{cases} 0, & z = d, 0 < y < d_y \\ mgd_z, & z = 0, 0 < y < d_y \\ 0, & \text{else} \end{cases}, \quad (6.34)$$

which corresponds to the intensity field  $I(y, z) = 2\epsilon_0 c \times mg(d_z - z) / \Re[\alpha_\lambda]$ . This situation is illustrated in fig. 6.17a. The proportionality constant in (6.34) was already introduced in in eqn. (2.3) as the AC Stark polarizability of Alkali atoms subjected to linearly polarized<sup>9</sup> light,

$$\frac{1}{2\epsilon_0 c} \Re[\alpha_\lambda] = \frac{\pi c^2 \Gamma_{\text{nat}}}{2\omega_{\text{D1}}^3} \left( \frac{1}{\Delta_{\text{D1}}} + \frac{2}{\Delta_{\text{D2}}} \right), \quad (6.35)$$

where  $\Delta_{\text{D1,2}}$  denotes the angular detuning from the D1- and D2-line, respectively. While the above relations are necessary to be able to tailor the proper slope of the optical gradient field, they can also be used to calculate the total optical power contained in the light field with dimensions  $d_y \times d_z$ . This is quite important from a technical point of view to ensure that the required total power is at all achievable, especially given the fact that spatial light modulation with DMDs can be inefficient with light utilization efficiency varying from a few percent to up to 70 % depending on the desired pattern.

The total optical power needed to counteract gravity in a region of dimensions  $d_y$  and  $d_z$  is then given by the simple integral:

$$P_t = \frac{2\epsilon_0 c}{\Re[\alpha_\lambda]} \int dy \int dz mg(d_z - z) = \frac{\epsilon_0 c}{\Re[\alpha_\lambda]} mg d_y d_z^2. \quad (6.36)$$

The strong scaling with the dimensions of the box makes it necessary to keep it as small as possible in order to keep  $P_t$  at realistic levels. The spatial extension of the tubes along gravity is expected to be  $\sim 250 \mu\text{m}$ , which would require a total power of about 4.3 W at the position of the atoms if we took that size for a square gradient light field. Assuming realistic losses of roughly 70 % of the light due to DMD efficiency and other factors, one would need 14.4 W after fiber delivery, which is unrealistically high. The situation can be salvaged by creating a light field of an unequal aspect ratio, which dramatically reduces the power needs since the lattice tubes will be arranged in a single row that can be illuminated for gravity compensation from the side. The scaling of eqn. 6.36 with box size is given in fig. 6.17b, where losses of 70 % have been added. While the size along gravity has to be kept fixed at 250  $\mu\text{m}$  or larger, there is some flexibility along the  $y$ -direction. However, to ensure that the overlap of the beam with the lattice tubes does not become too sensitive to pointing jitter as its size is decreased,  $d_y$  should remain larger than 20  $\mu\text{m}$ . In this situation, one would require about 1.5 W incident on the DMD, which is technically attainable given our experimental conditions.

<sup>9</sup>Circular polarization makes the potential dependent on the internal spin state of the atom, which is clearly not desirable here as one needs to address all states in the same manner.

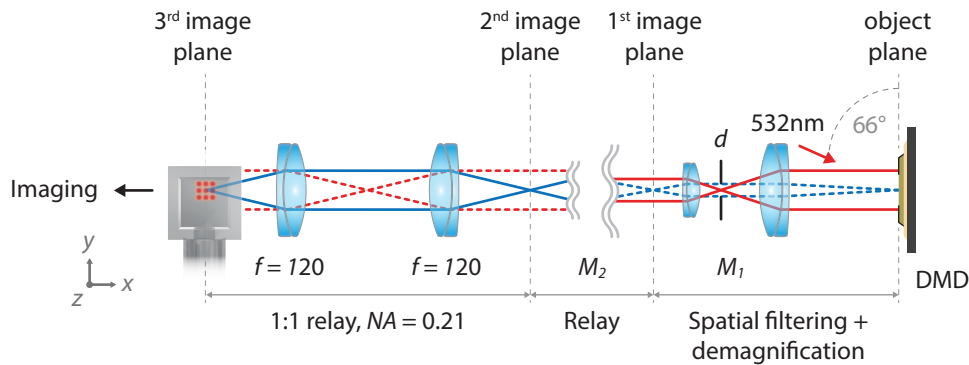


**Figure 6.18.:** Optical system to image the DMD pattern onto the atoms. The object plane is sent through an optical low pass filter to create a smooth intensity map and demagnified by a factor of 40 using additional relay optics. The last 1:1 telescope serves to project both the DMD pattern as well as the modulated optical pumping beam onto the atoms. The two light fields are combined via a dichroic element.

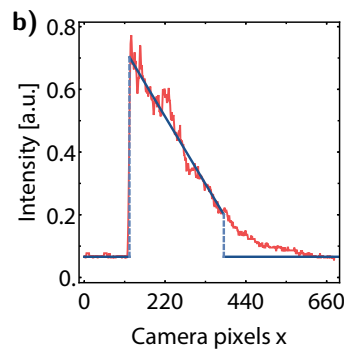
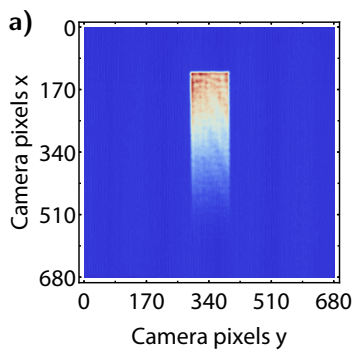


**Figure 6.19.:** Preliminary result of an optical gradient field. The example depicted here was created using the DMD test setup described in B.1 without iterative feedback. a) Density map of the intensity profile. b) Linear fit (blue) to a cross section (orange) along the gradient.

### Experimental realization using a digital micromirror device

Since a DMD is a binary light modulator, the generation of profiles containing intensity gradients is not straightforward. In order to achieve intensity modulation on the grayscale level, the ideal reflectance pattern is first dithered using the Steinberg-Floyd error diffusion algorithm [234]. The resulting (binary) profile is then blurred using a low-pass Fourier filter embedded in a 4f-correlator to generate smooth intensity maps. The quality of the obtained result is then improved using iterative feedback, which successively increases the overlap of the actual pattern with the target pattern. As the experimental implementation of a DMD is an extensive topic, the reader is referred to sec. B.1 for the main details regarding the general operation as well as the programming of the device.

The envisioned imaging system to map the pattern of the spatial light modulator onto the atoms is shown in fig. 6.18. The DMD chip is illuminated by an elliptical Gaussian beam provided by the laser setup shown in fig. 6.15. The intensity can be tuned with a PID providing feedback to an AOM before the cleaning fiber. The aspect ratio of the

beam must be chosen to maximize light utilization efficiency given that the target profile is a rectangular gradient light field with an aspect ratio of 10:1. After modulation of the intensity field, the resulting profile is passed through an optical low pass filter to convert the binary half-toned pattern into a smooth intensity map. Afterwards, it is propagated to the science cell via relay telescopes and de-magnified in the process.

In fig. 6.19 a preliminary result of a gradient intensity map created with the DMD is shown. The pattern was generated using a low-power test setup and recorded in the focal plane of the Fourier low pass filter. The latter was used to remove high frequency noise and to smooth out the intensity profile. However, iterative feedback was not yet utilized in this case, which is the reason why the surface still displays some noticeable roughness and deviations from the ideal target pattern. Nevertheless, these defects will be largely diminished after additional optimization. For reference, in ideal conditions and by using active refinement, RMS errors as low as  $\sim 0.20\%$  have been reported with DMDs [235, 236]. The first experimental results presented here are therefore already very promising for the future compensation of gravity using gradient light fields.

## Chapter 7

### Summary and outlook

The main results presented in this text concern two complementary aspects of experimental research using cold atoms, pertaining to species-specific and universal physics, respectively.

In chapters 3 and 4 we described the characterization of a previously unreported closed-channel dominated ( $s, d$ )-wave Feshbach resonance in  $^{40}\text{K}$  between the states  $m_F = +9/2, +7/2$ , which is part of an ongoing study of the scattering properties of the positive Zeeman states at low magnetic fields. In particular, the spectrum of the inelastic loss rate was determined for different temperatures and trap depths, which enabled us to identify the losses as two-body processes and to establish the dominant entrance channel to be  $s$ -wave in nature. The experimental findings were found to stand in good agreement with numerical simulations provided by E. Tiesinga [129, 137]. Moreover, we investigated the dynamics of the spin populations driven by the resonantly enhanced inelastic collisions. The underlying coupling between the  $s$ -wave entrance channel and the  $d$ -wave bound state is mediated by the magnetic dipole interaction, causing the redistribution of angular momentum between spin- and orbital degrees of freedom. The experimentally observed spin trajectories were analyzed using simple rate equation models and found to be consistent with the predictions regarding the contributing bound state based on angular momentum conservation.

Chapters 5 and 6 detailed the progress towards the experimental study of the dimensional crossover between the Tomonaga-Luttinger liquid in 1D and the Landau-Fermi liquid in 3D. Despite the fact that the two limiting regimes are well understood, the interpolating physics remains unexplored. We aim on studying this crossover using strongly interacting imbalanced Fermi gases of  $^{40}\text{K}$ , which are loaded into a large spacing 2D optical lattice. Over the course of this chapter, we described the fundamental design considerations regarding the dimensional tunability of the lattice's dynamics in terms of the effective mass as well as the requirements for momentum-resolved RF spectroscopy and momentum refocusing. Furthermore, the realization of high-field imaging as well as the scheme for optical re-pumping into dark states to isolate a single row of tubes were presented. Several milestones of the ongoing technical implementation were then described in detail. This concerned the setup of the high power laser system as well as the optical lattice, whose spacing was then characterized using matter-wave diffraction. In addition, the

site-resolved imaging system was constructed and tested using the lattice. Finally, the experimental progress towards the optical compensation of gravity as well as the creation of harmonic confinement for momentum refocusing were summarized.

### Future experiments and next steps

The next milestone towards the experimental realization of dimensional crossovers between the Fermi- (FL) and Tomonaga-Luttinger-liquid (TLL) is the preparation of a single array of tubes using the optical pumping scheme described in sec. 6.2.6 with the crossed optical dipole trap providing vertical confinement. Once implemented, the first three- and one-dimensional in-situ density profiles can be taken, which already allows to perform thermometry in either case when interactions are tuned to be weak. Afterwards, the ‘matter-wave lens’ for momentum refocusing and the optical gradient field created by the DMD can be installed at the same time as they share a common optical path and laser source. The complete experimental platform can then be benchmarked using a non-interacting Fermi gas to verify, for instance, that the momentum distribution is measured accurately by the refocusing technique. Finally, momentum resolved RF spectroscopy can be tested and calibrated by performing it in the known limits of the Fermi-liquid in 3D and the Luttinger-liquid in 1D.

Once fully implemented, the experimental platform can be used to address a wide range of physical phenomena in addition to the dimensional FL-TLL crossover as outlined in sec. 5.5. A first exciting prospect would be to study how spin transport in a strongly interacting Fermi gas is modified by the reduced dimensionality. This can be done, for instance, by detecting the dynamical evolution of the local imbalance between spin-up and spin-down components, which are in the process of mixing with one another. Experimentally, this can be achieved by separating their centers of mass using a magnetic gradient, which is then switched off to let the clouds drift back to their common rest position. To date, such transport studies have been carried out in three- and two-dimensional Fermi gases with strong interactions [237–239], clearly demonstrating the quantum-limited nature of the spin transport.

Another interesting question to address experimentally concerns the validity of the Tomonaga-Luttinger model, which is based on the assumption of a linearized dispersion relation. As was pointed out in 5.2, non-linear terms appear as soon as kinetic and interaction energies become comparable. This leads to a modification of the excitation spectrum which is reminiscent of Fermi-liquid behavior. While behavior consistent with Fermi-TLL theory was already observed in [58] where interactions were kept sufficiently weak, a complementary approach would be to investigate eventual deviations from the TLL model as interactions become stronger.

Finally, the specific combination of a two-component Fermi gas of  $^{40}\text{K}$  and 1D confine-

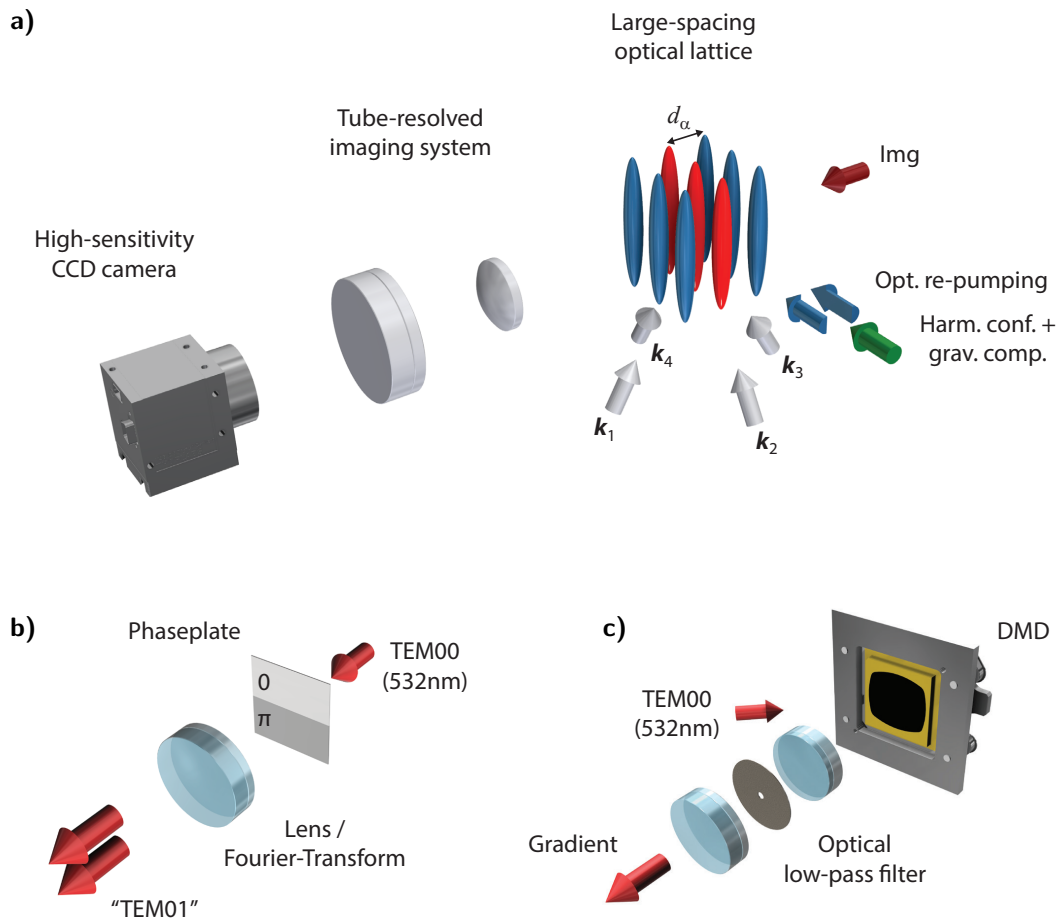


**Figure 7.1.: Simplified overview of the complete experimental platform.** a) Large-spacing optical lattice with site-resolved imaging system and custom optical potentials as well as spatially modulated optical pumping. b) Creation of a TEM01-like potential using a 0- $\pi$  phaseplate in conjunction with an optical Fourier transformation. c) Generation of a smooth gradient potential using a digital micro-mirror device (DMD) and a 4f-correlator hosting an optical low-pass filter.

ment may facilitate the study of itinerant ferromagnetism as proposed in [240]. In the ferromagnetic phase, all atoms are in the same superposition of the two spin states, which corresponds to a system of identical Fermions. By contrast, the paramagnetic phase is characterized by a statistical mixture of the two spins, which implies that the energy is lower. As a result, this configuration is more attractive for Fermions and, therefore, a ferromagnetic ground state in 3D exists only when there are strong repulsive interactions between the spin components (Stoner criterion [241]). In 3D atomic gases, such a situation arises when the s-wave scattering length is large and positive, which is usually accompanied by dimer formation [242–244]. In reduced dimensions, inelastic losses are decreased but the energy differences between the ferro- and nonferromagnetic state are even larger [245, 246]. However, following [240], this can be overcome by taking advantage

of interactions beyond the Stoner model, which can be realized particularly well with  $^{40}\text{K}$ . By ramping the magnetic field in-between the s-wave (even in 1D) and p-wave (odd in 1D) Feshbach resonances at 202 G and 198.8 G, respectively, one can have at the same time inter-component repulsion and momentum-dependent odd-wave interaction among one of the components, with the latter causing the groundstate to be ferromagnetic. While this proposal appears promising, it remains to be verified whether it can be implemented in our case given the experimental parameters and constraints of the envisioned 1D Fermi gas.

On the three-dimensional side, many open questions about strongly interacting Fermi gases still remain despite the plethora of past experimental research. In chapter 4 we have studied the two-body decay properties and spin dynamics of a thermal two-component Fermi gas in the vicinity of a  $(s, d)$ -wave Feshbach resonance. In this context, inelastic losses and heating represented the two principle means to probe the properties of this closed-channel dominated resonance. An extension of this study is to make the transition to the strongly interacting regime using an open-channel dominated resonance and use the (weaker) inelastic losses to probe non-trivial properties of the resulting strongly correlated many-body system.

### Three-body contact of strongly interacting Fermions

Unlike resonant bosonic gases, two-component Fermi gases do not display the same high levels of three-body recombination when tuned close to a Feshbach resonance. The underlying reason is that the probability to find two fermions with the same spin at close range is strongly reduced by virtue of the Pauli-exclusion principle. In the asymptotic limits of the BEC-BCS crossover, the inelastic processes experienced by fermions are well understood, both experimentally [247–249] and theoretically [250–252]. On the BEC side of the resonance, inelastic losses are dominated by two-body interactions between atoms and dimers or between pairs of dimers. On the BCS side, s-wave collisions between three fermions are suppressed by Pauli-exclusion [253], so that the main decay mechanism is a three-body process facilitated by p-wave collisions. However, the behavior at unitarity when  $1/a \rightarrow 0$  remains unknown. The interest in studying the latter lies in the fact that one may gain access to non-trivial three-body correlations, which naturally make a connection to the strong interactions of nuclear physics as well as to the corresponding processes in the crust of neutron stars [254]. If short-ranged, the three-body interactions can be treated perturbatively and one can define a three-body contact parameter via the probability of finding three atoms with spins  $\{\uparrow, \uparrow, \downarrow\}$  within a given hyperradius  $\epsilon$ ,

$$N_{\uparrow\uparrow\downarrow}(R < \epsilon) = \int_{R < \epsilon} d^3r_1 d^3r_2 d^3r_3 g_{\uparrow\uparrow\downarrow}(\mathbf{r}_1, \mathbf{r}_2, \mathbf{r}_3) \underset{\epsilon \rightarrow 0}{\sim} C_3 \frac{\epsilon^{2s+2}}{2s+2},$$

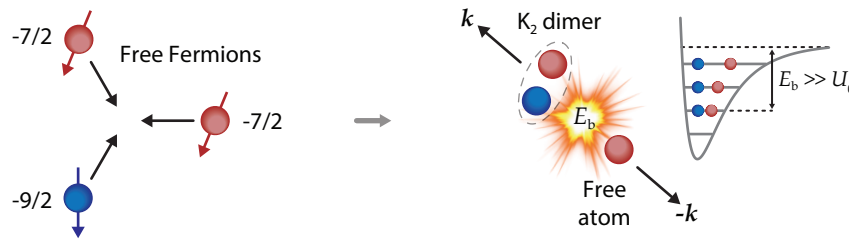


**Figure 7.2.: Three-body recombination in a two-component Fermi gas.** A (deeply) bound two-body state can only be formed when a third atom participates in the inelastic collision to ensure conservation of momentum. The released binding energy  $E_b \sim k_B \times 1$  K is usually much larger than typical optical trap depths  $U_0 \sim k_B \times 0.5$  mK, causing the dimer and the free atom to be lost from the trapping potential.

where  $g_{\uparrow\uparrow\downarrow}(\mathbf{r}_1, \mathbf{r}_2, \mathbf{r}_3) = \langle \hat{\psi}_{\uparrow}(\mathbf{r}_1) \hat{\psi}_{\uparrow}(\mathbf{r}_2) \hat{\psi}_{\downarrow}(\mathbf{r}_3) \hat{\psi}_{\downarrow}(\mathbf{r}_3) \hat{\psi}_{\uparrow}(\mathbf{r}_2) \hat{\psi}_{\uparrow}(\mathbf{r}_1) \rangle$  denotes the correlation function and  $\mathcal{C}_3$  the three-body contact parameter. The latter can be probed via three-body losses, the rate of which is assumed to be given as per  $\dot{n} = -\gamma\mathcal{C}_3$  with the underlying reasoning being that the loss rate should be proportional to the probability of finding three atoms at the same time with a hyperradius smaller than the potential range [255–257]. However, this requires the knowledge of the appropriate scaling laws depending on the temperature of the sample. At  $T = 0$  only the length scale  $1/k_F$  remains, resulting in the exotic form of the rate equation for the density:

$$\dot{n} \sim - \sum_{i,j} \alpha_{i,j} n^{(2s_{i,j}-5)/3}$$

For  $T \ll T_F$  one finds that  $\dot{n} \sim -n^{2.85}$ , which corresponds to the lowest exponent in the above expression representing the largest contribution to the three-body losses. At high temperatures the usual scaling of  $\dot{n} \sim -n^3/T^{0.23}$  should be recovered since three-body correlations become negligible [255].

A thorough study of three-body losses in strongly interacting Fermi gases may thus represent a way to probe the three-body correlations at short range and, by direct extension, of the contact parameter  $\mathcal{C}_3$  [255]. To that end, the appropriate rate equations for density and temperature (see [257] for additional details) have to be fitted to experimentally determined atom number trajectories obtained at unitarity. More concretely, the measurement procedure would consist of preparing degenerate samples of  $^{40}\text{K}$  on top of its canonical Feshbach resonance at  $B = 202$  G and recording the remaining number of atoms as function of hold time. In this context, the well-known scalings for inelastic losses in the BEC- and BCS limits provide both a reference and a means for calibration.



## Chapter 8

### Acknowledgements

First of all, I would like to express my gratitude towards the members of the jury, for having taken the time to be part of my defense committee. Furthermore, I want to thank my thesis supervisors, Christophe Salomon and Frédéric Chevy, for having given me the opportunity to obtain my PhD as a member of their research group.

A cold atom experiment is a tremendous team effort that requires the longterm commitment and hard work of many people in order to function and evolve. When dedicating so much of one's time to this collective effort, the atmosphere in the lab and the relationships with the coworkers naturally represent an extremely important aspect of every single day. In this context, I want to especially thank my 'co-thésars' Cédric Enesa, Markus Bohlen, Clément de Daniloff and Daniel Suchet, for the great times inside and outside of the lab. Moreover, I want to thank Cédric Enesa in particular, for all of the memorable evenings and nights spent on "working" in P9 and in the social area. Those weekly diversions were not only incredibly fun, but they also helped me to get through the tougher periods during my time in Paris. His unique sense of humor and easygoing personality have also had a profoundly positive impact on the overall atmosphere of the experiment.

FerMix has undergone a far-reaching transformation over the past years, which is in no small part due to the efforts of Julian Struck. His unwavering dedication and drive in the lab have brought about an immense number of improvements of the experiment in almost all of its aspects. The time during which I had the pleasure of working with him certainly represented the most fulfilling years of my PhD. Julian was always ready to share his vast knowledge and technical expertise, which gave me the opportunity to grow a lot as a physicist and experimentalist. In addition, I am extremely grateful for the many hours he has invested in helping me with the preparations for the defense.

In this spirit, I also want to thank Tarik Yefsah, who has made all of these positive developments possible in the first place. Moreover, his support and plethora of suggestions on how to improve the defense presentation were both awesome and absolutely invaluable!

For the helpful tips and proof-reading of the thesis manuscript I would like to thank Julian Struck, Frédéric Chevy, Cédric Enesa, Torben Pöplau and Cornelia Reimann.

I would also like to express my gratitude towards all of the members of the workshop, without whom FerMix could not have been built. In particular, I want to thank Mathieu

Sardin, who has machined a great number of parts for the experiment and was always ready to put in extra work whenever something was needed urgently. Many thanks go as well to the administration and the electronics workshop of LKB as well as to the other teams of our group.

Furthermore, I would like to thank my family and friends for their support during my time in Paris. And finally, special thanks go to Scottie, who put up with my constant absence and obsession with the experiment for all of those years!

## **Appendix**



## Appendix A

### Quasi-thermalization of collisionless Fermions

1. **Analog simulation of Weyl particles with cold atoms.** *D. Suchet, M. Rabinovic, T. Reimann, N. Kretschmar, F. Sievers, C. Salomon, J. Lau, O. Goulko, C. Lobo and F. Chevy.* *Europhysics Letters* **114**, 26005 (2016).

In this letter we report on a novel approach to study the dynamics of harmonically confined Weyl particles using magnetically trapped fermionic atoms. We find that after a kick of its center of mass, the system relaxes towards a steady state even in the absence of interactions, in stark contrast with massive particles which would oscillate without damping. Remarkably, the equilibrium distribution is non-Boltzmann, exhibiting a strong anisotropy which we study both numerically and experimentally.

2. **Quasi-thermalization of Fermions in quadrupole potentials.** *J. Lau, O. Goulko, D. Suchet, T. Reimann, C. Enesa, F. Chevy and C. Lobo.* To be submitted to *Phys. Rev. A*.

We analyze some puzzling features of an experiment with a noninteracting classical gas of atoms in a quadrupole trap. Surprisingly, after a momentum kick, the momentum distribution remains anisotropic at long times, characterized by different temperatures along the different directions even though the motion along each direction is not independent of the others; also, the kick energy is not transmitted to orthogonal directions. To understand this we solve two closely related models, a spherically symmetric trap  $\simeq r^\alpha$  and a strongly confined gas along one direction, a "pancake" trap. We find that in the spherical trap the gas preserves the anisotropy of the kick at long times and explain this using the conservation of angular momentum and the virial theorem. Depending on the value of  $\alpha$  we find that the kick can cool or heat the orthogonal directions. We find also a first order phase transition if the spherical symmetry is broken, which is manifested as a discontinuity in the temperature behaviours. We explain this in terms of the orbital precession of the planes of motion due to the non-spherical part of the potential. The pancake trap is studied in terms of an effective 2D potential obtained by averaging the fast motion along the strongly confined direction and is shown to be quantitatively similar to the quadrupole case. The temperature anisotropy and direction independence are shown to result from the change in the 2D effective potential due to the kick.

## Analog simulation of Weyl particles with cold atoms

DANIEL SUCHET<sup>1</sup>, MIHAIL RABINOVIC<sup>1</sup>, THOMAS REIMANN<sup>1</sup>, NORMAN KRETSCHMAR<sup>1</sup>, FRANZ SIEVERS<sup>1</sup>, CHRISTOPHE SALOMON<sup>1</sup>, JOHNATHAN LAU<sup>2</sup>, OLGA GOULKO<sup>3</sup>, CARLOS LOBO<sup>2</sup> and FRÉDÉRIC CHEVY<sup>1</sup>

<sup>1</sup> *Laboratoire Kastler Brossel, ENS-PSL Research University, CNRS, UPMC, Collège de France  
24, rue Lhomond, 75005 Paris, France*

<sup>2</sup> *Mathematical Sciences, University of Southampton - Highfield Southampton, SO17 1BJ, UK*

<sup>3</sup> *Department of Physics, University of Massachusetts - Amherst, MA 01003, USA*

received on 25 April 2016; accepted by G. Shlyapnikov on 1 May 2016

published online 18 May 2016

PACS 67.85.-d – Ultracold gases, trapped gases

PACS 05.20.Dd – Kinetic theory

PACS 05.70.Ln – Nonequilibrium and irreversible thermodynamics

**Abstract** – In this letter we report on a novel approach to study the dynamics of harmonically confined Weyl particles using magnetically trapped fermionic atoms. We find that after a kick of its center of mass, the system relaxes towards a steady state even in the absence of interactions, in stark contrast with massive particles which would oscillate without damping. Remarkably, the equilibrium distribution is non-Boltzmann, exhibiting a strong anisotropy which we study both numerically and experimentally.



Copyright © EPLA, 2016

**Introduction.** – Weyl fermions were introduced for the first time in 1929 as massless solutions of the Dirac equation [1]. Despite constituting one of the paradigms of contemporary high-energy physics, their existence in Nature has remained unconfirmed until very recently. While at first suggested to describe neutrinos, the observation of flavor oscillations implying a non-zero rest mass ruled out this hypothesis [2]. It had been pointed out that they could be observed in the form of low-energy excitations of crystalline structures with a linear dispersion relation around a so-called Weyl point. The non-trivial topology of such Weyl semimetals is responsible for the Adler-Bell-Jackiw chiral anomaly [3,4] which leads to remarkable properties such as negative magnetoresistance, anomalous Hall effect and non-local transport [5]. Moreover, the confinement of quasiparticles obeying a linear dispersion relation was suggested as a way to engineer individual quantum dots [6], notably for the improvement of multiple exciton generation in solar cells [7].

The mere existence of Weyl points in reciprocal space requires a broken time-reversal or inversion symmetry, which are challenging to implement experimentally. As a consequence, observations of Weyl particles were reported only recently in 3D compounds such as HgCdTe, HgMnTe [8], TaAs [9,10] as well as in photonic crystals [11]. Owing to their high degree of control and versatility, cold atoms offer a promising and complementary route for the experimental study of Weyl fermions. Early proposals in

this context were based on the band structure of cold atoms in 3D optical lattices extending the 2D Harper Hamiltonian [12]. Yet another approach is analog simulation where one takes advantage of the mathematical equivalence between two seemingly different physical systems. Such mapping were successfully used in the past to relate, for instance, Anderson localization to the  $\delta$ -kicked rotor [13–15], quantum magnetism to the filling factor of an optical lattice [16,17], the solutions of the Dirac equation to the dynamics of ion chains [18,19], or quantum Hall edge states to the eigenmodes of classical coupled pendula [20].

In this letter, we report on the analog simulation of Weyl particles in a harmonic potential using a dilute gas of cold magnetically trapped atoms. Using a canonical mapping exchanging position and momentum in the system's Hamiltonian, we address the dynamics of an ensemble of non-interacting Weyl particles after excitation of their center of mass (CoM). The system's ensuing relaxation towards a steady state exhibits intriguing dynamics, resulting in a strongly anisotropic and non-thermal momentum distribution of the cold gas. Our observations are interpreted using a kinetic model based on virial theorem and energy conservation.

**Mapping.** – The magnetic quadrupole trap is a common technique for confining neutral atoms [21]. It is made up of a pair of coils carrying anti-parallel currents, creating

close to their symmetry center a linear magnetic field  $\mathbf{B}_0(\mathbf{r}) = b(\alpha_x x, \alpha_y y, \alpha_z z)$ , where  $z$  is the symmetry axis of the coils. Here  $b$  denotes the magnetic-field gradient and Maxwell's equations imply that  $\alpha_x = \alpha_y = 1$ ,  $\alpha_z = -2$ . For a spin-(1/2) atom of mass  $m$  carrying a magnetic moment  $\mu$ , the coupling to this field leads to the single-particle Hamiltonian

$$h(\mathbf{r}, \mathbf{p}) = \frac{p^2}{2m} - \mu \boldsymbol{\sigma} \cdot \mathbf{B}_0(\mathbf{r}), \quad (1)$$

where  $\boldsymbol{\sigma}$  are the Pauli matrices. By means of the canonical mapping  $X_i = cp_i/\mu b\alpha_i$  and  $P_i = -\mu b\alpha_i x_i/c$  with  $c$  being an arbitrary velocity scale, the Hamiltonian (1) becomes

$$H = c \boldsymbol{\sigma} \cdot \mathbf{P} + \frac{1}{2} \sum_i k_i X_i^2. \quad (2)$$

The first term corresponds to the kinetic energy  $c\boldsymbol{\sigma} \cdot \mathbf{P}$  of a massless Weyl particle moving at velocity  $c$  while the second one is readily identified as an anisotropic harmonic potential, characterized by spring constants  $k_i = \alpha_i^2 \mu^2 b^2 / mc^2 = \alpha_i^2 k$  along each direction  $i$ . This mapping is at the core of our work and it shows that neutral atoms confined by a linear potential can be used to simulate experimentally the dynamics of Weyl particles.

The single-particle trajectories of the Weyl particles can be obtained using Ehrenfest's theorem applied to the Hamiltonian (2). Using uppercase (lowercase) symbols for the phase-space coordinates of the Weyl particles (spin-(1/2) atoms), we obtain respectively in the Heisenberg representation:

$$\dot{X}_i = c\sigma_i, \quad \dot{p}_i = \mu b\alpha_i \sigma_i, \quad (3)$$

$$\dot{P}_i = -k_i X_i, \quad \dot{x}_i = p_i/m, \quad (4)$$

$$\dot{\boldsymbol{\sigma}} = \frac{2c}{\hbar} \boldsymbol{\sigma} \times \mathbf{P}, \quad \dot{\boldsymbol{\sigma}} = \frac{2\mu}{\hbar} \boldsymbol{\sigma} \times \mathbf{B}(\mathbf{r}). \quad (5)$$

Equations (3) to (5) are fully quantum, but in the following we will focus on the classical regime, and consider the operator mean values. Noting that  $\langle \boldsymbol{\sigma} \rangle^2 = 1$ , The first of eqs. (3) immediately shows that even in a harmonic trap Weyl particles move at a constant velocity  $c$ . Equations (5) describe respectively the particle's spin precession around the momentum  $\mathbf{P}$  and magnetic field  $\mathbf{B}$ . The adiabatic following results in the conservation of helicity and of the Zeeman populations, giving rise to topological properties. The analogy existing between these two equations allows to draw a parallel between a peculiar feature of Weyl particles, the Klein paradox [22], and the well-known Majorana losses [23–26] for magnetic traps. The Klein paradox states if the rate of change of the particle's energy is too high (*i.e.* much larger than  $2Pc/\hbar$  for Weyl particles), the spin will not follow the momentum adiabatically and the helicity of the particle is not conserved. The resulting transfer of the particle to negative energy states leads to dramatic effects, such as the suppression of back-scattering for electrons in 1D

carbon nanotubes [27]. For the equivalent picture of magnetically trapped atoms, in regions where the Larmor frequency  $2\mu B/\hbar$  is smaller than the rate of change of the Zeeman energy, the atomic spin will not follow adiabatically the direction of the local magnetic field. This results in Majorana losses. The absence of backscattering in carbon nanotubes then appears as equivalent to the impossibility to trap atoms in a 1D magnetic quadrupole. Furthermore, for an ensemble of particles at temperature  $T$ , we can define a Klein loss rate  $\Gamma_{\text{Klein}}$  equivalent to the Majorana rate  $\Gamma_{\text{Maj}}$ :

$$\Gamma_{\text{Maj}} \simeq \frac{\hbar}{m} \left( \frac{\mu_B b}{k_B T} \right)^2, \quad \Gamma_{\text{Klein}} \simeq \hbar k \left( \frac{c}{k_B T} \right)^2. \quad (6)$$

Just like Majorana losses prevent the existence of a true thermodynamic equilibrium in a quadrupole trap, the Klein paradox prevents stable trapping of Weyl particles in external potentials [6]. Nevertheless, at high enough temperature such as that considered in our experiments below, particles spend little time close to 0 and we can neglect Majorana-Klein losses. Particles of positive and negative helicities can therefore be described by the effective Hamiltonians

$$H_{\pm} = \pm c|P| + \sum_i \frac{k_i X_i^2}{2}. \quad (7)$$

The negative-helicity Hamiltonian  $H_-$  is not bounded from below, which implies diverging trajectories. This directly corresponds to the anti-trapped high-field seeking states of the atomic problem. In the following we shall therefore restrict our study to the case of metastable, positive-helicity particles.

**Results.** – Using the mapping derived above, we explore the dynamics of Weyl particles using a sample of spin-polarized  ${}^6\text{Li}$  atoms confined in a quadrupole magnetic trap.

The experimental preparation of the sample starts with a dual species magneto-optical trap which is loaded with fermionic  ${}^6\text{Li}$  and  ${}^{40}\text{K}$  [28]. In a second step the clouds are subjected to blue detuned D1 molasses [29,30], cooling both species down to the  $50 \mu\text{K}$  regime. Subsequently the atoms are optically pumped into their low-field seeking stretched Zeeman states  $|F = 3/2, m_F = 3/2\rangle$  and  $|9/2, 9/2\rangle$ , respectively. Finally, we ramp a magnetic quadrupole field up to  $b = 80 \text{ G/cm}$  within 500 ms, capturing  $10^7$   ${}^6\text{Li}$  and  $10^9$   ${}^{40}\text{K}$  atoms. Inter-species- as well as  $p$ -wave collisions among  ${}^{40}\text{K}$  atoms [31] allow for the complete thermalization of the two clouds at approximately  $T_0 = 300 \mu\text{K}$ . This value is high enough to preclude Majorana losses during the experiment's duration and is well below the  $p$ -wave collision threshold. After thermalization the  ${}^{40}\text{K}$  atoms are removed from the trap by shining in resonant light, which leaves  ${}^6\text{Li}$  unaffected.

We deliver a momentum kick to the cloud by quickly turning on a magnetic bias field  $\mathbf{B}$  which shifts the center of the trapping potential by a distance  $\delta$  for a short

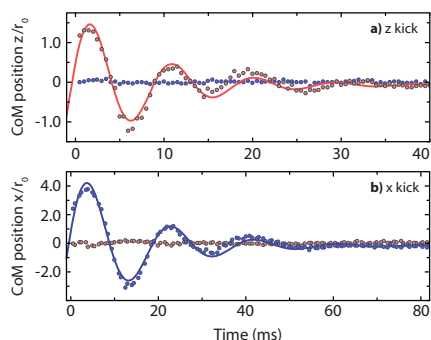


Fig. 1: (Colour online) Center-of-mass oscillations of the lithium cloud after a kick along the symmetry axis of the coils  $z$  (a) and along  $x$ , within the symmetry plane (b). Blue squares (respectively, red circles) are experimental data along  $x$  (respectively,  $z$ ). Solid lines are exponentially damped sinusoidal oscillations. Damping results solely from dephasing of single-particle trajectories. Equivalently, this corresponds to momentum oscillations of Weyl particles in a harmonic trap. Here,  $r_0 = k_B T / \mu_B b \sim 0.6$  mm and  $t_0 = \sqrt{m k_B T} / \mu_B b \sim 1$  ms.

time  $\tau$ . Maximum trap center displacements are of order  $\delta \sim 7 r_0$  along  $x$  and  $\delta \sim 5 r_0$  along  $z$ , where  $r_0 = k_B T / \mu_B b \sim 0.6$  mm is the characteristic thermal size of the cloud. The kick duration  $\tau$  is typically a few ms, being constrained by the coil inductances and eddy currents in the surrounding vacuum chamber. During the kick, the ensemble acquires an overall momentum of magnitude  $q \sim \mu_B b \tau$ , similar to free fall in gravity. The potential is then quickly brought back to its initial position, and the cloud is left to evolve during a variable time  $t$  before switching off all fields to perform a time of flight measurement of the momentum distribution. Temperatures and kick velocities are measured with a time-of-flight (TOF) technique: the trapping potential is abruptly switched-off and the atomic cloud expands freely during a few ms, before it gets imaged on a CCD camera by resonant light absorption. The center-of-mass velocity can be extracted by tracking the center of the distribution during the TOF, while the temperature is measured using the standard deviation of the position distribution for sufficiently long TOF expansion times. A limitation for the accurate determination of the kick amplitude originates from transient currents lasting about 3 ms, which appear while abruptly switching off the quadrupole magnetic trap with gradients of the order of 100 G/cm. The transient magnetic field creates a position-dependent Zeeman effect which deforms the atomic-cloud profile at short TOF durations. This results in a potential error in the measurement of the center-of-mass momentum with or without kick. For instance, in the absence of a kick we observe a small parasitic velocity  $v_0$  which is proportional to the magnetic gradient  $b$  and reaches 30 cm/s at our highest value  $b = 165$  G/cm. Therefore, to infer the actual momentum delivered to the cloud solely by the kick, we subtract  $v_0$  measured after

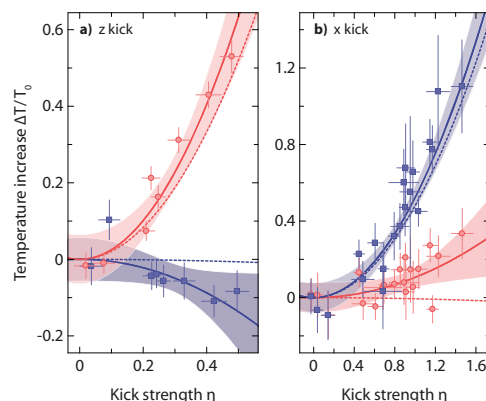


Fig. 2: (Colour online) Temperature increase  $\Delta T / T_0 = (T - T_0) / T_0$  along  $x$  (blue squares) and  $z$  (red circles) as a function of the normalized CoM momentum  $\eta$  acquired during the kick. (a)  $z$  momentum kick at  $b = 70$  G/cm. (b)  $x$  momentum kick at  $b = 55$  G/cm. Solid lines are quadratic fits to the experimental data with coefficients given in the text. Error bars represent the temperature statistical uncertainty and shaded zones give the 95% confidence level of the fits. Dashed lines are results of numerical simulations presented in fig. 3.

the thermalization time of 500 ms from the velocity right after the kick. The fit errors are given by the error bars in fig. 2 and account for our statistical errors of typically  $0.05 / m k_B$  on temperature. Performing the experiment with 4 different magnetic-field gradients, we estimate a systematic uncertainty of  $0.2 / m k_B$  for the fitted coefficient of the parabolic dependence of the heating on the momentum kick strength in fig. 2.

For Weyl fermions, this excitation corresponds to displacing the Weyl point in momentum space, waiting until the distribution has moved by a distance  $\mathbf{R}$  and switching the Weyl point back to its initial position. The resulting time evolution of the position (respectively, momentum) distribution of the lithium atoms (respectively, Weyl particles) is shown in fig. 1. Even though collisions are absent, oscillations are damped as a consequence of the dephasing between single-particle trajectories. The initially imparted energy is converted into internal energy of the cloud and the distribution reaches a steady state within a few units of time  $t_0 = \sqrt{m k_B T} / \mu_B b \sim 1$  ms.

To characterize the steady state, we kicked the cloud along the  $z$ - and  $x$ -directions and measured i) the center-of-mass velocity right after the kick and ii) the respective steady-state momentum distribution after a sufficiently long relaxation time, typically  $250 t_0$ . We define the steady state's effective temperature along direction  $i$  as the second moment of the momentum (respectively, position) distribution:

$$k_B T_i = \frac{\langle p_i^2 \rangle}{m} = k_i \langle X_i^2 \rangle, \quad (8)$$

where  $\langle \cdot \rangle$  denotes the statistical average.

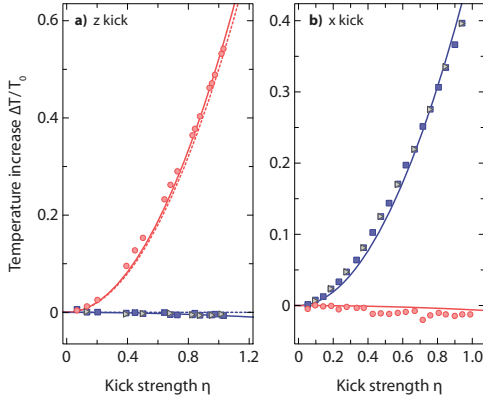


Fig. 3: (Colour online) Numerical simulation of the temperature increase as a function of the normalized CoM momentum kick  $\eta$ . Data points are obtained by solving the classical equations of motion along  $\mathbf{x}$  (blue squares),  $\mathbf{y}$  (gray triangles) and  $\mathbf{z}$  (red circles). In the simulation, kick duration is kept constant at  $\tau = 0.6t_0$  for  $\mathbf{z}$  and  $\tau = 3t_0$  for  $\mathbf{x}$ , with increasing values of displacement  $\delta$ . The effective temperatures along  $\mathbf{x}$  and  $\mathbf{y}$  are equal and almost totally decoupled from  $\mathbf{z}$ . Solid lines are the best quadratic fits to the data:  $\Delta T_x/T_0 = \Delta T_y/T_0 = 0.48 \times \eta^2$  and  $\Delta T_z/T_0 = -0.006 \times \eta^2$  for a kick along  $\mathbf{x}$  and  $\Delta T_x/T_0 = \Delta T_y/T_0 = -0.006 \eta^2$ ,  $\Delta T_z/T_0 = 0.52 \eta^2$  for a kick along  $\mathbf{z}$ . The dashed line in (a) is given by eq. (16), assuming zero cross-thermalization between  $\mathbf{z}$  and  $\mathbf{x}$ .

The heating  $\Delta T$  and the center-of-mass momentum  $\mathbf{q}$  induced by the momentum kick are extracted from the difference between the corresponding values at quasi-equilibrium and the ones measured right after the kick. While for a fully thermalized system the temperatures in both directions should be equal, our results presented in fig. 2, show a very strong anisotropy, thus demonstrating that the final distribution is non-thermal. The temperature increases much more in the direction of the kick than in the transverse directions. A kick in the  $\mathbf{z}$ -direction produces strong heating along  $\mathbf{z}$ , but a much weaker energy transfer along  $\mathbf{x}$ . Conversely, a kick in the  $(\mathbf{x}, \mathbf{y})$ -plane results in smaller heating in the  $\mathbf{z}$ -direction than along  $\mathbf{x}$ . Quantifying the strength of the kick through the dimensionless parameter

$$\eta = \frac{\langle q \rangle}{\sqrt{mk_B T_0}} = \sqrt{\frac{\sum_i k_i \langle R_i \rangle^2}{k_B T_0}}, \quad (9)$$

we find that for kicks along  $\mathbf{x}$  the best quadratic fits are given by  $\Delta T_x/T_0 = 0.52(5)_{\text{stat}}(20)_{\text{syst}} \times \eta^2$  and  $\Delta T_z/T_0 = 0.10(4)_{\text{stat}}(5)_{\text{syst}} \times \eta^2$ . For kicks along the strong axis  $\mathbf{z}$ ,  $\Delta T_z/T_0 = 0.63(7)_{\text{stat}}(20)_{\text{syst}} \times \eta^2$  and  $\Delta T_x/T_0 = -0.14(5)_{\text{stat}}(8)_{\text{syst}} \times \eta^2$ .

*Numerics.* In order to interpret these results, we performed single-particle dynamics simulations on an ensemble of  $10^5$  particles. As in the experiment, an excitation is applied to the initial distribution by displacing the trap

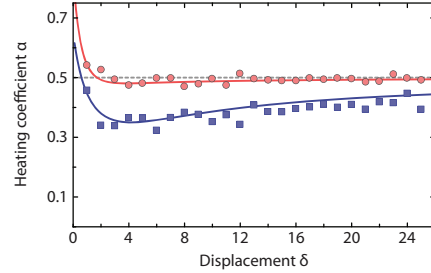


Fig. 4: (Colour online) Heating coefficient  $\alpha$  along the kick direction *vs.* Weyl point displacement  $\delta$  in momentum space (respectively, trap center displacement in position space) for kicks along  $\mathbf{x}$  (blue) and  $\mathbf{z}$  (red).  $\alpha$  is defined as  $\alpha = \Delta T/(T_0 \eta^2)$ , relating excess temperature to kick strength  $\eta$  (see text). For kicks along  $\mathbf{z}$ ,  $\alpha_z \sim 0.5$  and is almost constant. On the contrary, for kicks along  $\mathbf{x}$ ,  $\alpha_x$  shows a strong dependence on displacement  $\delta$ . Solid lines are derived from eqs. (13), (14) and (10), (11). Filled symbols are results from numerical simulations.

center (respectively, the Weyl point in momentum space) by an amount  $\delta$  for a duration  $\tau$  before bringing it back to its initial position. To simulate the effect of coil response time and eddy currents, we consider excitations of constant duration and increasing displacement. The simulation does not include any collisions, and yet we observe, as in the experiment, a relaxation towards a steady state after  $\sim 100t_0$  as all calculated moments of the distribution up to 8th order reach a stationary value. We also reproduce the strong anisotropy between the  $\mathbf{z}$ - and  $\mathbf{x}$ -direction (see fig. 3). Numerical simulations also provide access to the  $\mathbf{y}$ -direction (not measured in the experiment), which also appears to be decoupled from the strong axis  $\mathbf{z}$ , but reaches the same final effective temperature as the other weak axis  $\mathbf{x}$ , regardless of the kick direction. The simulated dynamics thus features a quasi-thermalization within the symmetry plane of the distribution.

More quantitatively, the relation between the center-of-mass momentum (respectively, center-of-mass position for Weyl particles) after the kick and the effective temperature in the steady state can be approximated by a quadratic relation  $\Delta T_{x,y,z}/T_0 = \alpha_{x,y,z} \eta^2$ , where the heating coefficients  $\alpha_i$  depend on the kick direction,  $\delta$  and  $\tau$ . For short excitation times,  $\alpha_i$  are nearly independent of  $\tau$ . Their explicit dependence on  $\delta$  is depicted in fig. 4.

For kicks along  $\mathbf{z}$ ,  $\alpha_z$  does not vary significantly with the trap displacement for the experimentally relevant choice  $\delta > 1$ , in which case  $\alpha_z = \alpha_0 = 0.5$ . The value of  $\tau$  essentially sets the strongest achievable kick  $\eta$  and we take  $\tau = 0.6t_0$  in the simulation to cover the experimental range of excitations. The heating coefficient  $\alpha_0 = 0.5$  is in agreement within error bars with the experimental result  $\alpha_z = 0.63(7)_{\text{stat}}(20)_{\text{syst}}$ . The decoupling of the  $\mathbf{x}$ -direction appears more pronounced in the simulation than in the experiment with  $\Delta T_x/T_0 = -0.006 \eta^2$ , to be compared to the experimental value  $\Delta T_x/T_0 = -0.14(5)_{\text{stat}}(8)_{\text{syst}} \times \eta^2$ ,

a difference we attribute to imperfections of the magnetic excitation procedure.

For kicks along  $\mathbf{x}$ ,  $\alpha_x$  strongly varies with the kick amplitude  $\delta$  (blue squares in fig. 4) and, therefore, a quantitative comparison with experiment requires a detailed modeling of the shape of the transient excitation currents, which is difficult. Nevertheless, fitting the duration  $\tau = 3t_0$  leads to  $\Delta T_x/T_0 = 0.48 \times \eta^2$  (to be compared to  $\Delta T_x/T_0 = 0.52(5)_{\text{stat}}(20)_{\text{syst}} \times \eta^2$ ) and  $\Delta T_z/T_0 = -0.006 \times \eta^2$  (to be compared to  $\Delta T_z/T_0 = 0.10(4)_{\text{stat}}(5)_{\text{syst}} \times \eta^2$ ). The chosen duration  $3t_0$  is consistent with the decay time of the eddy currents in our chamber ( $\sim 3$  ms).

*A simple model.* The heating of Weyl particles along the excitation direction can be understood from the constraints imposed on the dynamics by energy conservation and virial theorem  $E_{\text{kin}} = 2E_{\text{pot}}$ . Here  $E_{\text{kin}} = \langle Pc \rangle$  and  $E_{\text{pot}} = \sum_i k_i \langle X_i^2 \rangle / 2$  are respectively the kinetic and potential energy of the Weyl particles, and the relation can be derived from its equivalent for massive particles in a linear trap. However, these two conditions are not sufficient to predict the final thermodynamic properties of the system. We therefore make two additional assumptions motivated by the results of the experiment and the simulations. i) Heating occurs predominantly along the kick direction and ii) whatever the kick's orientation may be, the final temperatures along the  $x$ - and  $y$ -directions are equal by symmetry. Under these conditions one finds for the final temperatures,

$$z\text{-kick: } \Delta T_x = \Delta T_y \ll \Delta T_z, \quad \Delta T_z \simeq \frac{2\Delta E}{3k_B}, \quad (10)$$

$$x\text{-kick: } \Delta T_x = \Delta T_y \simeq \frac{\Delta E}{3k_B}, \quad \Delta T_z \ll \Delta T_{x,y}, \quad (11)$$

where  $\Delta E$  is the energy transferred to the cloud through the excitation. Our numerical simulations satisfy (10), (11) for the redistribution of the imparted energy.

In order to relate  $\Delta E$  to the experimental kick strength  $\eta$ , we describe the dynamics of the cloud during the excitation through Liouville's equation for the phase-space density  $f(\mathbf{R}, \mathbf{P}, t)$ ,

$$\partial_t f(\mathbf{R}, \mathbf{P}; t) = -\mathcal{L}f(\mathbf{R}, \mathbf{P}; t). \quad (12)$$

The Liouville operator is defined as  $\mathcal{L} = \partial_{\mathbf{P}} H_+^{\text{exc}} \cdot \partial_{\mathbf{R}} - \partial_{\mathbf{R}} H_+^{\text{exc}} \cdot \partial_{\mathbf{P}}$  with  $H_+^{\text{exc}} = H_+(\mathbf{R}, \mathbf{P} - \boldsymbol{\delta})$  being the shifted Weyl-point Hamiltonian. The formal solution to this equation is  $f(\mathbf{R}, \mathbf{P}, \tau) = \exp(-\tau\mathcal{L})[f_0]$ ; for small excitation times  $\tau$ , we can Taylor-expand this expression and obtain

$$\langle \mathbf{R} \rangle = \tau \int d^3\mathbf{r} d^3\mathbf{p} f_0(\mathbf{V}_{\text{exc}} - \mathbf{V}), \quad (13)$$

$$\Delta E = \frac{\tau^2}{2} \int d^3\mathbf{r} d^3\mathbf{p} f_0 \sum_i k_i (\mathbf{V}_{\text{exc}} - \mathbf{V})_i^2, \quad (14)$$

where  $\mathbf{V} = \partial_{\mathbf{P}} H_+$  is the velocity and  $\mathbf{V}_{\text{exc}} = \partial_{\mathbf{P}} H_+^{\text{exc}}$ . The relative scalings of  $\Delta E$  and  $\langle \mathbf{R} \rangle$  with  $\tau$  confirm that

$\alpha \propto \Delta E / \langle \mathbf{R} \rangle^2$  does not depend on the excitation duration in the short-time limit. The values of  $\alpha$  corresponding to eqs. (13), (14) and (10), (11) are presented as solid lines in fig. 4 and confirm the validity of the simulations.

For kicks along the  $\mathbf{z}$ -direction, we estimate the value of  $\alpha_z$  by considering large displacements  $\delta$ , leading to

$$\Delta E = \frac{3}{4} E_0 \eta^2. \quad (15)$$

Interestingly, the energy gain is in fact larger than the value  $E_0 \eta^2 / 2$  associated with the center-of-mass shift, because the cloud also expands in momentum space during the excitation whereby it gains additional kinetic energy. Inserting these asymptotic developments in eqs. (10) and (11), we finally obtain for  $\mathbf{z}$  kicks the relative temperature increase along the excitation direction

$$\frac{\Delta T}{T_0} = \frac{\eta^2}{2}, \quad (16)$$

corresponding to  $\alpha_z = 0.5$ , as discussed above and found in fair agreement with the experimental value.

**Conclusion.** – Contrary to massive particles, Weyl fermions do not obey Kohn's theorem [32] stating that the center of mass of an ensemble of non-relativistic massive particles oscillates in a 3D harmonic potential without dephasing at frequencies  $\sqrt{k_i/m}$ . Instead, after an excitation, Weyl fermions move at constant speed even in a quadratic potential. Dephasing of the single-particle trajectories gives rise to damping of the center-of-mass motion and to an anisotropic spread of the position distribution, corresponding to an effective heating. In the symmetry plane, the steady-state distribution is almost decoupled from the strong axis but reach the same effective temperature along both directions regardless of the kick orientation, displaying a quasi-thermalization.

It should also be pointed out the anisotropic heating is not specific to our choice of spring constants for harmonic trap (2), which are in turn constrained by the mapping from the quadrupole potential. Additional simulations have shown that the same behavior is observed for arbitrary anisotropic potentials  $V(\mathbf{r}) = (k_0 x^2 + k_0 y^2 + k_z z^2) / 2$ . Even in a fully isotropic situation  $k_z = k_0$ , the two unexcited directions are partially decoupled from the excited one and reach the same final temperatures, as the kick orientation breaks the overall symmetry.

It is crucial to note that in our experiments the energy transfer from the center of mass to the internal energy of the distribution does not depend on interactions between particles. It is solely due to the complexity of the single-particle trajectories in phase-space [33], which originates from the non-harmonic and non-separability of the underlying Hamiltonian (7). This absence of collisions is responsible for the non-thermal nature of the final distribution. Indeed, according to thermodynamics' second law, Boltzmann's distribution maximizes the entropy of the system for a given energy. In our experiment, we start

with a thermal cloud characterized by a total energy  $E$  and equilibrium entropy  $S(E)$ . A perfect momentum kick delivers an additional energy  $\Delta E$  per particle, but does so without increasing the system's entropy. The latter is then conserved throughout the ensuing evolution because the ensemble remains collisionless. The quasi-equilibrium state thus exhibits a larger energy  $E + \Delta E$  for the same entropy  $S$ , in contradiction to the usual entropy growth expected for a collisional system. The absence of real thermalization is then revealed by the anisotropic temperatures measured in the long-time limit. Weyl particles in a harmonic trap therefore provide an intriguing case of quasi-thermalization, midway between massive particles that do not equilibrate and collisional systems that reach a real Boltzmann thermal equilibrium (like in [34]). As shown in [35], this situation can nevertheless be described within the framework of generalized Gibbs ensembles as integrable systems in which a large number of constants of motion —here, the single-particle Hamiltonian of individual atoms— prevents true thermalization [36].

Finally, the canonical mapping presented here is not limited to the simulation of Weyl particles, but can address a broader range of problems. For instance, in a Ioffe-Pritchard trap a bias field gives rise to a non-zero magnetic field at the trap center and the overall field is of the form  $B = \sqrt{B_0^2 + b^2 \sum_i \alpha_i^2 x_i^2}$ . In this case, the analog system would be described by the relativistic kinetic energy  $E = \sqrt{m^2 c^4 + p^2 c^2}$  where the mass can be tuned through  $B_0$ . Another interesting situation arises in a hybrid trap consisting of the superposition of an optical dipole trap and a 2D magnetic quadrupole trap, where the Hamiltonian takes the form  $h = \frac{p^2}{2m} + \frac{m\omega^2}{2}(x^2 + y^2) + \frac{m\omega_z^2 z^2}{2} - \mu_B b(\sigma_x x - \sigma_y y)$ . Applying our mapping to the variables  $(x, y, p_x, p_y)$  leads to the equivalent Hamiltonian  $H = \frac{P^2}{2m} + \frac{m\omega^2}{2}(X^2 + Y^2) + \frac{m\omega_z^2 Z^2}{2} - \frac{\mu_B b}{m\omega}(\sigma_x P_x + \sigma_y P_y)$ , which turns out to describe a 2D spin-orbit coupled particle [37]. Finally, in the same trap, it is also possible to engineer a Rashba coupling by taking  $X = p_y/m\omega$ ,  $P_x = -m\omega y$ ,  $Y = p_x/m\omega$ ,  $P_y = -m\omega x$ .

\*\*\*

The authors would like to thank J. DALIBARD and F. GERBIER for stimulating discussions. We are grateful to E. DEMLER for pointing out to us the analogy to massless relativistic particles. OG acknowledges support from the NSF under the Grant No. PHY-1314735. CS expresses his gratitude to the A. VON HUMBOLDT foundation and to Prof. I. BLOCH and T. W. HÄNSCH for their kind hospitality at LMU and MPQ. This work was supported by Région Île de France (Dim nanoK/IFRAF),

Institut de France (Louis D. Prize) and the European Union (ERC grant ThermoDynaMix).

*Note added in proofs:* The authors are grateful to M. WEITZ for indicating ref. [38], in which an insightful experimental simulation of the 1D Klein paradox with cold atoms in a bichromatic optical lattice is presented.

## REFERENCES

- [1] WEYL H., *I. Z. Phys.*, **56** (1929) 330.
- [2] BARGER V., MARFATIA D. and WHISNANT K., *Physics of Neutrinos* (Princeton University Press) 2012.
- [3] ADLER S. L., *Phys. Rev.*, **177** (1969) 2426.
- [4] BELL J. S. and JACKIW R., *Nuovo Cimento A*, **60** (1969) 47.
- [5] HOSUR P. and QI X., *C. R. Phys.*, **14** (2013) 857.
- [6] SILVESTROV P. and EFETOV K., *Phys. Rev. Lett.*, **98** (2007) 016802.
- [7] DELERUE C. and ALLAN G., *Frontiers in Optics 2011/Laser Science XXVII, LWH* (APS) 2011.
- [8] ZHOLUDEV M. S. *et al.*, *Nat. Phys.*, **10** (2014) 233.
- [9] XU S. *et al.*, *Science*, **349** (2015) 613.
- [10] HUANG S. *et al.*, *Nat. Commun.*, **6** (2015) 7373.
- [11] LU L. *et al.*, *Science*, **349** (2015) 622.
- [12] LU L. *et al.*, *Phys. Rev. Lett.*, **114** (2015) 25301.
- [13] GREMAPEL D. R. *et al.*, *Phys. Rev. A*, **29** (1984) 1639.
- [14] CASATI G. *et al.*, *Phys. Rev. Lett.*, **62** (1989) 345.
- [15] CHABÉ J. *et al.*, *Phys. Rev. Lett.*, **101** (2008) 255702.
- [16] SACHDEV S. *et al.*, *Phys. Rev. B*, **66** (2002) 075128.
- [17] SIMON J. *et al.*, *Nature*, **472** (2011) 307.
- [18] GERRITSMAN R. *et al.*, *Nature*, **463** (2010) 68.
- [19] GERRITSMAN R. *et al.*, *Phys. Rev. Lett.*, **106** (2011) 060503.
- [20] SÜSTRUNK R. and HUBER S. D., *Science*, **349** (2015) 47.
- [21] METCALF H. J. *et al.*, *Phys. Rev. Lett.*, **54** (1985) 2596.
- [22] KLEIN O., *Z. Phys.*, **53** (1929) 157.
- [23] MAJORANA E., *Nuovo Cimento*, **9** (1932) 43.
- [24] BERGEMAN T. H. *et al.*, *J. Opt. Soc. Am. B*, **6** (1989) 2249.
- [25] SUKUMAR C. V. and BRINK D. M., *Phys. Rev. A*, **56** (1997) 2451.
- [26] PETRICH W. *et al.*, *Phys. Rev. Lett.*, **74** (1995) 3352.
- [27] ANDO T. *et al.*, *J. Phys. Soc. Jpn.*, **67** (1998) 2857.
- [28] RIDINGER A. *et al.*, *Eur. Phys. J. D*, **65** (2011) 223.
- [29] SIEVERS F. *et al.*, *Phys. Rev. A*, **91** (2015) 023426.
- [30] FERNANDES D. *et al.*, *EPL*, **100** (2012) 63001.
- [31] DEMARCO B. *et al.*, *Phys. Rev. Lett.*, **82** (1999) 4208.
- [32] KOHN W., *Phys. Rev.*, **123** (1961) 1242.
- [33] SURKOV E. L. *et al.*, *Phys. Rev. A*, **49** (1994) 4778.
- [34] DAVIS K. *et al.*, *Phys. Rev. Lett.*, **75** (1995) 5205.
- [35] CHOMAZ P. *et al.*, *Ann. Phys.*, **320** (2005) 135.
- [36] RIGOL M. *et al.*, *Phys. Rev. Lett.*, **98** (2007) 050405.
- [37] KOLLER A. P. *et al.*, *Phys. Rev. A*, **92** (2015) 033608.
- [38] SALGER T. *et al.*, *Phys. Rev. Lett.*, **107** (2011) 240401.

## Quasi-Thermalisation of Fermions in quadrupole potentials

Johnathan Lau †,<sup>1</sup> Olga Goulko,<sup>2</sup> Daniel Suchet,<sup>3</sup> Thomas Reimann,<sup>4</sup> Cédric Enesa,<sup>4</sup> Frédéric Chevy,<sup>4</sup> and Carlos Lobo<sup>1</sup>

<sup>1</sup>*Mathematical Sciences, University of Southampton, Highfield, Southampton, SO17 1BJ, United Kingdom*

<sup>2</sup>*Department of Physics, University of Massachusetts, Amherst, MA 01003, USA*

<sup>3</sup>*École polytechnique, 61 Avenue de Saxe, 75007 Paris, France*

<sup>4</sup>*Laboratoire Kastler Brossel, ENS-PSL Research University, CNRS, UPMC, Collège de France 24, rue Lhomond, 75005 Paris, France*

(Dated: January 20, 2019)

We analyze some puzzling features of an experiment with a noninteracting classical gas of atoms in a quadrupole trap. Surprisingly, after a momentum kick, the momentum distribution remains anisotropic at long times, characterized by different temperatures along the different directions even though the motion along each direction is not independent of the others; also, the kick energy is not transmitted to orthogonal directions. To understand this we solve two closely related models, a spherically symmetric trap  $\simeq r^\alpha$  and a strongly confined gas along one direction, a “pancake” trap. We find that in the spherical trap the gas preserves the anisotropy of the kick at long times and explain this using the conservation of angular momentum and the virial theorem. Depending on the value of  $\alpha$  we find that the kick can cool or heat the orthogonal directions. We find also a first order phase transition if the spherical symmetry is broken, which is manifested as a discontinuity in the temperature behaviours. We explain this in terms of the orbital precession of the planes of motion due to the non-spherical part of the potential. The pancake trap is studied in terms of an effective 2D potential obtained by averaging the fast motion along the strongly confined direction and is shown to be quantitatively similar to the quadrupole case. The temperature anisotropy and direction independence are shown to result from the change in the 2D effective potential due to the kick.

PACS numbers: 03.65.Vf, 37.10.Jk, 67.85.-d

### I. INTRODUCTION

The theoretical study of classical mechanics in the absence of interactions, i.e. pure Hamiltonian dynamics, has a long history [? ]. An important part of it concerns the nature of the long-time behaviour of noninteracting systems in confining potentials, when the motion does not go off to infinity. However, its experimental study is not as well developed since there are very few systems which have both the absence of interactions and the long lifetime necessary.

Cold gases of spin polarised fermionic atoms have unique characteristics which allow us to study experimentally *pure* Hamiltonian dynamics (without collisions or mean-field), since they combine both low loss rates and easy imaging making them well suited for the study of the long-time behaviour of these systems. Perhaps their most important feature is that they can motivate new questions even in this well-studied topic. The phenomena we will study are also related to problems known in the context of cooling of bosonic atoms [? ? ] in the early days of studies of cold atoms. There the issue was of cross-thermalization of the motion of atoms in quadrupole potentials.

We will analyze a recent experiment conducted with  $10^7$  spin polarised  ${}^6\text{Li}$  fermionic atoms trapped in a magnetic quadrupole potential [? ]. After being sympathetically cooled with a gas of  ${}^{40}\text{K}$  which is later removed from the system, the  ${}^6\text{Li}$  gas remains in thermal equilibrium at a temperature  $T_0$  much higher than the Fermi temperature, making the gas non-degenerate but low enough for  $p$ -wave interactions to be negligible. Also, the atoms are fully spin polarised so  $s$ -wave scattering is forbidden due to their fermionic nature. For the same reason the mean field interactions are negligible. Hence, it behaves as a *classical non-interacting gas* where the motion of each atom is unaffected by the other atoms.

The quadrupole trapping potential experienced by the atoms is of the form

$$V(\mathbf{r}) = \mu_B b \sqrt{x^2 + y^2 + 4z^2}. \quad (1)$$

where  $\mu_B$  is the Bohr magneton and  $b$  is the magnetic field gradient, a positive quantity.

This potential is *non-integrable* since it has three degrees of freedom but only two constants of the motion (total energy  $E$  and angular momentum  $L_z$ ). As a consequence its dynamics exhibits chaotic behaviour in some regimes. In contrast, the more usual potential of standard atomic traps is a sum of harmonic terms of the form  $V_1(x) + V_2(y) + V_3(z)$  so that we can define three conserved energies, leading to an integrable problem. Note

<sup>†</sup>Deceased 21 May 2016

that, since the quadrupole potential cannot be written as the sum of potentials as in the harmonic case, the motion along one direction is not independent of the other two so that momentum and energy are constantly being exchanged between the three directions as the atom moves along the orbit.

After the gas reaches its initial thermal equilibrium state, it receives a “momentum kick”  $\mathbf{q}$  along a specific direction using a short magnetic bias field pulse which shifts every atom’s momentum  $\mathbf{p} \rightarrow \mathbf{p} + \mathbf{q}$  and increases its energy by  $\mathbf{p} \cdot \mathbf{q}/m + q^2/2m$ . But since the original (thermal) distribution before the kick is an even function of each component of  $\mathbf{p}$ , the first term drops out when averaged over the gas, so that the average energy change  $\Delta E$  per atom is:

$$\Delta E = q^2/2m. \quad (2)$$

After the kick, the gas evolves in the quadrupole trap for around 500ms before being released, a considerably longer time than the typical “period” of a thermal atom.

A time-of-flight measurement is then made of the doubly integrated momentum distribution:

$$np_x = \int dp_y dp_z n(p_x, p_y, p_z) \quad (3)$$

where  $n(\mathbf{p})$  is the momentum distribution. We define analogously  $np_{y,z}$ .

This very simple experimental protocol gives rise to some surprises [? ]:

1. *Stationary distribution*: by the time the gas is released, it has reached an apparently stationary distribution. Note that the appearance of a stationary distribution would not happen in the standard harmonic trap since a momentum kick would lead to undamped oscillations of the center of mass.

This stationary state of the gas is not due to collisions but to the fact that, in the quadrupole trap, the orbits of different atoms will have different, incommensurate periods leading to the relative dephasing of individual trajectories. This dephasing, when averaged over the whole gas, leads to a stationary distribution.

We might be tempted to consider that irreversibility has set in by this stage. In reality this is not true since the absence of collisions implies that no thermalization has occurred and the Boltzmann entropy remains constant.

2. *Anisotropic temperatures*: the long time stationary momentum distributions fit closely to a thermal distribution<sup>2</sup>  $np_{i=x,y,z} \propto \exp(-p_i^2/2mk_B T_i)$  but with  $T_x = T_y \neq T_z$ . In particular  $T_{x,y} < T_z$  if the

kick is along  $z$ , and if the kick is along  $x$ , then we still have  $T_x = T_y$  but now  $T_{x,y} > T_z$ . This is unexpected because the quadrupole potential is non-separable, continuously transferring energy and momentum between all directions for each atom, so we might expect naïvely that on average  $T_x \sim T_y \sim T_z$ , i.e. there would be a certain degree of ergodicity.

3. *Apparent separability of the  $z$  and  $x-y$  distributions*: for a kick along  $z$ , the width of the momentum distribution along  $x$  and  $y$  seems to be unchanged (i.e.  $T_{x,y} \simeq T_0$ ) whereas  $T_z$  increases. The energy increase  $\Delta E$  due to the kick is entirely concentrated into the  $z$  direction so that  $\Delta E \simeq 3/2 k_B \Delta T_z$  with  $\Delta T_z \equiv (T_z - T_0)$ . Likewise, if the kick is along  $x$ , the increase in kinetic energy along the  $z$  is negligible ( $T_z \simeq T_0$ ) but both  $T_x$  and  $T_y$  increase by the same amount ( $T_x = T_y$ ) so that  $\Delta E \simeq 3k_B \Delta T_x$ . This behaviour is consistent with a separation of the dynamics into  $z$  and  $xy$  plane components even though the potential is non-separable.

The naïve, straightforward conclusion from these observations is that *the gas seems to have thermalised in the absence of collisions (since the doubly-integrated momentum distributions [3](#) become gaussian-like, a hallmark of thermalization) but with some effective “decoupling” of the motion along  $z$  and  $xy$  directions leading to different temperatures  $T_z$  and  $T_{xy}$ .*

## A. Simulations

To further investigate these questions we simulate the experiment using molecular dynamics [? ? ] in a quadrupole potential without interactions. From now on we set  $m = k_B T_0 = \mu_B b = 1$ , which is equivalent to choosing  $m$  as the mass unit,  $l_0 = k_B T_0 / \mu_B b$  as the unit of length and  $t_0 = \sqrt{mk_B T_0} / \mu_B b$  as the unit of time.

The state of the gas can be described by the Boltzmann distribution  $f(\mathbf{r}, \mathbf{p}, t)$  which we normalize to unity:

$$\int d^3 \mathbf{r} \int d^3 \mathbf{p} f(\mathbf{r}, \mathbf{p}, t) = 1 \quad (4)$$

so that all extensive quantities are to be taken as averages per atom. All gas observables can be expressed in terms of ensemble averages over this distribution. For example, the final measured momentum distribution  $np_x$  from [3](#) is given by

$$np_x = \int d^3 \mathbf{r} \int dp_y dp_z f(\mathbf{r}, \mathbf{p}, t \rightarrow \infty). \quad (5)$$

To simulate this distribution we perform molecular dynamics simulations of the gas where the trajectory of each atom is calculated following the classical equations of motion. This method gives us full access to all observables, including the Boltzmann distribution itself. For

<sup>2</sup> for a discussion of the apparent thermalization see Appendix [A](#).

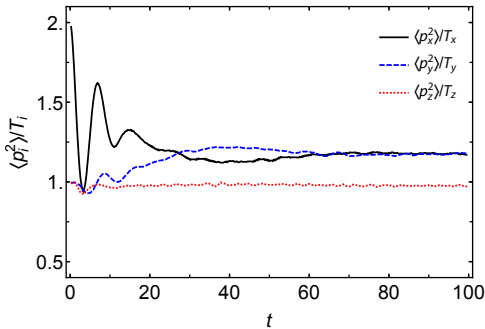


Figure 1. Kinetic energy per atom in the quadrupole trap along different directions as a function of time after a kick  $q = 1$  along  $x$  at  $t = 0$ . The energies seem to reach a stationary state after some time. The kinetic energy along  $z$  is almost unchanged from its initial value  $\sim 1$  but the energies along  $x$  and  $y$  increase by the same amount to a final value  $\sim 1.2$ .

example, we can measure the phase-space average  $\langle p_i^2 \rangle$  for  $i = x, y, z$  over the entire system as a function of time by averaging over the trajectories of individual atoms:

$$\langle p_i^2 \rangle_t \equiv \int d^3\mathbf{r} \int d^3\mathbf{p} p_i^2 f(\mathbf{r}, \mathbf{p}, t) \simeq \frac{1}{N} \sum_{\text{all atoms}} p_i^2(t), \quad (6)$$

We start with a gas of  $N = 10^5$  atoms sampled from the initial Boltzmann distribution at temperature  $k_B T_0 = 1$  with a momentum kick of  $q_x$  along  $x$ :

$$f \propto \exp\left(-\frac{(p_x - q_x)^2 + p_y^2 + p_z^2}{2} - V(x, y, z)\right) \quad (7)$$

(analogously for a kick  $q_z$  along  $z$  etc.) and let each individual atom evolve according to the classical trajectory. The time evolution is calculated using the velocity Verlet algorithm [? ?]. We use a time step  $\Delta t = 0.001t_0$ , which provides sufficient accuracy, as the error of the algorithm is of the order  $\mathcal{O}(\Delta t^2)$ .

The results of our simulations confirm the experimental observations. In Fig. 1 we plot  $\langle p_i^2 \rangle_t$  from which we can find an effective temperature defined analogously to the experiment:

$$T_i \equiv \langle p_i^2 \rangle_{t \rightarrow \infty} \text{ so that } \Delta T_i \equiv \langle p_i^2 \rangle_{t \rightarrow \infty} - \langle p_i^2 \rangle_{t=0}. \quad (8)$$

The gas reaches a stationary state after a few periods; generally we have  $T_x \sim T_y \neq T_z$  and for a kick along  $x$  we have  $T_z \sim T_0 < T_{x,y}$ .

We can be more quantitative regarding the  $\Delta T_i$ . We first notice that the quadrupole potential 1 is homogeneous of order one, (a potential homogeneous of order  $\alpha$  has the property that  $V(\lambda\mathbf{r}) = \lambda^\alpha V(\mathbf{r})$ ). So we can apply the Virial Theorem which leads to the following relation [? ]:

$$\Delta E = \frac{3}{2}(\Delta T_x + \Delta T_y + \Delta T_z). \quad (9)$$

Furthermore, for small kicks we can derive some symmetry considerations and a sum rule. Defining the matrix  $\Theta_{ij}$  as

$$\Delta T_i \equiv \sum_j \Theta_{ij} \frac{q_j^2}{2} \quad (10)$$

where  $i, j = x, y, z$ , it is possible to show that this matrix is symmetric so that, for small kick momentum, we have that  $\Theta_{ij} = \Theta_{ji}$ . This means that the degree of transverse heating is identical along different directions.

More generally it is straightforward to show using 2 and 9 that, if the potential is homogeneous of order  $\alpha$ , the  $\Theta_{ij}$  satisfy the constraint

$$\sum_j \Theta_{ij} = \frac{2\alpha}{2 + \alpha}. \quad (11)$$

For potentials with axial symmetry around the  $z$  axis, which is the case of the quadrupole trap, the fact that the matrix is symmetric and that in any kick  $\Delta T_x = \Delta T_y$  imply that the matrix can be written using only three distinct elements  $\theta_{1,2,3}$  as

$$\Theta = \begin{pmatrix} \theta_1 & \theta_1 & \theta_2 \\ \theta_1 & \theta_1 & \theta_2 \\ \theta_2 & \theta_2 & \theta_3 \end{pmatrix}. \quad (12)$$

Using the sum rule we find  $\theta_2 + 2\theta_1 = \theta_3 + 2\theta_2 = 2/3$  which leaves us with a single unknown parameter. The experimentally measured value  $\Delta T_z / q_z^2 / 2 = 2/3$  (see point 3 of the Introduction) implies  $\theta_3 = 2/3$ ,  $\theta_2 = 0$  and  $\theta_1 = 1/3$ , the latter also being in agreement with the measured value.

The quadrupole simulations confirm the experimental observations (1-3) (see Fig 1) even though there is a small correction to the experimental values: a slight cooling of the directions transverse to the kick so that  $\Theta_{xx} = 0.36$  (instead of  $1/3$ ) and  $\Theta_{xz} = -0.05$ . So the observation of point 3, the apparent separability of the  $z$  and  $x - y$  distributions seems not to be perfect but rather an excellent approximation. <sup>3</sup>

## B. Anisotropy of the momentum distribution

We can study the gas dynamics by analyzing individual atomic trajectories and then averaging over initial conditions. However the trajectories can be quite difficult to find due to the nonintegrability of the potential. To show this we constructed a Poincaré map: in Fig. 2, we see that there are both chaotic and quasi-integrable regions. A study of the gas starting from its individual

<sup>3</sup> We also investigated anisotropic potentials, finding very similar behaviour.

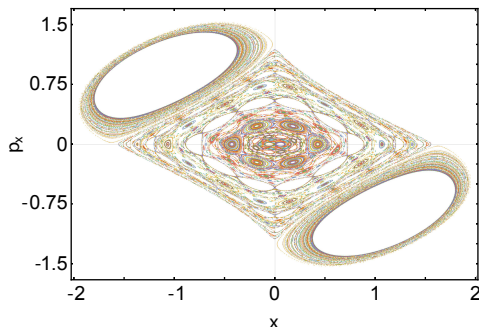


Figure 2. Poincaré map of the quadrupole potential. We study trajectories with the same energy but different initial phase-space coordinates. The values of  $x$  and  $p_x$  are recorded whenever  $z = 0$  and  $p_z > 0$ . We see the appearance of small islands denoting invariant torii close to which quasi-integrable trajectories evolve, separated by contiguous regions of chaotic dynamics.

trajectories would be quite complex analytically. For this reason, it is easier to study not the potential **1** but cases which might contain the same physics but in which all or nearly all trajectories are integrable or quasi-integrable. For example let us consider the family of potentials

$$V_\epsilon(x, y, z) = \sqrt{x^2 + y^2 + (1 + \epsilon)z^2}. \quad (13)$$

When  $\epsilon = 3$  we get the quadrupole potential **(1)**. But if we take  $\epsilon = 0$  the potential becomes spherically symmetric and therefore integrable. Alternatively, if  $\epsilon \gg 1$  then we are left with a highly confined potential along the  $z$  direction (a ‘‘pancake’’) so that the motion simplifies again and an effective motion in the  $x - y$  plane can be studied.

We will begin with the study of the spherical potential in section **II** which, surprisingly, exhibits many of the phenomena of the quadrupole potential, including the anisotropy of the momentum distribution. After this we will analyze the pancake case in section **III**, comparing both of these limits with the quadrupole potential.

## II. SPHERICAL POTENTIAL

The simulations in the quadrupole potential suggest that after perturbing an equilibrium gas along a particular direction, the ensemble average of the momentum widths  $\langle p_i^2 \rangle_t$  converges to a stationary distribution in the long time limit  $t \rightarrow \infty$ . In particular, we observed that  $\langle p_x^2 \rangle_\infty = \langle p_y^2 \rangle_\infty$  and in general  $\langle p_x^2 \rangle_\infty \neq \langle p_z^2 \rangle_\infty$ .

Calculating the final momentum widths  $\langle p_i^2 \rangle_\infty$  for a gas of atoms in the quadrupole potential from first principles is difficult without understanding the individual trajectories. Therefore, as mentioned above, it is a natural simplification to consider instead the case where we

remove the anisotropy in the quadrupole potential:

$$V_{\epsilon=0}(x, y, z) = \sqrt{x^2 + y^2 + z^2} = r, \quad (14)$$

where  $r$  is the radial coordinate (for the rest of this section we will drop the subscript  $\epsilon = 0$ ). Naïvely, one would expect that perturbing a gas along any direction in such an spherical potential will lead to an isotropic distribution at long times:  $\langle p_x^2 \rangle_\infty = \langle p_y^2 \rangle_\infty = \langle p_z^2 \rangle_\infty$ . However, as we shall see, the final momentum width along the direction of the perturbation will be different to that along perpendicular directions. To anticipate some of the conclusions of this section: this is intuitively plausible: in a spherical potential all three components of angular momentum are conserved, so the motion of each atom is confined to a plane passing through  $r = 0$  and perpendicular to its angular momentum. The population of each plane is therefore constant during the motion. In thermal equilibrium, this population is the same for all planes but a momentum kick will cause a transfer of atoms between planes, so that the population of each plane will depend on its angle relative to the kick direction. This anisotropy in populations in the distribution is preserved at long times again due to conservation of angular momentum and translates into different final temperatures along the different directions.

### A. Averages over the motion in planes

With a particle in a central field [? ? ], the trajectory stays on the plane perpendicular to its angular momentum  $\mathbf{L}$  which includes the origin  $r = 0$ . Using polar coordinates  $(r, \theta)$  for the plane, the energy  $E$  is given by the usual expression:

$$E = \frac{1}{2} (\dot{r}^2 + r^2 \dot{\theta}^2) + V(r) = \frac{1}{2} \left( \dot{r}^2 + \frac{L^2}{r^2} \right) + V(r) \quad (15)$$

where  $L = |\mathbf{L}| = r^2 \dot{\theta} = \text{constant}$ . In a potential such as **(14)**, the motion is confined between two values of the radial coordinate  $r_{\min} \leq r \leq r_{\max}$  which are solutions of  $\dot{r} = 0$ . During the time in which  $r$  varies from  $r_{\max}$  to  $r_{\min}$  and back, the radius vector turns through an angle  $\Delta\theta$ . The condition for the path to be closed is that this angle should be a rational fraction of  $2\pi$ , i.e. that  $\Delta\theta = 2\pi m/n$ , where  $m$  and  $n$  are integers. But according to Bertrand’s theorem [? ] the only central potentials for which all paths are closed are Kepler’s ( $\propto -\frac{1}{r}$ ) and the harmonic potential ( $\propto r^2$ ). For all other potentials (and excluding the particular case of trajectories with zero angular momentum), the trajectory will behave as in Fig. **3**: it will become dense everywhere, filling the allowed annulus region isotropically so that the orbital density is only a function of the radius  $r$  as the propagation time tends to infinity.

Using Bertrand’s theorem, we would like to analyse the long time behaviour of trajectories, in particular the time

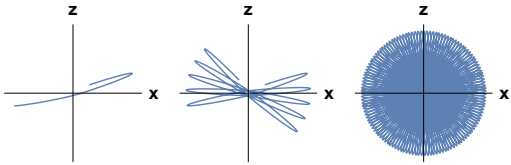


Figure 3. Orbit of atom in a plane with a central potential  $V(r) = r$  after increasingly long times from left to right. Since the trajectory never closes, according to Bertrand's theorem, it fills the annular region between  $r_{\max}$  and  $r_{\min}$  in an isotropic, dense fashion as  $t \rightarrow \infty$ .

averages of different quantities. For a quantity  $A(t)$ , the time average of a quantity  $\bar{A}$  is defined as (cf. 6):

$$\bar{A} \equiv \lim_{t \rightarrow \infty} \frac{1}{t} \int_0^t A(t') dt'. \quad (16)$$

We can convert the time average to one over the orbital density discussed above by a change of variables. We immediately conclude that, since Bertrand's theorem implies that the orbital density is isotropic, so will the time average also be:

$$\overline{x^2} = \overline{y^2} \quad (17)$$

$$\overline{p_x^2} = \overline{p_y^2}. \quad (18)$$

We will use this fact to calculate  $\langle p_i^2 \rangle_\infty$  for a gas of atoms.

### B. Calculation of momentum averages in terms of integrals of planes

Although our purpose is to study the potential  $V(r) = r$  as a limiting case of the family 13, it is straightforward to consider in this section a more general potential than (14), namely

$$V(r) = r^\alpha \quad (19)$$

with  $0 < \alpha \neq 2$ . This will allow us to examine qualitatively different behaviour as a function of  $\alpha$ . The case  $\alpha = 2$  corresponds to the isotropic harmonic potential for which in general (17) and (18) are not true. For  $\alpha = 1$  we recover (14).

For a gas in a spherical potential, the atoms belonging to the same plane in coordinate space are also confined to the same plane in momentum space making each plane an independent system. So our strategy will be to treat the motion in each plane separately and then add over all of them at the end. For this we choose a coordinate system (see Appendix B) where two of the coordinates (the angles  $\theta$  and  $\phi$ ) define the plane, and the remaining four correspond to the in-plane coordinates ( $u$  and  $v$ ) and momenta ( $p_u$  and  $p_v$ ). Then we can write the total energy as

$$\langle E \rangle = \int_0^\pi d\phi \int_0^\pi d\theta \langle E \rangle_{\text{plane}}. \quad (20)$$

where  $\langle E \rangle_{\text{plane}}$  is the average energy of all the planes lying between  $\theta$  and  $\theta + d\theta$ ,  $\phi$  and  $\phi + d\phi$ . Even though the probability density  $f(\mathbf{r}, \mathbf{p}, t)$  is a function of time, the energy of each atom is constant in time as the potential is time-independent and there is no exchange of energy between the atoms, so the average energy is also a constant. Therefore if we know the probability density  $f(\mathbf{r}, \mathbf{p}, t)$  at any one time, we will know the average energy for all time. This allows us to calculate the final momentum widths  $\langle p_i^2 \rangle_\infty$  from the distribution of energies at  $t = 0$  after the initial momentum kick.

Since the class of potentials (19) is homogeneous of order  $\alpha$  we use the Virial Theorem:

$$\overline{K} = \frac{\alpha}{2} \overline{V}. \quad (21)$$

where  $K$  is the kinetic energy and the averages are over time as in 16. Note that the Virial Theorem is valid both for each atom individually as well as for the entire gas. If we assume that at long times, when the gas has reached a steady state, the ergodic hypothesis applies for such systems, we can replace the time average with the ensemble average

$$\langle K \rangle = \frac{\alpha}{2} \langle V \rangle. \quad (22)$$

As each plane is a closed individual system, (22) also applies to

$$\langle K \rangle_{\text{plane}} = \frac{\alpha}{2} \langle V \rangle_{\text{plane}}, \quad (23)$$

and using (23),  $\langle E \rangle_{\text{plane}}$  can be written as

$$\begin{aligned} \langle E \rangle_{\text{plane}} &= \langle K \rangle_{\text{plane}} + \langle V \rangle_{\text{plane}} \\ &= \frac{2 + \alpha}{\alpha} \langle K \rangle_{\text{plane}} \\ &= \frac{2 + \alpha}{2\alpha} (\langle p_u^2 \rangle + \langle p_v^2 \rangle). \end{aligned} \quad (24)$$

According to Bertrand's Theorem, Kepler's potential  $V(r) = -\frac{k}{r}$  and radial harmonic oscillator  $V(r) = \frac{1}{2}kr^2$  are the only two types of central force potentials where all bound orbits are also closed orbits. Therefore, if we restrict ourselves to cases where  $0 < \alpha \neq 2$  where almost all orbits are open (except for the circular orbit), we see that  $\langle p_u^2 \rangle = \langle p_v^2 \rangle$  as  $t \rightarrow \infty$  so that, following the argument of section II A,

$$\langle p_u^2 \rangle = \langle p_v^2 \rangle = \frac{\alpha}{2 + \alpha} \langle E \rangle_{\text{plane}}. \quad (25)$$

We can now express the the averages of  $p_x^2$ ,  $p_y^2$  and  $p_z^2$  through  $\langle E \rangle_{\text{plane}}$  as shown in Appendix C (assuming that the final distribution does not depend on  $\phi$ )

$$T_{x,y} = \langle p_{x,y}^2 \rangle = \frac{\alpha\pi}{2(2 + \alpha)} \int_0^\pi d\theta \langle E \rangle_{\text{plane}} (1 + \sin^2 \theta) \quad (26)$$

$$T_z = \langle p_z^2 \rangle = \frac{\alpha\pi}{2 + \alpha} \int_0^\pi d\theta \langle E \rangle_{\text{plane}} \cos^2 \theta. \quad (27)$$

It remains now to calculate  $\langle E \rangle_{\text{plane}}$  as a function of  $\theta$  and  $\phi$  after the momentum kick.

### C. Momentum Kick

We perturb the Maxwell-Boltzmann distribution in a potential given by (19) at  $t = 0$  by applying a momentum kick  $q_z$  along the  $z$ -direction. The resulting initial distribution at temperature  $k_B T_0 = 1$  is:

$$f(\mathbf{r}, \mathbf{p}, t = 0) = A \exp\left(-\frac{p_x^2 + p_y^2 + (p_z - q_z)^2}{2} - r^\alpha\right) \quad (28)$$

where

$$A = \frac{3}{8\sqrt{2\pi}^{5/2}\Gamma\left(\frac{3+\alpha}{\alpha}\right)}. \quad (29)$$

If we transform (28) using (B3), we get:

$$f = A \exp\left(-\frac{q_z^2}{2}\right) \exp(-r^\alpha) \exp\left(-\frac{p_r^2 - 2p_r q_z \cos\theta \sin\alpha_p}{2}\right). \quad (30)$$

Using (30), we can calculate  $\langle V \rangle_{\text{plane}} = \langle r^\alpha \rangle$ ,  $\langle K \rangle_{\text{plane}} = \langle p_r^2 \rangle / 2m$  and finally  $\langle E \rangle_{\text{plane}} = \langle V \rangle_{\text{plane}} + \langle K \rangle_{\text{plane}}$ .

$$\langle V \rangle_{\text{plane}}(t = 0) = \frac{3|\cos\theta|}{\alpha\pi} e^{-\frac{q_z^2}{2}} e^{\frac{q_z^2 \cos^2\theta}{4}} \times \left[ I_1\left(\frac{q_z^2 \cos^2\theta}{4}\right) \frac{q_z^2 \cos^2\theta}{4} + I_0\left(\frac{q_z^2 \cos^2\theta}{4}\right) \left(\frac{1}{2} + \frac{q_z^2 \cos^2\theta}{4}\right) \right] \quad (31)$$

$$\langle K \rangle_{\text{plane}}(t = 0) = \frac{|\cos\theta|}{8\pi} \exp\left(-\frac{q_z^2}{2}\right) \exp\left(\frac{q_z^2 \cos^2\theta}{4}\right) \times \left[ q_z^2 I_1\left(\frac{q_z^2 \cos^2\theta}{4}\right) \cos^2\theta (4 + q_z^2 \cos^2\theta) + I_0\left(\frac{q_z^2 \cos^2\theta}{4}\right) (6 + 6q_z^2 \cos^2\theta + q_z^4 \cos^4\theta) \right] \quad (32)$$

where  $I_0$  and  $I_1$  are modified Bessel functions of the first kind. Since  $\langle E \rangle_{\text{plane}}$  does not change with time we can use this to obtain the  $\langle p_i^2 \rangle$  at  $t \rightarrow \infty$  via Eqs. (26,27). For  $\alpha = 1$  the resulting expressions read

$$\langle p_x^2 \rangle = \frac{q_z^2}{12} + \frac{5}{6} + \frac{1}{2q_z^2} - \frac{\sqrt{2}}{2q_z^3} F\left(\frac{q_z}{\sqrt{2}}\right), \quad (33)$$

$$\langle p_z^2 \rangle = \frac{q_z^2}{6} + \frac{4}{3} - \frac{1}{q_z^2} + \frac{\sqrt{2}}{q_z^3} F\left(\frac{q_z}{\sqrt{2}}\right), \quad (34)$$

where  $F$  is the Dawson function. In Fig. 4 we show the excellent agreement of the simulations with these analytical predictions.

For a small momentum kick, we can find some illuminating expressions. Expanding  $\langle E \rangle_{\text{plane}}$  about  $q_z = 0$  up to  $\mathcal{O}(q_z^2)$  we obtain from (26) and (27)

$$T_{x,y} \approx 1 + \frac{5\alpha - 2}{20(2 + \alpha)} q_z^2 \quad (35)$$

$$T_z \approx 1 + \frac{2 + 5\alpha}{10(2 + \alpha)} q_z^2. \quad (36)$$

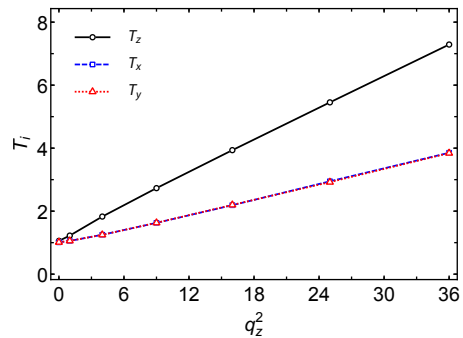


Figure 4. Isotropic potential (19) with  $\alpha = 1$  for different kick strengths  $q_z$  in  $z$ -direction. Comparing simulation results for  $\langle p_x^2 \rangle$ ,  $\langle p_y^2 \rangle$  and  $\langle p_z^2 \rangle$  with the analytical predictions (33) and (34). Note that the predicted  $\langle p_x^2 \rangle$  and  $\langle p_y^2 \rangle$  are identical.

For the case  $\alpha = 1$  we find

$$T_{x,y} \approx 1 + \frac{1}{20} q_z^2 \Rightarrow \Delta T_{x,y} = \frac{1}{10} \Delta E, \quad (37)$$

$$T_z \approx 1 + \frac{7}{30} q_z^2 \Rightarrow \Delta T_z = \frac{7}{15} \Delta E. \quad (38)$$

which satisfies the Virial Theorem 9. Comparing with the quadrupole experiment (point 3 of the Introduction) where  $\Delta T_{x,y} = 0$  and  $\Delta T_z = 2/3 \Delta E$ , we see that the spherical case leads to some increased heating in the  $xy$  plane although small.

In terms of the matrix  $\Theta_{ij}$  from 10, for a spherically symmetric case we can show that

$$\Theta_{ij} = \begin{pmatrix} \theta_1 & \theta_2 & \theta_2 \\ \theta_2 & \theta_1 & \theta_2 \\ \theta_2 & \theta_2 & \theta_1 \end{pmatrix} \quad (39)$$

so that e.g.  $\Delta T_x = \theta_1 q_x^2 / 2$  and  $\Delta T_y = \theta_2 q_y^2 / 2$ . As before, using the sum rule, we find that  $\theta_1 + 2\theta_2 = 2/3$  so that the matrix depends only on a single unknown parameter. Then (35) and (36) imply that

$$\theta_1 = \frac{2 + 5\alpha}{5(2 + \alpha)} \text{ and } \theta_2 = \frac{5\alpha - 2}{10(2 + \alpha)} \quad (40)$$

which satisfy the sum rule 11. For the case  $\alpha = 1$  (14) we get  $\theta_1 = 7/15$  and  $\theta_2 = 1/10$ .

### D. Heating and cooling of transverse directions

These results allow us to answer an interesting question: if we kick the gas along a direction, do the transverse directions heat or cool?

For an interacting gas, we know collisions will distribute the energy along all directions, hence the transverse directions will be heated by the same amount as the kicked direction. For an ideal gas in e.g. a harmonic potential, the transverse directions will not be affected.

Using (35) and (36) we see that, for a noninteracting gas in a spherical potential of the form (19), we can have different types of behaviour (up to  $\mathcal{O}(q_z^2)$ ) for the transverse directions:

- for  $\alpha < \frac{2}{5}$ : cooling;
- for  $\alpha = \frac{2}{5}$ : no change;
- for  $\alpha > \frac{2}{5}$ : heating.

This surprising result tells us that it is possible in some cases to *cool* the gas along some directions while heating it up along others. In fact, as we will see later the quadrupole potential is of this type: it cools along the  $x$  and  $y$  directions if kicked along  $z$ . Nevertheless, the spherical potential, which most closely resembles it, with  $\alpha = 1$ , behaves more conventionally since it heats up.

### E. Population redistribution due to kick

We would like to gain some insight into why the final momentum widths are different  $\langle p_x^2 \rangle = \langle p_y^2 \rangle \neq \langle p_z^2 \rangle$  for  $q_z \neq 0$ .

We can rewrite 26 using the fact that the total energy of the gas  $E_{\text{total}}(q=0) + \Delta E$  with  $\Delta E$  given by 2, can be expressed as the sum of the plane energies:

$$E_{\text{total}}(q=0) + \frac{q_z^2}{2} = \int_0^\pi d\phi \int_0^\pi d\theta \langle E \rangle_{\text{plane}} = \pi \int_0^\pi d\theta \langle E \rangle_{\text{plane}} \quad (41)$$

The term  $E_{\text{total}}(q=0)$  can be easily found from the  $q_z=0$  limit of 31 and 32. It follows that:

$$\begin{aligned} \langle p_{x,y}^2 \rangle &= \frac{\alpha\pi}{2(2+\alpha)} \int_0^\pi d\theta \langle E \rangle_{\text{plane}} (1 + \sin^2 \theta) \\ &= \frac{\alpha}{2(2+\alpha)} \left( \frac{q^2}{2} + \frac{6+3\alpha}{2\alpha} + \pi \int_0^\pi d\theta \langle E \rangle_{\text{plane}} \sin^2 \theta \right) \\ &\stackrel{\alpha=1}{=} \frac{1}{6} \left( \frac{q_z^2}{2} + \frac{9}{2} \right) + \frac{\pi}{6} \int_0^\pi d\theta \sin^2 \theta \langle E \rangle_{\text{plane}}. \end{aligned} \quad (42)$$

We can study how each of the terms in  $\langle p_x^2 \rangle$  varies with  $q_z$ . In Fig. 5, we can see that the contribution of the integral term of 42 is small compared to the  $q_z^2$  term and becomes less important as  $q_z$  increases.

To understand why the integral term becomes small, we can investigate how  $\langle E \rangle_{\text{plane}}$  changes as a function of  $\theta$  for different values of  $q_z$ . From Fig. 6, we can see that the value of  $\langle E \rangle_{\text{plane}}$  near  $\theta=0$  and  $\theta=\pi$  increases with increasing  $q_z$  and the opposite happens near  $\theta=\pi/2$ . As the integrand multiplies this factor by  $\sin^2 \theta$  which is 0 at  $\theta=0, \pi$  and peaks at  $\theta=\pi/2$  the integral will decrease as  $q_z$  increases.

To make it even clearer, it is useful to plot not  $\langle E \rangle_{\text{plane}}$  but  $\langle E \rangle_{\text{plane}} / |\cos \theta|$  which removes the effect of the Jacobian B2 which simply accounts for the variation of the density of planes as a function of  $\theta$ , leaving us with the change in plane energy as a result of the kick.

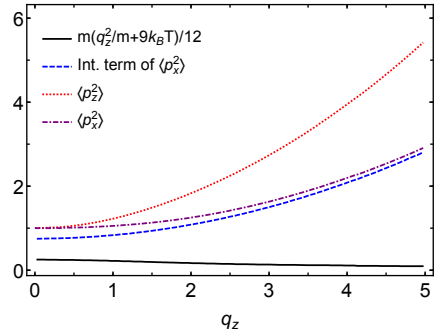


Figure 5. Comparing the different terms of  $\langle p_x^2 \rangle$  in 42 with  $\langle p_x^2 \rangle$  34 for different value of momentum kick  $q_z$  with  $m = k_B T = 1$ .

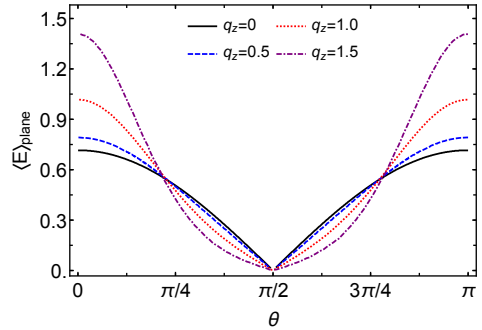


Figure 6. Using 31 and 32 to plot  $\langle E \rangle_{\text{plane}}(\theta)$  for different value of momentum kick  $q_z$ .

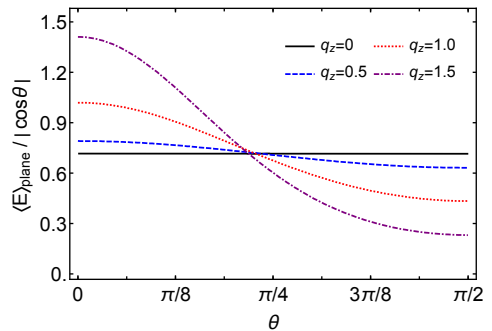


Figure 7. Using Eqs 31 and 32 to plot  $\langle E \rangle_{\text{plane}}(\theta) / |\cos \theta|$  for different value of momentum kick  $q_z$ .

From Fig. 7, we can see that when there is no momentum kick, the energy of all the planes are the same. When we apply a momentum kick along the  $z$ -axis, planes lying along that direction ( $\theta=0$  or  $\pi$ ) gain energy whereas directions close  $\theta=\pi/2$  lose it. This means that, when we project the energy of each plane to obtain the momentum

widths,  $\langle p_z^2 \rangle > \langle p_x^2 \rangle$ .

We can also see that as  $q_z \rightarrow \infty$ ,  $\langle E \rangle_{\text{plane}} / |\cos \theta|$  is only non-zero at  $\theta = 0$  and  $\pi$  which explains the momentum widths ratio constraint derived in C10 (note that Fig. 8 agrees with the ratio constraint).

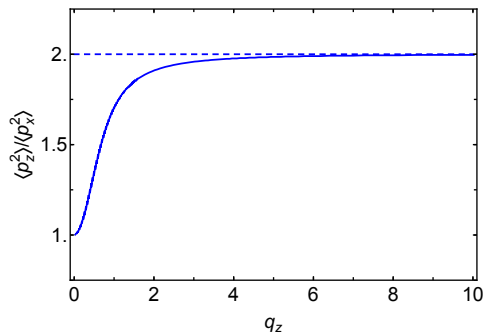


Figure 8. Using 31 and 32 to plot the ratio between  $\langle p_z^2 \rangle$  and  $\langle p_x^2 \rangle$  for different value of momentum kick  $q_z$ .

### F. Memory loss in isotropic potentials

A natural question arising from the study of this section is whether a gas can remember in which direction it was kicked after a long time has passed. For example we could start with a gas in thermal equilibrium in an isotropic potential, i.e. a spherically (3D) or circularly (2D) symmetric potential, apply a momentum kick along an arbitrary direction and wait for a very long time. Is the final gas distribution anisotropic? I.e. does it preserve a memory of the direction of the kick?

In a collisional gas, the extra energy from the momentum kick is redistributed along all directions equally leading to isotropic heating and therefore a loss of memory.

A non-interacting gas in a harmonic oscillator preserves this memory because its center of mass oscillates along the kick direction indefinitely.

However, quite surprisingly, a non-interacting gas in non-separable potential can also preserve it due to the existence of integrals of motion which encode the direction. For example in a 3D spherical potential the memory is associated with the three components of angular momentum  $L_{x,y,z}$  being integrals of the motion as we have seen.

An interesting question is: can there be memory loss with no interactions and a non-separable potential? Unexpectedly the answer is yes: for example a gas in a 2D circular symmetric potential has  $\langle p_x^2 \rangle = \langle p_y^2 \rangle$  due to Bertrand's theorem, so memory is lost (excluding harmonic and Kepler's potential). There is only a single component of angular momentum so the direction cannot be encoded in the integrals of the motion. After the kick the extra energy is redistributed to all directions, the "orbit density" becomes isotropic as  $t \rightarrow \infty$  which

leads to loss of memory. This macroscopic loss of information is due to ergodicity of the individual trajectories rather than to collisions. Of course, microscopically the memory is preserved since, if we reversed the momenta of all atoms at the same time, we could recover the initial kicked distribution.

### G. First order transition due to breaking of the potential's spherical symmetry

As we have seen, if we start with an isotropic equilibrium thermal distribution in a spherical trap ( $\epsilon = 0$ ) and we kick the gas along the  $z$  direction then, when  $t \rightarrow \infty$ , we find that  $T_x = T_y \neq T_z$ . Likewise, by spherical symmetry, kicking along the  $x$  direction will lead to the temperatures along the perpendicular directions being equal ( $T_y = T_z \neq T_x$ , see Fig 9).

However, this is in seeming contradiction with the experimental results for the quadrupole case ( $\epsilon = 3$ ), see point 2 of the Introduction and Fig 1, where a kick along the  $x$  direction leads to  $T_x = T_y$ . It seems that, breaking the spherical symmetry by setting  $\epsilon > 0$  and making the  $z$  direction unequal, enforces a cylindrical symmetry of the steady state gas distribution along the perpendicular directions after the kick. This discrepancy in behaviour indicates a discontinuous (first order) transition in gas behaviour as a function of  $\epsilon$  when going from spherical to non-spherical potentials.

To study this better we plot the three final temperatures after a kick along  $x$  as a function of  $\epsilon$  near  $\epsilon = 0$  (Fig 9). We see that, at  $\epsilon = 0$ ,  $T_y = T_z < T_x$  as expected. However, for values of  $\epsilon$  immediately above that, we find that  $T_x = T_y > T_z$ , the behaviour of the quadrupole trap. In other words:

$$\lim_{\epsilon \rightarrow 0} \lim_{t \rightarrow \infty} \langle p_x^2 - p_y^2 \rangle_t \neq \lim_{t \rightarrow \infty} \lim_{\epsilon \rightarrow 0} \langle p_x^2 - p_y^2 \rangle_t \quad (43)$$

the lhs being zero and the rhs not. We will see that the reason for this is due to  $\langle p_x^2 - p_y^2 \rangle_t$  relaxing to zero with a relaxation or dephasing time scale  $\tau$  which diverges as  $\epsilon \rightarrow 0$ .

There is a characteristic relaxation time  $\tilde{\tau}$  before the momentum widths reach their final steady state value during which there is a gradual dephasing of the orbits of atoms with different angular momenta and energy in each plane. This timescale is related to the width of the thermal distribution and does not depend on  $\epsilon$  as  $\epsilon \rightarrow 0$ . From dimensional analysis we see that  $\tilde{\tau} \sim \sqrt{T_0}$ .

However, there is a second much longer characteristic relaxation time  $\tau$  during which  $T_x$  and  $T_y$  converge to each other and which was not present in the perfectly spherical case. This timescale appears because of the rotation (precession) of the orbital planes of each atom around the  $z$  axis and is due to the potential's anisotropy. This phenomenon is known in astronomy when studying the orbit of satellites around slightly non-spherical planets, where it is called nodal precession [?].

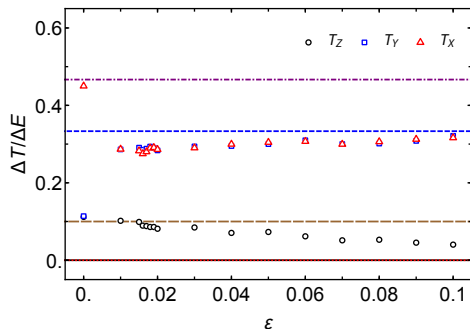


Figure 9. Behaviour of the final temperatures  $\Delta T_i/\Delta E$  as a function of the anisotropy  $\epsilon$  near the spherical limit after a kick along  $x$ . At  $\epsilon = 0$   $T_z = T_y$  after which there is a discontinuous change in the temperatures due to the breaking of spherical symmetry along  $z$ . Data are obtained by numerical simulation over 100 000 atoms. Dotted lines show the prediction for an isotropic trap (37, 38), dashed lines show the values  $\Theta_{zx} = 0$  and  $\Theta_{xx} = 1/3$  for the quadrupole configuration.

For sufficiently small  $\epsilon$  and at long times  $t \gg \tau$ , we expect that  $\langle p_x^2 - p_y^2 \rangle_t$  will decay at long times as some function of  $t/\tau$  where the decay time scale is given by

$$\tau \sim \sqrt{T_0} \times \epsilon^\nu. \quad (44)$$

The value of  $\nu$  is independent of the kick strength if it is weak enough, and the dependence on  $\sqrt{T_0}$  sets the dimensions of  $\tau$ . We show in Appendix D that  $\nu = -1$  so that  $\tau \sim 1/\epsilon$ ; this is confirmed in Fig. 10.

While Bertrand's equilibrium leads to a higher temperature along the kicked direction, the orbital precession redistributes the energy equally between the  $x$ - and  $y$ -axes, leading eventually to the equilibration of  $T_x$  and  $T_y$ . The first process takes place in about 40 time units, while the latter process is much slower as the anisotropy is smaller, as shown in Fig. 10.

This analysis leads to quantitative predictions for the final temperatures at small anisotropy, particular for the temperature discontinuities. For  $\epsilon \gtrsim 0$ , the imparted energy gets first redistributed in the plane, before the orbital precession slowly equilibrates temperatures so that we can express the final temperatures in terms of the spherical temperatures 37, 38:

$$\Delta T_x^{\epsilon \rightarrow 0} = \Delta T_y^{\epsilon \rightarrow 0} = \frac{1}{2} (\Delta T_x^{\epsilon=0} + \Delta T_y^{\epsilon=0}) \quad (45)$$

$$= \frac{17}{60} \Delta E \quad \text{and} \quad (46)$$

$$\Delta T_z^{\epsilon \rightarrow 0} = \Delta T_z^{\epsilon=0} \quad (47)$$

$$= \frac{1}{10} \Delta E. \quad (48)$$

From here we can extract the matrix elements of 12 since in the above equations  $\Delta E = q_x^2/2$ :  $\theta_1 = 17/60$ ,  $\theta_2 = 1/10$ , which means that  $\theta_3 = 7/15$ .

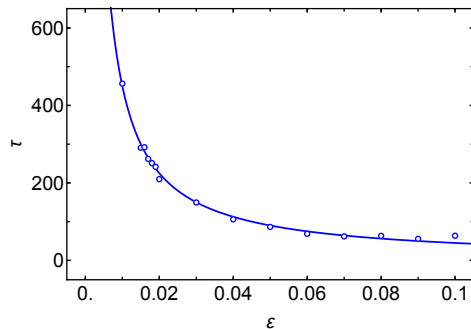


Figure 10. Equilibration time as a function of the trap anisotropy  $\epsilon$ . The equilibration time is defined as the time required for  $T_y$  to reach 99% of the steady  $T_x$  value. The solid line is a fit  $A \times \epsilon^{-1}$  following the expression (44). The best fit leads to an R-squared value of 0.99.

This prediction is in very good agreement with the results presented in Fig. 9 and is valid near  $\epsilon = 0$  as long as  $\tau \gg \tilde{\tau}$ .

### III. PANCAKE POTENTIAL

In the previous section we analyzed the spherically symmetric case which could be solved analytically. There is another case where the motion can be solved analytically, namely the limit when the confinement along the  $z$ -direction is strong ( $\epsilon \gg 1$ ). As we will see later, this case exhibits behaviour which is much closer to the quadrupole.

We consider the case of strong confinement of the gas along the  $z$  direction of the potential 13 with  $\epsilon \gg 1$  so that

$$V(\mathbf{r}) = \sqrt{x^2 + y^2 + (1 + \epsilon)z^2} \simeq \sqrt{\rho^2 + \epsilon z^2} \quad (49)$$

where we have used cylindrical coordinate  $\rho = \sqrt{x^2 + y^2}$ . Since potential is tightly confined, motion along the  $z$  direction is fast compared to that in the plane. To check this we compare  $t_z$ , the period of oscillation along  $z$  with the period of oscillation along  $\rho$ ,  $t_\rho$ , the characteristic timescales of the two motions.

An atom whose motion is along the  $x$ -axis experiences a potential  $V = x$ , whereas if the atom moves along the  $z$ -axis sees a potential  $V = \epsilon z$ . Assuming that both of these atoms have the same overall thermal energy  $T$ , then, in the first case, its period of oscillation is  $T_\rho \propto \sqrt{E}$  whereas in the second case it is  $T_z \propto \sqrt{E}/\epsilon$  so that  $T_\rho/T_z = \epsilon \gg 1$  so that the approximation of considering the motion along  $z$  to be fast compared with that in the plane is justified.

We start by analysing the motion of a single atom. We

split up the energy as:

$$E = \frac{p_\rho^2}{2} + \frac{p_\phi^2}{2\rho^2} + E_z \quad (50)$$

with  $p_\rho$  and  $p_\phi$  being the canonically conjugate momenta and  $\phi = \arctan(y/x)$  is the angle with the  $x$  axis in the  $xy$  plane.  $E$ ,  $p_\phi$  are constants of the motion (the latter being the angular momentum  $L_z$  which is always conserved due to the potential being independent of  $\phi$ ). Also,

$$E_z = \frac{p_z^2}{2} + \sqrt{\rho^2 + \epsilon z^2} \quad (51)$$

We now replace  $p_z, z$  with the action-angle variables  $I, \eta$  in the usual way. In particular

$$\begin{aligned} I &= \oint p_z \frac{dz}{2\pi} = 4 \int_0^{z_{\max}} p_z \frac{dz}{2\pi} \\ &= \frac{2\sqrt{2}}{\pi} \int_0^{\sqrt{\frac{E_z - \rho^2}{\epsilon}}} \sqrt{E_z - \sqrt{\rho^2 + \epsilon z^2}} dz \\ &= \frac{2\sqrt{2}}{\pi\sqrt{\epsilon}} I_0 \end{aligned} \quad (52)$$

with the definition

$$I_0 \equiv \int_0^{\sqrt{E_z - \rho^2}} \sqrt{E_z - \sqrt{\rho^2 + z'^2}} dz' \quad (53)$$

where we made the substitution  $z' = \sqrt{\epsilon}z$  to show that  $I \propto 1/\sqrt{\epsilon}$ , since  $I_0$  does not depend on  $\epsilon$ . Note that, for the same reason, in 53  $E_z$  depends implicitly only on  $I_0$  and  $\rho$  but not on  $\epsilon$ .

The trajectory  $p_z(z)$  is determined by 51 and therefore depends on  $E_z$  and  $\rho$ . Also, since  $\rho$  is slowly varying, by the standard arguments,  $I$  (or  $I_0$ ) can be considered an adiabatic invariant (i.e. another constant) for the motion in the plane.

A simple approximate solution to 53 which allows us to express  $E_z$  explicitly in terms of  $I_0$  and  $\rho$  is

$$E_z(I_0, \rho) = \left( \frac{3}{2} I_0 + \rho^{3/2} \right)^{2/3} \quad (54)$$

which allows us to rewrite 50 as

$$E = \frac{p_\rho^2}{2} + \frac{p_\phi^2}{2\rho^2} + \left( \frac{3}{2} I_0 + \rho^{3/2} \right)^{2/3} \quad (55)$$

and we see that the effective potential for the radial motion is a sum of the centrifugal term plus a confining term increasing linearly at large distances.

Since we had originally three degrees of freedom, a particular trajectory is completely determined by the three integrals of the motion  $E$ ,  $p_\phi$  and  $I_0$ . Therefore, the time averaged in-plane kinetic energy

$$\frac{p_\rho^2}{2} + \frac{p_\phi^2}{2\rho^2} \quad (56)$$

is also determined by these constants.

It is now clear that the averaged kinetic energy is only a function of the constants of the motion  $E$ ,  $p_\phi$ , and  $I_0$  for that orbit.

The adiabatic principle tells us that the atom executes a motion in the plane under the effective potential  $E_z$  given by 54. Since  $I_0$  is not the same for all atoms, each atom moves in slightly different potentials, labelled by their value of  $I_0$ .

When we apply a kick to an atom along  $z$  at a time  $t_0$ , its in-plane momenta  $p_\phi$ ,  $p_\rho$  and its position  $\rho$ ,  $z$  are unchanged. What changes instead is its momentum  $p_z$  and therefore its corresponding kinetic energy  $p_z^2/2 \rightarrow (p_z + q)^2/2 = p_z^2/2 + p_z q + q^2/2$ . After averaging over the whole gas, the term  $p_z q$  drops out so that only the third term remains, an average increase of kinetic energy of  $q^2/2$  per atom (and so of  $E_z(\rho_0)$  as we see from 51). This has two effects: it changes the effective potential 54 and it increases the total energy  $E$ . Since  $I_0$  is an increasing function of  $E_z$ , an increase of the kinetic energy along  $z$  at  $t_0$  implies an instantaneous change  $I_0 \rightarrow I_0 + \Delta I_0$ ,  $\Delta I_0 > 0$ . In the subsequent motion, the effective potential is changed  $E_z(I_0, \rho) \rightarrow E_z(I_0 + \Delta I_0, \rho)$ , transforming it into a shallower effective 2D potential as we can see from 54. On the other hand, the increased kinetic energy also means an increased total energy  $E \rightarrow E + \Delta E$ :

$$\Delta E = E_z(I_0 + \Delta I_0, \rho_0) - E_z(I_0, \rho_0) \quad (57)$$

The first effect leads naturally to a reduction in speed in the plane, i.e. a reduction in the average in-plane kinetic energy 56. However, the increase  $\Delta E$  has the opposite effect, that of increasing the average kinetic energy. This latter effect is dominant for atoms which were near the bottom of the potential at the moment of the kick whereas the reduction in  $\Delta E$  is most felt by those which were away from the centre.

To determine what happens to the gas as a whole, we resort to simulations. We compare the results of the pancake case after a kick along  $z$  with a very large  $\epsilon$  with the case of a 2D gas in the effective potential 54, with the same number of atoms, temperature and kick momentum  $q$ .

For the simulation of the 2D gas, we use the same initialization of the system as for the regular pancake case, namely the kicked Boltzmann distribution with potential (49). Then for each individual atom we evaluate  $I_0$  via Eq. (54), where  $E_z$  and  $\rho$  are determined by the initial position and momentum coordinates of the atom. The subsequent time-evolution of each atom is governed by Eq. (55), where the last term corresponds to the new effective potential 54 which replaces the regular pancake potential (49) ( $I_0$  is assumed constant for each atom during the time-evolution). Note that we only evaluate the movement of the gas in the  $xy$  plane in this approximation—the position and momentum coordinates in  $z$ -direction do not appear in the equations.

We are also able to use the same method to study the

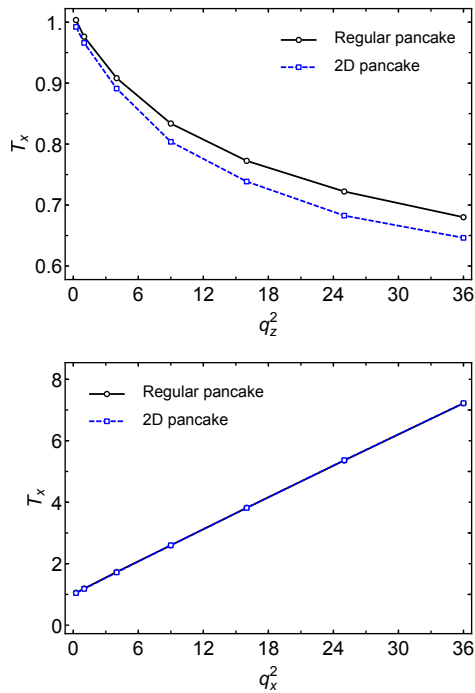


Figure 11. Comparison of the 2D potential given by 54 and the pancake potential. Here  $\epsilon = 100$ , but larger  $\epsilon$  values produced consistent results. The plots are for  $\langle p_x^2 \rangle$  as a function of  $q_z^2$  (top panel), and as a function of  $q_x^2$  (bottom panel). Dashed lines are to guide the eye. Note that the two potentials give almost identical results for the heating along the kick direction and a small discrepancy for the orthogonal cooling.

change in average kinetic energy along  $z$  due to a kick in the plane along  $x$ .

Our findings are in Fig. 11. We see that there is excellent agreement between the 3D pancake gas and the 2D especially for the heating along the direction of the kick. Although both show cooling of the transverse directions, the agreement is less good there, a fact which we attribute to the inexact ansatz 54.

So the physical interpretation of the pancake case is clear: there is a slight overall cooling of the transverse directions when the gas is kicked along the  $z$  direction due to the effective potential becoming shallower for the atoms closer to the center of the trap. This effect dominates over the heating of the atoms near the edges of the gas, although not by much so that the overall cooling is very small.

#### IV. COMPARING THE POTENTIALS

In Fig. 12 we compare the quadrupole potential with the two others we have discussed, the spherical and the pancake. It is clear that the quadrupole behaviour is much closer to that of the pancake so that, in this re-

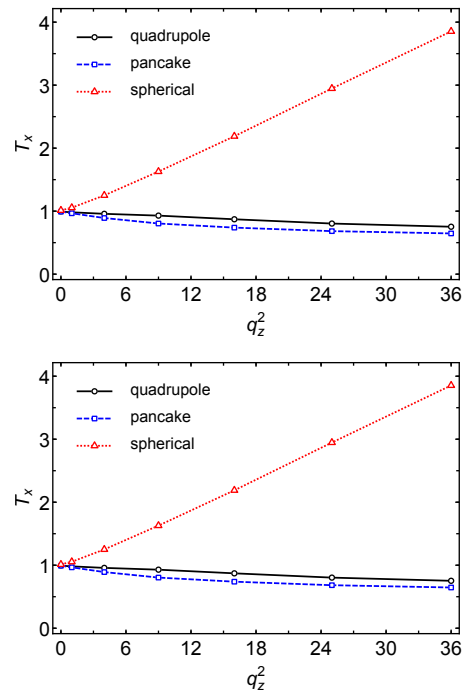


Figure 12. Comparison of three types of potential: spherical ( $\epsilon = 0$ ), quadrupole ( $\epsilon = 3$ ) and pancake ( $\epsilon = 100$ ) showing the much better agreement between the quadrupole and the pancake compared with the spherical case. The top panel shows  $\langle p_z^2 \rangle$  and the bottom panel  $\langle p_x^2 \rangle$  as a function of the momentum kick  $q_z^2$  in  $z$ -direction. The red solid lines are the analytical predictions (33) and (34) for the spherical potential. Dashed lines for the other potentials are to guide the eye.

spect, it seems that the  $\epsilon = 3$  is already very close to the limit of  $\epsilon = \infty$ . There is a remarkably good quantitative agreement between the two cases. For example we obtain approximately the same heating and cooling in both the kicked and transverse directions. We find for the pancake  $\Theta_{xx} = 0.38$  and  $\Theta_{zx} = -0.09$  which can be compared with the very similar values for the quadrupole  $\Theta_{xx} = 0.36$  and  $\Theta_{zx} = -0.05$  mentioned in the Introduction.

In the Introduction we mentioned two puzzles; one was the anisotropy of the temperatures along the kicked and orthogonal directions in the quadrupole potential. Both the spherical and pancake potentials exhibit this. For the spherical case this is due to a geometric reason, the fact that the kick redistributes the atoms into planes which are more aligned with the direction of the kick. They will subsequently remain there due to the conservation of angular momentum. In the pancake case this is due to strong potential anisotropy coming from the large value of  $\epsilon$ . This latter reason is responsible also for the anisotropy in the quadrupole potential.

Also, in the spherical case we saw that the temperatures of the kicked direction and of the plane orthogo-

nal to it were different. In the quadrupole case we find generally in all simulations that  $T_x = T_y \neq T_z$ . This was interpreted in terms of the 2D effective description where Bertrand's theorem applies; it leads naturally to the isotropy of the distribution in the  $xy$  plane. Clearly the quadrupole gas has this behaviour for the same reason.

The second puzzle was the apparent (near) separability of the kicked and orthogonal directions, i.e. that the kick energy is *not* redistributed into the momentum distributions of all directions but rather it is concentrated only in the kick direction. As we see from Fig. 12, the spherical and pancake potentials behave very differently: the pancake reproduces closely the quadrupole's separability (in fact a slight cooling of the orthogonal directions) while the spherical potential shows a clear heating of those directions. The reason for the separability in the quadrupole case can be traced to the 2D model where it is due to a near cancellation of the contributions of the atoms which, at the moment of the kick, are close to the center of the trap and are cooled and that of the atoms at the periphery which are heated.

## V. CONCLUSIONS

We began with some puzzling experimental results for a classical gas in a quadrupole trap: momentum kicks along one direction seemed to affect only that direction, despite the fact that the potential is non-separable. By analyzing the extreme case of the spherical potential ( $\epsilon = 0$ ) we understood that in some systems, the constants of the motion (e.g. the angular momentum components) can allow the system to retain a memory of the direction of the kick so that in an *isotropic* system, the long time momentum distribution can remain anisotropic. This however did not explain some of the features the quadrupole case. We then investigated the pancake case (large  $\epsilon$ ) which is much closer to the quadrupole and exhibits many of the same features such as cooling of the degrees of freedom transverse to the kick direction. We found numerically that this case is much closer to the quadrupole and gives us an explanation of the experimental results in terms of the effective 2D potential.

## ACKNOWLEDGMENTS

The authors would like to thank

### Appendix A: "Thermalization" of the momentum distributions

We mentioned in the Introduction that the gas seemed to have thermalized in the absence of interactions since both from the experiments and the simulations show that

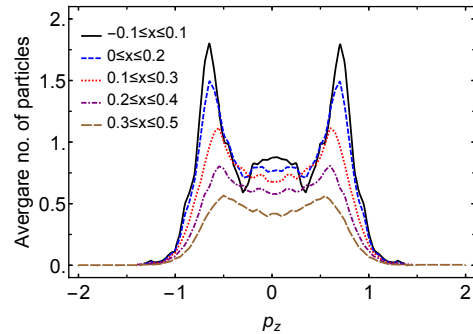


Figure 13. The long time Boltzmann distribution  $f$  after a kick along  $z$  plotted as a function of  $p_z$  keeping all other variables  $x, y, z, p_x, p_y$  fixed and for different values of  $x$ . To obtain a nonzero number of atoms in the six dimensional volume we considered a narrow region in phase space given by the coordinates in the figure and divided it into bins. We plot the number of atoms in each bin averaged over time. It can be seen that  $f$  does not resemble a gaussian thermal function and that the three peaks feature becomes more prominent for  $x$  closer to the centre. Similar results are found plotting along all other coordinates.

the doubly-integrated momentum distributions **3** become gaussian after the kick.

Of course, since the effective temperatures deduced from the width of the gaussians are different ( $T_z \neq T_{x,y}$ ) the state cannot be a true thermal state. Indeed, collisions are necessary to redistribute the kick energy  $\Delta E$  among all accessible microstates of energy  $E + \Delta E$  so that the entropy increases too  $S(E) \rightarrow S(E + \Delta E)$  whereas in this experiment,  $E \rightarrow E + \Delta E$  but entropy is unchanged ( $S(E)$ ). Nevertheless, as can be seen from the experimental results, several "thermal" properties *can* be achieved, e.g. equilibration of temperatures along the  $x$  and  $y$  directions.

We can ask to what extent the final state of the gas is close to a thermal state. For example, could it be e.g. a product of three different Gaussians (with different temperatures) of the type

$$f \sim e^{-p_x^2/2T_x} e^{-p_y^2/2T_y} e^{-p_z^2/2T_z} \times e^{-V/T} \quad ? \quad (\text{A1})$$

It is easy to see that this is not possible since it does not satisfy the time independent collisionless Boltzmann equation. We can plot  $f$  as a function of one of its six coordinates keeping all others fixed as in Fig. 13 which shows a markedly non bell-shaped curve. In fact, the gaussian character is only restored upon integration of the other five coordinates of the Boltzmann distribution e.g.:

$$np_x = \int d^3\mathbf{r} \int dp_y dp_z f(\mathbf{r}, \mathbf{p}, t \rightarrow \infty) \propto e^{-p_x^2/2mk_B T_x} \quad (\text{A2})$$

which raises the question of why averages over complex distributions such as those of Fig. 13 lead to a gaussian

ansatz. We will not consider this question further here, leaving it for further study.

### Appendix B: Coordinate transformation for the spherical case

(Add diagram) In a spherical potential the motion of each atom is confined to a plane through the origin and perpendicular to its angular momentum. To treat the gas in each plane as a separate system it is convenient to choose coordinates where the motion in each plane is described by in-plane 2D coordinates along orthogonal axes labelled  $(u, v)$  with corresponding momenta  $(p_u, p_v)$ . To relate these to the rectangular coordinates we define two angles  $\theta$  and  $\phi$ .  $\theta$  is the angle between the  $z$  axis and the  $v$  axis.  $\phi$  is the angle between the  $x$ -axis and the projection of the  $v$ -axis onto the  $x$ - $y$  plane. Both angles are in the interval  $[0, \pi]$ . The coordinate transformation is thus:

$$\begin{aligned} x &= u \sin \phi + v \sin \theta \cos \phi \\ y &= -u \cos \phi + v \sin \theta \sin \phi \\ z &= v \cos \theta \\ p_x &= p_u \sin \phi + p_v \sin \theta \cos \phi \\ p_y &= -p_u \cos \phi + p_v \sin \theta \sin \phi \\ p_z &= p_v \cos \theta. \end{aligned} \quad (\text{B1})$$

Note that it is not a canonical transformation since the Jacobian is:

$$J_1 = |(p_u v - p_v u) \cos \theta|. \quad (\text{B2})$$

The  $\cos \theta$  term has a simple interpretation: the angular density of planes having an angle  $\theta$  with the  $z$ -axis is largest for small  $\theta$  and drops to zero when  $\theta = \pi/2$  since then there is only one plane perpendicular to the  $z$ -axis. In most cases, the calculation becomes simpler if we use polar coordinates in the plane:

$$\begin{aligned} u &= r \cos \alpha_r \\ v &= r \sin \alpha_r \\ p_u &= p_r \cos \alpha_p \\ p_v &= p_r \sin \alpha_p, \end{aligned}$$

where  $\alpha_r$  and  $\alpha_p$  are in the interval  $(0, 2\pi]$ . The transformation (B1) becomes:

$$\begin{aligned} x &= r \cos \alpha_r \sin \phi + r \sin \alpha_r \sin \theta \cos \phi \\ y &= -r \cos \alpha_r \cos \phi + r \sin \alpha_r \sin \theta \sin \phi \\ z &= r \sin \alpha_r \cos \theta \\ p_x &= p_r \cos \alpha_p \sin \phi + p_r \sin \alpha_p \sin \theta \cos \phi \\ p_y &= -p_r \cos \alpha_p \cos \phi + p_r \sin \alpha_p \sin \theta \sin \phi \\ p_z &= p_r \sin \alpha_p \cos \theta. \end{aligned} \quad (\text{B3})$$

The Jacobian for the transformation (B3) is

$$J_2 = r^2 p_r^2 |\sin(\alpha_r - \alpha_p) \cos \theta|. \quad (\text{B4})$$

As the Boltzmann function  $f(x, y, z, p_x, p_y, p_z, t)$  is normalised to unity, if we apply the transformations (B1) or (B3), the following quantities will also normalise to unity either in the  $(u, v, p_u, p_v, \theta, \phi)$  or in the  $(r, \alpha_r, p_r, \alpha_p, \theta, \phi)$  coordinates:

$$\begin{aligned} 1 &= \int_0^\pi d\phi \int_0^\pi d\theta \int_{-\infty}^\infty dp_u \int_{-\infty}^\infty dp_v \int_{-\infty}^\infty du \int_{-\infty}^\infty dv J_1 f \\ &= \int_0^\pi d\phi \int_0^\pi d\theta \int_0^{2\pi} d\alpha_p \int_0^\infty dp_r \int_0^{2\pi} d\alpha_r \int_0^\infty dr J_2 f. \end{aligned}$$

The average energy  $\langle E \rangle$  is given by

$$\langle E \rangle(t) \equiv \langle E \rangle_t = \int d^3 \mathbf{r} \int d^3 \mathbf{p} f(\mathbf{r}, \mathbf{p}, t) E(\mathbf{r}, \mathbf{p}). \quad (\text{B5})$$

It is useful to define an energy  $\langle E \rangle_{\text{plane}}(\theta, \phi)$  which is the average energy of all the planes lying between  $\theta$  and  $\theta + d\theta$ ,  $\phi$  and  $\phi + d\phi$

$$\langle E \rangle_{\text{plane}}(\theta, \phi) \equiv \int_0^{2\pi} d\alpha_r \int_0^{2\pi} d\alpha_p \int_0^\infty dp_r \int_0^\infty dr J_2 f E \quad (\text{B6})$$

so that the total energy is, cf. (20),

$$\langle E \rangle = \int_0^\pi d\phi \int_0^\pi d\theta \langle E \rangle_{\text{plane}}. \quad (\text{B7})$$

Note that, after the kick,  $\langle E \rangle_{\text{plane}}$  is independent of time as the number of atoms on each plane is constant.

### Appendix C: Averages over momenta

Using the transformation (B1), we can write the averages of  $p_x^2$ ,  $p_y^2$  and  $p_z^2$  as:

$$\langle p_x^2 \rangle = \langle p_u^2 \sin^2 \phi \rangle + \langle p_v^2 \sin^2 \theta \cos^2 \phi \rangle + 2\langle p_u p_v \sin \theta \sin \phi \cos \phi \rangle, \quad (\text{C1})$$

$$\langle p_y^2 \rangle = \langle p_u^2 \cos^2 \phi \rangle + \langle p_v^2 \sin^2 \theta \sin^2 \phi \rangle - 2\langle p_u p_v \sin \theta \sin \phi \cos \phi \rangle, \quad (\text{C2})$$

$$\langle p_z^2 \rangle = \langle p_v^2 \cos^2 \theta \rangle. \quad (\text{C3})$$

The first term of (C1) can be written in terms of  $\langle E \rangle_{\text{plane}}$  using (25),

$$\begin{aligned} \langle p_u^2 \sin^2 \phi \rangle &= \int_0^\pi d\phi \sin^2 \phi \int_0^\pi d\theta \int_{-\infty}^\infty dv \int_{-\infty}^\infty du \int_{-\infty}^\infty dp_v \int_{-\infty}^\infty dp_u J_1 f(u, v, p_u, p_v, \theta, \phi, t) p_u^2 \\ &= \int_0^\pi d\phi \sin^2 \phi \int_0^\pi d\theta \frac{m\alpha}{2 + \alpha} \langle E \rangle_{\text{plane}}. \end{aligned} \quad (\text{C4})$$

Using similar technique, (C1), (C2) and (C3) can be written as:

$$\langle p_x^2 \rangle = \frac{m\alpha}{2 + \alpha} \int_0^\pi d\phi \sin^2 \phi \int_0^\pi d\theta \langle E \rangle_{\text{plane}} + \frac{m\alpha}{2 + \alpha} \int_0^\pi d\phi \cos^2 \phi \int_0^\pi d\theta \sin^2 \theta \langle E \rangle_{\text{plane}} + 2\langle p_u p_v \sin \theta \sin \phi \cos \phi \rangle \quad (\text{C5})$$

$$\langle p_y^2 \rangle = \frac{m\alpha}{2 + \alpha} \int_0^\pi d\phi \cos^2 \phi \int_0^\pi d\theta \langle E \rangle_{\text{plane}} + \frac{m\alpha}{2 + \alpha} \int_0^\pi d\phi \sin^2 \phi \int_0^\pi d\theta \sin^2 \theta \langle E \rangle_{\text{plane}} - 2\langle p_u p_v \sin \theta \sin \phi \cos \phi \rangle \quad (\text{C6})$$

$$\langle p_z^2 \rangle = \frac{m\alpha}{2 + \alpha} \int_0^\pi d\phi \int_0^\pi d\theta \cos^2 \theta \langle E \rangle_{\text{plane}}. \quad (\text{C7})$$

The third term in (C5) and (C6) when written explicitly is:

$$\langle p_u p_v \sin \theta \sin \phi \cos \phi \rangle = \int_0^\pi d\phi \sin \phi \cos \phi \int_0^\pi d\theta \sin \theta \int_{-\infty}^\infty dv \int_{-\infty}^\infty du \int_{-\infty}^\infty dp_v \int_{-\infty}^\infty dp_u J_1 f(u, v, p_u, p_v, \theta, \phi, t) p_u p_v. \quad (\text{C8})$$

If  $f(u, v, p_u, p_v, \theta, \phi, t)$  is independent of  $\phi$  then (C8) equals to zero. If  $\langle E \rangle_{\text{plane}}$  is also independent of  $\phi$ , (C5), (C6) and (C7) will be reduced to:

$$\langle p_x^2 \rangle = \frac{m\alpha\pi}{2(2 + \alpha)} \int_0^\pi d\theta \langle E \rangle_{\text{plane}} (1 + \sin^2 \theta)$$

$$\langle p_y^2 \rangle = \frac{m\alpha\pi}{2(2 + \alpha)} \int_0^\pi d\theta \langle E \rangle_{\text{plane}} (1 + \sin^2 \theta)$$

$$\langle p_z^2 \rangle = \frac{m\alpha\pi}{2 + \alpha} \int_0^\pi d\theta \langle E \rangle_{\text{plane}} \cos^2 \theta.$$

We can see that  $\langle p_x^2 \rangle$  and  $\langle p_y^2 \rangle$  are equal. If we look at the ratio between  $\langle p_x^2 \rangle$  and  $\langle p_z^2 \rangle$ :

$$\frac{\langle p_x^2 \rangle}{\langle p_z^2 \rangle} = 2 \frac{\int_0^\pi \langle E \rangle_{\text{plane}} \cos^2 \theta}{\int_0^\pi \langle E \rangle_{\text{plane}} (1 + \sin^2 \theta)}, \quad (\text{C9})$$

as  $\langle E \rangle_{\text{plane}}(\theta) \geq 0$ , the ratio of the integrals will be between 0 and 1, therefore we can derive an inequality:

$$\langle p_z^2 \rangle \leq 2\langle p_x^2 \rangle. \quad (\text{C10})$$

## Appendix D: Calculation of dephasing rate

### 1. Initial distribution

We wish to study

$$\langle p_x^2 - p_y^2 \rangle_t = \int dr^3 dp^3 (p_x^2 - p_y^2) f(\mathbf{r}, \mathbf{p}, t) \quad (\text{D1})$$

However, since the gas is noninteracting, we can find time-dependent averages by following the position of individual atoms starting from an initial distribution of the gas and then averaging over that distribution. For example, to find  $\langle p_x^2 - p_y^2 \rangle_t$ , instead of finding the time dependence of the Boltzmann distribution  $f$ , we calculate the quantity  $p_x^2(t) - p_y^2(t)$  for each atom starting at the initial position  $(\mathbf{r}_0, \mathbf{p}_0)$  and then average over  $\mathbf{r}_0, \mathbf{p}_0$  weighted by the initial distribution:

$$\langle p_x^2 - p_y^2 \rangle_t = \int d\mathbf{r}_0 d\mathbf{p}_0 [p_x^2(t) - p_y^2(t)]_{\mathbf{r}_0, \mathbf{p}_0} \times f(\mathbf{r}_0, \mathbf{p}_0, t = 0) \quad (\text{D2})$$

We take the initial distribution from 7 and expand in powers of  $q$ :

$$\begin{aligned} f(t = 0) &\propto \exp\left(-\frac{(p_x - q)^2 + p_y^2 + p_z^2}{2T}\right) \exp\left(-\frac{V(x, y, z)}{T}\right) \\ &= \left(1 + \frac{p_x q}{T} - \frac{q^2}{2T} + \frac{1}{2} \left(\frac{p_x q}{T}\right)^2 + O(q^3)\right) f_{q=0} \end{aligned} \quad (\text{D3})$$

The first and third terms in the brackets do not contribute to D2 since they are spherically symmetric and remain so during time evolution. The second term  $\propto p_x q$  is odd under the parity transformation  $x, p_x \rightarrow -x, -p_x$ . Since this parity is preserved under time evolution, the integral of this term is zero for all time. The only term that contributes to D2 is the one proportional to  $(p_x q)^2$ . Therefore keeping the lowest nonzero term we obtain:

$$f(t = 0) = \frac{1}{2} \left(\frac{p_x q}{T}\right)^2 f_{q=0} \quad (\text{D4})$$

## 2. Precession of the orbital planes

To find this contribution we will make the crucial assumption that its orbital plane precesses slowly around the  $z$  axis compared with the fast motion in each plane so that we are allowed to use the virial theorem to calculate averages in the plane as in section

An orbital plane which is precessing will be characterised by a constant angle  $\theta$  and a rate of precession  $\dot{\phi}$ . To find this rate we consider a perturbation of the planar orbit in the limit of a small correction to the spherical potential. Since  $|\epsilon| \ll 1$ , we expand the potential in [13](#) to order  $\mathcal{O}(\epsilon)$ :

$$V = \sqrt{x^2 + y^2 + (1 + \epsilon)z^2} \simeq r + \Delta H \quad (\text{D5})$$

with

$$\Delta H \equiv \frac{z^2}{2r}\epsilon \quad (\text{D6})$$

being the perturbation of the Hamiltonian.

The rate of rotation of the orbital plane  $\dot{\phi}$  is given by [[?](#)]:

$$\dot{\phi} = \frac{1}{l} \frac{\partial \overline{\Delta H}}{\partial \cos i} \quad (\text{D7})$$

where  $i$  is the inclination of the orbital plane and is related to  $\theta$  via  $i = \frac{\pi}{2} - \theta$ ,  $l$  is the magnitude of angular momentum.  $\overline{\Delta H}$  is the time-averaged value of  $\Delta H$  calculated using the orbits of the *unperturbed* Hamiltonian.

If the orbit in the plane were closed, the averaging would be over the period of the unperturbed orbit. In our potential, almost all orbits are open so the period is not well defined. However if we average over a time on the order  $\tilde{\tau}$ , then we can assume that the plane of the orbit (i.e.  $\theta$ ) remains fixed during that time but that the time average over the motion in the plane has achieved a stationary value:

$$\overline{\Delta H} \equiv \frac{1}{\tilde{\tau}} \int_0^{\tilde{\tau}} \Delta H dt \quad (\text{D8})$$

and applying the co-ordinate transformation in ([B1](#)):

$$\frac{z^2}{\sqrt{x^2 + y^2 + z^2}} = \frac{v^2 \cos^2 \theta}{\sqrt{u^2 + v^2}} \quad (\text{D9})$$

$$= \frac{v^2}{\sqrt{u^2 + v^2}} \cos^2 \theta. \quad (\text{D10})$$

The last step uses the fact that the angle of the plane  $\theta$  has not changed appreciably after a time  $t$ .

Assuming that the averages over the time  $\tilde{\tau}$  are well reproduced using the Virial Theorem (since the unperturbed potential is simply  $V_{\epsilon=0} = r$ ), we know that:

$$\begin{aligned} E &= \frac{3}{2} \overline{V_{\epsilon=0}} \\ &= \frac{3}{2} \overline{\sqrt{u^2 + v^2}} \\ &= \frac{3}{2} \left( \overline{\frac{u^2}{\sqrt{u^2 + v^2}}} + \overline{\frac{v^2}{\sqrt{u^2 + v^2}}} \right). \end{aligned} \quad (\text{D11})$$

If we assume

$$\frac{\overline{u^2}}{\sqrt{u^2 + v^2}} = \frac{\overline{v^2}}{\sqrt{u^2 + v^2}} \quad (\text{D12})$$

we get

$$\frac{\overline{v^2}}{\sqrt{u^2 + v^2}} = \frac{E}{3}. \quad (\text{D13})$$

Therefore the perturbed Hamiltonian averaged over  $\tilde{\tau}$  is:

$$\begin{aligned} \overline{\Delta H} &= \frac{\epsilon E}{6} \cos^2 \theta \\ &= \frac{\epsilon E}{6} \sin^2 i \end{aligned} \quad (\text{D14})$$

and the rotation rate of the orbital plane is:

$$\begin{aligned} \dot{\phi} &= \frac{\epsilon E}{6l} \frac{\partial}{\partial \cos i} (\sin^2 i) \\ &= -\frac{\epsilon E}{3l} \cos i = -\frac{\epsilon E}{3l} \sin \theta \end{aligned} \quad (\text{D15})$$

so that the plane precesses at a constant rate. For a single atom on a plane  $\theta$ ,  $\phi$  (similarly to the calculations in [C](#))

$$\begin{aligned} \langle p_x^2 \rangle &= \langle p_u^2 \rangle \sin^2 \phi + \langle p_v^2 \rangle \sin^2 \theta \cos^2 \phi \\ &\quad + 2 \langle p_u p_v \rangle \sin \theta \sin \phi \cos \theta \end{aligned} \quad (\text{D16})$$

and similarly for  $\langle p_y^2 \rangle$ . The last term is zero  $\langle p_u p_v \rangle \rightarrow 0$  because of the isotropy due to Bertrand's theorem. Using [26](#) with  $\alpha = 1$  we get

$$\langle p_x^2 - p_y^2 \rangle_t = \frac{E}{3} \cos^2 \theta (\sin^2 \phi - \cos^2 \phi) \quad (\text{D17})$$

Here,  $\theta$  is a constant whereas  $\phi(t) = \phi_0 + \dot{\phi}t$ .

To find the total value, we use [D2](#):

$$\begin{aligned} \langle p_x^2 - p_y^2 \rangle_t &= \int d\mathbf{r}_0 d\mathbf{p}_0 (p_x^2(t) - p_y^2(t)) \times \left( \frac{p_{x0} q}{T} \right)^2 f_{q=0}(\mathbf{r}_0, \mathbf{p}_0) \\ &= \int d\mathbf{r}_0 d\mathbf{p}_0 \frac{E(\mathbf{r}_0, \mathbf{p}_0)}{3} \cos^2 \theta_0 (\sin^2 \phi(t) - \cos^2 \phi(t)) \\ &\quad \times \left( \frac{p_{x0} q}{T} \right)^2 f_{q=0}(\mathbf{r}_0, \mathbf{p}_0) \end{aligned} \quad (\text{D18})$$

We see that  $\langle p_x^2 - p_y^2 \rangle_t$  is a function of  $\epsilon t$  so  $\tau \sim 1/\epsilon$  since the only time dependence is through  $\dot{\phi}$ . So we conclude that in [44](#),  $\nu = -1$ .

## Appendix B

### Additional experimental setups and data

#### B.1. Tailoring arbitrary optical potentials using a digital micromirror device

Digital micromirror devices (DMD) are binary spatial light modulators made up of an two-dimensional array of micro-mirrors (see fig. B.1. These MEMS-type mirrors (microelectromechanical system) can switch light either on or off and also acts as a two dimensional echelle diffraction grating with, in our case, a pitch of  $d = 10.8 \mu\text{m}$ . At an angle of incidence of  $\vartheta_i$ , the exit angles  $\vartheta_n$  of the symmetric orders  $(n, n)$  are given by [258]:

$$\sin\left(\frac{\vartheta_i}{\sqrt{2}}\right) + \sin\left(\frac{\vartheta_n}{\sqrt{2}}\right) = \frac{n\lambda}{d}, \quad (\text{B.1})$$

where  $\lambda = 532 \text{ nm}$  denotes the wavelength of the incident light. The envelope of the diffracted intensity field is a  $\text{sinc}^2$  function, which is typically centered around the  $(0, 0)$ th order for conventional gratings. However, given that the DMD can tilt each micromirror by an angle of  $\pm 12^\circ$ , this constraint is lifted. In order to use the given optical power as efficiently as possible<sup>1</sup>, the angle of incidence has to be chosen in a way that matches the center of the  $\text{sinc}^2$  to one of the diffraction orders. This mode of operating a grating is usually referred to as 'blazed' and is oftentimes encountered in diode lasers, where the grating is typically used in the so called Littrow configuration [228]. The latter implies that the angle of incidence matches the one of a diffracted order, which serves to re-inject the diode with the spectrally filtered light. For the DMD the geometry has to be chosen differently as the light is supposed to be propagated to the atoms after having been modulated. This creates constraints based on the size of the incident beam and of the optics that are to be used to process the created pattern, the latter being intimately related to the resolution requirements. Taking  $\vartheta_n = 0$  and  $\vartheta_i \approx 24^\circ$ , one finds that  $n \approx 6$ . Further technical details regarding the general operation of DMDs as gratings can be found in [259–269].

---

<sup>1</sup>As was pointed out in 6.2.8, compensating gravity of a small cloud ( $\sim 50 \times 300 \mu\text{m}$ ) with off-resonant light at 532 nm already requires a total optical power of 1 W! Given that the maximum light utilization of a DMD is typically only 50-60%, one cannot afford to waste power for this application.

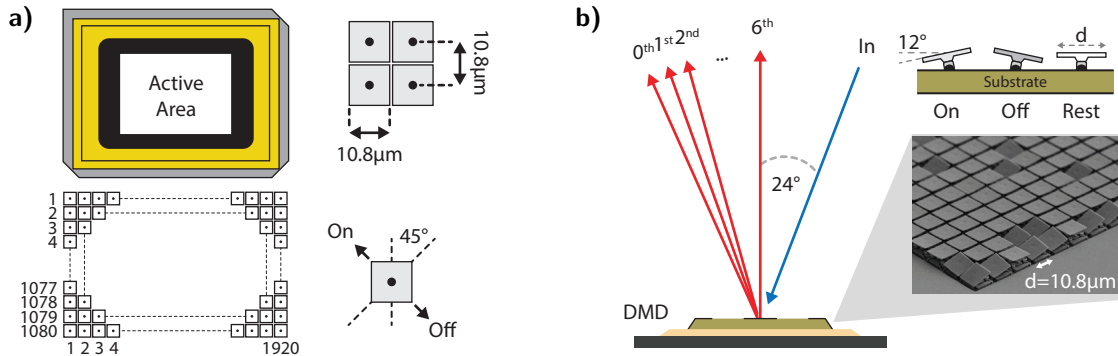


**Figure B.1:** Overview of the basic mechanical and optical properties of a DMD. a) Illustration of the basic layout of the DMD chip containing the array of  $1920 \times 1080$  micromirrors. b) Operation of a DMD as a blazed diffraction grating and close-up view of the actual MEMS mirrors (adapted from [270]).

### Error diffusion

If the DMD was an ideal light modulator whose reflectivity could be tuned smoothly from 0 to 1 as a function of position, any target profile  $I_{\text{tar}}$  could be created by subjecting the input profile  $I_{\text{in}}$  to the reflectance pattern

$$R_{\text{id}}(x, y) = \frac{I_{\text{tar}}(x, y)}{I_{\text{in}}(x, y)}. \quad (\text{B.2})$$

However, each pixel of the DMD can only be switched on ('image') or off ('dump'), which corresponds to unity or zero reflectivity and naturally implies that no gray levels in-between can be created. This situation creates two main problems that need to be addressed: First, one must find a method of how to display reflectance patterns on a binary device that somehow approximate the ideal one as defined above. Second, once this facsimile is found, gray levels have to be introduced by means of additional processing of the light fields.

There are many technical applications in every day life where a binary pattern needs to be made to appear as if it contained continuous gray levels. The process of printing newspapers using small dots of various sizes is one example in this context, which also inspires the approach to modulate light fields in seemingly non-binary way using a DMD. When viewing such 'dithered' patterns from afar, they appear as if they contained continuous gray levels because the eye lacks the resolving power to distinguish between the dots. The basic idea for the DMD is now to switch on more pixels in regions where high light intensity is desired while doing the opposite in regions that are supposed to be darker.<sup>2</sup> There are a number of dithering algorithms that can be used to determine how

<sup>2</sup>When a DMD is used as part of a video projector, the on/off timing of the mirrors is used to create the

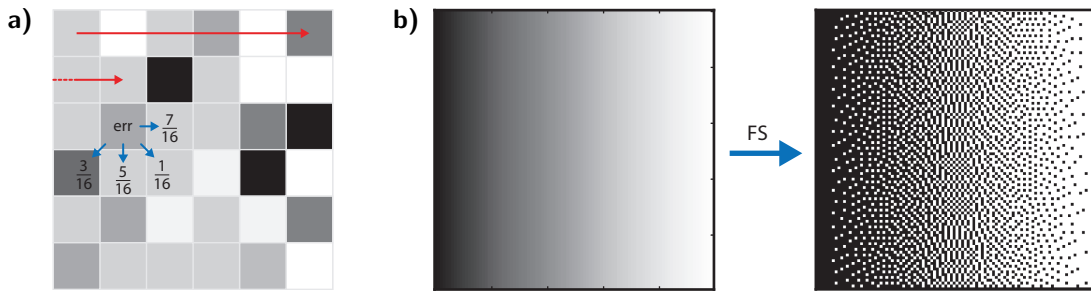


**Figure B.2.: Floyd-Steinberg error diffusion algorithm.** a) Schematic illustration of the propagation of the error in reflectivity to neighboring pixels. b) Example of the dithering algorithm being applied to a  $100 \times 100$  gradient map with values between 0 and 1.

one has to switch the mirrors of a DMD to obtain a halftoned version of  $R_{id}(x, y)$ . All of these algorithms are based on the process of error diffusion, where a given pixel's ideal reflectance  $0 \leq \bar{p}_{ij} \leq 1$  is compared to a certain fixed threshold  $p_{th}$ . If  $\bar{p}_{ij} > p_{th}$ , the pixel is set to 'on'  $p_{ij} = 1$  whereas it is set to 'off'  $p_{ij} = 0$  in the case when  $\bar{p}_{ij} \leq p_{th}$ . The resulting error  $\Delta_{ij} = \bar{p}_{ij} - p_{ij}$  is then distributed in weighted manner to the surrounding pixels in forward direction as the algorithm scans over the pattern. Note that for the relations given so far, the errors coming in from preceding pixels, which would alter the on/off decision, were omitted for clarity. In practice, the algorithm starts at the top row on the left and then moves toward the right before jumping back to the left side of the ensuing row. As it moves through the pattern row by row, it essentially 'pushes' the errors in front of it and works them into the on/off decisions. Depending on the pattern, a non-zero error may remain after the last pixel has been treated.

Here we employ the Floyd-Sternberg algorithm [234] due to its high degree of diffusion at minimal computational effort. An illustration is given in fig. B.2a and an example of a dithered gradient map can be found in B.2b.

### Spatial filtering

Despite its altered appearance, the light field created using a dithered pattern is still binary in nature and does not yet contain any intermediate gray levels other than 0 and 1. In order to rectify this situation the light field emerging from the DMD is subjected to an optical low pass filter, which removes a certain number of high spatial frequencies from the Fourier spectrum of the image. This blurring process is implemented in practice using a lens system in  $4f$  configuration with a variable size pinhole in the Fourier plane as depicted

---

appearance of gray levels as the switching times of  $\sim 10\,000\text{ s}^{-1}$  are much faster than the processing speed of the human eye and brain, leading to a temporal averaging of the perceived images. Similarly, a seemingly colored image can be produced by rapidly cycling the wavelength of the DMD's illumination light through red, green and blue.

in fig. B.5. This system represents one basic realization of the 4F-correlator [228] known from Fourier optics. Let  $O(x, y)$  be the intensity pattern at the object plane and  $I(x, y)$  the one of the image plane. In the absence of a pupil stop in the Fourier plane, the action of a symmetric  $4f$  imaging system on the input field is simply given by two successive Fourier transforms, which will merely invert the image as  $I(x, y) = \text{FT} [\text{FT} [O(x, y)]]^2 = O(-x, -y)$ . By introducing a circular aperture  $p(x, y)$  of appropriately chosen diameter  $a$  in the focal plane of the objective lens, one can selectively block certain Fourier components. The collector lens then reconstructs the image from an incomplete Fourier spectrum, which lacks certain high spatial frequencies:

$$I(x, y) = \text{FT} [p(x, y) \times \text{FT} [O(x, y)]]^2. \quad (\text{B.3})$$

Given that the sharp structures of an image are contained exactly in the high frequencies,  $I(x, y)$  will appear blurred with respect to the original input pattern  $O(x, y)$ .

In practice, the optimization of the size of the aperture depends on the pattern one wishes to create with the DMD. For example, if one aims to create a flat top potential, there will be a trade off between the RMS flatness, which increases as more spatial frequencies are removed, and the edge steepness of the profile that will broaden at the same time. This situation is shown in fig. B.4 for a square box light field created by the DMD. Another factor coming into play is the light utilization efficiency.

### Iterative refinement

The procedures outlined above can be complemented by providing active feedback to the DMD to improve the output profile [271]. The basic idea is to perform error diffusion as well as smoothing and then record the obtained result  $I_{\text{out}}$  to compare it to the intended profile  $I_{\text{tar}}$ . A better reflectance pattern can then be determined iteratively by using the error to improve upon the previous reflectivity pattern:

$$I_{\text{err}}(n) = I_{\text{tar}}(n) - I_{\text{out}}(n) \quad (\text{B.4})$$

$$I_{\text{tar}}(n + 1) = I_{\text{tar}}(n) + m \tanh(I_{\text{err}}(n)), \quad (\text{B.5})$$

where  $n = 1, 2, 3, \dots$  denotes the number of iterations. Note that error diffusion has to be performed at each stage of the iterative process. The addition of the  $\tanh$  term introduces a smoothing effect to the feedback.

### Programming of the DMD

Our DMD is has a chipset of the type DLP9500, which belongs to the DLP Discovery4100 series of Texas Instruments ('Digital Light Processing') that offers the highest degree of

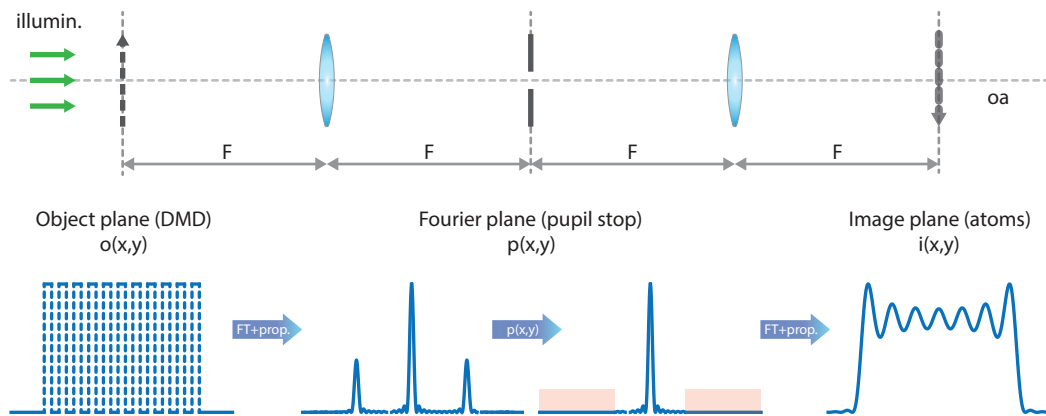


**Figure B.3.: Optical low pass filter based on a symmetric  $4f$  correlator.** Its mode of operation is illustrated using an array of rectangular functions as test image  $o(x, y)$ . The filter is comprised of four steps: Propagation and first Fourier transform; Removal of spatial frequencies by a pupil stop; Inverse Fourier transform from a reduced spectrum and propagation to the image plane, where a blurred image  $i(x, y)$  is formed.

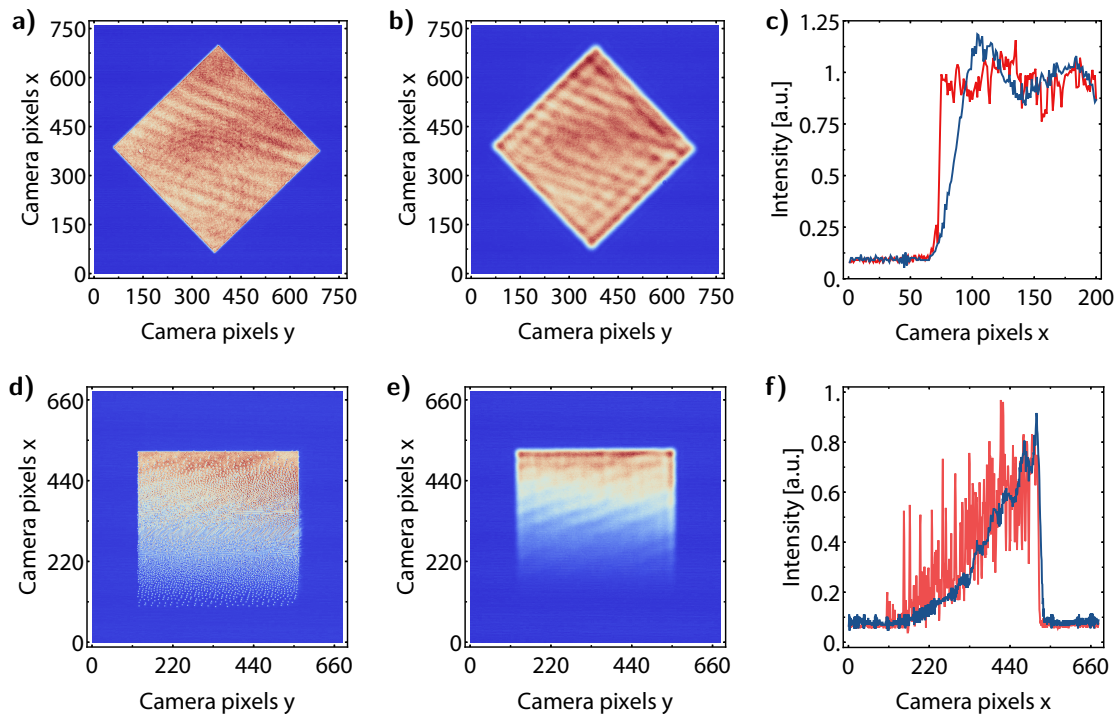


**Figure B.4.: Example of a low pass filter applied to a pattern of the DMD.** a) Bare output of the DMD (no error diffusion or feedback) imaged with a  $4f$  lens system with a wide open pupil stop in the Fourier plane. b) Same as in a) but with a narrow pinhole aperture of  $\sim 1$  mm. c) Close up of the right edge along the central horizontal cross section of the patter. Orange: iris open (sharp), Blue: iris almost closed (blurred). d,e,f) Same as above but for a gradient intensity pattern created by using error diffusion.

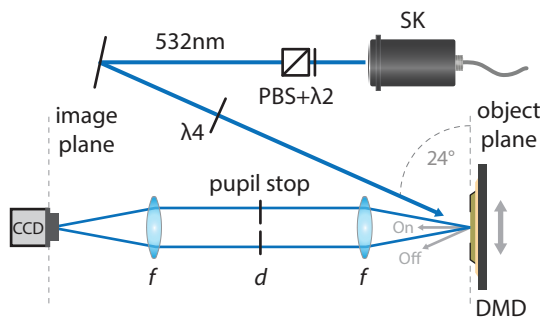


**Figure B.5:** Test setup for the initial characterization of the DMD. The green light of up to is provided by a fibered diode laser running at 532 nm. SK: large area beam collimator, LPF: optical low pass filter ( $4f$  lens system + pinhole),  $d_{\text{ph}}$ : diameter of the diaphragm, CCD: camera,  $\lambda/4$ : quarter wave plate,  $\lambda/2$ : half wave plate, PBS: polarizing beam splitter cube.

individual micromirror control. It is equipped with an electronic subsystem by Vialux ('SuperSpeed V-Module') that enables and facilitates rapid communication with as well as flexible programming of the micromirror array. This controller board is a proprietary FPGA design and can be accessed via USB3.0 to drive the DMD using the ALP-4.3 controller suite. The application programming interface (API) of the V-module contains DLL C-libraries, which can be accessed by common coding platforms such as C++ or LabView. In our case, we access the functions contained in these libraries via Python as it also facilitates the straightforward implementation of the error diffusion and the iterative refinement alongside the basic control knobs of the DMD. The code is based on previous work carried out in the Bloch group at MPQ Garching [258].

The DLP9500 has a resolution of  $1920 \times 1080$  pixels with a mirror pitch of  $d = 10.8 \mu\text{m}$ . The active area of the mirror array has dimensions of  $20.7 \times 11.7 \text{ mm}^2$ . In combination with the controller module V-9501 the maximum switching rate of 1bit black and white patterns amounts to 17 857 Hz with a buffer size of 31068 (64Gbit) or 62137 (128Gbit) binary patterns. These dynamic quantities are not that relevant when one aims to project only static intensity patterns, however they do limit the DMD once time-varying light fields are required. Note in particular that the switching rate of  $\sim 18 \text{ kHz}$  is only a factor of 10 higher than typical trapping frequencies of an optical dipole trap.

### Test setup

The first setup and characterization of the DMD was conducted using the test setup depicted in fig. B.5. The light is provided by a low power diode laser running at a wavelength of 532 nm, whose output is mode-cleaned by a single-mode fiber. The beam is collimated at a diameter of  $2\omega_0 \approx 10 \text{ mm}$  by a large aperture fiber collimator with an effective focal length of 100 mm. For mere testing purposes such a large beam is preferable since the central region of the Gaussian corresponding to  $200 \times 200$  pixels of the DMD then varies only by 2%, corresponding to almost homogeneous illumination. While this speeds up initial tests with the DMD, as soon as light utilization efficiency plays a role, the illumination beam has to be shaped to an appropriate size and aspect ratio first depending

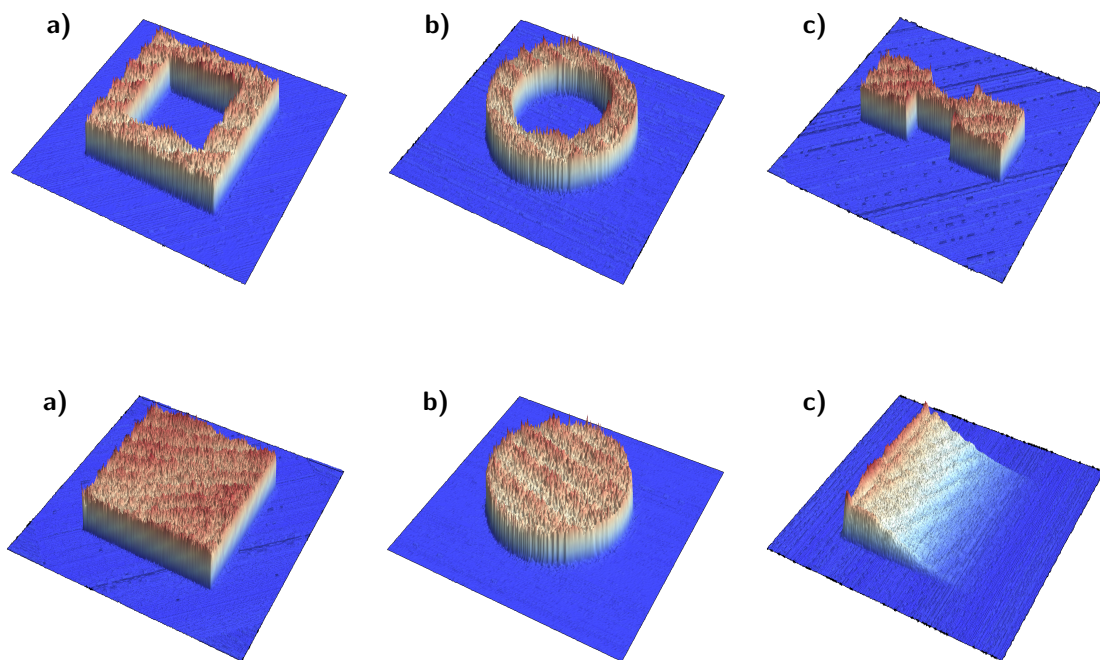


**Figure B.6.:** Examples of basic profiles created with the DMD. a) Square box. b) Ring. c) Reservoir. d,e) Square and round flattop c) Gradient.

on the desired output pattern. Moreover, its cross section at the plane of the DMD must be taken into account when performing error diffusion in conjunction with spatial filtering. A collection of examples of basic intensity patterns is given in fig. B.6.

## B.2. Magnetic field stability for RF spectroscopy

The disadvantage of the narrow width resonance of  $^{40}\text{K}$  at 202 G is that the scattering length  $a$  will scale comparatively quickly with the magnetic field. From the unitary regime attained at 202.10 G to the background at  $B > 215$  G,  $a$  drops from infinity to a few hundred Bohr radii  $a_0$  over the course of just a few Gauss. In order to precisely tune the Fermi gas onto a desired interaction strength, the magnetic bias field must therefore be stable down to the mG level. In order to quantify the impact of fluctuations in the magnetic field one can consider the resulting variation of  $1/k_F a(B)$ . In essence, this is a function of the geometry of the trapping potential and the atom number. In fig. B.7b the situation is plotted on top of the resonance for two shallow trap depths of the lattice with an angle of intersection of  $\alpha = 25^\circ$ . The potential depths have been chosen low on purpose in order to ensure that the relation  $k_F = \sqrt{2mE_F}/\hbar$  is valid, that is to say that the Fermi gas is three-dimensional. The deviation in the single beam dipole trap after evaporation is shown for comparison. As is evident the magnitude of magnetic field fluctuations should be less than  $\pm 25$  mG, which corresponds to a stability on the  $2.5 \times 10^{-4}$  level with respect to the total field. The latter scales linearly with the current flowing through the electromagnets, implying that the supply should be stable on the  $10^{-4}$  to  $10^{-5}$  level.

A more fundamental constraint is given by the ambient magnetic field, which may contain stray AC and DC fields created, for example, by nearby devices or elevators, as well as permanent magnets. While the latter are of no real concern as they can easily be compensated (provided they do not change over time) using compensation coils, rapidly alternating magnetic fields can broaden the magnetic field experienced by the atoms in an uncontrollable manner. On top of a Feshbach resonance, this would result in a random modulation of the interaction strength. Slow drifts that occur on timescales between shots or on a day-to-day basis are detrimental to the reproducibility of the experimental conditions. The slow drifts of the ambient magnetic field in the vicinity of the science cell were recorded using a highly sensitive hall probe. The detected *peak-to-peak* stability of the background field is found to be better than  $\Delta B_{\text{max}} = 18$  mG. This figure also includes the oscillations due to temperature drifts in the lab, which alter the detectivity of the hall sensor and the high precision voltmeter. Note that fluctuations faster than 0.25 Hz were not resolved.

The requirement regarding the stability of the current supply outlined above is technically feasible, but already implies a high level of performance. For that reason, we use a slow but highly stable current supply (High Finesse UCS 30/15), which can deliver up to 30 A. This corresponds to maximum bias fields of 240 G at a specified stability of some  $10^{-5}$  when an internal setpoint is used. In terms of magnetic field uncertainty, this figure translates into  $\Delta B_{\text{max}} = 0.4$  mG. However, additional fluctuations can be introduced via the supply's analog modulation channel as long as their frequencies are within the accepted bandwidth.

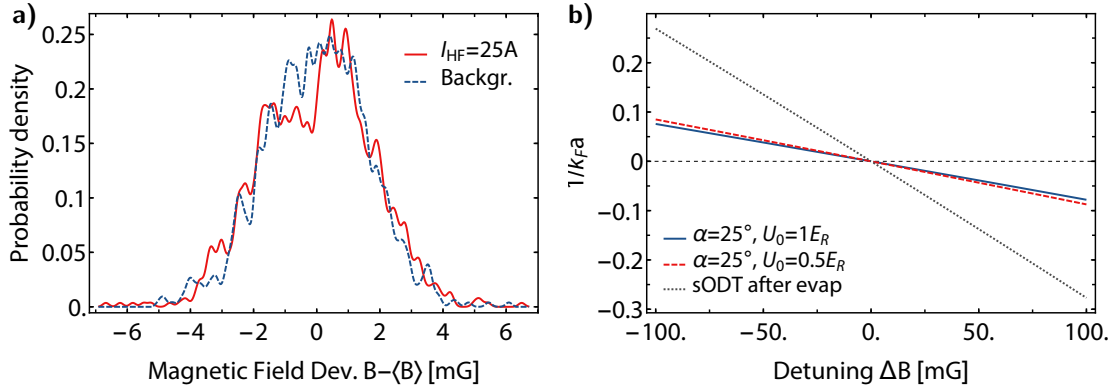


**Figure B.7.: Magnetic field stability.** a) The histogram was recorded over the course of roughly 1 h using a temperature-compensated Hall probe placed in the vicinity of the science cell. Its analog output was captured with a high-precision voltmeter with a sampling rate of 0.25 Hz. The data was binned with a step width of 0.1 mG to obtain a smooth histogram. b) Variation of  $1/k_{Fa}$  with the detuning  $\Delta B$  from the s-wave resonance at  $B_0 = 202.10$  G. The parameters used for the case of the optical dipole trap (dotted orange line) correspond to typical values obtained after evaporation:  $\omega_{\perp} = 2\pi \times 120$  Hz,  $\omega_{\parallel} = 2\pi \times 1$  Hz and  $N_{\sigma} = 1 \times 10^6$ .

The uncertainty of the AM setpoint is given by the experiment's control hardware (see sec. 2.4) as well as the intermediate analog optocoupler that protects the supply from voltage spikes. The relative peak-to-peak fluctuations over the course of 8 h at the AM input with frequencies up to 0.25 Hz were found to amount to  $8.54 \times 10^{-6}$  (bare output of analog card) and  $6.95 \times 10^{-5}$  (with analog optocoupler)<sup>3</sup>. The latter translates into a variation of the produced magnetic field of  $\Delta B_{\max} = 1.68$  mG, which essentially stems from the optocoupler's sensitivity to changes of the ambient temperature.

The histogram of a precise long-term measurement over 1 h of the magnetic field produced by high finesse at 80 % of its maximum current is shown in fig. B.7a. An equivalent measurement of the background is shown for comparison. Up to fluctuations faster than 0.25 Hz, one finds a relative peak-to-peak stability of at least  $7.3 \times 10^{-5}$  corresponding to fluctuations of  $\Delta B_{\max} = 13.2$  mG. Note that the peak-to-peak fluctuations of the background already amount to  $\Delta B_{\max} = 11.1$  mG, suggesting that the accuracy of the measurement is not sufficient. Another direct measurement of the supply's current stability for an output of 8 A yielded peak-to-peak fluctuations of 1.45 mA, which would translate into  $\Delta B = 11.7$  mG at  $B \simeq 64$  G. As these peak-to-peak figures represent longterm behavior, we can therefore consider them to represent a lower bound for the stability of the current supply.

Fluctuations faster than 10 Hz were not captured by any of the measurements described so far and can be observed only indirectly via MW/RF spectroscopy as presented in sec. 3.3.

<sup>3</sup>The output of the analog NI card was set to 8.2 V out of the maximum 10 V for these measurements.

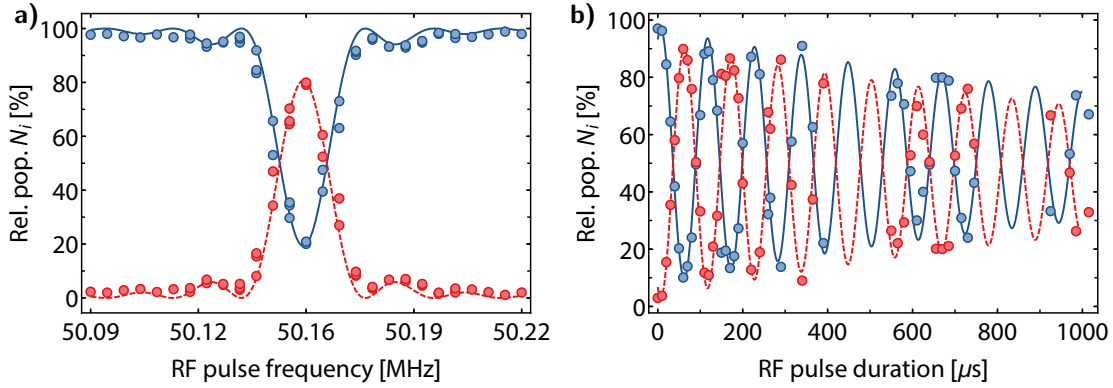


**Figure B.8.: Magnetic field fluctuations and Rabi oscillations of  $^{40}\text{K}$  at high magnetic fields  $B \simeq 240$  G.** a) Resonance curve of the magnetic dipole transition between  $| -9/2 \rangle$  and  $| -7/2 \rangle$ . Pairs of spin populations were obtained from a single shot using double imaging. The fitted widths amount to 100 kHz, corresponding to a magnetic field uncertainty of 5 mG. b) Coherent Rabi oscillations with  $\Omega = 9$  kHz. Blue:  $N_{-9/2}/N_{\text{tot}}$ , red:  $N_{-7/2}/N_{\text{tot}}$ ; fast successive imaging.

The width of the obtained Lorentzian signal can be translated directly into an uncertainty of the magnetic field using the Breit-Rabi formula, which captures drifts over the course of the entire measurement as well as very fast fluctuations during the probing time step. In fig. B.8a the full width was found to be 5 mG at a magnetic field of  $B \simeq 240$  G and using the RF transitions between the negative spin states as probes. These fluctuations are consistent with the ones detected by the precision hall probe<sup>4</sup> and were recorded while actively syncing the experimental sequence to the 50 Hz mains (see sec. 2.4). The latter has two effects. First, it causes the magnetic field set at the beginning of a given time step to be different from shot to shot. Second, if the length of the time step is on the order of 20 ms, the fluctuations of the magnetic field will cause the atoms' detuning to vary over time. While the latter effect can be circumvented by shortening the duration of the MW pulse, the former issue can only be addressed by synchronizing the Cicero sequence with the AC mains frequency. A crucial test to verify that the RF spectroscopy of strongly interacting gases will eventually only be limited by the Fourier-width of the pulse itself, is the observation of coherent Rabi-oscillations between neighboring spin states. In presence of 50 Hz, these oscillations are very difficult to observe at long times due to the dephasing from shot to shot. The corresponding measurement establishing that sufficiently long coherence times can be achieved with the remaining (minimal) magnetic field uncertainties of  $\sim 5$  mG is shown in fig. B.8b. The fitted coherence time of  $\tau_{\text{coh}} \geq 800 \mu\text{s}$  is more than sufficient for RF spectroscopy of interacting Fermi gases.

<sup>4</sup>Note that the results obtained with the hall probe were given in terms of peak-to-peak fluctuations! The full RMS width at a 13.5 % level of the corresponding probability distribution is therefore smaller, amounting to roughly 4.5 mG.

### B.3. A high power optical dipole trap for Lithium

An overview of the current design of the laser system is given in fig. B.9. The output of the laser head with a wavelength of 1070 nm and a maximum power of 300 W is collimated at a beam waist of 2.5 mm. The setup is intended to provide two different kinds of dipole traps. The first one is fibered with a reduced maximum optical power of 25 W at the position of the atoms, which can be used either as primary dipole trap to replace the current one described in sec. 2.11.2, or as a crossed trap when higher levels of compression are required. The intensity can be controlled by providing feedback to an AOM that is installed before the high power fiber coupling. The stabilization circuit is similar to the one shown in fig. 2.16. In order to achieve the intensity figure mentioned above, about 50 W are needed as initial power assuming typical (high power) AOM diffraction- and fiber coupling efficiencies of 70 %. The latter should be optimized as much as possible to be able to keep the needed optical power as low as possible in order to minimize thermal lensing in the AOM crystal. The fiber can be attached to either of the ODT outcouplers around the science cell instead of the Innolight Mephisto (see fig. 2.12).

The second ODT generated by the setup is a deep large volume trap that is delivered free-space to the science cell. Its purpose is to facilitate the capture of  ${}^6\text{Li}$  at the moment of release from the quadrupole trap. The power will be controlled by means of a rotatable waveplate, which enables slow ramps of the intensity, and by providing additional feedback to the pump current modulation input of the laser controller. The latter enables one to stabilize the optical power at sufficiently high bandwidth at the expense of minor changes of the beam's waist. Moreover, the polarization optics must have a large extinction ratios to ensure accurate control and reproducibility of the set power.

There are several other consequences arising from the high optical intensities of the laser. First, the dipole force of a beam carrying more than 100 W at a diameter of  $\sim 1$  mm is sufficiently strong to accelerate the deposition of dust on optical surfaces. Eventually, such accumulations of impurities can ignite given the high intensity of the laser and irreversibly damage the material. A second effect connected to high power is an increased sensitivity to fluctuations in the air, which can translate into violent pointing jitter on the order of  $\sim 1$  mm for our beam parameters. This affects mostly the high power path of the laser system and hence the position stability of the dipole trap at the position of the atoms (pointing noise), but also the fiber coupling of the low power part since the PID is not fast enough to compensate by increasing the power (intensity noise). Either one represents a source of parametric heating for the atoms and must be avoided. Third, there is an increased fire and health risk since even stray transmissions through mirrors can be quite powerful, especially when focused down. To combat all of the problems raised so far, the setup has to be kept in an airtight enclosure, which includes the path of the high power beam all the way until the science cell.

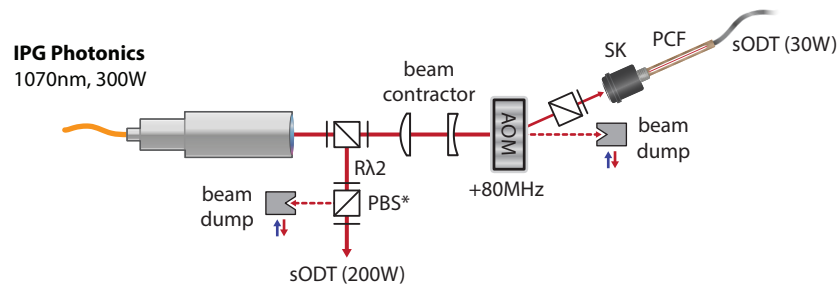


**Figure B.9.: Schematic illustration of the laser system.** Laser: IPG Photonics YLR-300-LP-WC (wavelength 1070 nm), R $\lambda$ 2: rotatable half-waveplate, PBS\*: high extinction polarizing beam splitter, beam dump: Eksma Optics 990-0820 water-cooled beam dump, AOM: Gooch & Housego 3110-197, PCF: NKT Photonics LMA-10 or aeroGuide Power-15-PM high power optical fiber.

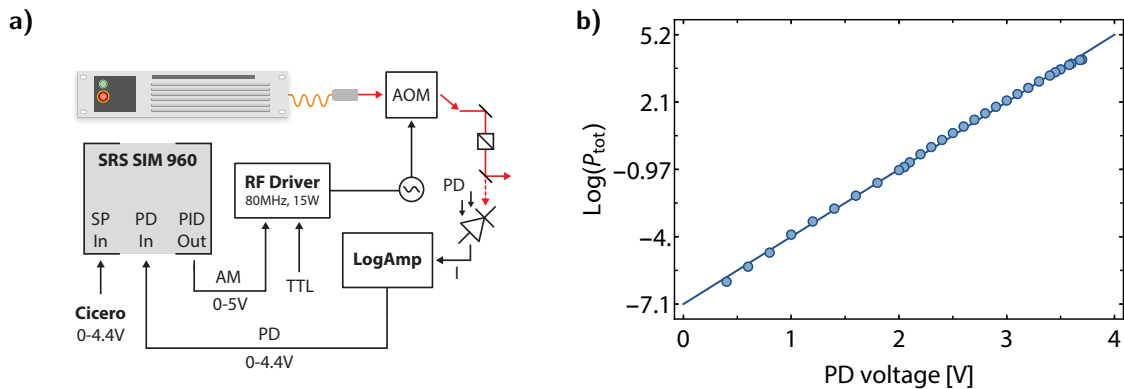


**Figure B.10.: Servo loop for intensity stabilization using a logarithmic amplifier.** a) Schematic overview of the circuit providing feedback to the AOM driver. b) Power conversion using the logarithmic amplifier. In this example, the maximum and minimum recorded powers were 56 W and 0.0036 W, respectively, corresponding to a dynamic range of more than four orders of magnitude.

**First iteration of the setup.** Before changing the laser system to the one described so far, a high power AOM was used to regulate the optical power of up to  $\sim 250$  W instead of a rotating waveplate. To avoid accumulation of dust and subsequent burning of the AOM crystal, it had to be placed in a custom flowbox. By creating a weak overpressure inside of the box, the accumulation of dust on the entry and exit surface of the AOM crystal was prevented while keeping beam pointing jitter minimal. During the sequence, the air flow was cut by means of an industrial electromechanical valve to stabilize the beam. Technical details regarding the homebuilt driver to operate the solenoid of the valve can be found in sec. B.4.2. In addition, the bottom support of the flowbox enables one to actively stabilize the temperature of the AOM in order to ensure consistent thermal conditions during operation (see fig. B.11). As the RF power is rather high with 15 W, preheating of

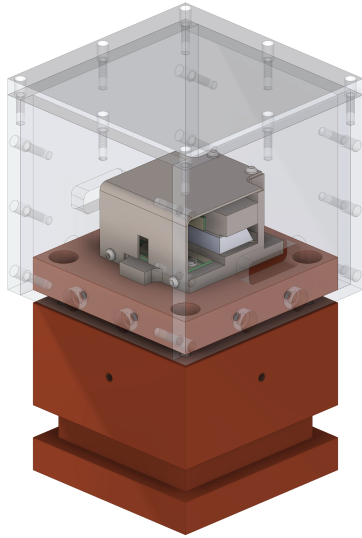


**Figure B.11.: Flowbox and heatsink for the high power AOM.** The AOM is mounted on a thin plate made of brass, which is connected to the larger heatsink below via a thermoelectric element. The larger body of the heatsink is made of brass due to its high thermal conductivity. The four threads on each side enable the mounting of additional heat sinks with fins to provide additional means for heat dissipation. The two large diameter inlets for the filtered air, which are located on the top of the flowbox, are not shown here. The openings of the flowbox also represent the entry and exit apertures for the high power beam passing through the AOM. The temperature of the AOM is measured with a thermistance and actively regulated through the Peltier element.

the AOM would take about 60 s, which is much too long considering the extremely high optical powers.

The intensity stabilization circuit is depicted in fig. B.10. It differs from the one shown previously in fig. 2.16 in that the dynamic range of optical powers that need to be covered is much larger. Therefore, a single linear photodiode is no longer sufficient. In order to deal with several decades of optical intensities, a logarithmic amplifier is used to convert the photo-current into a voltage of the PID module. An example of the resulting power conversion is given in fig. B.10b. While this method does increase the dynamic range and prevents one from having to use two photodiodes, which renders the stabilization circuit much more complex, it also comes at the expense of increased noise.

Owing to the presence of high optical intensities inside of the AOM crystal, thermal jitter and -lensing were major points of concern of the original version of the laser system. These effects can be detrimental to the mode quality of the ODT as well as to its tendency to cause parametric heating due to fast modulations of the beam pointing. A characterization of the waist at a total power of 50 W as a function of position is given in fig. B.13, which is fitted using the well known relation for ideal Gaussian beams,

$$\omega(z) = \omega_0 \sqrt{1 + (z/z_R)^2}.$$

Here,  $\omega_0$  denotes the beam waist and  $z_R = \pi\omega_0^2/\lambda$  represents the Rayleigh length. While this analysis represents an approximation at best, it does highlight whether the high power ODT deviates noticeably from the desired Gaussian behavior. In fig. B.13 one can clearly see that the wings do follow the ideal behavior more than the region around the beam's waist, which displays a slight tilt as well as a reduced curvature.

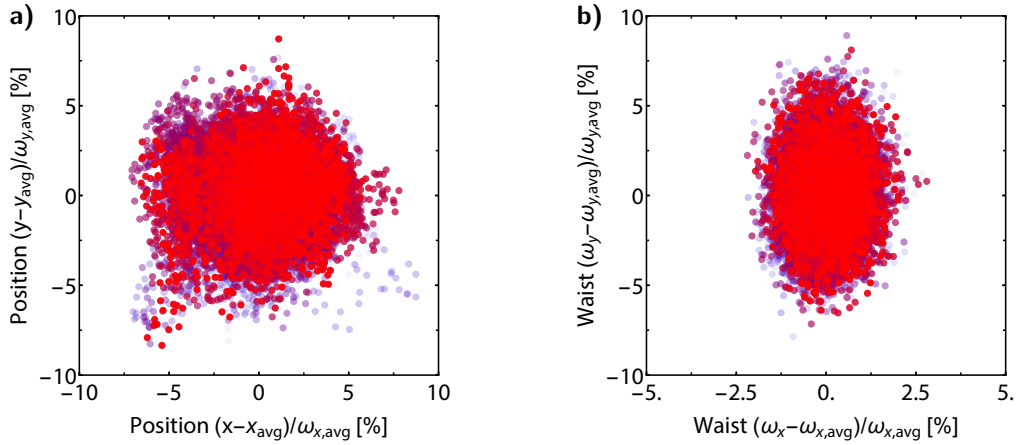


**Figure B.12.: Characterization of the beam quality of the original setup at 50 W.** a) Pointing jitter over the course of 6 min recorded at 190 Hz. b) Evolution of the waist over the same period of time. Note that the axes are not scaled equally.

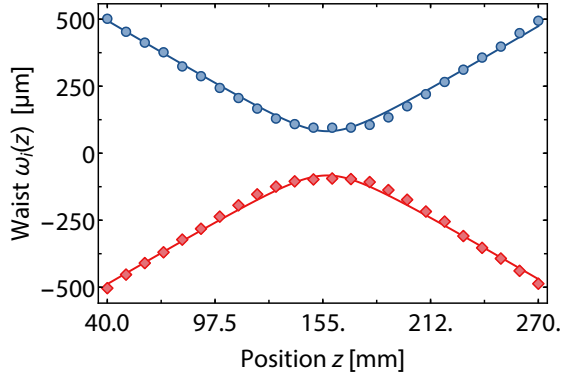


**Figure B.13.: Evolution of the waist with position.** Blue/orange data points: waist along x and y extracted from 1D integrated Gaussian fits to the recorded beam profiles (only half of the data is shown for clarity). Solid lines: fits to the data using the function  $\omega(z) = \omega_0 \sqrt{1 + (z/z_R)^2}$  of an ideal Gaussian beam. The total optical power of the beam was 50 W after the AOM.

A survey of the stability over time of the waist and the center of intensity over the course of 6 min are given in fig. B.12. The pointing jitter appears to amount to about 10 % of the waist and the size of the mode itself fluctuates between 10 % and 5 %, depending on the direction. The asymmetry of the latter might point to thermal effects in the AOM crystal.

**Loading behavior.** So far, the high power part of the IPG setup has been tested with  $^{40}\text{K}$  and only in this configuration of the setup, where loading efficiencies of up to 30 % after the magnetic trap were achieved. While the main dipole trap can perform as well, it only does so when the experiment operates at peak efficiency. Typical loading efficiencies are between 10 % and 20 %. The IPG, on the other hand, can be used at a larger waist since any loss in trap depth is easily compensated by increasing the optical power. This increased trap volume facilitates the loading and increase the traps tolerance with respect to the initial conditions of the atoms after RF-evaporation. While increasing the waist at constant trap depth improves the loading efficiency, it also implies increasingly large axial

cloud sizes, which ultimately fixes a maximum loading efficiency as the atoms will end up touching the glass cell at some point. This effect can be reduced by adding a magnetic gradient to increase the restoring force along the axial direction, however this method is obviously limited as the magnetic trap must not become too strong since, otherwise, it would prevent loading of the ODT or begin to pull back atoms.

A common problem with high power fiber lasers is that due to their linewidth of several nm one cannot easily form a crossed trap without risking to excite molecular photo association lines. Thorough polarization of the second beam may alleviate this problem, as was demonstrated with  ${}^6\text{Li}$  in [89]. In our case, a crossed trap was formed with the narrow band Mephisto MOPA dipole trap. While the difference in wavelengths amounts to 6 nm, the linewidth of our IPG of 4 nm might still suffice to induce molecular losses when crossed with the other ODT, especially considering that the beams do not intersect one another at  $90^\circ$  (see fig. 2.12). However, we found experimentally that no such losses occur for  ${}^{40}\text{K}$  on a timescale of several seconds when loading the cross during evaporation.



**B.4. Electronics schematics**

**B.4.1. Atomic source security system**

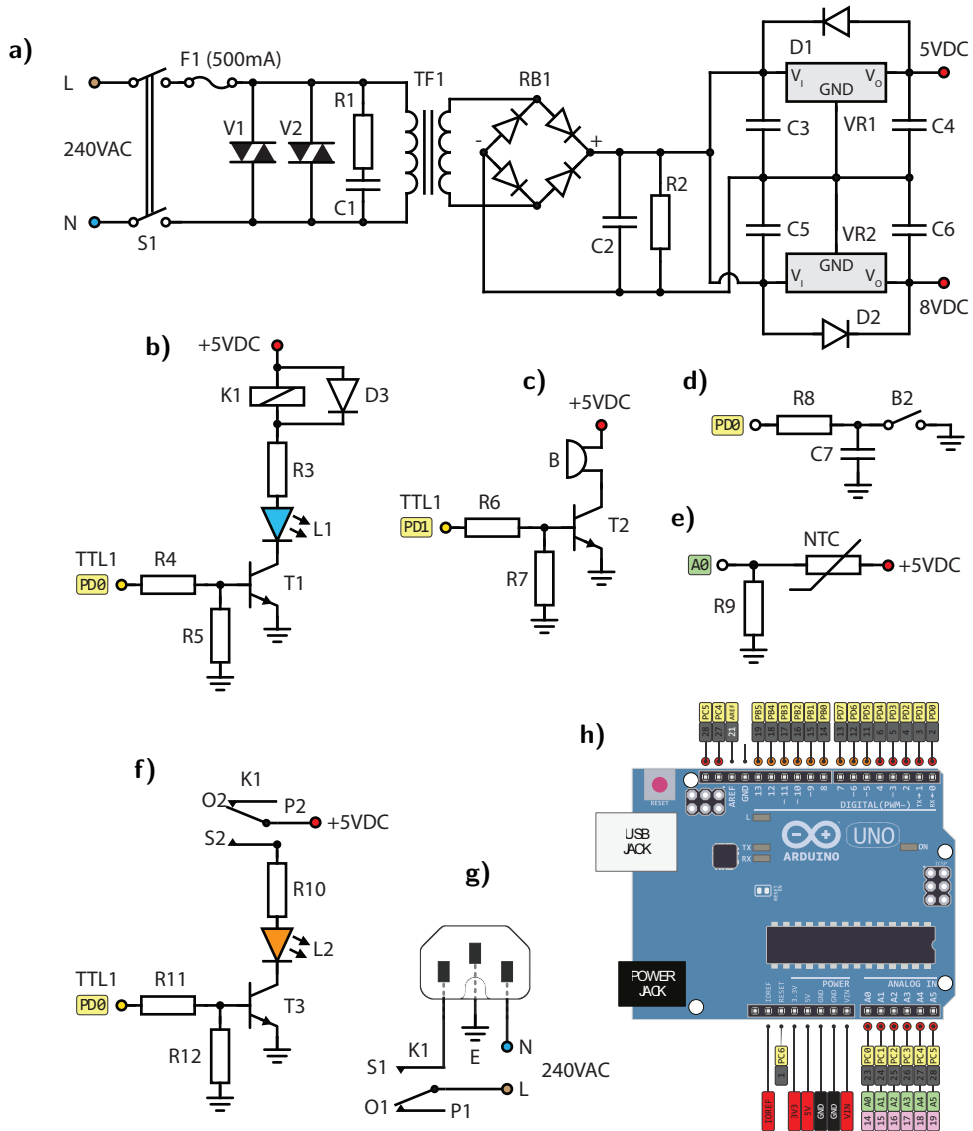


**Figure B.14:** Abbreviated circuit diagram of the security system. a) Dual voltage linearly regulated power supply. b) Relay circuit. c) Alarm buzzer. d) Menu button. e) Thermistances. f) Indicator light. g) AC mains outlet. h) Arduino microcontroller.



**Figure B.15:** Front panel of the security system. USB: programming port, BNC: Inputs for temperature sensors or interlocks, Button (left): menu, Button (lower right): On/off switch for the monitoring electronics, Flip switch (upper right): Day/night mode.

### B.4.2. Driver for solenoid valves

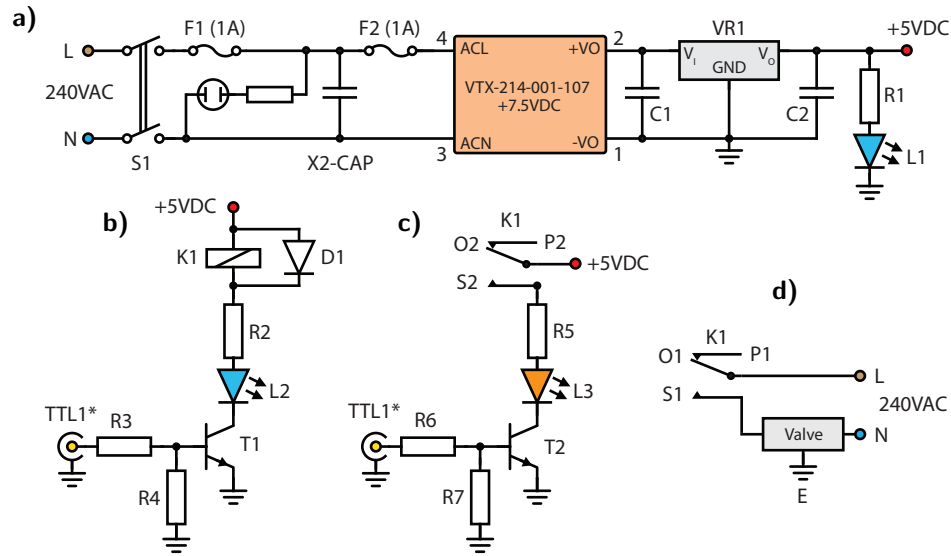


**Figure B.16.** Abbreviated circuit diagram of the valve driver. a) Power supply. b) Relay switching circuit with external TTL input. c) Relay indicator light. d) External valve and relay circuit.

### B.4.3. AOM driver supply and breakout box

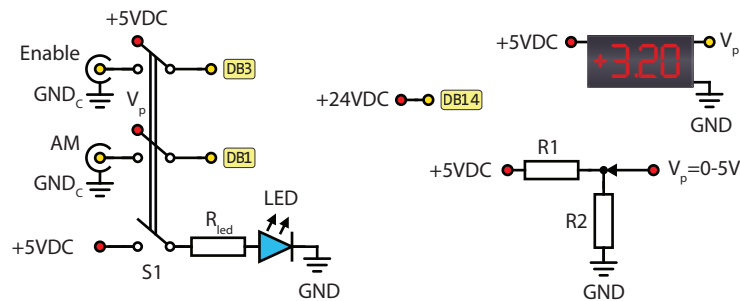


**Figure B.17.** Circuit diagram of one driver channel. Left: 8-pole switch and status LED. Right: voltmeter with liquid crystal display and rotary potentiometer. 5 V and 24 V supplies not shown.



**Figure B.18.** Front panel. Switch: remote control (LED on) or local override mode (LED off). BNC connectors: Analog and digital modulation channels of the RF drivers (blocked in override mode). Potentiometer: analog tuning voltage in override mode, displayed on the LCD panels.

## B.5. Additional figures and tables



**Figure B.19.: New Potassium reservoir.** Left: custom stainless steel mount holding the ampule in place. The height ensures that the angle-valve can be used to crack open the ampule under vacuum. Right: reservoir after installation and additional bake-outs.

$ m_I, m_J\rangle$	1	2	3	4	5	6	7	8	9	10	11	12	13	14	15	16	17	18
$ +4, +\frac{1}{2}\rangle$	0	0	0	0	0	0	0	0	0	100	0	0	0	0	0	0	0	0
$ +3, +\frac{1}{2}\rangle$	0	0	0	0	0	0	0	0	70	0	30	0	0	0	0	0	0	0
$ +2, +\frac{1}{2}\rangle$	0	0	0	0	0	0	0	53	0	0	0	47	0	0	0	0	0	0
$ +1, +\frac{1}{2}\rangle$	0	0	0	0	0	0	41	0	0	0	0	0	59	0	0	0	0	0
$ +0, +\frac{1}{2}\rangle$	0	0	0	0	0	32	0	0	0	0	0	0	0	69	0	0	0	0
$  -1, +\frac{1}{2}\rangle$	0	0	0	0	24	0	0	0	0	0	0	0	0	0	76	0	0	0
$  -2, +\frac{1}{2}\rangle$	0	0	0	17	0	0	0	0	0	0	0	0	0	0	0	83	0	0
$  -3, +\frac{1}{2}\rangle$	0	0	10	0	0	0	0	0	0	0	0	0	0	0	0	0	90	0
$  -4, +\frac{1}{2}\rangle$	0	5	0	0	0	0	0	0	0	0	0	0	0	0	0	0	0	95
$ +4, -\frac{1}{2}\rangle$	0	0	0	0	0	0	0	0	30	0	70	0	0	0	0	0	0	0
$ +3, -\frac{1}{2}\rangle$	0	0	0	0	0	0	0	47	0	0	0	53	0	0	0	0	0	0
$ +2, -\frac{1}{2}\rangle$	0	0	0	0	0	0	59	0	0	0	0	0	41	0	0	0	0	0
$ +1, -\frac{1}{2}\rangle$	0	0	0	0	0	68	0	0	0	0	0	0	0	32	0	0	0	0
$ +0, -\frac{1}{2}\rangle$	0	0	0	0	76	0	0	0	0	0	0	0	0	0	24	0	0	0
$  -1, -\frac{1}{2}\rangle$	0	0	0	83	0	0	0	0	0	0	0	0	0	0	0	17	0	0
$  -2, -\frac{1}{2}\rangle$	0	0	90	0	0	0	0	0	0	0	0	0	0	0	0	0	10	0
$  -3, -\frac{1}{2}\rangle$	0	95	0	0	0	0	0	0	0	0	0	0	0	0	0	0	0	5
$  -4, -\frac{1}{2}\rangle$	100	0	0	0	0	0	0	0	0	0	0	0	0	0	0	0	0	0

**Table B.1.: Basis decomposition of the ground state Zeeman levels of  $^{40}\text{K}$ .** The 18 spin states of the two ground state manifolds are expanded into the  $\{I, m_I; J, m_J\}$  basis at a magnetic bias field of 230 G. All coefficients are squared and given in percent. Red shaded columns: basis vectors of the ground state manifold accessible from  $|1'\rangle$ ,  $|2'\rangle$  and  $|3'\rangle$  via spontaneous emission; Blue shaded columns: states with non-zero contributions of these basis vectors.



## Appendix C

### Supplementary theoretical references and experimental methods

#### C.1. Absorption imaging and thermometry of fermionic Potassium

In order to probe the density- and momentum distribution of the atomic ensembles, we employ standard absorption imaging. A near-resonant laser beam is passed through the atoms and thereby attenuated before being imaged and magnified onto a CCD camera. This technique is destructive due to the incoherent nature of the photon scattering processes and does not probe the dispersive properties of the atomic cloud. In the limit of weak light intensities, the transmitted beam profile is given by the well-known Beer-Lambert-Bouguer law [228],

$$I_T(x, y) = I_0(x, y)e^{-D(x, y)} \quad , \quad D(x, y) = \sigma \int n(x, y, z)dz, \quad (\text{C.1})$$

where  $I_0$  and  $I_T$  denote the light's intensity profiles before and after passage through the atoms, respectively. The optical density  $D(x, y)$  is comprised of the absorption cross-section  $\sigma$  and the column number density  $n_{2D}(x, y) = \int n(x, y, z)dz$ . While the spatial extension of the cloud is directly accessible via the pixel size of the camera as well as the magnification of the imaging system, the extraction of the atom number from the "shadow" cast by the atoms requires knowledge of the involved optical transitions and their probability amplitudes. Unless the addressed transition is cycling and therefore behaves like an ideal two-level system, the standard expression of the scattering cross section has to be modified in order to incorporate all of the partaking Clebsch-Gordan coefficients:

$$\sigma = C^2 \times \frac{3\lambda_L^2}{2\pi} \frac{1}{1 + 4\Delta^2/\Gamma^2}. \quad (\text{C.2})$$

Here  $\sigma_0 = 3\lambda^2/(2\pi)$  is the resonant scattering cross section of a two-level system,  $\Delta = \omega_L - \omega_0$  is the detuning of the imaging laser of wavelength  $\lambda_L$  from resonance and  $\Gamma$  denotes the linewidth of the transition. In a mere two-level system,  $C = 1$  holds. This is also the case when a cycling transition is used for imaging, i.e. a line where no additional channels other than the principal one are available for stimulated absorption or spontaneous emission. In  $^{40}\text{K}$  this situation is present, for example, when exciting the stretched ground Zeeman states  $|F = 9/2, m_F = \pm 9/2\rangle$  to  $|F' = 11/2, m'_F = \pm 11/2\rangle$

using  $\sigma^\pm$  polarized light. In the case where multiple spin states of the ground- and excited state hyperfine manifolds are involved,  $C$  can be taken to be the average over all of the involved Clebsch-Gordan coefficients, normalized to the one of the cycling transition. For vanishing magnetic fields (i.e. degenerate Zeeman levels), one finds for the D2 line of  $^{40}\text{K}$  that  $C^2 = 0.4$  and  $C^2 = 0.5$  for  $^6\text{Li}$ . One should note that the underlying assumption here is that the cross section does not depend on the laser intensity and on the level of attenuation by the atoms. This condition holds if  $I_0$  is much smaller than the saturation intensity  $I_{\text{sat}}$  of the imaging transition. Moreover, in this case parasitic optical pumping into other states via spontaneous emissions (or even stimulated absorption) will occur, the impact of which depends on the total exposure time. In the presence of magnetic fields, this depumping process can render atoms dark to the imaging light. In general, to ensure that the cloud is properly illuminated, the optical density should fulfill  $D(x, y) \ll 4$  at the same time, implying that no portion of the probe beam is completely absorbed and re-scattered by the atoms (i.e. the shadow is perfectly black). Technically, the above criteria are realized by choosing  $I_0 \sim 0.1 I_{\text{sat}}$  and keeping the exposure- and illumination times as short as possible to disturb the atomic sample as little as possible. This applies both to the problem associated with the energy transferred to the atoms as well as to the possibility of repumping processes to other (dark) states by the imaging light. While short light pulses of  $25\mu\text{s}$  can be easily realized with acousto-optical modulators, the minimal exposure time of the camera is usually much longer than that. Therefore, a large amount of noise in the form of stray light is also imaged in a parasitic way, and has to be subtracted when reconstructing the optical density from the captures of the CCD camera:

$$D(x, y) = \ln \left( \frac{I_0(x, y) - I_{\text{bg}}(x, y)}{I_{\text{T}}(x, y) - I_{\text{bg}}(x, y)} \right). \quad (\text{C.3})$$

Here,  $I_0(x, y)$  represents a picture of the mere imaging light in the absence of atoms while  $I_{\text{T}}(x, y)$  denotes the absorption picture.  $I_{\text{bg}}(x, y)$  is a capture of only the parasitic stray light, which is naturally present in the imaging system.

Now, the most straightforward way to infer the total atom number  $N$  present in the atomic sample is by integrating over the experimentally recorded optical density:

$$N = \frac{1}{\sigma} \int D(x, y) dx dy = \int n_{2\text{D}}(x, y) dx dy. \quad (\text{C.4})$$

This way, any single image of the atomic sample gives a-priori access to the number of scattering centers present. However, the extraction of the temperature requires, in general, knowledge about the nature of the confining potential (e.g. trapping frequencies) as well as about the underlying distribution function (Fermions or Bosons, thermal or quantum-degenerate) because one must somehow relate the size of the cloud to its thermodynamic

state. As will be detailed below, this amounts to fitting the proper expression of the column density to the experimentally recorded 2D- or (integrated) 1D-density profiles,  $n_{1D} = \int n_{2D} dx_i$ .

There are two principal options how one can take the absorption image: The exposure can be done in-situ, i.e. the confining potential is present while the illumination pulse is shone in, or the atoms are first released from their trap. Naturally, the appropriate fit functions in both cases have to be chosen differently. The former method has the advantage of capturing the atoms' actual density profile in the trap, but suffers from the fact that the ensembles are usually very small and dense, which requires highly magnified- as well as highly resolved imaging and tends to introduce saturation effects due to large optical densities, as was discussed above. Moreover, the inhomogeneous nature of any trapping potential can give rise to spatially varying imaging frequencies, which introduces additional complications into the image capture- and evaluation process. These disadvantages can be circumvented by switching off the trap prior to imaging. Assuming the absence of any scattering resonance, the atoms are then left to expand freely (ballistically) during a given period of time (time-of-flight). Given that the momentum of each particle remains conserved during time-of-flight, the size of the cloud gives direct insight into the initial momentum distribution and temperature of the sample.

For an ideal gas, which is being released from a harmonic trap with cylindrical symmetry along  $z$  at  $t = 0$ , the density distribution has to be rescaled according to  $x'_i = x_i / \sqrt{1 + \omega_i^2 t^2}$  (with  $x_i = x, y, z$ ). After a typical expansion time of a few ms, the density distribution will have evolved to [63]:

$$n(\mathbf{r}, t) = \frac{n(\mathbf{r}', t = 0)}{(1 + \omega_r^2 t^2) \sqrt{1 + \omega_z^2 t^2}}. \quad (\text{C.5})$$

Here, the  $\omega_i$ 's denote the radial and axial trapping frequencies and  $t$  is the total expansion time. It is a peculiarity of the harmonic trap that the overall shape of the density distribution is maintained along the different symmetry axes as the cloud expands ballistically. An additional prerequisite for this behavior is that many vibrational levels along every direction have to be occupied, which is usually the case for both classical ( $k_B T \gg \hbar \omega_\nu$ ) and quantum degenerate gases ( $E_F \gg \hbar \omega_\nu$ ).

*Degenerate Fermi Gas.* By inserting the well known density distribution of non interacting harmonically trapped Fermions into the above equation and integrating along the imaging axis (here:  $x$ ), one obtains for the column density after time-of-flight:

$$n_{2D}(y, z, t) = -\frac{1}{\sqrt{(1 + \omega_r^2 t^2) (1 + \omega_z^2 t^2)}} \frac{m (k_B T)^2}{2\pi \hbar^3 \omega_r} \text{Li}_2 \left( -Z e^{-\frac{y^2}{2\sigma_r^2} - \frac{z^2}{2\sigma_z^2}} \right) \quad (\text{C.6})$$

The fit function for 1D integrated optical densities is then readily calculated to read

$$n_{1D}(y, t) = -\frac{1}{\sqrt{1 + \omega_r^2 t^2}} \sqrt{\frac{m}{2\pi}} \frac{(k_B T)^{5/2}}{\hbar^3 \omega_z \omega_r} \text{Li}_{5/2} \left( -Z e^{-\frac{y^2}{2\sigma_r^2}} \right). \quad (\text{C.7})$$

Here, the fugacity of the ensemble is defined as  $Z = e^{\beta\mu}$ . An additional dependence on time is contained in the cloud radii as per

$$\sigma_r^2(t) = \frac{k_B T}{m\omega_r^2} (1 + \omega_r^2 t^2) \quad , \quad \sigma_z^2(t) = \frac{k_B T}{m\omega_z^2} (1 + \omega_z^2 t^2). \quad (\text{C.8})$$

Given that the amplitude and the width of the above distributions are related, there are only two fitting parameters provided the trapping frequencies are known. This way, one can determine the temperature and atom number at the same time, which is particularly useful in order to calibrate the machine in terms of absolute atom number. An example was already given in figure 2.18. Finally, in order to quantify the degree of degeneracy of the Fermi gas, the relative temperature can be determined through the measured size of the cloud:

$$\frac{T}{T_F} = \frac{m\omega_y^2 \sigma_y^2}{\hbar\bar{\omega} (6N)^{1/3} (1 + \omega_y^2 t^2)}. \quad (\text{C.9})$$

*Classical limit.* At high temperatures, the above expressions for the densities converge toward Gaussian distributions, which are in general faster and easier to fit than polylogarithmic functions. Moreover, in both cases, the aspect ratio of the cloud  $\sigma_z/\sigma_r \rightarrow 1$  as  $t \gg 1/\omega_v$ , i.e. the density distribution loses its initial asymmetry and becomes spherical after sufficiently long expansion times. In this limit, the density profile reflects directly the initial momentum distribution of the cloud, regardless of the type of the trapping potential.<sup>1</sup> Provided that the atomic gas is thermal and consequently Boltzmann-distributed in momentum space, then one can also measure the temperature without knowledge of the details of the trapping potential. By taking multiple absorption images for different, sufficiently long expansion times as mentioned above, one can determine the effective temperatures of the gas by fitting the resulting Gaussian cloud sizes  $\sigma_i(t)$  to the expression

$$\sigma_i^2(t) = \sigma_0^2 + \frac{k_B T_i}{m} t^2 \quad , \quad i = x, y, z, \quad (\text{C.10})$$

where  $\sigma_0$  denotes the initial (in-situ) cloud size. In a harmonic trap, the underlying assumption is exactly true for a classical gas, while for a degenerate gas this method starts to become unreliable around  $T/T_F \sim 0.3$  (see [63] for details).

---

<sup>1</sup>It should be reemphasized that this is only true for non-interacting particles!

## C.2. Determination of trapping frequencies

In order to infer correct atomic densities or temperatures from absorption images, the knowledge of the underlying harmonic trapping frequencies defined in sec. 2.11.2 is paramount. As was mentioned earlier, the Fermi fit relies heavily on the knowledge these frequencies because the temperature is calculated by inferring the initial size prior to ballistic flight. In the case of optical dipole traps formed by Gaussian beams, one can measure these frequencies by exciting center-of-mass oscillations or breathing modes, provided the compression ratio  $\eta = U_0/k_B T$  is large enough.

The latter requirement ensures the applicability of the harmonic approximation as the thermal distribution does not sample the non-harmonic wings of the Gaussian beam's intensity profile<sup>2</sup>. The center-of-mass of harmonically trapped atoms is supposed to keep oscillating indefinitely, even when strong interactions are present in the system (Kohn theorem). As soon as anharmonic terms enter into the potential, the oscillations will start to display dampening, which is readily the case along the axial direction of the beam due to the naturally weak degree of confinement. The behavior is different in the case of oscillations of the cloud size, which always display dampening as soon as interactions are present among the atoms. By extension of this fact, they represent a means to measure the collision rate in the atomic sample.

Excitation of such collective modes is done by rapidly changing the optical potential in order to impart energy onto the trapped atoms without losing them. This can be done via fast compression, switching off the laser power for a few  $\mu\text{s}$  or by using a magnetic gradient field to accelerate the atoms. In fig. C.1 several examples of such measurements are shown. Here, the laser was abruptly switched off and back on in order to excite the atoms. While both CoM and breathing modes were present along the transverse directions, only the latter is depicted here. Note that the frequency of a cloud size oscillation in the non-interacting regime has to be divided by two in order to extract the true trapping frequency. Axial oscillations concern only the CoM position as the spatial extent of the cloud is less reliable to fit due to the large axial size with respect to the field of the view of the imaging system. The Gaussian beam waist  $\omega_0$  can be extracted by fitting the measured frequencies to the optical power  $P$  at the position of the atoms as per the well known relations [272]:

$$\nu_{\perp} = \frac{1}{2\pi} \sqrt{\frac{4U_0}{m\omega_0^2}} \quad \text{and} \quad \nu_{\parallel} = \frac{1}{2\pi} \sqrt{\frac{2U_0}{mz_R^2}}, \quad (\text{C.11})$$

with  $U_0 \sim P$  denoting the potential depth of the dipole trap as introduced in sec. 2.11.2.  $\omega_0$  denotes the Gaussian beam's waist and  $z_R$  its Rayleigh range. Another method to probe the trap frequencies is by inducing parametric heating on purpose. To do so, one modulates the

<sup>2</sup>In practice we find that  $\eta > 10$  is recommended to avoid anharmonic behavior.

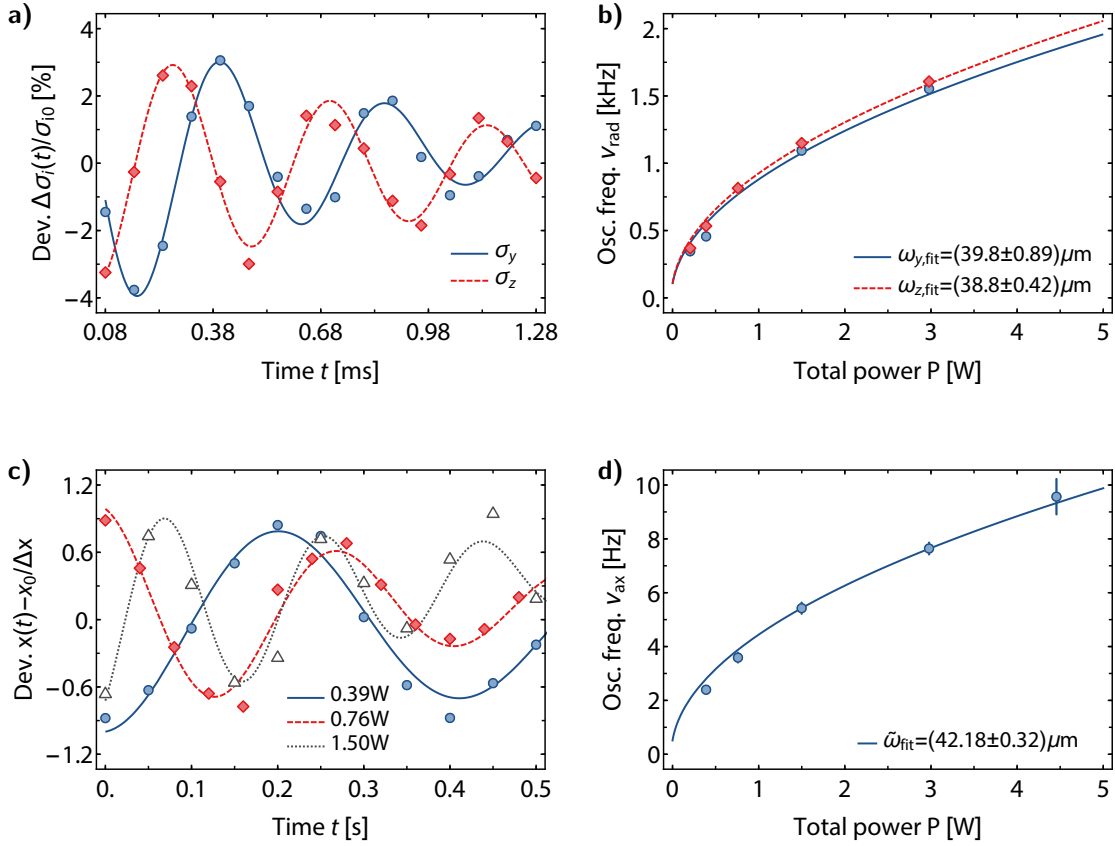


**Figure C.1: Measurement of harmonic trapping frequencies in a single optical dipole trap.** a) Breathing-mode oscillations of the transverse cloud sizes. b) Oscillations along the radial degrees of freedom for various powers. c) Axial center-of-mass oscillations are given for three different optical intensities. b) and d) depict the relation of the measured frequencies to the optical power, from which the waist can be inferred as a fit parameter.

laser intensity for a sufficiently long time at twice the trapping frequency in order to drive transitions between even motional states of the harmonic oscillator<sup>3</sup>. The transition rate between states  $|k\rangle$  and  $|l\rangle$  due a small intensity modulation  $\omega_x \rightarrow \omega_x(I(t)/I_0)^{1/2}$  of duration  $T$  is given by [273]:

$$R_{kl} = \left(\frac{m\omega_x^2}{2\hbar}\right)^2 \int_{-\infty}^{+\infty} dt' e^{i\omega_{kl}t'} \langle (I(t)/I_0 - 1)(I(t+t')/I_0 - 1) \rangle |\langle k|x^2|l\rangle|^2 \quad (\text{C.12})$$

where  $\langle \cdot \rangle$  denotes the correlation function of the fluctuations. Note that the matrix element in the above equation vanishes for odd excitations with  $l = k + 1$ . A modulation can result in strong heating of the trapped cloud when its power spectrum contains large

<sup>3</sup>One could also do this by modulating the pointing of the laser, which is much more cumbersome from an experimental point of view.

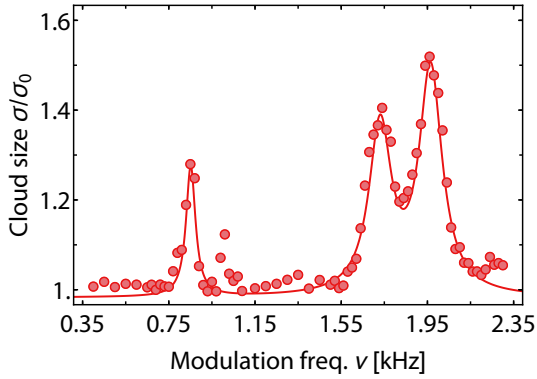


**Figure C.2.: Spectrum of parametric heating induced in a crossed optical dipole trap.** The ODT beam's intensity is modulated at frequency  $\nu$  for a certain period of time  $\tau \gg 1/\nu$ , allowing for several oscillation cycles before it is brought back to its nominal value. Afterwards, the cloud size is recorded after a sufficiently long wait time to let the atoms thermalize first. The resulting excitation spectrum contains peaks at positions  $\tilde{\nu}_k = 2\nu_k$  ( $k = x, y, z$ ).

contributions at  $\pm 2\omega_x$ . The corresponding rate is given by

$$R_{k,k\pm 2} = \frac{\pi\omega_x^2}{16} S(2\omega_x)(k+1 \pm 1)(k \pm 1), \quad (\text{C.13})$$

with  $S(2\omega_x)$  denoting the one-sided power spectrum evaluated at  $\omega = 2\omega_x$ . Experimentally, strong heating can be easily detected by tracking the cloud size after excitation along any direction provided the sample undergoes a sufficient number of collisions to rethermalize the different directions. An example of this method is shown in fig. C.2, where it was used to measure the trap frequencies of a crossed dipole trap. Provided there is sufficiently fast thermalization, this approach has the huge advantage of being independent of the orientation of the imaging axis with respect to the dipole trap. In the example shown here it was used for that reason because one degree of freedom of the crossed trap was temporarily inaccessible via absorption imaging, which prevents one from observing the corresponding center-of-mass oscillations to measure the trapping frequency along that direction.

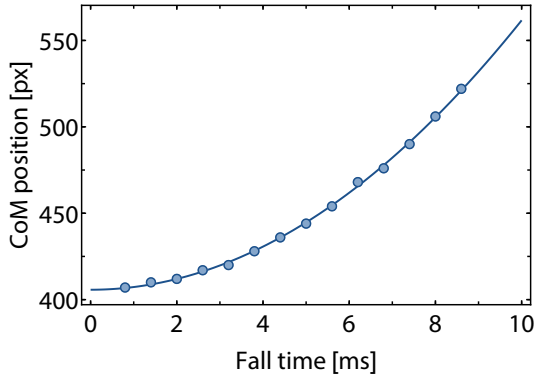


**Figure C.3.: Example of a calibration curve for the magnification.** The atoms are released from their trapping potential and left to fall freely under the action of gravity. The CoM-position of the cloud is tracked for many values of the drift time to sample the parabolic trajectory with high precision. The magnification is obtained as fit parameter, yielding here for example  $1/M_{\text{fit}} = 0.490(4)$  in the case of  $x$ -imaging.

### C.3. Calibration of imaging magnification

Prealignment of any imaging system is usually done using a resolution target, which is placed at a known position with respect to the actual object plane containing the atoms. The corresponding distance defines by how much the lenses will need to be moved after focusing them on the temporary target. While this method is quite effective in positioning the optical elements, the magnification needs to be verified experimentally in order to obtain a precise value. This can be done by letting an atomic sample fall freely and recording its center-of-mass position as a function of time  $z(t)$ . The resulting parabola contains the magnification  $M$  as fit parameter as it translates the actual distance covered by atoms into what is seen by the CCD camera. If  $M = 1$ , one would obtain exactly that  $z(t) = gt^2/2$  with  $g$  denoting the gravitational acceleration. An example of such a calibration is shown in fig. C.3. At the moment of release, no additional accelerating forces should be present at the position of the atoms. This concerns for instance stray magnetic gradients originating from Eddy currents, which can be easily created when switching off strong magnetic traps or bias fields. In ideal conditions, the trajectory  $z(t)$  of the center-of-mass of the atomic cloud as seen by the camera is given by:

$$\tilde{z}(t) = \frac{1}{Ms_p} \left( \frac{g}{2} t^2 + \tilde{z}_0 \right).$$

Here,  $s_p$  denotes the size of the camera pixels and  $\tilde{z}$  is the position expressed in terms of pixels. The magnification  $M$  is obtained as fit parameter. It is important that the atoms are allowed to fall over an extended period of time in order to sample as well the wings of the parabola, thereby ensuring a high fidelity fit that cannot be obtained if only the bottom of the parabola is mapped out. As the drop time is fixed by gravity, a constraint exists regarding the temperature of the atomic sample. If too hot, the atoms will expand too quickly and render detection more challenging the longer the drift time.

### C.4. Alkali atoms in static magnetic fields

When non-interacting alkali atoms are subjected to a static magnetic field, their single particle dynamics as well as their internal structure are governed by the Hamiltonian [96]:

$$\hat{H} = \frac{\hat{p}^2}{2m} + \hat{H}_0 + \hat{H}_{\text{so}} + \hat{H}_{\text{hfs}} + \hat{H}_z. \quad (\text{C.14})$$

The first term corresponds to the kinetic energy of the center-of-mass of the atom and  $\hat{H}_0$  denotes the spinless valence electron evolving in the electrostatic field of the core and the inner electron shells. In the case of Alkalis, the energy levels of the valence electron depend on the principal quantum number  $n$  just like Hydrogen, but also on its orbital angular momentum  $\hat{L}$  since the geometrical shape of the orbitals alters the amount of overlap the electron has with the inner occupied shells. The altered eigenenergies are given by the expression  $E_0(n, L) = -R_y/(n - \delta_{n,L})^2$ , where  $\delta_{n,L}$  denotes the quantum defect and  $R_y$  the Rydberg constant. The transition between the ground state  $nS$  and the first excited state  $nP$  is usually referred to as the Alkali D-line.

The second term  $\hat{H}_{\text{so}}$  incorporates the coupling between the electronic spin and the orbital angular momentum, taking on the form,  $\hat{H}_{\text{so}} = A_{\text{fs}} \hat{L} \cdot \hat{S}$ . This term lifts the degeneracy of the  $\hat{J} = \hat{L} + \hat{S}$  levels, thereby dividing the first excited state  $nP$  state into  $nP_{1/2}$  and  $nP_{3/2}$ , which splits the Alkali D-line into a doublet. The fine structure splitting between the two excited states is given by

$$\Delta E_{\text{fs}} = A_{\text{fs}} (J(J+1) - L(L+1) - S(S+1)).$$

The third term  $\hat{H}_{\text{hf}}$  incorporates the coupling to the angular momentum of the nucleus and can be expressed as

$$\hat{H}_{\text{hf}} = \frac{A_{\text{hfs}}}{\hbar^2} \hat{I} \cdot \hat{J} + \frac{B_{\text{hfs}}}{\hbar^2} \frac{3(\hat{I} \cdot \hat{J})^2 + 3\hbar(\hat{I} \cdot \hat{J})/2 - I^2 J^2}{2I(2I-1)(2J-1)},$$

where  $A_{\text{hfs}}$  and  $B_{\text{hfs}}$  denote the magnetic dipole and electric quadrupole constants, respectively. The last term  $\hat{H}_z$  describes the interaction between the various magnetic moments  $\hat{\mu}_i$  and an external magnetic field  $\mathbf{B}$ ,

$$\hat{H}_z = -(\hat{\mu}_S + \hat{\mu}_L + \hat{\mu}_I) \cdot \mathbf{B} = (g_J \hat{J} - g_I \hat{I}) \cdot \mathbf{B}.$$

Here,  $\hat{\mu}_L = -\mu_B g_L \hat{L}$  denotes the moment associated with the orbital angular momentum, for which the Landé factor is  $g_L = 1 - m_e/m_{\text{nuc}} \approx 1$ . The intrinsic momentum of the electron implies a magnetic moment of  $\hat{\mu}_S = \mu_B g_S \hat{S}$  with  $g_S \approx 2$  as predicted by the Dirac equation. Finally, for the nuclear spin one has similarly  $\hat{\mu}_I = -\mu_B g_I \hat{I}$  with the

gyromagnetic factor  $g_I$  depending on the nucleus at hand. This Landé factor is usually much smaller than one.

**Zeeman limit** At low magnetic fields the corresponding energy shift is much smaller than the hyperfine splitting and can be treated as a perturbation. In this situation the  $\hat{I} \cdot \hat{J}$  coupling is dominant and the total angular momentum  $\hat{F}$  precesses around the direction of the magnetic field  $B$ . Consequently, the basis  $\{F, m_F\}$  represents a good set of quantum numbers and, up to first order, the change in potential energy of the state  $|F, m_F\rangle$  is then simply given by the diagonal elements of  $\hat{H}_z$  as per

$$\Delta E(B) - \Delta E_{\text{hfs}} = \langle F, m_F | \hat{H}_z | F, m_F \rangle = \mu_B g_F m_F |B|. \quad (\text{C.15})$$

Here,  $\mu_B$  represents the Bohr-Magneton and  $g_F$  the Landé factor of the hyperfine manifold under consideration:

$$g_F = g_J \frac{F(F+1) + J(J+1) - I(I+1)}{2F(F+1)} + g_I \frac{F(F+1) + I(I+1) - J(J+1)}{2F(F+1)}. \quad (\text{C.16})$$

$\Delta E_{\text{hfs}}$  denotes the hyperfine splitting at zero field, which is given by

$$\Delta E_{\text{hfs}} = \frac{A_{\text{hfs}}}{2} (F(F+1) - I(I+1) - J(J+1)). \quad (\text{C.17})$$

**Paschen-Back limit** In the strong field regime  $\hat{I}$  and  $\hat{J}$  precess independently around the direction of the magnetic field, so that now  $\{I, m_I; J, m_J\}$  provides a sensible set of basis states. The corresponding energy shift of the state  $|I, m_I; J, m_J\rangle$  with respect to  $\hat{H}_{\text{so}} + \hat{H}_z$  is given by

$$\Delta E(B) - \Delta E_{\text{hfs}} = \mu_B (g_J m_J + g_I m_I) |B|. \quad (\text{C.18})$$

The shift due to the hyperfine Hamiltonian  $\hat{H}_{\text{hfs}}$  can be determined as per

$$\begin{aligned} \Delta E_{\text{hfs}} = \langle I, m_I; J, m_J | \hat{H}_{\text{hfs}} | I, m_I; J, m_J \rangle = & A_{\text{hfs}} m_I m_J + \\ & + B_{\text{hfs}} \frac{9m_I^2 m_J^2 - 3I(I+1)m_J^2 - 3J(J+1)m_I^2 + IJ(I+1)(J+1)}{4IJ(2I+1)(2J+1)}. \end{aligned}$$

**Breit-Rabi formula** For states with zero orbital angular momentum  $L = 0$ , the eigenenergies of the valence electron can be calculated analytically, which is the case for the ground states of both  $^{40}\text{K}$  and  $^6\text{Li}$ . The energy of the stretched Zeeman states is given by

$$\Delta E = \frac{A_{\text{hfs}}}{2\hbar^2} I \pm \frac{\mu_B}{\hbar} \left( \frac{1}{2} g_J + g_I I \right) |B|, \quad m_F = I \pm \frac{1}{2} \quad (\text{C.19})$$

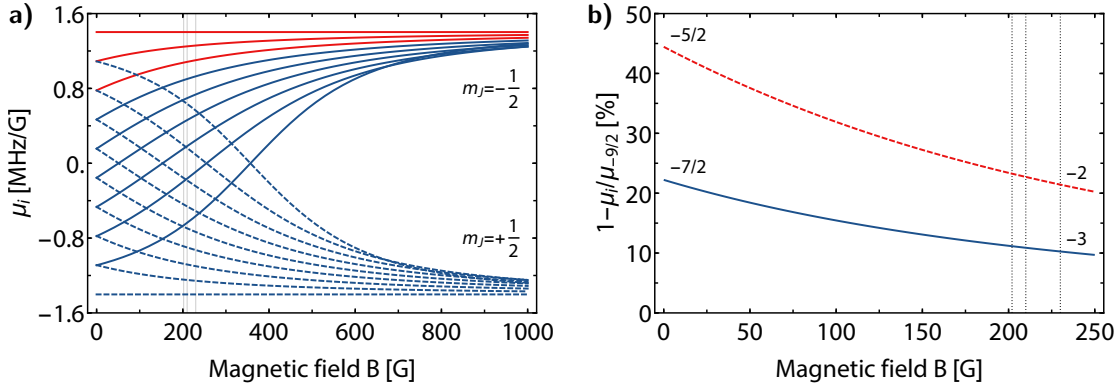


**Figure C.4.: Magnetic moments of the ground state Zeeman levels of  $^{40}\text{K}$ .** a) Magnetic moments vs. magnetic field strength as per eqn. (C.21). Red (top to bottom): negative Zeeman states  $m_F = -9/2, -7/2, -5/2$ , Blue:  $m_J = +1/2$ , Blue-dashed:  $m_J = -1/2$ . b) Relative differences between the magnetic moments of  $-7/2$  and  $-5/2$  and the stretched state  $-9/2$ . Gridlines (left to right): s-wave Feshbach resonance at 202 G, zero-crossing of the scattering length at 210 G, typical background bias field at 230 G.

which is equal to the above expressions for the low- and high field limit. For the remaining states, it can be shown that

$$\Delta E = -\frac{A_{\text{hfs}}}{4\hbar^2} + g_I \mu_B m_F |B| \pm \frac{A_{\text{hfs}}}{2} \left( I + \frac{1}{2} \right) \times \sqrt{1 + \frac{2\mu_B (g_I - g_J) m_F}{A_{\text{hfs}} (I + 1/2)^2} |B| + \frac{\mu_B^2 (g_I - g_J)^2}{A_{\text{hfs}}^2 (I + 1/2)^2} |B|^2} \quad (\text{C.20})$$

holds for  $|m_F| < I + 1/2$ . It should be pointed out that, strictly speaking, the total angular momentum is only a good quantum number at zero magnetic field. While the above equations are valid for any value of the field,  $m_F$  has to be taken as more of a label at high fields. It denotes the eigenstate, to which the system adiabatically connects as  $B \rightarrow 0$ . For the excited states, the Hamiltonian has to be solved numerically in order to obtain the Zeeman shifts for arbitrary values of the magnetic field, as is shown fig. C.7.

The Breit-Rabi formula can be used to conveniently calculate the magnetic moments of the ground Zeeman states for any magnetic field as per

$$\mu_i(\vec{B}) = \left. \frac{\partial E_i}{\partial B} \right|_{B=\vec{B}} \quad (\text{C.21})$$

In fig. C.4a, this relation is shown for  $^{40}\text{K}$  and C.4b depicts the corresponding relative difference of magnetic momenta of the lowest-lying spin states.

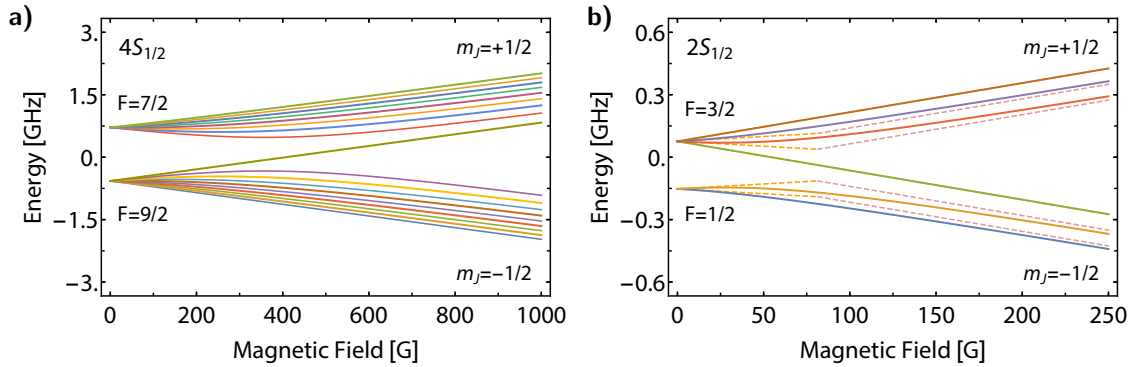


**Figure C.5.: Zeeman energy shifts of the electronic hyperfine ground states  $nS_{1/2}$ .** a) Breit-Rabi plot for the two ground states  $F = 9/2, 7/2$  of  $^{40}\text{K}$ . b) Breit-Rabi plot for  $^6\text{Li}$  with ground state manifolds  $F = 1/2$  and  $F = 3/2$ .

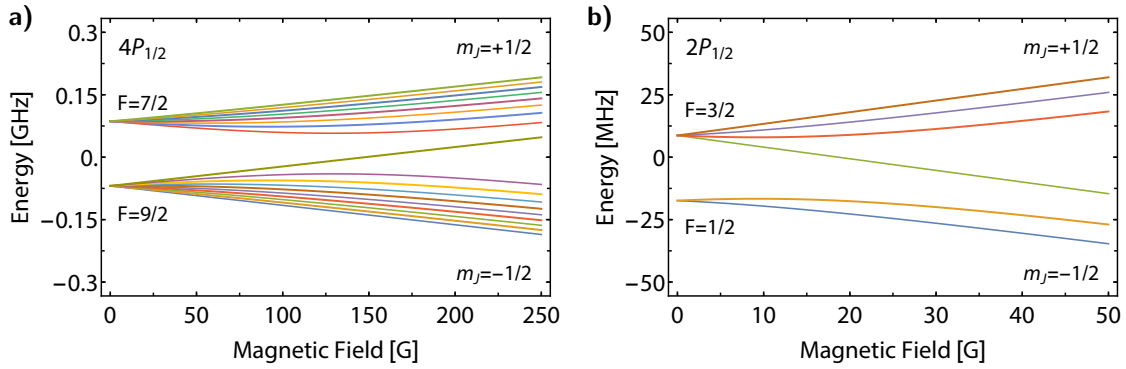


**Figure C.6.: Zeeman energy shifts of the first excited hyperfine states  $nP_{1/2}$ .** a) Numerical calculation of the eigenenergies for the two states with  $F = 9/2, 7/2$  of  $^{40}\text{K}$ . b) Numerical calculation of the eigenenergies for  $^6\text{Li}$  with  $F = 1/2$  and  $F = 3/2$ .

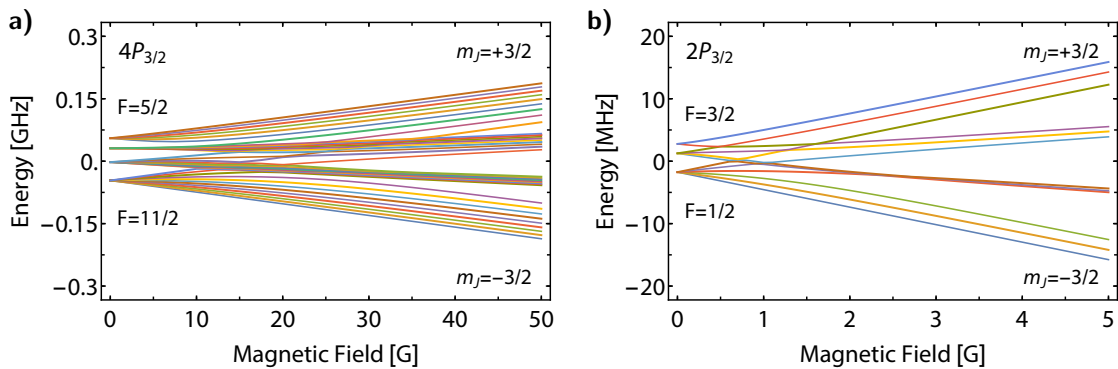


**Figure C.7.: Zeeman energy shifts of the second excited hyperfine states  $nP_{3/2}$ .** a) Numerical calculation of the eigenenergies for the four states  $F = 11/2, 9/2, 7/2, 5/2$  of  $^{40}\text{K}$ . b) Numerical calculation of the eigenenergies for  $^6\text{Li}$  with  $F = 5/2, 3/2, 1/2$ .

**C.5. Survey of the known Feshbach resonances of  $^{40}\text{K}$** 

$m_{F,1}, m_{F,2}$	$M_T$	Partial wave	$B_0$ [G]	$\Delta B_L$ [G]	Reference
+1/2, -1/2	0	s	15(4)	4	[274]
	0	s	31(4)	5	"
	0	s	53(4)	5	"
	0	s	88(4)	4	"
	0	s	246(0.8)	2.4	"
	0	s	389(1)	5.5	"
+3/2, -3/2	0	s	95(4)	23	"
	0	s	182(4)	12	"
+5/2, -5/2	0	s	61(4)	21	"
+7/2, -7/2	0	s	34.3(0.8)	10.8	"
	0	s	147.1(3)	0.8	"
+9/2, -9/2	0	s	17.6(0.3)	5.4	"
+9/2, -7/2	+1	s	13.9(0.2)	1.3	"
	+1	s	28.4(0.3)	6.1	"
+9/2, -5/2	+2	s	27.3(0.3)	4.8	"
	+2	s	63.4(0.7)	30	"
+9/2, -3/2	+3	s	53(4)	14	"
	+3	s	137(8)	53	"
+9/2, -1/2	+4	s	114(8)	>40	"
-9/2, -7/2	-8	s	202.10(7)	7.0(2),7.5(1)	[91, 92]
-9/2, -5/2	-7	s	224.21(5)	9.7(6),7.6(1)	[91, 92]
-7/2, -5/2	-6	s	174	7	[91]
-7/2, -5/2	-6	s	228.8(4)	2.4(3)	"
-7/2, -3/2	-5	s	168.5(4)	-	"
-7/2, -3/2	-5	s	260.3(6)	-	"
-5/2, -3/2	-4	s	22.1(3)	0.7(2)	"
-5/2, -3/2	-4	s	178(1)	6(1)	"
-5/2, -3/2	-4	s	254.8(9)	5(1)	"
-3/2, -1/2	-2	s	37.2(3)	3.6(4)	"
-3/2, -1/2	-2	s	102.1(1)	0.4(1)	"
-3/2, -1/2	-2	s	138.2(1)	1.1(1)	"
-3/2, -1/2	-2	s	219.1(1)	3.5(5)	"
-3/2, -1/2	-2	s	292.3(4)	11.5(2)	"
+7/2, +5/2	+6	s	312(1.8)	4(1.5)	"
-7/2, -7/2	-7	p	198.8		[93]
+9/2, -7/2	+1	p	139		[274]
-9/2, -5/2	-7	p	215(5)		[91]
-7/2, -7/2	-6, -8	p	198.30(2)		"
-7/2, -7/2	-7	p	198.80(5)		"

$m_{F,1}, m_{F,2}$	$M_T$	Partial wave	$B_0$ [G]	$\Delta B_L$ [G]	Reference
$-5/2, -5/2$	$-4, -6$	$p$	232.8(2),232.8(2)		[91]
$-5/2, -5/2$	$-5$	$p$	233.6(2),233.4(2)		"
$-5/2, -5/2$	$-5$	$p$	245.4(4),245.3(5)		"
$-5/2, -3/2$	$-3, -5$	$p$	262.2(2)		"
$-5/2, -3/2$	$-4$	$p$	262.6(2)		"
$-3/2, -3/2$	$-3$	$p$	287(1.8)		"
$-3/2, -3/2$	$-3$	$p$	311.8(4)		"
$-3/2, -1/2$	$-2$	$p$	338(1.8)		"
$-1/2, -1/2$	$-1$	$p$	373(1.8)		"
$+5/2, +5/2$	$+5$	$p$	68(1.8)		"
$+5/2, +5/2$	$+5$	$p$	102(1.8)		"
$+5/2, +5/2$	$+5$	$p$	139(1.8)		"
$+5/2, +5/2$	$+5$	$p$	324(1.8)		"
$+5/2, +9/2$	$+7$	$p$	44(1.8)		"
$+7/2, +7/2$	$+6, +8$	$p$	43.8(2)		"
$+7/2, +7/2$	$+7$	$p$	44.7(2)		"
$+7/2, +7/2$	$+6, +8$	$p$	45.2(2)		"
$+7/2, +7/2$	$+7$	$p$	46.4(2)		"

## Bibliography

- [1] S. F. Novaes. *Standard Model: An Introduction*. In: (Jan. 2000). arXiv: 0001283 [hep-ph] (see p. [13](#)).
- [2] L. Landau and E. Lifschitz. *Quantum mechanics*. Pergamon Press, 1979 (see p. [13](#)).
- [3] R. P. Feynman, R. B. Leighton, and M. Sands. *THE FEYNMAN LECTURES ON PHYSICS, VOL. III*. Basic Books, 2015 (see p. [13](#)).
- [4] W. Pauli. *Über den Zusammenhang des Abschlusses der Elektronengruppen im Atom mit der Komplexstruktur der Spektren*. In: *Zeitschrift für Physik* 31.1 (Feb. 1925), pp. 765–783 (see p. [13](#)).
- [5] F. J. Dyson and A. Lenard. *Stability of Matter. I*. In: *Journal of Mathematical Physics* 8.3 (Mar. 1967), pp. 423–434 (see p. [13](#)).
- [6] A. Lenard and F. J. Dyson. *Stability of Matter. II*. In: *Journal of Mathematical Physics* 9.5 (May 1968), pp. 698–711 (see p. [13](#)).
- [7] L. Landau and E. Lifschitz. *Statistical Physics Part 1*. Pergamon Press, 1980 (see p. [13](#)).
- [8] C. Kittel. *Introduction to SOLID STATE PHYSICS*. New York, USA: John Wiley & Sons, Inc. 1953 (see pp. [14](#), [128](#)).
- [9] J. Bardeen, L. N. Cooper, and J. R. Schrieffer. *Theory of Superconductivity*. In: *Physical Review* 108.5 (Dec. 1957), pp. 1175–1204 (see p. [14](#)).
- [10] L. D. Landau. *The theory of a Fermi liquid*. In: *Sov. Phys. JETP* 3.6 (1956), p. 920. arXiv: arXiv:1011.1669v3 (see pp. [15](#), [111](#)).
- [11] L. Landau and E. Lifschitz. *Statistical Physics Part 2*. Pergamon Press, 1980 (see p. [15](#)).
- [12] H. J. Schulz. *Proceedings of Les Houches Summer School LXI: Fermi liquids and non-Fermi liquids*. Ed. by E. Akkermans, G. J. Montambaux, J. Pichard, and J. Zinn-Justin. Amsterdam: Elsevier, Mar. 1995. arXiv: 9503150v2 [cond-mat] (see pp. [15](#), [111](#)).
- [13] J. G. Bednorz and K. A. Müller. *Peroovskite-type oxides - The new approach to high-Tc superconductivity*. In: *Reviews of Modern Physics* 60.3 (July 1988), pp. 585–600 (see p. [15](#)).

- [14] W. Hofstetter and T. Qin. *Quantum simulation of strongly correlated condensed matter systems*. In: Journal of Physics B: Atomic, Molecular and Optical Physics 51.8 (Apr. 2018), p. 082001 (see pp. 15, 16).
- [15] M. Troyer and U.-J. Wiese. *Computational Complexity and Fundamental Limitations to Fermionic Quantum Monte Carlo Simulations*. In: Physical Review Letters 94.17 (May 2005), p. 170201 (see p. 15).
- [16] E. Y. Loh, J. E. Gubernatis, R. T. Scalettar, S. R. White, D. J. Scalapino, and R. L. Sugar. *Sign problem in the numerical simulation of many-electron systems*. In: Physical Review B 41.13 (May 1990), pp. 9301–9307 (see p. 15).
- [17] I. Bloch, J. Dalibard, and S. Nascimbène. *Quantum simulations with ultracold quantum gases*. In: Nature Physics 8.4 (Apr. 2012), pp. 267–276 (see pp. 15, 16).
- [18] M. J. T. Lewis. *Surveying Instruments of Greece and Rome*. Cambridge: Cambridge University Press, 2001 (see p. 15).
- [19] R. P. Feynman. *Simulating physics with computers*. In: International Journal of Theoretical Physics 21.6-7 (June 1982), pp. 467–488 (see p. 15).
- [20] C. N. Cohen-Tannoudji. *Nobel Lecture: Manipulating atoms with photons*. In: Reviews of Modern Physics 70.3 (July 1998), pp. 707–719 (see p. 15).
- [21] A. Ashkin. *Acceleration and Trapping of Particles by Radiation Pressure*. In: Physical Review Letters 24.4 (Jan. 1970), pp. 156–159 (see p. 15).
- [22] T. Hänsch and A. Schawlow. *Cooling of gases by laser radiation*. In: Optics Communications 13.1 (Jan. 1975), pp. 68–69 (see p. 15).
- [23] W. D. Phillips and H. Metcalf. *Laser Deceleration of an Atomic Beam*. In: Physical Review Letters 48.9 (Mar. 1982), pp. 596–599 (see p. 15).
- [24] S. Chu, J. E. Bjorkholm, A. Ashkin, and A. Cable. *Experimental Observation of Optically Trapped Atoms*. In: Physical Review Letters 57.3 (July 1986), pp. 314–317 (see p. 15).
- [25] E. L. Raab, M. Prentiss, A. Cable, S. Chu, and D. E. Pritchard. *Trapping of Neutral Sodium Atoms with Radiation Pressure*. In: Physical Review Letters 59.23 (Dec. 1987), pp. 2631–2634 (see p. 15).
- [26] A. L. Migdall, J. V. Prodan, W. D. Phillips, T. H. Bergeman, and H. J. Metcalf. *First Observation of Magnetically Trapped Neutral Atoms*. In: Physical Review Letters 54.24 (June 1985), pp. 2596–2599 (see p. 15).
- [27] M. H. Anderson, J. R. Ensher, M. R. Matthews, C. E. Wieman, and E. A. Cornell. *Observation of Bose-Einstein Condensation in a Dilute Atomic Vapor*. In: Science 269.5221 (July 1995), pp. 198–201 (see p. 15).

- [28] K. B. Davis, M. O. Mewes, M. R. Andrews, N. J. van Druten, D. S. Durfee, D. M. Kurn, and W. Ketterle. *Bose-Einstein Condensation in a Gas of Sodium Atoms*. In: Physical Review Letters 75.22 (Nov. 1995), pp. 3969–3973 (see p. 15).
- [29] M. R. Matthews, B. P. Anderson, P. C. Haljan, D. S. Hall, C. E. Wieman, and E. A. Cornell. *Vortices in a Bose-Einstein Condensate*. In: Physical Review Letters 83.13 (Sept. 1999), pp. 2498–2501 (see p. 16).
- [30] M. R. Andrews. *Observation of Interference Between Two Bose Condensates*. In: Science 275.5300 (Jan. 1997), pp. 637–641 (see p. 16).
- [31] I. Bloch, T. W. Hänsch, and T. Esslinger. *Measurement of the spatial coherence of a trapped Bose gas at the phase transition*. In: Nature 403.6766 (Jan. 2000), pp. 166–170 (see p. 16).
- [32] B. DeMarco. *Onset of Fermi Degeneracy in a Trapped Atomic Gas*. In: Science 285.5434 (Sept. 1999), pp. 1703–1706 (see p. 16).
- [33] W. Ketterle, D. S. Durfee, and D. M. Stamper-Kurn. *Making, probing and understanding Bose-Einstein condensates*. In: (Apr. 1999). arXiv: 9904034v2 [cond-mat] (see p. 16).
- [34] W. Ketterle and M. W. Zwierlein. *Making, probing and understanding ultracold Fermi gases*. In: June 2006 (Jan. 2008), pp. 20–30. arXiv: 0801.2500 (see pp. 16, 17, 61, 62, 110).
- [35] V. Letokhov. *Laser Control of Atoms and Molecules*. Oxford University Press, 2007 (see p. 16).
- [36] I. Bloch, J. Dalibard, and W. Zwerger. *Many-body physics with ultracold gases*. In: Reviews of Modern Physics 80.3 (July 2008), pp. 885–964. arXiv: 0704.3011 (see pp. 16, 18, 109, 110, 124).
- [37] F. Jendrzejewski, A. Bernard, K. Müller, P. Cheinet, V. Josse, M. Piraud, L. Pezzé, L. Sanchez-Palencia, A. Aspect, and P. Bouyer. *Three-dimensional localization of ultracold atoms in an optical disordered potential*. In: Nature Physics 8.5 (May 2012), pp. 398–403 (see p. 16).
- [38] H. Ott. *Single atom detection in ultracold quantum gases: a review of current progress*. In: Reports on Progress in Physics 79.5 (May 2016), p. 054401. arXiv: arXiv:1602.08422v2 (see p. 16).
- [39] P. Törmä. *Physics of ultracold Fermi gases revealed by spectroscopies*. In: Physica Scripta 91.4 (2016). arXiv: 1511.03109 (see p. 16).
- [40] M. Aidelsburger. *Artificial gauge fields and topology with ultracold atoms in optical lattices*. In: Journal of Physics B: Atomic, Molecular and Optical Physics 51.19 (Oct. 2018), p. 193001 (see p. 16).

- [41] C. Chin, R. Grimm, P. Julienne, and E. Tiesinga. *Feshbach Resonances in Ultracold Gases*. In: *Reviews of Modern Physics* 3 (2008) (see pp. [16](#), [79](#), [80](#), [82](#), [83](#), [86](#)).
- [42] S. Baier, D. Petter, J. H. Becher, A. Patscheider, G. Natale, L. Chomaz, M. J. Mark, and F. Ferlaino. *Realization of a Strongly Interacting Fermi Gas of Dipolar Atoms*. In: *Physical Review Letters* 121.9 (Aug. 2018), p. 093602 (see p. [16](#)).
- [43] Y. Tang, W. Kao, K.-Y. Li, and B. L. Lev. *Tuning the Dipole-Dipole Interaction in a Quantum Gas with a Rotating Magnetic Field*. In: *Physical Review Letters* 120.23 (June 2018), p. 230401 (see p. [16](#)).
- [44] J. W. Park, S. A. Will, and M. W. Zwierlein. *Ultracold Dipolar Gas of Fermionic  $^{23}\text{Na}^{40}\text{K}$  Molecules in Their Absolute Ground State*. In: *Physical Review Letters* 114.20 (May 2015), p. 205302 (see p. [16](#)).
- [45] S. de Léséleuc, D. Barredo, V. Lienhard, A. Browaeys, and T. Lahaye. *Optical Control of the Resonant Dipole-Dipole Interaction between Rydberg Atoms*. In: *Physical Review Letters* 119.5 (Aug. 2017), p. 053202 (see p. [16](#)).
- [46] R. Grimm. *Ultracold Fermi gases in the BEC-BCS crossover: a review from the Innsbruck perspective*. In: (2007), pp. 1–50. arXiv: 0703091 [cond-mat] (see pp. [17](#), [79](#)).
- [47] A. Edelman and P. Littlewood. *Superconductivity: The persistence of pairs*. In: *Nature Materials* 14.6 (2015), pp. 565–566 (see p. [17](#)).
- [48] F. Chevy and C. Mora. *Ultra-cold polarized Fermi gases*. In: *Reports on Progress in Physics* 73.11 (Nov. 2010), p. 112401. arXiv: 1003.0801 (see pp. [17](#), [110](#), [114](#)).
- [49] C. A. Sá De Melo. *When fermions become bosons: Pairing in ultracold gases*. In: *Physics Today* 61.10 (2008), pp. 45–51 (see p. [18](#)).
- [50] M. Randeria. *Ultracold Fermi gases: Pre-pairing for condensation*. In: *Nature Physics* 6.8 (2010), pp. 561–562 (see p. [18](#)).
- [51] A. Perali, P. Pieri, L. Pisani, and G. C. Strinati. *BCS-BEC Crossover at Finite Temperature for Superfluid Trapped Fermi Atoms*. In: *Physical Review Letters* 92.22 (June 2004), p. 220404 (see p. [18](#)).
- [52] M. Inguscio, W. Ketterle, and S. Stringari, eds. *Quantum Matter at Ultralow Temperatures*. IOS Press, 2016 (see pp. [17](#), [109](#), [110](#), [113](#)).
- [53] C. Salomon, G. V. Shlyapnikov, and L. F. Cugliandolo, eds. *Les Houches 2010 Session XCIV: Many-Body Physics with Ultracold Gases*. Vol. 94. Oxford University Press, 2013, pp. 1–376 (see p. [18](#)).
- [54] A. Schwartz, M. Dressel, G. Grüner, V. Vescoli, L. Degiorgi, and T. Giamarchi. *On-chain electrostatics of metallic TMTSF<sub>2</sub>X salts: Observation of Tomonaga-Luttinger liquid*. In: *Physical Review B* 58.3 (July 1998), pp. 1261–1271 (see p. [19](#)).

- [55] Z. Yao, H. W. C. Postma, L. Balents, and C. Dekker. *Carbon nanotube intramolecular junctions*. In: *Nature* 402.6759 (Nov. 1999), pp. 273–276 (see p. 19).
- [56] F. Milliken, C. Umbach, and R. Webb. *Indications of a Luttinger liquid in the fractional quantum Hall regime*. In: *Solid State Communications* 97.4 (Jan. 1996), pp. 309–313 (see p. 19).
- [57] O. M. Auslaender. *Spin-Charge Separation and Localization in One Dimension*. In: *Science* 308.5718 (Apr. 2005), pp. 88–92 (see p. 19).
- [58] T. L. Yang, P. Grišins, Y. T. Chang, Z. H. Zhao, C. Y. Shih, T. Giamarchi, and R. G. Hulet. *Measurement of the Dynamical Structure Factor of a 1D Interacting Fermi Gas*. In: *Physical Review Letters* 121.10 (Sept. 2018), p. 103001. arXiv: 1803.06331 (see pp. 19, 110, 149, 156).
- [59] B. DeMarco. *Quantum Behavior of an Atomic Fermi Gas*. In: PhD Thesis (2001), pp. 1–318 (see pp. 26, 58).
- [60] D. R. Fernandes. *Trapping and cooling of fermionic alkali atoms to quantum degeneracy. Sub-Doppler cooling of Potassium-40 and Lithium-6 in gray molasses*. PhD thesis. 2014, p. 236 (see pp. 26, 37, 38, 44, 59).
- [61] D. Suchet. *Simulating the dynamics of harmonically trapped Weyl particles with cold atoms*. PhD thesis. 2016 (see pp. 26, 35, 44, 45, 57, 75, 94).
- [62] A. Ridinger. *Towards quantum degenerate Fermi mixtures : Photoassociation of weakly bound  $6\text{Li}40\text{K}$  molecules*. PhD thesis. 2011 (see pp. 26, 28, 30, 32, 35).
- [63] M. Rabinovic. *Quasithermalization of fermions in a quadrupole potential and evaporative cooling of 40K to quantum degeneracy*. PhD thesis. 2017 (see pp. 30, 31, 33, 35, 39, 45, 47, 62, 84, 85, 209, 210).
- [64] T. Salez. *Towards quantum degenerate atomic Fermi mixtures*. PhD thesis. 2011 (see pp. 30, 32, 35).
- [65] M. Berglund and M. E. Wieser. *Isotopic compositions of the elements 2009 (IUPAC Technical Report)\**. In: *Pure Appl. Chem* 83.2 (2011), pp. 397–410 (see p. 31).
- [66] F. Sievers. *Ultracold Fermi mixtures and simultaneous sub-Doppler laser cooling of fermionic  $6\text{Li}$  and  $40\text{K}$* . PhD thesis. 2014 (see pp. 32, 37, 38).
- [67] C. Klempt, T. Van Zoest, T. Henninger, O. Topic, E. Rasel, W. Ertmer, and J. Arlt. *Ultraviolet light-induced atom desorption for large rubidium and potassium magneto-optical traps*. In: *Physical Review A - Atomic, Molecular, and Optical Physics* (2006). arXiv: 0509241 [cond-mat] (see p. 33).
- [68] C. N. Cohen-Tannoudji and D. Guery-Odelin. *Advances In Atomic Physics: An Overview*. World Scientific Publishing, 2011, p. 796 (see pp. 34, 53).

- [69] J. Dalibard. *Une brève histoire des atomes froids*. Collège de France, Paris, 2014 (see pp. [34](#), [36](#), [37](#)).
- [70] P. M. Duarte, R. A. Hart, J. M. Hitchcock, T. A. Corcovilos, T. L. Yang, A. Reed, and R. G. Hulet. *All-optical production of a lithium quantum gas using narrow-line laser cooling*. In: *Physical Review A - Atomic, Molecular, and Optical Physics* (2011). arXiv: 1109.6635 (see p. [36](#)).
- [71] D. Rio Fernandes, F. Sievers, N. Kretzschmar, S. Wu, C. Salomon, and F. Chevy. *Sub-Doppler laser cooling of fermionic 40 K atoms in three-dimensional gray optical molasses*. In: *EPL (Europhysics Letters)* 100.6 (Dec. 2012), p. 63001 (see p. [37](#)).
- [72] F. Sievers, N. Kretzschmar, D. R. Fernandes, D. Suchet, M. Rabinovic, S. Wu, C. V. Parker, L. Khaykovich, C. Salomon, and F. Chevy. *Simultaneous sub-Doppler laser cooling of fermionic Li6 and K 40*. In: *Physical Review A* 91.2 (Feb. 2015), p. 023426 (see p. [37](#)).
- [73] G. Salomon, L. Fouché, P. Wang, A. Aspect, P. Bouyer, and T. Bourdel. *Gray-molasses cooling of 39 K to a high phase-space density*. In: *EPL (Europhysics Letters)* 104.6 (Dec. 2013), p. 63002 (see p. [37](#)).
- [74] D. Nath, R. K. Easwaran, G. Rajalakshmi, and C. S. Unnikrishnan. *Quantum-interference-enhanced deep sub-Doppler cooling of 39K atoms in gray molasses*. In: *Physical Review A* 88.5 (Nov. 2013), p. 053407 (see p. [37](#)).
- [75] A. T. Grier, I. Ferrier-Barbut, B. S. Rem, M. Delehayé, L. Khaykovich, F. Chevy, and C. Salomon.  *$\Lambda$ -enhanced sub-Doppler cooling of lithium atoms in D1 gray molasses*. In: *Physical Review A* 87.6 (June 2013), p. 063411 (see p. [37](#)).
- [76] A. Burchianti, G. Valtolina, J. A. Seman, E. Pace, M. De Pas, M. Inguscio, M. Zaccanti, and G. Roati. *Efficient all-optical production of large Li6 quantum gases using D1 gray-molasses-cooling*. In: *Physical Review A* 90.4 (Oct. 2014), p. 043408 (see p. [37](#)).
- [77] Q. Bouton, R. Chang, A. L. Hoendervanger, F. Nogrette, A. Aspect, C. I. Westbrook, and D. Clément. *Fast production of Bose-Einstein condensates of metastable helium*. In: *Physical Review A* 91.6 (June 2015), p. 061402 (see p. [37](#)).
- [78] H.-Z. Chen, X.-C. Yao, Y.-P. Wu, X.-P. Liu, X.-Q. Wang, Y.-X. Wang, Y.-A. Chen, and J.-W. Pan. *Production of large K41 Bose-Einstein condensates using D1 gray molasses*. In: *Physical Review A* 94.3 (Sept. 2016), p. 033408 (see p. [37](#)).
- [79] G. Colzi, G. Durastante, E. Fava, S. Serafini, G. Lamporesi, and G. Ferrari. *Sub-Doppler cooling of sodium atoms in gray molasses*. In: *Physical Review A* 93.2 (Feb. 2016), p. 023421 (see p. [37](#)).

- [80] G. D. Bruce, E. Haller, B. Peaudecerf, D. A. Cotta, M. Andia, S. Wu, M. Y. H. Johnson, B. W. Lovett, and S. Kuhr. *Sub-Doppler laser cooling of 40K with Raman gray molasses on the D2 line*. In: Journal of Physics B: Atomic, Molecular and Optical Physics 50.9 (May 2017), p. 095002 (see p. 37).
- [81] S. Rosi, A. Burchianti, S. Conclave, D. S. Naik, G. Roati, C. Fort, and F. Minardi.  *$\Lambda$ -enhanced grey molasses on the D2 transition of Rubidium-87 atoms*. In: Scientific Reports 8.1 (Dec. 2018), p. 1301 (see p. 37).
- [82] M. E. Gehm. *Properties of 6Li*. PhD thesis. 2003, pp. 1–33 (see pp. 41, 81).
- [83] T. G. Tiecke. *Properties of Potassium*. 2011 (see pp. 41, 81, 95).
- [84] T. L. Gustavson, A. P. Chikkatur, A. E. Leanhardt, A. Görlitz, S. Gupta, D. E. Pritchard, and W. Ketterle. *Transport of Bose-Einstein Condensates with Optical Tweezers*. In: Physical Review Letters (2002). arXiv: 0108496 [cond-mat] (see p. 41).
- [85] K. Nakagawa, Y. Suzuki, M. Horikoshi, and J. B. Kim. *Simple and efficient magnetic transport of cold atoms using moving coils for the production of Bose-Einstein condensation*. In: Applied Physics B: Lasers and Optics (2005) (see p. 41).
- [86] J. Walraven. *Quantum Gases - Collisions and Statistics*. University of Vienna, 2013 (see pp. 43, 120).
- [87] C. Enesa. *Towards quantum degenerate Fermi mixtures*. 2015 (see p. 44).
- [88] M. E. Gehm, K. M. O'Hara, T. A. Savard, and J. E. Thomas. *Dynamics of noise-induced heating in atom traps*. In: Physical Review A 58.5 (Nov. 1998), pp. 3914–3921 (see p. 55).
- [89] A. Trenkwalder and U. Rudolf Grimm. *Creation of a Strongly Interacting Fermi-Fermi Mixture of 6 Li and 40 K dissertation by*. PhD thesis. University of Innsbruck, 2011 (see pp. 55, 201).
- [90] T. G. Tiecke. *Properties of Potassium*. In: Physics 02.20 (2010), pp. 1–14 (see p. 57).
- [91] A. Ludewig. *Feshbach resonances in 40 K*. PhD thesis. University of Amsterdam, 2012 (see pp. 62, 80, 219, 220).
- [92] T. G. Tiecke, M. R. Goosen, A. Ludewig, S. D. Gensemer, S. Kraft, S. J. J. M. F. Kokkelmans, and J. T. M. Walraven. *Broad Feshbach Resonance in the Li6-K40 Mixture*. In: Physical Review Letters 104.5 (Feb. 2010), p. 053202. arXiv: 0908.2071 (see pp. 62, 219).
- [93] T. G. Tiecke. *Feshbach resonances in ultracold mixtures of the fermionic quantum gases 6Li and 40K*. PhD thesis. University of Amsterdam, 2010 (see pp. 62, 219).

- [94] A. L. Stancik and E. B. Brauns. *A simple asymmetric lineshape for fitting infrared absorption spectra*. In: *Vibrational Spectroscopy* 47.1 (May 2008), pp. 66–69 (see p. 70).
- [95] M. Auzinsh, D. Budker, and S. M. Rochester. *Optically Polarized Atoms: Understanding Light-Atom Interactions*. 1st. New York, NY: Oxford University Press, 2010 (see pp. 71, 73).
- [96] C. J. Foot. *Atomic Physics*. In: *Nature* 71.2 (2005), pp. 35–6. arXiv: arXiv : 1011 . 1669v3 (see pp. 72, 215).
- [97] H. I. EWEN and E. M. PURCELL. *Observation of a Line in the Galactic Radio Spectrum: Radiation from Galactic Hydrogen at 1,420 Mc./sec.* In: *Nature* 168.4270 (Sept. 1951), pp. 356–356 (see p. 72).
- [98] H. C. van de Hulst, C. A. Muller, and J. H. Oort. *The spiral structure of the outer part of the Galactic System derived from the hydrogen emission at 21 cm wavelength*. In: *Bulletin of the Astronomical Institutes of the Netherlands* 12 (1954), p. 117 (see p. 72).
- [99] L. ESSEN and J. V. L. PARRY. *An Atomic Standard of Frequency and Time Interval: A Cæsium Resonator*. In: *Nature* 176.4476 (Aug. 1955), pp. 280–282 (see p. 72).
- [100] A. Kastler. *Nobel Lecture: Optical methods for studying Hertzian resonances*. In: *Physics* (1966), pp. 186–204 (see p. 73).
- [101] D. A. Steck. *Quantum and Atom Optics*. University of Oregon, 2007 (see p. 74).
- [102] L. D. Landau. *On the theory of transfer of energy at collisions II*. In: *Phys. Z. Sowjetunion* 2.46 (1932) (see p. 74).
- [103] C. Zener. *Non-Adiabatic Crossing of Energy Levels*. In: *Proceedings of the Royal Society A: Mathematical, Physical and Engineering Sciences* 137.833 (Sept. 1932), pp. 696–702 (see p. 74).
- [104] E. C. G. Stueckelberg. *Theorie der unelastischen Stösse zwischen Atomen*. In: *Helvetica Physica Acta* 5 (1933), p. 369 (see p. 74).
- [105] E. Majorana. *Atomi orientati in campo magnetico variabile*. In: *Il Nuovo Cimento* 9.2 (Feb. 1932), pp. 43–50 (see p. 74).
- [106] J. R. Rubbmark, M. M. Kash, M. G. Littman, and D. Kleppner. *Dynamical effects at avoided level crossings: A study of the Landau-Zener effect using Rydberg atoms*. In: *Physical Review A* 23.6 (June 1981), pp. 3107–3117. arXiv: arXiv : 1011 . 1669v3 (see p. 75).

- [107] M. P. Köppinger, D. J. McCarron, D. L. Jenkin, P. K. Molony, H. W. Cho, S. L. Cornish, C. R. Le Sueur, C. L. Blackley, and J. M. Hutson. *Production of optically trapped RbCs 87 Feshbach molecules*. In: Physical Review A - Atomic, Molecular, and Optical Physics 89.3 (2014), pp. 31–33. arXiv: 1312.3551 (see pp. 79, 98).
- [108] J. W. Park, S. A. Will, and M. W. Zwierlein. *Ultracold Dipolar Gas of Fermionic Na23K40 Molecules in Their Absolute Ground State*. In: Physical Review Letters 114.20 (May 2015), p. 205302 (see p. 79).
- [109] F. Seeßelberg, N. Buchheim, Z.-K. Lu, T. Schneider, X.-Y. Luo, E. Tiemann, I. Bloch, and C. Gohle. *Modeling the adiabatic creation of ultracold polar 23Na40K molecules*. In: Physical Review A 97.1 (Jan. 2018), p. 013405 (see p. 79).
- [110] C. E. Klauss, X. Xie, C. Lopez-Abadia, J. P. D’Incao, Z. Hadzibabic, D. S. Jin, and E. A. Cornell. *Observation of Efimov Molecules Created from a Resonantly Interacting Bose Gas*. In: Physical Review Letters 119.14 (Oct. 2017), p. 143401 (see p. 79).
- [111] A. Marte, T. Volz, J. Schuster, S. Dürr, G. Rempe, E. G. M. van Kempen, and B. J. Verhaar. *Feshbach Resonances in Rubidium 87: Precision Measurement and Analysis*. In: Physical Review Letters 89.28 (Dec. 2002), p. 283202. arXiv: 0210651 [cond-mat] (see p. 79).
- [112] S. Dürr, T. Volz, N. Syassen, G. Rempe, E. van Kempen, S. Kokkelmans, B. Verhaar, and H. Friedrich. *Dissociation of Feshbach molecules into different partial waves*. In: Physical Review A 72.5 (Nov. 2005), p. 052707. arXiv: 0507580 [cond-mat] (see pp. 79, 98).
- [113] S. Knoop, T. Schuster, R. Scelle, A. Trautmann, J. Appmeier, M. K. Oberthaler, E. Tiesinga, and E. Tiemann. *Feshbach spectroscopy and analysis of the interaction potentials of ultracold sodium*. In: Physical Review A - Atomic, Molecular, and Optical Physics 83.4 (2011), pp. 1–10. arXiv: 1102.0572 (see pp. 79, 98).
- [114] C. L. Blackley, C. R. Le Sueur, J. M. Hutson, D. J. McCarron, M. P. Köppinger, H. W. Cho, D. L. Jenkin, and S. L. Cornish. *Feshbach resonances in ultracold 85Rb*. In: Physical Review A - Atomic, Molecular, and Optical Physics 87.3 (2013), pp. 1–7. arXiv: 1212.5446 (see pp. 79, 98).
- [115] M.-J. Zhu, H. Yang, L. Liu, D.-C. Zhang, Y.-X. Liu, J. Nan, J. Rui, B. Zhao, J.-W. Pan, and E. Tiemann. *Feshbach loss spectroscopy in an ultracold Na23K40*. In: Physical Review A 96.6 (Dec. 2017), p. 062705. arXiv: 1709.01260 (see p. 79).
- [116] L. Tanzi, C. R. Cabrera, J. Sanz, P. Cheiney, M. Tomza, and L. Tarruell. *Feshbach resonances in potassium Bose-Bose mixtures*. In: (Oct. 2018), pp. 1–9. arXiv: 1810.12453 (see p. 79).

- [117] Y. Cui, M. Deng, L. You, B. Gao, and M. K. Tey. *Broad Feshbach resonances in ultracold alkali-metal systems*. In: Physical Review A 98.4 (Oct. 2018), p. 042708. arXiv: 1808.03917 (see p. 79).
- [118] X.-P. Liu, X.-C. Yao, R. Qi, X.-Q. Wang, Y.-X. Wang, Y.-A. Chen, and J.-W. Pan. *Feshbach spectroscopy of an ultracold  $K41Li6$  mixture and  $K41$  atoms*. In: Physical Review A 98.2 (Aug. 2018), p. 022704 (see p. 79).
- [119] T. Hartmann, T. A. Schulze, K. K. Voges, P. Gersema, M. W. Gempel, E. Tiemann, A. Zenesini, and S. Ospelkaus. *Feshbach resonances in  $Na23+K39$  mixtures and refined molecular potentials for the NaK molecule*. In: (Oct. 2018), pp. 1–9. arXiv: 1810.00608 (see p. 79).
- [120] T. A. Schulze, T. Hartmann, K. K. Voges, M. W. Gempel, E. Tiemann, A. Zenesini, and S. Ospelkaus. *Feshbach spectroscopy and dual-species Bose-Einstein condensation of  $Na23 - K39$  mixtures*. In: Physical Review A 97.2 (2018), pp. 1–9. arXiv: arXiv:1709.03796v1 (see p. 79).
- [121] F. Ferlaino, C. D’Errico, G. Roati, M. Zaccanti, M. Inguscio, G. Modugno, and A. Simoni. *Feshbach spectroscopy of a  $K$ - $Rb$  atomic mixture*. In: Physical Review A - Atomic, Molecular, and Optical Physics 73.4 (2006), pp. 1–4. arXiv: 0510630 [cond-mat] (see pp. 79, 98).
- [122] T. Schuster, R. Scelle, A. Trautmann, S. Knoop, M. K. Oberthaler, M. M. Haverhals, M. R. Goosen, S. J. Kokkelmans, and E. Tiemann. *Feshbach spectroscopy and scattering properties of ultracold  $Li + Na$  mixtures*. In: Physical Review A - Atomic, Molecular, and Optical Physics 85.4 (2012), pp. 1–8. arXiv: 1202.1199 (see pp. 79, 98).
- [123] H. W. Cho, D. J. McCarron, M. P. Köppinger, D. L. Jenkin, K. L. Butler, P. S. Julienne, C. L. Blackley, C. R. Le Sueur, J. M. Hutson, and S. L. Cornish. *Feshbach spectroscopy of an ultracold mixture of  $85Rb$  and  $133Cs$* . In: Physical Review A - Atomic, Molecular, and Optical Physics 87.1 (2013), pp. 1–5. arXiv: 1208.4569 (see pp. 79, 98).
- [124] S. Dong, Y. Cui, C. Shen, Y. Wu, M. K. Tey, L. You, and B. Gao. *Observation of broad  $p$ -wave Feshbach resonances in ultracold  $Rb85 - Rb87$  mixtures*. In: Physical Review A 94.6 (2016), pp. 1–7. arXiv: 1610.01739 (see p. 79).
- [125] Y. Cui, C. Shen, M. Deng, S. Dong, C. Chen, R. Lü, B. Gao, M. K. Tey, and L. You. *Observation of Broad  $d$ -Wave Feshbach Resonances with a Triplet Structure*. In: Physical Review Letters 119.20 (2017), pp. 1–5. arXiv: 1709.08794 (see pp. 79, 84, 97).
- [126] S. Will. *From Atom Optics to Quantum Simulation*. Vol. 53. Springer Theses 9. Berlin, Heidelberg: Springer Berlin Heidelberg, 2013, p. 235. arXiv: arXiv:1106.3562 (see pp. 61, 62, 80).

- [127] C. Ticknor, C. A. Regal, D. S. Jin, and J. L. Bohn. *Multiplet structure of Feshbach resonances in nonzero partial waves*. In: *Physical Review A* 69.4 (Apr. 2004), p. 042712. arXiv: 0310121 [physics] (see pp. 82, 97).
- [128] P. Törmä and K. Sengstock, eds. *Cold Atoms Vol.3: Quantum Gas Experiments: Exploring Many-Body States*. Imperial College Press, 2015 (see pp. 82, 117).
- [129] E. Tiesinga. *Private communication*. 2017 (see pp. 84, 85, 93, 96, 106, 155).
- [130] A. Zenesini, B. Huang, M. Berninger, S. Besler, H.-C. Nägerl, F. Ferlaino, R. Grimm, C. H. Greene, and J. V. Stecher. *Resonant five-body recombination in an ultracold gas of bosonic atoms*. In: *New Journal of Physics* 15.4 (Apr. 2013), p. 043040. arXiv: arXiv:1205.1921v1 (see p. 86).
- [131] F. H. Mies, E. Tiesinga, and P. S. Julienne. *Manipulation of Feshbach resonances in ultracold atomic collisions using time-dependent magnetic fields*. In: *Physical Review A* 61.2 (Jan. 2000), p. 022721 (see p. 88).
- [132] V. A. Yurovsky and A. Ben-Reuven. *Three-body loss of trapped ultracold Rb87 atoms due to a Feshbach resonance*. In: *Physical Review A* 67.5 (May 2003), p. 050701 (see p. 88).
- [133] B. D. Esry, C. H. Greene, and J. P. Burke. *Recombination of three atoms in the ultracold limit*. In: *Physical Review Letters* 83.9 (1999), pp. 1751–1754 (see p. 89).
- [134] O. I. Kartavtsev and J. H. Macek. *Low-energy three-body recombination near a Feshbach resonance*. In: *Few-Body Systems* 31.2-4 (2002), pp. 249–254 (see p. 89).
- [135] O. J. Luiten, M. W. Reynolds, and J. T. M. Walraven. *Kinetic theory of the evaporative cooling of a trapped gas*. In: *Physical Review A* 53.1 (Jan. 1996), pp. 381–389 (see p. 91).
- [136] Q. Beaufils, A. Crubellier, T. Zanon, B. Laburthe-Tolra, E. Maréchal, L. Vernac, and O. Gorceix. *Feshbach resonance in d-wave collisions*. In: *Physical Review A - Atomic, Molecular, and Optical Physics* 79.3 (2009), pp. 1–8. arXiv: 0811.4282 (see pp. 92, 97).
- [137] E. Tiesinga. *Private communication*. 2017 (see pp. 95, 97, 105, 106, 155).
- [138] P. O. Fedichev, M. W. Reynolds, and G. V. Shlyapnikov. *Three-Body Recombination of Ultracold Atoms to a Weakly Bound s-Level*. In: *Physical Review Letters* 77.14 (Sept. 1996), pp. 2921–2924. arXiv: 9605009 [atom-ph] (see p. 96).
- [139] D. S. Petrov. *Three-body problem in Fermi gases with short-range interparticle interaction*. In: *Physical Review A* 67.1 (Jan. 2003), p. 010703. arXiv: 0209246 [cond-mat] (see p. 96).
- [140] C. Chin, V. Vuletić, A. J. Kerman, and S. Chu. *High Resolution Feshbach Spectroscopy of Cesium*. In: *Physical Review Letters* 85.13 (Sept. 2000), pp. 2717–2720 (see p. 98).

- [141] A. Marte, T. Volz, J. Schuster, S. Dürr, G. Rempe, E. G. M. van Kempen, and B. J. Verhaar. *Feshbach Resonances in Rubidium 87: Precision Measurement and Analysis*. In: Physical Review Letters 89.28 (Dec. 2002), p. 283202. arXiv: 0210651 [cond-mat] (see p. 98).
- [142] M. Berninger, A. Zenesini, B. Huang, W. Harm, H. C. Nägerl, F. Ferlaino, R. Grimm, P. S. Julienne, and J. M. Hutson. *Feshbach resonances, weakly bound molecular states, and coupled-channel potentials for cesium at high magnetic fields*. In: Physical Review A - Atomic, Molecular, and Optical Physics 87.3 (2013), pp. 1–17. arXiv: 1212.5584 (see p. 98).
- [143] E. Tiesinga. *Private communication*. 2017 (see p. 106).
- [144] S. Giorgini, L. P. Pitaevskii, and S. Stringari. *Theory of ultracold atomic Fermi gases*. In: Reviews of Modern Physics 80.4 (2008), pp. 1215–1274. arXiv: 0706.3360 (see p. 109).
- [145] L. Radzihovsky and D. E. Sheehy. *Imbalanced Feshbach-resonant Fermi gases*. In: Reports on Progress in Physics 73.7 (July 2010), p. 076501. arXiv: 0911.1740 (see p. 109).
- [146] A. I. Larkin and Y. N. Ovchinnikov. *Nonuniform state of superconductors*. In: Sov. Phys. JETP 20.762 (1965) (see p. 109).
- [147] P. Fulde and R. A. Ferrell. *Superconductivity in a Strong Spin-Exchange Field*. In: Physical Review 135.3A (Aug. 1964), A550–A563 (see p. 109).
- [148] A. M. Clogston. *Upper Limit for the Critical Field in Hard Superconductors*. In: Physical Review Letters 9.6 (Sept. 1962), pp. 266–267 (see p. 109).
- [149] B. S. Chandrasekhar. *A NOTE ON THE MAXIMUM CRITICAL FIELD OF HIGH-FIELD SUPERCONDUCTORS*. In: Applied Physics Letters 1.1 (Sept. 1962), pp. 7–8 (see p. 109).
- [150] A. Schirotzek, C.-H. Wu, A. Sommer, and M. W. Zwierlein. *Observation of Fermi Polarons in a Tunable Fermi Liquid of Ultracold Atoms*. In: Physical Review Letters 102.23 (June 2009), p. 230402. arXiv: 0902.3021 (see pp. 110, 113, 114).
- [151] S. Nascimbène, N. Navon, K. J. Jiang, F. Chevy, and C. Salomon. *Exploring the thermodynamics of a universal Fermi gas*. In: Nature 463.7284 (Feb. 2010), pp. 1057–1060. arXiv: 0911.0747 (see pp. 110, 114).
- [152] N. Navon, S. Nascimbene, F. Chevy, and C. Salomon. *The Equation of State of a Low-Temperature Fermi Gas with Tunable Interactions*. In: Science 328.5979 (May 2010), pp. 729–732 (see p. 110).

- [153] S. Nascimbène, N. Navon, S. Pilati, F. Chevy, S. Giorgini, A. Georges, and C. Salomon. *Fermi-Liquid Behavior of the Normal Phase of a Strongly Interacting Gas of Cold Atoms*. In: Physical Review Letters 106.21 (May 2011), p. 215303. arXiv: 1012.4664 (see pp. 110, 114).
- [154] Y. Sagi, T. E. Drake, R. Paudel, R. Chapurin, and D. S. Jin. *Breakdown of the Fermi Liquid Description for Strongly Interacting Fermions*. In: Physical Review Letters 114.7 (Feb. 2015), p. 075301. arXiv: 1409.4743 (see pp. 110, 114, 118).
- [155] Z. Yan, P. B. Patel, B. Mukherjee, R. J. Fletcher, J. Struck, and M. W. Zwierlein. *Boiling a Unitary Fermi Liquid*. In: (Nov. 2018). arXiv: 1811.00481 (see p. 110).
- [156] L. Radzihovsky and D. E. Sheehy. *Imbalanced Feshbach-resonant Fermi gases*. In: Reports on Progress in Physics 73.7 (2010). arXiv: 0911.1740 (see p. 110).
- [157] Y.-i. Shin, C. H. Schunck, A. Schirotzek, and W. Ketterle. *Phase diagram of a two-component Fermi gas with resonant interactions*. In: Nature 451.7179 (Feb. 2008), pp. 689–693 (see p. 110).
- [158] A. Vogler, R. Labouvie, G. Barontini, S. Eggert, V. Guarrera, and H. Ott. *Dimensional Phase Transition from an Array of 1D Luttinger Liquids to a 3D Bose-Einstein Condensate*. In: Physical Review Letters 113.21 (Nov. 2014), p. 215301. arXiv: 1410.1739 (see pp. 110, 121).
- [159] M. G. Ries, A. N. Wenz, G. Zürn, L. Bayha, I. Boettcher, D. Kedar, P. A. Murthy, M. Neidig, T. Lompe, and S. Jochim. *Observation of Pair Condensation in the Quasi-2D BEC-BCS Crossover*. In: Physical Review Letters 114.23 (June 2015), p. 230401 (see p. 110).
- [160] P. A. Murthy, I. Boettcher, L. Bayha, M. Holzmann, D. Kedar, M. Neidig, M. G. Ries, A. N. Wenz, G. Zürn, and S. Jochim. *Observation of the Berezinskii-Kosterlitz-Thouless Phase Transition in an Ultracold Fermi Gas*. In: Physical Review Letters 115.1 (June 2015), p. 010401 (see p. 110).
- [161] A. T. Sommer, L. W. Cheuk, M. J. H. Ku, W. S. Bakr, and M. W. Zwierlein. *Evolution of Fermion Pairing from Three to Two Dimensions*. In: Physical Review Letters 108.4 (Jan. 2012), p. 045302 (see p. 110).
- [162] Y. Zhang, W. Ong, I. Arakelyan, and J. E. Thomas. *Polaron-to-Polaron Transitions in the Radio-Frequency Spectrum of a Quasi-Two-Dimensional Fermi Gas*. In: Physical Review Letters 108.23 (June 2012), p. 235302 (see p. 110).
- [163] M. Feld, B. Fröhlich, E. Vogt, M. Koschorreck, and M. Köhl. *Observation of a pairing pseudogap in a two-dimensional Fermi gas*. In: Nature 480.7375 (Nov. 2011), pp. 75–78 (see p. 110).

- [164] B. Fröhlich, M. Feld, E. Vogt, M. Koschorreck, W. Zwerger, and M. Köhl. *Radio-Frequency Spectroscopy of a Strongly Interacting Two-Dimensional Fermi Gas*. In: *Physical Review Letters* 106.10 (Mar. 2011), p. 105301 (see p. 110).
- [165] H. Moritz, T. Stöferle, K. Günter, M. Köhl, and T. Esslinger. *Confinement Induced Molecules in a 1D Fermi Gas*. In: *Physical Review Letters* 94.21 (June 2005), 210401 (1–4) (see pp. 110, 115, 121).
- [166] Y.-A. Liao, A. S. C. Rittner, T. Paprotta, W. Li, G. B. Partridge, R. G. Hulet, S. K. Baur, and E. J. Mueller. *Spin-imbalance in a one-dimensional Fermi gas*. In: *Nature* 467.7315 (Sept. 2010), pp. 567–569 (see p. 110).
- [167] F. Serwane, G. Zurn, T. Lompe, T. B. Ottenstein, A. N. Wenz, and S. Jochim. *Deterministic Preparation of a Tunable Few-Fermion System*. In: *Science* 332.6027 (Apr. 2011), pp. 336–338 (see p. 110).
- [168] G. Zürn, A. N. Wenz, S. Murmann, A. Bergschneider, T. Lompe, and S. Jochim. *Pairing in Few-Fermion Systems with Attractive Interactions*. In: *Physical Review Letters* 111.17 (Oct. 2013), p. 175302 (see p. 110).
- [169] A. N. Wenz, G. Zurn, S. Murmann, I. Brouzos, T. Lompe, and S. Jochim. *From Few to Many: Observing the Formation of a Fermi Sea One Atom at a Time*. In: *Science* 342.6157 (Oct. 2013), pp. 457–460 (see p. 110).
- [170] M. C. Revelle, J. A. Fry, B. A. Olsen, and R. G. Hulet. *1D to 3D Crossover of a Spin-Imbalanced Fermi Gas*. In: *Physical Review Letters* 117.23 (Nov. 2016), p. 235301. arXiv: 1605.06986 (see pp. 110, 121).
- [171] G. Pagano, M. Mancini, G. Cappellini, P. Lombardi, F. Schäfer, H. Hu, X.-J. Liu, J. Catani, C. Sias, M. Inguscio, and L. Fallani. *A one-dimensional liquid of fermions with tunable spin*. In: *Nature Physics* 10.3 (Mar. 2014), pp. 198–201. arXiv: 1408.0928 (see p. 110).
- [172] M. Casula, D. M. Ceperley, and E. J. Mueller. *Quantum Monte Carlo study of one-dimensional trapped fermions with attractive contact interactions*. In: *Physical Review A* 78.3 (Sept. 2008), p. 033607 (see p. 110).
- [173] G. Orso. *Attractive Fermi Gases with Unequal Spin Populations in Highly Elongated Traps*. In: *Physical Review Letters* 98.7 (Feb. 2007), p. 070402 (see p. 110).
- [174] H. Hu, X.-J. Liu, and P. D. Drummond. *Phase Diagram of a Strongly Interacting Polarized Fermi Gas in One Dimension*. In: *Physical Review Letters* 98.7 (Feb. 2007), p. 070403 (see p. 110).
- [175] X. W. Guan, M. T. Batchelor, C. Lee, and M. Bortz. *Phase transitions and pairing signature in strongly attractive Fermi atomic gases*. In: *Physical Review B* 76.8 (Aug. 2007), p. 085120 (see p. 110).

- [176] T. Mizushima, K. Machida, and M. Ichioka. *Direct Imaging of Spatially Modulated Superfluid Phases in Atomic Fermion Systems*. In: Physical Review Letters 94.6 (Feb. 2005), p. 060404 (see p. 110).
- [177] K. Yang. *Inhomogeneous superconducting state in quasi-one-dimensional systems*. In: Physical Review B 63.14 (Mar. 2001), p. 140511 (see p. 110).
- [178] P. Törmä. *Lecture Notes: Fermi liquid theory*. 2015 (see pp. 111–113).
- [179] P. Nozieres. *Theory of Interacting Fermi Systems*. Addison Wesley Longman, 1997 (see p. 111).
- [180] T. Giamarchi. *Interactions in Quantum Fluids*. In: (July 2010). arXiv: 1007.1030 (see p. 111).
- [181] T. Giamarchi, A. Iucci, and C. Berthod. *Lecture Notes: Introduction to Many Body physics*. 2008 (see p. 112).
- [182] G. V. Shlyapnikov. *Lecture Notes: Ultracold quantum Gases Part 2 - Degenerate Fermi gases* (see p. 112).
- [183] C. A. Regal and D. S. Jin. *Measurement of Positive and Negative Scattering Lengths in a Fermi Gas of Atoms*. In: Physical Review Letters 90.23 (June 2003), p. 230404 (see p. 114).
- [184] S. Gupta. *Radio-Frequency Spectroscopy of Ultracold Fermions*. In: Science 300.5626 (June 2003), pp. 1723–1726 (see pp. 114, 117).
- [185] C. Chin. *Observation of the Pairing Gap in a Strongly Interacting Fermi Gas*. In: Science 305.5687 (Aug. 2004), pp. 1128–1130 (see p. 114).
- [186] Y. Shin, C. H. Schunck, A. Schirotzek, and W. Ketterle. *Tomographic rf Spectroscopy of a Trapped Fermi Gas at Unitarity*. In: Physical Review Letters 99.9 (Aug. 2007), p. 090403 (see p. 114).
- [187] A. Schirotzek, Y.-i. Shin, C. H. Schunck, and W. Ketterle. *Determination of the Superfluid Gap in Atomic Fermi Gases by Quasiparticle Spectroscopy*. In: Physical Review Letters 101.14 (Oct. 2008), p. 140403 (see p. 114).
- [188] J. T. Stewart, J. P. Gaebler, and D. S. Jin. *Using photoemission spectroscopy to probe a strongly interacting Fermi gas*. In: Nature 454.7205 (Aug. 2008), pp. 744–747 (see p. 114).
- [189] M. W. Zwierlein, C. A. Stan, C. H. Schunck, S. M. F. Raupach, S. Gupta, Z. Hadzibabic, and W. Ketterle. *Observation of Bose-Einstein Condensation of Molecules*. In: Physical Review Letters 91.25 (Dec. 2003), p. 250401 (see p. 114).
- [190] C. A. Regal, C. Ticknor, J. L. Bohn, and D. S. Jin. *Creation of ultracold molecules from a Fermi gas of atoms*. In: Nature 424.6944 (July 2003), pp. 47–50 (see p. 114).

- [191] C. H. Schunck, Y. Shin, A. Schirotzek, M. W. Zwierlein, and W. Ketterle. *Pairing Without Superfluidity: The Ground State of an Imbalanced Fermi Mixture*. In: *Science* 316.5826 (May 2007), pp. 867–870 (see p. 114).
- [192] C. H. Schunck, Y.-i. Shin, A. Schirotzek, and W. Ketterle. *Determination of the fermion pair size in a resonantly interacting superfluid*. In: *Nature* 454.7205 (Aug. 2008), pp. 739–743 (see p. 114).
- [193] H. J. Schulz, G. Cuniberti, and P. Pieri. *Fermi liquids and Luttinger liquids*. In: (1998). arXiv: 9807366v2 [cond-mat] (see pp. 114–116).
- [194] F. D. M. Haldane. *Luttinger liquid theory of one-dimensional quantum fluids: I. Properties of the Luttinger model and their extension to the general 1D interacting spinless Fermi gas*. In: *J. Phys. C: Solid State Phys* 14 (1981), pp. 2585–2609 (see p. 114).
- [195] A. Recati, P. O. Fedichev, W. Zwerger, and P. Zoller. *Fermi one-dimensional quantum gas: Luttinger liquid approach and spin charge separation*. In: *Journal of Optics B: Quantum and Semiclassical Optics* 5.2 (Apr. 2003), S55–S64 (see pp. 114–116).
- [196] H. Moritz, T. Stöferle, M. Köhl, and T. Esslinger. *Exciting Collective Oscillations in a Trapped 1D Gas*. In: *Physical Review Letters* 91.25 (Dec. 2003), p. 250402. arXiv: 0307607 [cond-mat] (see p. 114).
- [197] D. S. Petrov, G. V. Shlyapnikov, and J. T. M. Walraven. *Regimes of Quantum Degeneracy in Trapped 1D Gases*. In: *Physical Review Letters* 85.18 (Oct. 2000), pp. 3745–3749. arXiv: 0006339 [cond-mat] (see p. 114).
- [198] W. Zwerger. *The BCS $\hat{=}$ BEC Crossover and the Unitary Fermi Gas (Lecture Notes in Physics)*. Vol. 836. 2012. arXiv: 1211.6245 (see p. 115).
- [199] X.-W. Guan, M. T. Batchelor, and C. Lee. *Fermi gases in one dimension: From Bethe ansatz to experiments*. In: *Reviews of Modern Physics* 85.4 (Nov. 2013), pp. 1633–1691. arXiv: 1301.6446 (see p. 115).
- [200] T. A. Hilker, G. Salomon, F. Grusdt, A. Omran, M. Boll, E. Demler, I. Bloch, and C. Gross. *Revealing hidden antiferromagnetic correlations in doped Hubbard chains via string correlators*. In: *Science* 357.6350 (Aug. 2017), pp. 484–487 (see p. 116).
- [201] A. Imambekov, T. L. Schmidt, and L. I. Glazman. *One-dimensional quantum liquids: Beyond the Luttinger liquid paradigm*. In: *Reviews of Modern Physics* 84.3 (Sept. 2012), pp. 1253–1306. arXiv: 1110.1374 (see pp. 116, 117).
- [202] M. Khodas, M. Pustilnik, A. Kamenev, and L. I. Glazman. *Fermi-Luttinger liquid: Spectral function of interacting one-dimensional fermions*. In: *Physical Review B* 76.15 (Oct. 2007), p. 155402. arXiv: 0702505 [cond-mat] (see p. 117).
- [203] P. Törmä. *Physics of ultracold Fermi gases revealed by spectroscopies*. In: *Physica Scripta* (2016). arXiv: 1511.03109 (see p. 117).

- [204] Q. Chen, Y. He, C.-C. Chien, and K. Levin. *Theory of radio frequency spectroscopy experiments in ultracold Fermi gases and their relation to photoemission in the cuprates*. In: Reports on Progress in Physics 72.12 (Dec. 2009), p. 122501. arXiv: 0810.1940 (see p. 117).
- [205] X.-X. RUAN, H. GONG, L. DU, Y. JIANG, W.-M. SUN, and H.-S. ZONG. *Momentum Resolved Radio Frequency Spectroscopy of a Unitary Fermi Gas With Extended Gmb Approximation*. In: Modern Physics Letters B 28.04 (2014), p. 1450028 (see p. 117).
- [206] R. Haussmann, M. Punk, and W. Zwerger. *Spectral functions and rf response of ultracold fermionic atoms*. In: Physical Review A 80.6 (Dec. 2009), p. 063612. arXiv: 0904.1333 (see p. 117).
- [207] Q. Chen and K. Levin. *Momentum resolved radio frequency spectroscopy in trapped fermi gases*. In: Physical Review Letters 102.19 (2009), pp. 1–4. arXiv: 0807.0830 (see p. 117).
- [208] M. Punk and W. Zwerger. *Theory of rf-Spectroscopy of Strongly Interacting Fermions*. In: Physical Review Letters 99.17 (Oct. 2007), p. 170404. arXiv: 0707.0792 (see p. 117).
- [209] E. V. Doggen and J. J. Kinnunen. *Momentum-resolved spectroscopy of a Fermi liquid*. In: Scientific Reports 5 (2015). arXiv: 1411.7207 [cond-mat.quant-gas] (see p. 118).
- [210] J. T. Stewart, J. P. Gaebler, and D. S. Jin. *Using photoemission spectroscopy to probe a strongly interacting Fermi gas*. In: Nature 454.7205 (Aug. 2008), pp. 744–747. arXiv: 0805.0026 (see p. 118).
- [211] B. Mukherjee, Z. Yan, P. B. Patel, Z. Hadzibabic, T. Yefsah, J. Struck, and M. W. Zwierlein. *Homogeneous Atomic Fermi Gases*. In: Physical Review Letters (2017). arXiv: 1610.10100 (see p. 119).
- [212] S. Tung, G. Lamporesi, D. Lobser, L. Xia, and E. A. Cornell. *Observation of the Presuperfluid Regime in a Two-Dimensional Bose Gas*. In: Physical Review Letters 105.23 (Dec. 2010), p. 230408. arXiv: 1009.2475 (see p. 119).
- [213] A. H. Van Amerongen, J. J. Van Es, P. Wicke, K. V. Kheruntsyan, and N. J. Van Druten. *Yang-Yang thermodynamics on an atom chip*. In: Physical Review Letters (2008). arXiv: 0709.1899 (see p. 119).
- [214] P. A. Murthy, D. Kedar, T. Lompe, M. Neidig, M. G. Ries, A. N. Wenz, G. Zürn, and S. Jochim. *Matter-wave Fourier optics with a strongly interacting two-dimensional Fermi gas*. In: Physical Review A 90.4 (Oct. 2014), p. 043611. arXiv: 1408.4680 (see pp. 119, 120).

- [215] I. Shvarchuck, C. Buggle, D. S. Petrov, K. Dieckmann, M. Zielonkowski, M. Kemmann, T. G. Tiecke, W. von Klitzing, G. V. Shlyapnikov, and J. T. Walraven. *Bose-Einstein Condensation into Nonequilibrium States Studied by Condensate Focusing*. In: Physical Review Letters (2002). arXiv: 0207599 [cond-mat] (see p. 119).
- [216] S. Biermann, A. Georges, A. Lichtenstein, and T. Giamarchi. *Deconfinement Transition and Luttinger to Fermi Liquid Crossover in Quasi-One-Dimensional Systems*. In: Physical Review Letters 87.27 (Dec. 2001), p. 276405. arXiv: 0107633 [cond-mat] (see p. 121).
- [217] E. Arrigoni. *Crossover to Fermi-liquid behavior for weakly coupled Luttinger liquids in the anisotropic large-dimension limit*. In: Physical Review B 61.12 (Mar. 2000), pp. 7909–7929 (see p. 121).
- [218] C. Castellani, C. Di Castro, and W. Metzner. *Dimensional crossover from Fermi to Luttinger liquid*. In: Physical Review Letters 72.3 (Jan. 1994), pp. 316–319 (see p. 121).
- [219] M. Greiner. *Ultracold quantum gases in three-dimensional optical lattice potentials*. PhD thesis. 2003, pp. 1–134 (see p. 124).
- [220] R. A. Williams. *Vortex nucleation in a rotating optical lattice of ultracold atoms*. PhD thesis. 2009, pp. 1–194 (see p. 126).
- [221] N. D. M. Neil W. Ashcroft. *Solid State Physics - Ashcroft, Neil W, Mermin, David N*. Hartcourt College Publishers, 1976, p. 826 (see p. 127).
- [222] M. Born, E. Wolf, A. B. Bhatia, P. C. Clemmow, D. Gabor, A. R. Stokes, A. M. Taylor, P. A. Wayman, and W. L. Wilcock. *Principles of Optics*. Cambridge: Cambridge University Press, 1999 (see p. 131).
- [223] G. K. Campbell. *87Rubidium Bose-Einstein Condensates in Optical Lattices*. PhD thesis. MASSACHUSETTS INSTITUTE OF TECHNOLOGY, 2006, pp. 1–142 (see p. 134).
- [224] T. Rom. *Bosonische und fermionische Quantengase in dreidimensionalen optischen Gittern*. In: (2009), p. 389 (see p. 134).
- [225] P. L. Gould, G. A. Ruff, and D. E. Pritchard. *Diffraction of atoms by light: The near-resonant Kapitza-Dirac effect*. In: Physical Review Letters 56.8 (Feb. 1986), pp. 827–830 (see p. 134).
- [226] P. J. Martin, B. G. Oldaker, A. H. Miklich, and D. E. Pritchard. *Bragg scattering of atoms from a sanding light wave*. In: Physical Review Letters 60.6 (1988), pp. 515–518 (see p. 134).
- [227] A. D. Cronin, J. Schmiedmayer, and D. E. Pritchard. *Optics and interferometry with atoms and molecules*. In: Reviews of Modern Physics 81.3 (July 2009), pp. 1051–1129. arXiv: 0712.3703 (see p. 135).

- [228] B. E. A. Saleh and M. C. Teich. *Fundamentals of Photonics*. Wiley Series in Pure and Applied Optics. New York, USA: John Wiley & Sons, Inc. Aug. 1991 (see pp. [144](#), [187](#), [190](#), [207](#)).
- [229] J. Dalibard. *Lames de phase*. 2007 (see pp. [144](#), [147](#)).
- [230] N. Passilly, F. Treussart, R. Hierle, R. de Saint Denis, K. Aït-Ameur, and J.-F. Roch. *Simple interferometric technique for generation of a radially polarized light beam*. In: Journal of the Optical Society of America A 22.5 (2005), p. 984 (see p. [145](#)).
- [231] N. L. Smith, W. H. Heathcote, G. Hechenblaikner, E. Nugent, and C. J. Foot. *Quasi-2D confinement of a BEC in a combined optical and magnetic potential*. In: Journal of Physics B: Atomic, Molecular and Optical Physics 38.3 (Feb. 2005), pp. 223–235. arXiv: 0410101 [cond-mat] (see p. [145](#)).
- [232] L. Chomaz. *Coherence and superfluidity of Bose gases in reduced dimensions : from harmonic traps to uniform fluids Lauriane Chomaz*. PhD thesis. École Normale Supérieure Paris, 2015 (see p. [146](#)).
- [233] R. de Saint Denis, N. Passilly, M. Laroche, T. Mohammed-Brahim, and K. Aït-Ameur. *Beam-shaping longitudinal range of a binary diffractive optical element*. In: Applied optics 45.31 (2006), pp. 8136–8141 (see p. [147](#)).
- [234] R. W. Floyd and L. Steinberg. *Adaptive algorithm for spatial greyscale*. In: Proc Soc Inf Disp 17 (1976), pp. 75–77 (see pp. [153](#), [189](#)).
- [235] J. Liang, R. N. Kohn, Jr., M. F. Becker, and D. J. Heinzen. *1.5% root-mean-square flat-intensity laser beam formed using a binary-amplitude spatial light modulator*. In: Applied Optics 48.10 (Apr. 2009), p. 1955 (see p. [154](#)).
- [236] J. Liang, R. N. Kohn, Jr., M. F. Becker, and D. J. Heinzen. *High-precision laser beam shaping using a binary-amplitude spatial light modulator*. In: Applied Optics 49.8 (Mar. 2010), p. 1323 (see p. [154](#)).
- [237] A. B. Bardon, S. Beattie, C. Luciuk, W. Cairncross, D. Fine, N. S. Cheng, G. J. Edge, E. Taylor, S. Zhang, S. Trotzky, and J. H. Thywissen. *Transverse demagnetization dynamics of a unitary fermi gas*. In: Science (2014). arXiv: 1310.5140 (see p. [156](#)).
- [238] S. Trotzky, S. Beattie, C. Luciuk, S. Smale, A. B. Bardon, T. Enss, E. Taylor, S. Zhang, and J. H. Thywissen. *Observation of the Leggett-Rice effect in a unitary Fermi gas*. In: Physical Review Letters (2015). arXiv: 1410.8517 (see p. [156](#)).
- [239] C. Luciuk, S. Smale, F. Böttcher, H. Sharum, B. A. Olsen, S. Trotzky, T. Enss, and J. H. Thywissen. *Observation of Quantum-Limited Spin Transport in Strongly Interacting Two-Dimensional Fermi Gases*. In: Physical Review Letters (2017). arXiv: 1612.00815 (see p. [156](#)).

- [240] Y. Jiang, D. V. Kurlov, X.-W. Guan, F. Schreck, and G. V. Shlyapnikov. *Itinerant ferromagnetism in one-dimensional two-component Fermi gases*. In: Physical Review A 94.1 (July 2016), p. 011601. arXiv: arXiv:1512.01392v1 (see p. 157).
- [241] E. C. Stoner. LXXX. *Atomic moments in ferromagnetic metals and alloys with non-ferromagnetic elements*. In: The London, Edinburgh, and Dublin Philosophical Magazine and Journal of Science 15.101 (May 1933), pp. 1018–1034 (see p. 157).
- [242] D. Pekker, M. Babadi, R. Sensarma, N. Zinner, L. Pollet, M. W. Zwierlein, and E. Demler. *Competition between Pairing and Ferromagnetic Instabilities in Ultracold Fermi Gases near Feshbach Resonances*. In: Physical Review Letters 106.5 (Feb. 2011), p. 050402 (see p. 157).
- [243] C. Sanner, E. J. Su, W. Huang, A. Keshet, J. Gillen, and W. Ketterle. *Correlations and Pair Formation in a Repulsively Interacting Fermi Gas*. In: Physical Review Letters 108.24 (June 2012), p. 240404 (see p. 157).
- [244] G.-B. Jo, Y.-R. Lee, J.-H. Choi, C. A. Christensen, T. H. Kim, J. H. Thywissen, D. E. Pritchard, and W. Ketterle. *Itinerant Ferromagnetism in a Fermi Gas of Ultracold Atoms*. In: Science 325.5947 (Sept. 2009), pp. 1521–1524 (see p. 157).
- [245] S. E. Gharashi and D. Blume. *Correlations of the Upper Branch of 1D Harmonically Trapped Two-Component Fermi Gases*. In: Physical Review Letters 111.4 (July 2013), p. 045302 (see p. 157).
- [246] X. Cui and T.-L. Ho. *Ground-state ferromagnetic transition in strongly repulsive one-dimensional Fermi gases*. In: Physical Review A 89.2 (Feb. 2014), p. 023611 (see p. 157).
- [247] T. Bourdel, L. Khaykovich, J. Cubizolles, J. Zhang, F. Chevy, M. Teichmann, L. Tarruell, S. J. J. M. F. Kokkelmans, and C. Salomon. *Experimental Study of the BEC-BCS Crossover Region in Lithium 6*. In: Physical Review Letters 93.5 (July 2004), p. 050401 (see p. 158).
- [248] C. A. Regal, M. Greiner, and D. S. Jin. *Lifetime of Molecule-Atom Mixtures near a Feshbach Resonance in K-40*. In: Physical Review Letters 92.8 (Feb. 2004), p. 083201 (see p. 158).
- [249] X. Du, Y. Zhang, and J. E. Thomas. *Inelastic Collisions of a Fermi Gas in the BEC-BCS Crossover*. In: Physical Review Letters 102.25 (June 2009), p. 250402 (see p. 158).
- [250] D. S. Petrov, C. Salomon, and G. V. Shlyapnikov. *Weakly Bound Dimers of Fermionic Atoms*. In: Physical Review Letters 93.9 (Aug. 2004), p. 090404 (see p. 158).
- [251] J. P. D’Incao and B. D. Esry. *Scattering Length Scaling Laws for Ultracold Three-Body Collisions*. In: Physical Review Letters 94.21 (June 2005), p. 213201 (see p. 158).

- [252] V. S. Babichenko and Y. Kagan. *Influence of Cooper pairing on the inelastic processes in a gas of Fermi atoms*. In: *Physical Review A* 85.3 (Mar. 2012), p. 033604 (see p. 158).
- [253] B. D. Esry, C. H. Greene, and H. Suno. *Threshold laws for three-body recombination*. In: *Physical Review A* 65.1 (Dec. 2001), p. 010705 (see p. 158).
- [254] H.-W. Hammer, A. Nogga, and A. Schwenk. *Colloquium : Three-body forces: From cold atoms to nuclei*. In: *Reviews of Modern Physics* 85.1 (Jan. 2013), pp. 197–217 (see p. 158).
- [255] S. Laurent. *Dynamics and stability of a Bose-Fermi mixture: counterflow of superfluids and inelastic decay in a strongly interacting gas*. PhD thesis. 2017 (see p. 159).
- [256] F. Werner. *Atomes froids piégés en interaction résonnante : gaz unitaire et problème à trois corps*. PhD thesis. ENS Paris, 2009 (see p. 159).
- [257] C. D. E. Daniloff. *Three-body losses in a Fermi Gas at unitarity*. 2018 (see p. 159).
- [258] K. Viebahn. *Laser Beam Shaping with a Digital Micromirror Device*. Tech. rep. June. Munich: Ludwig-Maximilians-Universität, 2013 (see pp. 187, 192).
- [259] V. Dagard. *Caractérisation optique d'une matrice de micro-miroirs*. Tech. rep. Paris: Collège de France (see p. 187).
- [260] J.-L. Ville. *Generation of highly tunable light potentials on a two-dimensional degenerate Bose gas*. Tech. rep. October 2014. Paris: Collège de France, 2015 (see p. 187).
- [261] E. Perego. *Generation of arbitrary optical potentials for atomic physics experiments using a Digital Micromirror Device*. Tech. rep. Florence: University of Florence, 2015 (see p. 187).
- [262] R. Santoso. *2D Optical Trapping Potential for the Confinement of Heteronuclear Molecules*. Tech. rep. Singapore: National University of Singapore, 2014 (see p. 187).
- [263] F. Etzold. *Laser Beam Shaping with a Digital Micromirror Device*. Tech. rep. Mainz: Johannes Gutenberg-Universität, 2013 (see p. 187).
- [264] P. P. J. Zupancic. *Dynamic Holography and Beamshaping using Digital Micromirror Devices*. Tech. rep. Cambridge: LMU Munich, Harvard University, 2013, p. 75 (see p. 187).
- [265] S. de Léséleuc. *Digital Micromirror Device*. Tech. rep. August. Zurich: Swiss Federal Institute of Technology, 2007, pp. 1–11 (see p. 187).
- [266] K. Hueck, A. Mazurenko, N. Luick, T. Lompe, and H. Moritz. *Note: Suppression of kHz-frequency switching noise in digital micro-mirror devices*. In: *Review of Scientific Instruments* 88.1 (2017), pp. 1–3. arXiv: 1611.03397 (see p. 187).

- [267] P. Zupancic, P. M. Preiss, R. Ma, A. Lukin, M. Eric Tai, M. Rispoli, R. Islam, and M. Greiner. *Ultra-precise holographic beam shaping for microscopic quantum control*. In: Optics Express 24.13 (June 2016), p. 13881. arXiv: 1604.07653 (see p. 187).
- [268] G. Gauthier, I. Lenton, N. M. Parry, M. Baker, M. J. Davis, H. Rubinsztein-Dunlop, and T. W. Neely. *Direct imaging of a digital-micromirror device for configurable microscopic optical potentials*. In: 3.10 (2016). arXiv: 1605.04928 (see p. 187).
- [269] L. Brandt, C. Muldoon, T. Thiele, J. Dong, E. Brainis, and A. Kuhn. *Spatial light modulators for the manipulation of individual atoms*. In: Applied Physics B 102.3 (Mar. 2011), pp. 443–450. arXiv: 1008.0987 (see p. 187).
- [270] T. Instruments. *Getting Started with TI DLP® Display Technology*. Tech. rep. January. 2015, p. 20 (see p. 188).
- [271] D. Bellem. *Generation of Spatially and Temporally Varying Light Potentials in Optical Lattices*. Tech. rep. Munich, 2011 (see p. 190).
- [272] R. Grimm, M. Weidemüller, and Y. B. Ovchinnikov. *Optical Dipole Traps for Neutral Atoms*. In: 2000, pp. 95–170 (see p. 211).
- [273] M. E. Gehm, K. M. O'Hara, T. A. Savard, and J. E. Thomas. *Dynamics of noise-induced heating in atom traps*. In: Physical Review A 58.5 (Nov. 1998), pp. 3914–3921 (see p. 212).
- [274] J. S. Krauser, J. Heinze, S. Götze, M. Langbecker, N. Fläschner, L. Cook, T. M. Hanna, E. Tiesinga, K. Sengstock, and C. Becker. *Investigation of Feshbach resonances in ultracold K40 spin mixtures*. In: Physical Review A 95.4 (Apr. 2017), p. 042701. arXiv: 1701.02085 (see p. 219).

## Résumé

L'exploration de systèmes quantiques à  $N$  corps fortement corrélés représente l'un des domaines de recherche les plus stimulants de la physique contemporaine. Au cours des trente dernières années, les vapeurs diluées d'atomes neutres en suspension dans le vide et contrôlées par un laser sont devenues une plate-forme polyvalente et formidable pour l'étude de tels systèmes. L'intérêt principal réside dans la capacité d'ajuster arbitrairement la force de l'interaction atomique au moyen de résonances de Feshbach induites magnétiquement, ainsi que la possibilité de créer une large gamme de potentiels via des champs optiques précisément adaptés. Cette thèse présente les résultats récents de l'expérience FerMix, consacrée à l'étude des systèmes quantiques à plusieurs corps fermioniques à des températures ultra-basses utilisant les atomes alcalins  $^{40}\text{K}$  et  $^6\text{Li}$ . Les principaux résultats présentés dans ce texte sont doubles. Premièrement, nous rapportons la caractérisation expérimentale d'une nouvelle résonance de Feshbach (s,d)-wave du  $^{40}\text{K}$ , dont les résultats sont comparés aux prédictions théoriques correspondantes. En particulier, le spectre du taux de perte inélastique est déterminé pour différentes températures et profondeurs de piège, ce qui nous permet d'identifier les pertes en tant que processus à deux corps. De plus, il est confirmé que le canal d'entrée dominant est de type s-wave. À l'aide de modèles d'équation de taux, nous analysons le réchauffement observé de l'ensemble atomique et trouvons que le comportement est cohérent avec l'état lié prévu  $L = 2$  présent dans le canal de sortie. Enfin, nous étudions expérimentalement la dynamique des populations de spin induite par les collisions inélastiques renforcées par résonance dans l'onde d, en observant un bon accord avec nos modèles numériques. En second lieu, nous résumons nos progrès dans l'étude des croisements dimensionnels entre le liquide de Tomonaga-Luttinger en 1D et le liquide de Landau-Fermi en 3D en utilisant les gaz de Fermi de  $^{40}\text{K}$  confinés dans un réseau optique à grand pas. Cela inclut à la fois les considérations de conception fondamentales et l'installation du matériel expérimental requis.

## Mots Clés

Gaz de Fermi ultra-froids, résonances de Feshbach, systèmes quantiques à  $N$  corps fortement corrélés, physique atomique, gaz quantique.

## Abstract

The exploration of strongly correlated quantum many-body systems represents one of the most challenging fields of research of contemporary physics. Over the past thirty years, dilute vapors of neutral atoms suspended in vacuum and controlled with laser light have become a versatile and powerful platform for the study of such systems. At the very heart lies the ability to arbitrarily tune the interaction strength by means of magnetically induced Feshbach resonances as well as the possibility to create a wide range of potential landscapes via precisely tailored optical fields. This thesis reports on the recent results of the FerMix experiment, which is dedicated to the study of fermionic quantum many-body systems at ultralow temperatures using the Alkali atoms  $^{40}\text{K}$  and  $^6\text{Li}$ . The main results presented in this text are twofold. First, we report on the experimental characterization of a novel (s,d)-wave Feshbach resonance in  $^6\text{Li}$ , the results of which are compared to the corresponding theoretical predictions. In particular, the spectrum of the inelastic loss rate is determined for different temperatures and trap depths, which enables us to identify the losses as two-body processes. Moreover, the dominant entrance channel is confirmed to be s-wave in nature. Using rate equation models we analyze the observed heating of the atomic ensemble and find the behavior to be consistent with the predicted  $L = 2$  bound state present in the exit channel. Finally, we investigate experimentally the dynamics of the spin populations driven by resonantly enhanced inelastic collisions in d-wave, observing good agreement with our numerical models. Second, we summarize our progress towards the study of dimensional crossovers between the Tomonaga-Luttinger liquid in 1D and the Landau-Fermi liquid in 3D using Fermi gases of  $^{40}\text{K}$  confined in a large spacing optical lattice. This includes both the fundamental design considerations as well as the implementation of the required experimental hardware.

## Keywords

Ultracold Fermi gases, Feshbach resonances, strongly correlated quantum many-body systems, atomic physics, quantum gases.